

SANDIA REPORT

SAND2020-9562

Printed September 2020



Sandia
National
Laboratories

Summary of Marine and Hydrokinetic (MHK) Composites Testing at Montana State University

David A. Miller
Daniel D. Samborsky
Mark T. Stoffels
Michael M. Voth
Jake D. Nunemaker
Kai J. Newhouse
Bernadette A. Hernandez-Sanchez

Prepared by
Sandia National Laboratories
Albuquerque, New Mexico
87185 and Livermore,
California 94550

Issued by Sandia National Laboratories, operated for the United States Department of Energy by National Technology & Engineering Solutions of Sandia, LLC.

NOTICE: This report was prepared as an account of work sponsored by an agency of the United States Government. Neither the United States Government, nor any agency thereof, nor any of their employees, nor any of their contractors, subcontractors, or their employees, make any warranty, express or implied, or assume any legal liability or responsibility for the accuracy, completeness, or usefulness of any information, apparatus, product, or process disclosed, or represent that its use would not infringe privately owned rights. Reference herein to any specific commercial product, process, or service by trade name, trademark, manufacturer, or otherwise, does not necessarily constitute or imply its endorsement, recommendation, or favoring by the United States Government, any agency thereof, or any of their contractors or subcontractors. The views and opinions expressed herein do not necessarily state or reflect those of the United States Government, any agency thereof, or any of their contractors.

Printed in the United States of America. This report has been reproduced directly from the best available copy.

Available to DOE and DOE contractors from

U.S. Department of Energy
Office of Scientific and Technical Information
P.O. Box 62
Oak Ridge, TN 37831

Telephone: (865) 576-8401
Facsimile: (865) 576-5728
E-Mail: reports@osti.gov
Online ordering: <http://www.osti.gov/scitech>

Available to the public from

U.S. Department of Commerce
National Technical Information Service
5301 Shawnee Rd
Alexandria, VA 22312

Telephone: (800) 553-6847
Facsimile: (703) 605-6900
E-Mail: orders@ntis.gov
Online order: <https://classic.ntis.gov/help/order-methods/>



ABSTRACT

Marine and hydrokinetic (MHK) energy technologies convert the energy of waves, tides, and river and ocean currents into electricity. The primary structure of MHK energy devices have difficult and challenging environments for which fiber reinforced plastics are often considered. For cost benefits, glass fiber reinforced plastics (GFRP) are the most prevalent system under consideration. Montana State University (MSU) and Sandia National Laboratories (SNL) have performed research into the moisture effects on the stiffness, strength, and damage of GFRPs for many years. This paper presents a summary of a portion of this effort and also provides references to the thesis and conferences that contain the detailed information. The results include models of moisture absorption, effects of stress on moisture uptake, effects of moisture on damage modes and development, laminate stacking order effects, and culminates with moisture uptake effects on a large sample of industry collected coupons.

ACKNOWLEDGEMENTS

The authors thank the Composites Engineering Research Laboratory, Composites Technology Development Inc., Hygrateck, Janicki Industries, Ocean Renewable Power Company, Polyone, and Verdant Power for contributing samples for evaluation. The authors also thank Lauren Ruedy, Ramesh Talreja, Budi Gunawan, James Nicholas, Francisco Presuel-Moreno, George Bonheyo, Scott Hughes, and Paul Murdy for technical discussions. This work was supported by the US Department of Energy, EERE Water Power Technologies Program. Sandia National Laboratories is a multimission laboratory managed and operated by National Technology and Engineering Solutions of Sandia LLC, a wholly owned subsidiary of Honeywell International Inc., for the U.S. Department of Energy's National Nuclear Security Administration under contract DE-NA0003525.

CONTENTS

1. Stress Assisted Diffusion	15
1.1. Stress Effects	16
1.2. Theoretical Background.....	16
1.2.1. Fiber Reinforced Polymer Composites.....	16
1.2.2. Diffusion.....	18
1.2.3. Fickian Diffusion.....	19
1.2.4. Diffusivity.....	20
1.2.5. Diffusivity of Unidirectional Fiber Composites	20
1.3. Maximum Absorption Capacity of Unidirectional Fiber Composites	21
1.3.1. Thermal and Pressure Effects	21
1.3.2. Free Volume.....	22
1.3.3. Maximum Absorption Capacity	23
1.3.4. Diffusivity.....	24
1.4. Model Development.....	24
1.4.1. Free Volume.....	24
1.4.2. Changes in Diffusion Parameters	25
1.4.3. Maximum Absorption Capacity	25
1.4.4. The Diffusion Coefficient.....	26
1.5. Finite Element Simulation of Diffusion.....	27
1.5.1. Overview	27
1.6. Thermal-Moisture Diffusion Analogy	27
1.6.1. Model Geometry	28
1.6.2. Boundary Conditions.....	29
1.7. Experimental Procedures.....	34
1.7.1. Experiment Overview	34
1.7.2. Materials.....	34
1.7.3. Manufacturing Procedures.....	35
1.7.4. Weight Gain Measurements	38
1.8. Results and Discussion.....	39
1.8.1. Overview	39
1.9. Summary of Results.....	40
1.9.1. Maximum Moisture Content	40
1.9.2. Diffusivity.....	45
1.10. Conclusions for Stress Assisted Diffusion.....	49
2. Damage Behavior of GFRP	50
2.1. Hygrothermally-Aged Composites.....	50
2.1.1. Damage/Defect Effects on Diffusion.....	50
2.1.2. Hygrothermal Aging Effects on Mechanical Properties	50
2.1.3. Hygrothermal Degradation Mechanisms.....	51
2.1.4. Acoustic Emission	51
2.1.5. AE Analysis Techniques	52
2.1.6. AE and Hygrothermal Aging	55
2.2. Matrix Characterization.....	55
2.2.1. Thermal Analysis: DSC	55
2.2.2. DSC Results	56
2.2.3. Neat Resin Diffusion and Swelling.....	59

2.2.4.	Neat Resin Diffusion and Swelling Results.....	60
2.3.	Static Tests.....	62
2.3.1.	Test Design.....	62
2.4.	Experimental Methods.....	64
2.4.1.	Materials and Manufacturing.....	64
2.4.2.	Sample Conditioning.....	65
2.4.3.	Mechanical Testing Procedures.....	65
2.4.4.	Acoustic Emission Setup and Data Collection.....	66
2.5.	Results.....	67
2.5.1.	Moisture Absorption and Desorption.....	67
2.5.2.	Theoretical Swelling Stresses in FRP laminates.....	69
2.5.3.	Lamina-Swelling Results.....	71
2.5.4.	Hygrothermal-aging Damage.....	72
2.5.5.	Mechanical Properties.....	75
2.5.6.	Stress-Strain Response.....	78
2.5.7.	Sample Failure Inspection.....	81
2.5.8.	Acoustic Emission.....	84
2.5.9.	Frequency Analysis.....	91
2.6.	Wave Propagation and Attenuation.....	95
2.6.1.	Sensor Test: Guided Ultrasonic.....	96
2.7.	Conclusions from Damage Progression.....	99
3.	Moisture Effect on Stacking Sequence and Off-Axis Strength.....	100
3.1.	Test Design.....	100
3.1.1.	Materials.....	100
3.1.2.	Water Submersion.....	101
3.1.3.	Test Matrices.....	101
3.2.	Visual Inspection of Damage.....	102
3.3.	Off-Axis Strength Reduction.....	103
3.3.1.	Moisture Absorption.....	103
3.3.2.	Static Strength Reduction.....	104
3.3.3.	AE Analysis.....	105
3.4.	Partial Saturation Strength Reduction.....	115
3.4.1.	Static Strength.....	115
3.4.2.	AE Data.....	116
3.5.	Conclusions For Off-Axis Plies and Stacking Sequence.....	120
4.	Hygrothermal Aging and Acoustic Emission Study of diverse Materials for MHK Applications.....	121
4.1.	Material Summary.....	121
4.2.	Experimental Methods.....	122
4.2.1.	Sample Preparation.....	122
4.2.2.	Conditioning and Moisture Uptake Measurements.....	123
4.3.	Results.....	123
4.3.1.	Moisture Absorption.....	123
4.4.	Mechanical Properties.....	126
4.4.1.	Acoustic Emission.....	132
4.4.2.	Frequency Content.....	134
4.5.	Conclusions of Hygrothermal Aging and Acoustic Emission of Diverse Materials.....	135

LIST OF FIGURES

Figure 1. Generalized moisture uptake curve for an epoxy composite.	15
Figure 2. A chart from a study at Montana State University demonstrating the loss in mechanical strength experienced by a fully saturated epoxy glass composite.	16
Figure 3. Cross section of typical [45/45] _s epoxy-glass laminate. SEM x15. †.....	17
Figure 4. Cross section of typical [45/45] _s epoxy-glass laminate. SEM x50 †.....	17
Figure 5. Cross section of typical [45/45] _s epoxy-glass laminate. SEM x200. Images: Montana State University, Composite Technologies Group, 2011.....	18
Figure 6. A simple diagram showing the diffusion process, note the movement of particles from high concentration to low concentration.	18
Figure 7. Change of moisture content with the square root of time. [1].....	20
Figure 8. Moisture uptake curves demonstrating the change in diffusivity due to changes in ambient temperature. [10].....	22
Figure 9. A Simple representation of how polymeric chains end, resulting in a void, which becomes free, unfilled, volume within the structure.....	23
Figure 10. Meshed two-dimensional finite element geometry at the sample mid-plane, PLANE55 element type.....	29
Figure 11. Meshed three-dimensional finite element geometry, one-eighth cross section of sample, SOLID70 element type.....	29
Figure 12. Saturation profile throughout the two-dimensional cross section at <i>time</i> = 50 hours. All edges are subjected to saturation conditions. Scale on bottom represents the wetness ratio, where a value of one denotes full saturation. Note: minimum saturation ratio value of only 0.089526 near center of the sample.....	30
Figure 13. Saturation profile throughout the two-dimensional cross section at <i>time</i> = 200 hours. Note: minimum saturation ratio value of 0.488952.	31
Figure 14. Saturation profile throughout the two-dimensional cross section at <i>time</i> = 500 hours. Note: minimum saturation ratio value of 0.867305.	31
Figure 15. Saturation profile throughout the two-dimensional cross section at <i>time</i> = 1200 hours. Note: minimum saturation value of 0.994422. Consequently, at this time the sample is very nearly fully saturated.	32
Figure 16. Saturation profile throughout the two-dimensional cross section at <i>time</i> = 2000 hours. Note: minimum saturation value of 0.999855. The sample has reached full saturation.....	32
Figure 17. A typical saturation ratio concentration profile of the three-dimensional cross section geometry of the sample. Note only three sides of the samples are exposed.....	33
Figure 18. Configuration for vacuum assisted resin transfer molding process.....	36
Figure 19. A completed composite sample as well as the springs used to provide the tensile stress to the sample. Note, at the right the PVC section is used to mitigate out of axis bending of sample as the spring has a large length.	38
Figure 20. Experimental average moisture gain curves for all samples considered. Note the dashed lines represent extrapolated data due to sample fracture of the 45 and 90-degree 30 MPa samples.	39
Figure 21. Experimental average weight gain curves for the 0 MPa samples.	40
Figure 22. Experimental average weight gain curves for the 18 MPa samples. The control curve is an average of all fiber angles of the 0 MPa samples shown in Figure 21.	41
Figure 23. Experimental average weight gain curves for the 30 MPa samples. The control curve is an average of all fiber angles of the 0 MPa samples shown in Figure 21. Note the dashed lines represent extrapolated data due to sample fracture of the 45 and 90-degree samples.	41

Figure 24. Fractured 45 and 90-degree 30 MPa samples alongside unstressed control samples demonstrating the severity of cracking seen within the structure of the samples.	42
Figure 25. 45-degree 0 MPa control sample alongside 30 MPa fractured sample detailing cracking in the epoxy.....	43
Figure 26. 90-degree 0 MPa sample alongside 30 MPa fractured sample detailing cracking in the epoxy.....	43
Figure 27. Initial linear portion of all moisture uptake curves, showing the relative changes in diffusivity between fiber angles and tensile loading. Where steeper slope represents a higher value of diffusivity.....	45
Figure 28. Initial linear portion of the moisture uptake curves for the 0-degree samples at all three magnitudes of applied tensile stress.	46
Figure 29. Initial linear portion of the moisture uptake curves for the 20-degree samples at all three magnitudes of applied tensile stress.	46
Figure 30. Initial linear portion of the moisture uptake curves for the 45-degree samples at all three magnitudes of applied tensile stress.	47
Figure 31. Initial linear portion of the moisture uptake curves for the 90-degree samples at all three magnitudes of applied tensile stress.	47
Figure 32. Typical AE waveform features.....	52
Figure 33. AE Data collection and processing flow chart.	53
Figure 34. FFT-Peak-frequency bins from literature review and previous work at MSU.....	54
Figure 35. DSC heating curves showing T_g for Hexion 135/1366 with 4% moisture by mass.....	56
Figure 36. Example second-cycle heating curves for DSC samples of each condition.....	58
Figure 37. T_g results for hygrothermally aged Hexion 135/1366.	58
Figure 38. A 3-piece mold for manufacturing neat resin cubes.	59
Figure 39. Neat resin cube bulk diffusion.....	60
Figure 40. Swelling strains during transient diffusion of neat resin cubes.	61
Figure 41. Neat resin cubes aged 5000 hours (left) and control (right).....	62
Figure 42. Cross section of swelling damage of neat resin (Hexion 135/1366) under an optical microscope (5X).....	62
Figure 43. Tensile test experimental setup.	66
Figure 44. Tensile test sensor layout.	66
Figure 45. Bulk moisture absorption curves.....	68
Figure 46. Thickness-normalized absorption curves with theoretical fickian diffusion.....	68
Figure 47. Bulk moisture desorption curves.....	69
Figure 48. Cross-ply hygrothermal stress distribution (k = lamina number; ϑ = ply angle).	71
Figure 49. Visible damage from hygrothermal aging in the cross-ply laminate.....	72
Figure 50. SEM: Crack in a backing strand in un-tested, saturated, 2-ply laminate.....	73
Figure 51. SEM: High magnification of crack in saturated 2-ply coupon.....	74
Figure 52. SEM: crack in outer 90° ply of saturated, untested, 4-ply laminate.....	74
Figure 53. Ultimate strengths for E-LT 3800/Epoxy system.....	76
Figure 54. Ultimate loads for E-LT 3800/Epoxy System.	77
Figure 55. Elastic moduli for E-LT 3800/Epoxy system.....	78
Figure 56. Stress-strain response of $[90]_2$ samples.....	79
Figure 57. Stress-strain response of $[0]_2$ samples.....	80
Figure 58. Stress-strain response of $[0/90]_s$ samples.....	80
Figure 59. Stress-strain response of $[90/0]_s$ samples.....	81
Figure 60. Failed $[90]_2$ coupons: Saturated (top), Dry (middle) desorbed (bottom).....	82

Figure 61. Failed [0] ₂ coupons.....	83
Figure 62. Failed [0/90] _s coupons.	83
Figure 63. Failed [90/0] _s coupons.	84
Figure 64. Average number of AE events.....	86
Figure 65. Accumulated AE energy for [90] ₂ samples.....	87
Figure 66. Accumulated AE energy for [0] ₂ samples.....	88
Figure 67. Accumulated AE energy for [90/0] _s samples.....	88
Figure 68. Accumulated AE energy for [0/90] _s samples.....	89
Figure 69. Total accumulated AE energies.	89
Figure 70. AE damage initiation strains.....	90
Figure 71. Frequency bin percentages [90] ₂	92
Figure 72. Frequency bin percentages [0] ₂	93
Figure 73. Frequency bin percentages [0/90] _s	94
Figure 74. Frequency bin percentages [90/0] _s	95
Figure 75. Root cause of the reduction in AE response.....	96
Figure 76. Sensor test schematic.....	97
Figure 77. Sensor test received amplitude for untested two-ply laminates.	98
Figure 78. Coupon 2442-5 and the damage seen after the coupon was removed from the saltwater bath.....	102
Figure 79. Coupon 2444-11 and the damage after the coupon was removed from the saltwater bath.....	103
Figure 80. Moisture absorption for off-axis samples to study the effects of fiber angle and moisture diffusion on static strength and AE signatures.....	104
Figure 81. Static strength for both dry and saturated coupons at various fiber angles. Consistent failures occurred for all layups and conditions.....	105
Figure 82. Percentage of damage mechanisms for [±15] samples. Frequency scatter plots are shown to the right, showing the development of damage throughout the test.....	107
Figure 83. Percentage of damage mechanisms for [±30] samples. Frequency scatter plots are shown to the right, showing the development of damage throughout the test.....	108
Figure 84. Percentage of damage mechanisms for [±45] samples. Frequency scatter plots are shown to the right, showing the development of damage throughout the test.....	109
Figure 85. Percentage of damage mechanisms for [15] ₂ samples. Frequency scatter plots are shown to the right, showing the development of damage throughout the test.....	110
Figure 86. Percentage of damage mechanisms for [30] ₂ samples. Frequency scatter plots are shown to the right, showing the development of damage throughout the test.....	111
Figure 87. Percentage of damage mechanisms for [45] ₂ samples. Frequency scatter plots are shown to the right, showing the development of damage throughout the test.....	112
Figure 88. Frequency distribution plotted against stress for a dry [±15] sample.....	113
Figure 89. Frequency distribution plotted against stress for a saturated [±15] sample.....	114
Figure 90. Ultimate strength vs time soaked for [0/90] _s and [90/0] _s coupons. Note: five tests performed for each layup at each time step.....	115
Figure 91. Ultimate strength vs % weight gain for [0/90] _s and [90/0] _s coupons. Note: five tests performed for each layup at each time step.....	116
Figure 92. Bin percentages for both layups in the control set.....	117
Figure 93. Percentage of AE events in each bin for [0/90] _s samples, varying moisture percentage.....	118
Figure 94. Percentage of AE events in each bin for [90/0] _s samples, varying moisture percentage.....	119
Figure 95. Mass uptake measurement curves for thermoplastic matrix systems.....	123
Figure 96. Mass uptake measurement curves for thermoset matrix systems.....	124

Figure 97. Mass uptake measurement curves for carbon and carbon-glass hybrid systems.....	124
Figure 98. Examples of failed coupons of MHK study materials (P series) showing common failure modes for these materials.	128
Figure 99. Examples of failed coupons of MHK study materials (J1-5, CE6, & N1) showing typical failure modes.	129
Figure 100. Examples of failed coupons of MHK study materials (J6-8 & CE1-5) showing typical failure modes.....	130
Figure 101. Summary of modulus degradation from conditioning. Error bars are range.....	130
Figure 102. Ultimate strength degradation from conditioning. Error bars are range.....	131
Figure 103. Failure strain degradation from conditioning. Error bars are range.....	131
Figure 104. Mean number of AE events for MHK study materials showing variability/consistency and the greater number of events from thermoplastics.....	132
Figure 105. Mean absolute energy per AE event showing variability.	133
Figure 106. Mean accumulated absolute energy per coupon showing variability.	133
Figure 107. Peak spectral frequency versus strain for glass and carbon fabric quasi-isotropic laminates.	134
Figure 108. Peak spectral frequency versus Strain (Top) and cumulative peak spectral frequency histogram (Bottom) for CE1, 2, 3, & 4 showing frequency shift in interphase activity (~150-250 kHz).	135

LIST OF TABLES

Table 1. Thermal-Moisture Diffusion analogy FEA input properties	27
Table 2. Material properties of Momentive Epikure resin system. UTS and UCS represent ultimate tensile and compressive strengths respectively.....	34
Table 3. Material properties from SNL/MSU/DOE database for Saertex-Hexion [0] ₂ composite plate. The designations 1 and 2 represent the material directions.	35
Table 4. Summary detailing the total number of each sample variation manufactured. Recall θ is the fiber angle, ϕ_f is the fiber volume fraction, and σ_x is the magnitude of the tensile stress applied.....	36
Table 5. Experimental, finite element model, and calculated values for the maximum moisture content level. Note the experimental values are presented as an average of all samples of that fiber angle, fiber volume fraction, and stress level.....	44
Table 6. Percent error from experimental maximum moisture content data.	44
Table 7. Experimental, finite element model, and calculated values for the diffusion coefficient. Note the experimental values are presented as an average of all samples of that fiber angle, fiber volume fraction, and stress level.....	48
Table 8. Percent error from experimental diffusivity data.....	48
Table 9. DSC Test method.....	55
Table 10 DSC sample conditioning and T _g results.....	57
Table 11. E-LT3800 Mechanical Test Matrix.....	63
Table 12. Lamina-swelling stress model inputs for Hexion/ Vectorply E-LT3800.	70
Table 13. Static test results	75
Table 14. AE general trends (averages).	84
Table 15. Frequency analysis bin ranges.....	91
Table 16. Sensor-test test matrix.....	97
Table 17. Sensor-test results (averaged).....	97

Table 18. Lists of tests completed to study the effects of moisture absorption on various off-axis laminates.....	101
Table 19. List of tests completed in order to study the effects moisture absorption on various stacking sequences.	101
Table 20. Summary of materials included in MHK study.....	121
Table 21. Mechanical data summary for materials included in MHK study*	126

This page left blank

EXECUTIVE SUMMARY

This collection of work details four areas of investigation within the Department of Energy, Sandia National Laboratories, and Montana State University (DOE/SNL/MSU) marine hydrokinetic (MHK) energy materials effort. Over a period extending beyond 5-years, many research efforts were performed to help the MHK industry identify structural properties, damage tolerance, and operational concerns related to material selection for MHK devices. Included in this summary are four different research projects from that time period.

The first section investigates the effect of moisture uptake into a continuous fiber composite, taking into account the effect of an applied uniaxial tensile stress on diffusion rate and maximum mass uptake. Both numerical and experimental results are included in the study for a single matrix material with multiple fiber orientations. The thesis which describes this work in totality can be found at <https://scholarworks.montana.edu/xmlui/bitstream/1/2733/1/StoffelsM0813.pdf>.

The second section investigates damage development and propagation in composite materials due to moisture uptake. Included in these experimental results are mechanical strength and in-situ acoustic emission results. Samples were tested before and after saturation and included samples which were saturated and subsequently dried to original condition. Results are compared from all three saturation conditions for unidirectional $[0]_2$ and $[90]_2$ and $[0/90]_s$ and $[90/0]_s$ layups. The thesis which describes this work in totality can be found at https://msu-primo.hosted.exlibrisgroup.com/permalink/f/1a5h0rp/01TRAILS_MSU_DSPACE1/14596

The third section investigates the effect of moisture uptake on glass composites with differing fiber angle and layup sequences. Both mechanical strength and in-situ acoustic emission results are presented for unidirectional and symmetric cross-ply coupons. These results demonstrate that moisture uptake alters the primary damage mode in off-axis plies, and that stacking sequence can have deleterious effects on strength as moisture is absorbed in the outer plies of a composite. The thesis which describes this work in totality can be found at <https://scholarworks.montana.edu/xmlui/handle/1/12516>.

The final section investigates the strength reduction and in-situ acoustic emission results for a wide breadth of fiber reinforced composite materials before and after moisture uptake. The evaluated coupons were provided from industrial suppliers and tested as potential materials for MHK applications. A diverse set of fiber-matrix combinations configured into a variety of layups totaling more than 30 laminates were mechanically tested in quasi-static uniaxial tension. The thesis which describes this work in totality can be found at <https://scholarworks.montana.edu/xmlui/handle/1/15551>.

This collection does not include all the research from the DOE/SNL/MSU collaboration; however, it does comprise the largest majority of the significant findings.

ACRONYMS AND DEFINITIONS

Abbreviation	Definition
D	Diffusion Coefficient
E	Young's Modulus
σ	Stress
ϵ	Strain
m	Moisture content in material
M	Percent moisture content in material
M_{∞}	Maximum percent moisture content
c	Concentration
u_f	Free Volume Fraction
ϕ	Volume Fraction
θ	Angle between fibers and loading direction
ρ	Density
ν	Poisson's Ratio
$\Delta V/V_0$	Volumetric Strain
Subscripts	
D	Diffusion Coefficient
E	Young's Modulus
σ	Stress
ϵ	Strain
m	Moisture content in material
M	Percent moisture content in material
M_{∞}	Maximum percent moisture content
c	Concentration
u_f	Free Volume Fraction
ϕ	Volume Fraction
θ	Angle between fibers and loading direction
ρ	Density
ν	Poisson's Ratio
$\Delta V/V_0$	Volumetric Strain

1. STRESS ASSISTED DIFFUSION

It is widely accepted that glass does not absorb moisture, leaving only the epoxy matrix material as the portion of the composite that will undergo the diffusion process. Once submerged for an extended period of time the epoxy glass composite will reach a level of maximum moisture content, and will stay at this moisture level throughout the remainder its submersion [1]. In order to observe this process a series of weight gain measurements are taken throughout the saturation process, a typical moisture uptake curve is shown in Figure 1.

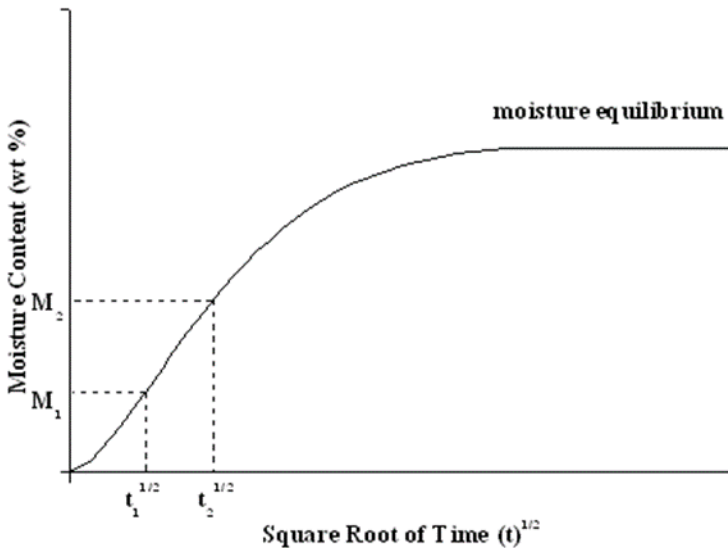


Figure 1. Generalized moisture uptake curve for an epoxy composite.

Composite Marine Hydrokinetic turbines operate under demanding environmental conditions, as they are completely submersed under water for long periods of time. This introduces a number of issues related to composite material design, primarily relating to moisture diffusion into the composite and how this diffusion ultimately influences its mechanical properties. In order to successfully design long lasting composite structures for use in MHK systems it is pertinent to understand the detailed relationship between this diffusion process and its effects on the resulting composite strength. In general, the mechanical strength of an epoxy resin decreases throughout the saturation process as seen in Figure 2. [2].

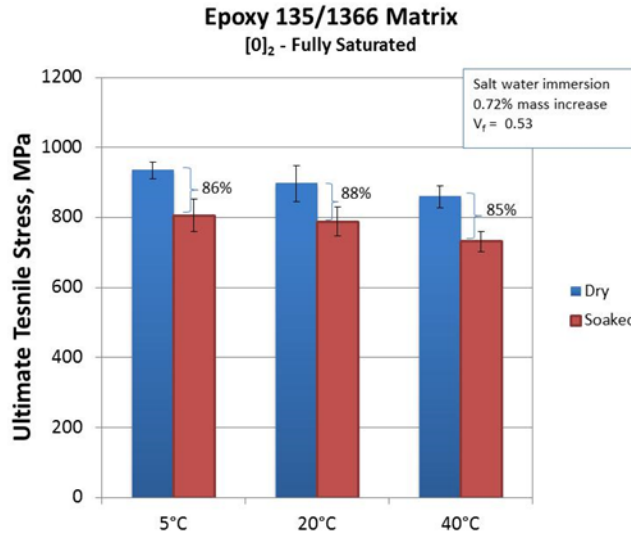


Figure 2. A chart from a study at Montana State University demonstrating the loss in mechanical strength experienced by a fully saturated epoxy glass composite.

As is clearly seen above the loss of strength due to moisture absorption is quite significant and could, without proper preparation, lead to failures in composite MHK structures. This diffusion process has been investigated in the past and is widely known to be accurate [1][3][4][5].

1.1. Stress Effects

As the structure in question will most certainly be subjected to a stress field, it is of substantial interest to explore the effects that these external stresses have on the diffusion process. It is suspected that various diffusion characteristics of the composite will drastically change due to applied stresses. Additionally, it is hypothesized that the relative magnitude at which diffusion parameters will change from the unstressed state is dependent on both the magnitude of applied stress and the fiber angle of the composite plate. Assuming these stresses have a notable effect on moisture diffusion in a composite material, it is of great importance to form a comprehensive understanding of this phenomenon and how it will ultimately affect the composites mechanical properties.

1.2. Theoretical Background

1.2.1. Fiber Reinforced Polymer Composites

Fiber reinforced polymer composites are constituted of successive layers of thin laminas, commonly referred to as plies. Each ply has its own set of mechanical properties, which are directly dependent upon orientation of the fibers and fiber volume. It follows that multi-directional stiffness in laminates is achieved through the use of different fiber orientations, or by using textile weaves [6]. Figure 3 - Figure 5 present a series of scanning electron microscope (SEM) cross sections of a four-ply epoxy-glass laminate. First, Figure 3 at a magnification of x15 displays all four plies that comprise the laminate, where the arrangement of the fiber bundles that make up each ply can clearly be seen. At x50 magnification Figure 4, provides clearer image the individual fibers. At a magnification of x200 Figure 5 shows how individual fibers are arranged within a fiber bundle.

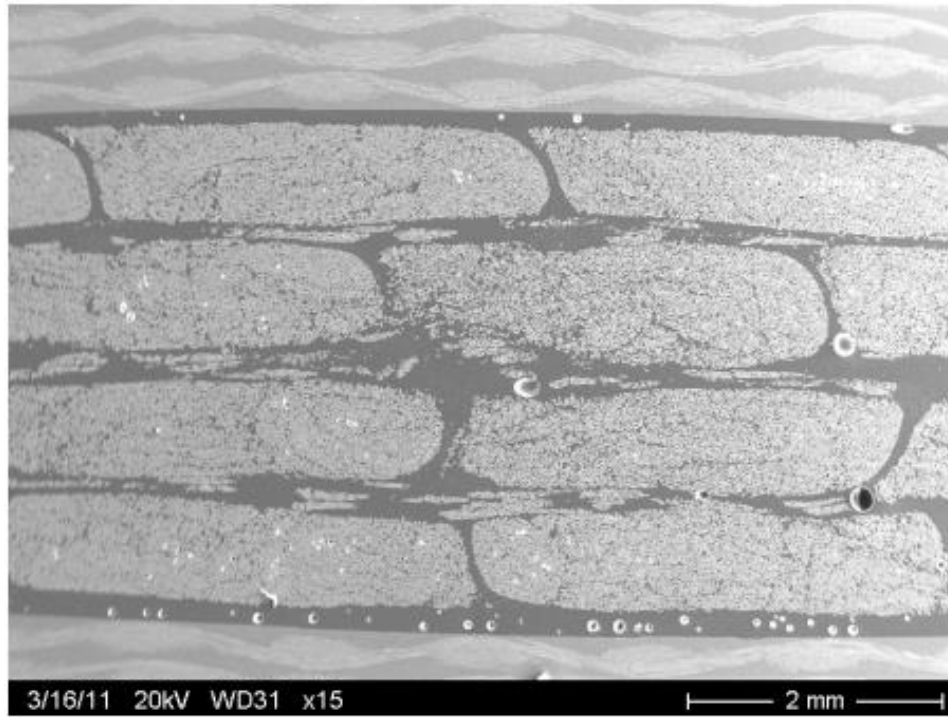


Figure 3. Cross section of typical $[45/45]_s$ epoxy-glass laminate. SEM x15. †

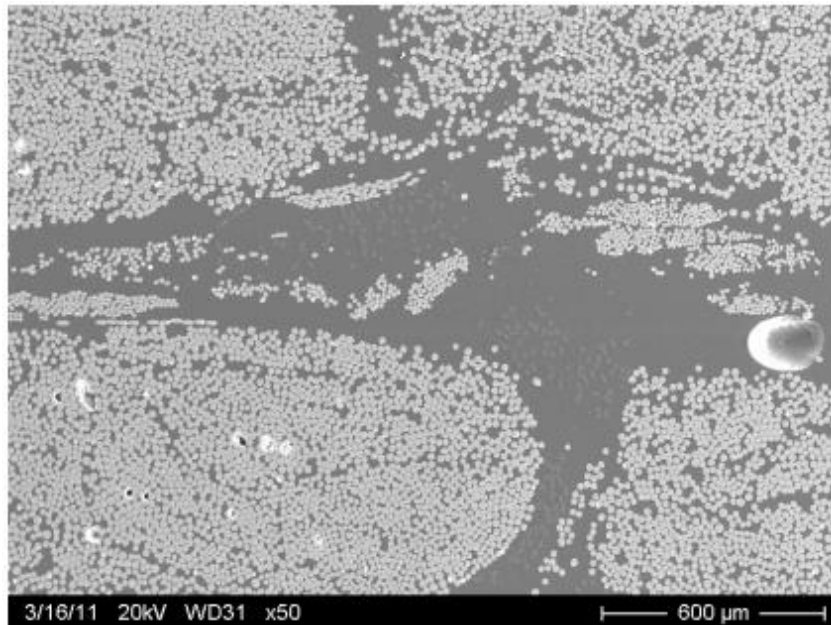


Figure 4. Cross section of typical $[45/45]_s$ epoxy-glass laminate. SEM x50 †

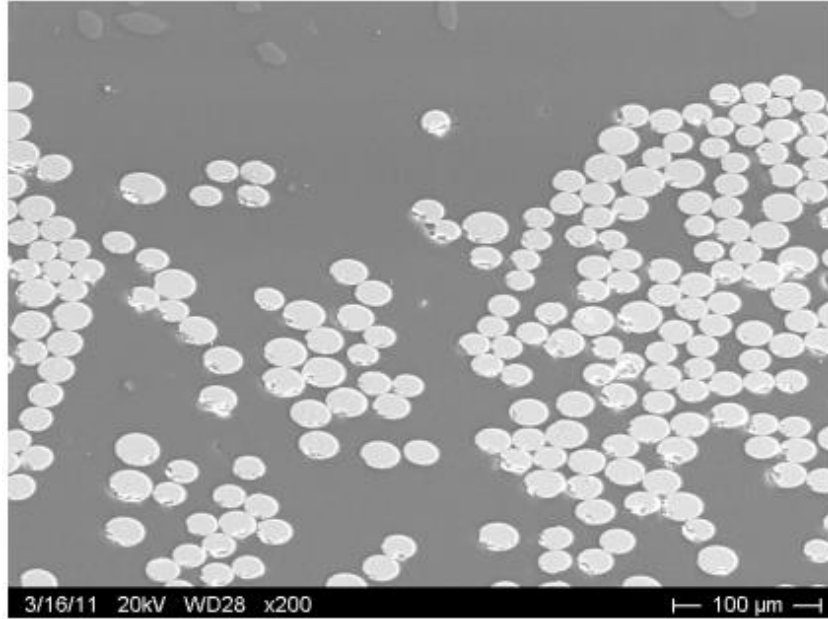


Figure 5. Cross section of typical [45/45]_s epoxy-glass laminate. SEM x200. Images: Montana State University, Composite Technologies Group, 2011.

1.2.2. Diffusion

Diffusion is a transport phenomenon that entails the movement of mass from an area of high concentration to an area of low concentration in ways not requiring bulk motion. The diffusion process is illustrated in Figure 6.

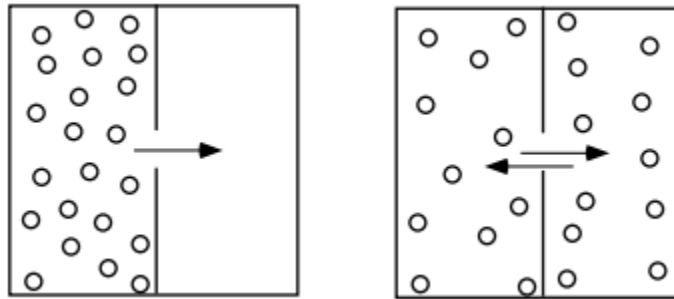


Figure 6. A simple diagram showing the diffusion process, note the movement of particles from high concentration to low concentration.

For the remainder of this study the concentration term being discussed will be that of moisture content held within a material. Moisture content, see equation (1), manifests itself as a weight gain or weight loss seen in a material, most commonly represented as percent moisture content.

$$M = M(t) = \frac{\text{Weight of saturated} - \text{Weight of dry}}{\text{Weight of dry}} \times 100 \quad (1)$$

Equation (1) presents the formulation used in calculating the percent moisture content held within a system. The *Weight of dry* term is the weight of a completely dry sample, while *Weight of saturated*

term is the weight of the sample after some amount of immersion time. Through using this relationship throughout the saturation process the moisture content within a system can be tracked as a function of immersion time t , yielding a moisture uptake curve. A material that follows Fickian diffusion principles, which will be discussed shortly, will all have the same shape of concentration vs. time curves. These uptake curves are initially linear and after a long period of time the curves asymptotically approach the maximum concentration level, at which point there is no longer a moisture concentration gradient to further drive the diffusion process. A typical Fickian moisture uptake curve is shown in Figure 1.

When discussing fiber reinforced polymer composites, the polymer matrix compound constitutes the preferred moisture penetration path for water molecules, especially when the fiber reinforcements are impermeable. Glass fibers, for example, are impermeable while carbon fibers do absorb a certain amount of water, though a very minute amount in comparison to that of a polymer matrix. Therefore, the water diffuses primarily into the polymer matrix when glass fiber reinforcements are used. As has been previously stated epoxy-glass composites are the most common advanced composites, especially throughout the energy industry, and consequently will be the focus of this study.

1.2.3. *Fickian Diffusion*

Fick's first law simply states that any given flux will always move from an area of high concentration to an area of low concentration. Therefore, for Fickian materials mass diffusion is driven by concentration gradients, mathematically this formulation is seen in equation (2). The negative sign in this relationship indicates mass diffuses in a downward gradient direction, as is expected (i.e. from areas of high concentration to low concentration).

$$J_i = -D_{ij} \frac{\partial C}{\partial x_j} \quad (2)$$

Where:

J_i = The moisture flux term

D_{ij} = The mass diffusivity tensor

C = The moisture concentration

x_j = The spatial coordinate of interest

Fick's second law of diffusion presents methods for determining how diffusion changes concentration with time. The second law of diffusion can be derived using both Fick's first law and the principle of mass conservation throughout the diffusion process.

If the material is homogenous the equation becomes

$$\frac{\partial C}{\partial t} = D_{ii} \frac{\partial^2 C}{\partial x_i^2} \quad (3)$$

1.2.4. Diffusivity

The diffusion coefficient D , also known as diffusivity, is a rate proportionality constant which relates the mass flux term and the concentration gradient. With units of (length²/time) the diffusion coefficient for any given substance defines the rate at which mass will diffuse due to a concentration gradient. A generalized moisture uptake curve is shown in Figure 7. Initially (where $t < t_L$) all moisture uptake curves are linear, when moisture content is plotted directly against \sqrt{t} the diffusivity becomes directly proportional to the initial slope of the uptake curve. After a long submersion time the curve asymptotically approaches a maximum moisture content level, M_∞ .

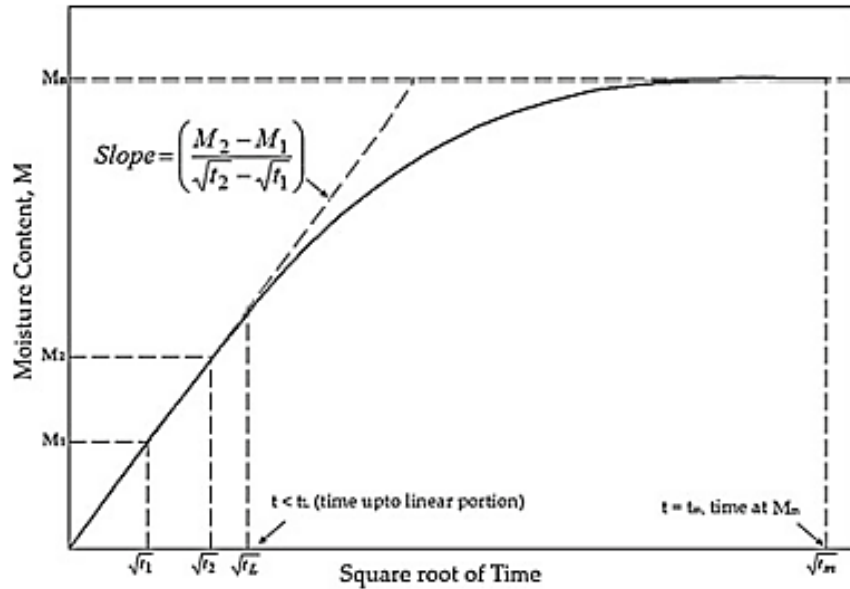


Figure 7. Change of moisture content with the square root of time. [1]

The formulation for D presented by Springer [1] is for a homogenous material with no edge diffusion, where only one diffusion coefficient is sufficient to describe the behavior of the entire material. Though, in many cases the edge diffusion effects cannot easily be neglected, as it does introduce errors into various diffusion calculations.

$$D = \pi \left(\frac{h}{4M_\infty} \right)^2 \left(\frac{M_2 - M_1}{\sqrt{t_2} - \sqrt{t_1}} \right)^2 \quad (4)$$

1.2.5. Diffusivity of Unidirectional Fiber Composites

For a unidirectional fiber reinforced epoxy composite D cannot be calculated directly if accounting for edge effects, as clearly a composite will have vastly different diffusivity values in each direction. In this case both the longitudinal and transverse diffusion coefficients must be represented in terms of fiber and matrix diffusion coefficients using the rule of mixtures. Following Springers derivation yields an expression for diffusivity D for a unidirectional fiber composite plate.

$$D = D_m \left[1 - 2\sqrt{\frac{\phi_f}{\pi}} \right] \left[\frac{h}{l} \sqrt{\frac{(1 - \phi_f)\cos^2\theta + \left(1 - 2\sqrt{\frac{\phi_f}{\pi}}\right)\sin^2\theta}{1 - 2\sqrt{\frac{\phi_f}{\pi}}}} \dots \right. \\ \left. + \frac{h}{w} \sqrt{\frac{(1 - \phi_f)\sin^2\theta + \left(1 - 2\sqrt{\frac{\phi_f}{\pi}}\right)\cos^2\theta}{1 - 2\sqrt{\frac{\phi_f}{\pi}}}} + 1 \right]^2 \quad (5)$$

This expression for D is a function of fiber angle, volume fraction, geometry of the plate, and the diffusivity of the matrix material. As the matrix is a homogenous material finding its diffusivity is relatively straight forward using equation (4).

1.3. Maximum Absorption Capacity of Unidirectional Fiber Composites

The maximum percent moisture content, M_∞ , is a fundamental quantity that defines the maximum amount of moisture that physically can be absorbed by a given system. Commonly, the maximum content of a specific homogenous epoxy system is initially defined experimentally by subjecting it to a moist environment until the rate of weight gain values become negligible. Studies have shown that epoxy resin systems generally have an M_∞ value in the range of 2.5-3.0%, prediction of these values can be done through the use of free volume theories which will be further investigated at a later point in this study.

Under the assumption that only the resin system absorbs moisture, as $D_f \ll D_m$, it then follows that the maximum moisture content for a unidirectional fiber composite directly correlates to the maximum percent content value for that of the resin system used. The following relationship is developed,

$$M_{\infty c} = \phi_m M_{\infty m} \frac{\rho_m}{\rho_c} \quad (6)$$

where $M_{\infty m}$ is the maximum content of the matrix and, ρ_m and ρ_c are the densities of the matrix and that of the composite respectively. The volume fraction term is introduced to scale the maximum content of the matrix accordingly. With the composite density ρ_c defined as follows,

$$\rho_c = \rho_f \phi_f + \rho_m \phi_m \quad (7)$$

1.3.1. Thermal and Pressure Effects

The moisture diffusion process is heavily dependent upon both temperature and pressure, though studies have shown [1] that within composite materials temperature approaches equilibrium on the order of 10^6 times quicker than the moisture concentration. It has also been documented that moisture concentration has minimal effects upon the diffusivity [6]. Therefore, assuming constant temperature conditions of the diffusing fluid, it can be assumed that the diffusion coefficient remains constant throughout its saturation process. Figure 8 presents moisture uptake curves for a single epoxy resin system taken at three different ambient temperature conditions. Note all the data

sets approach near the same maximum moisture content, though the diffusivity increases as the temperature of the fluid increases.

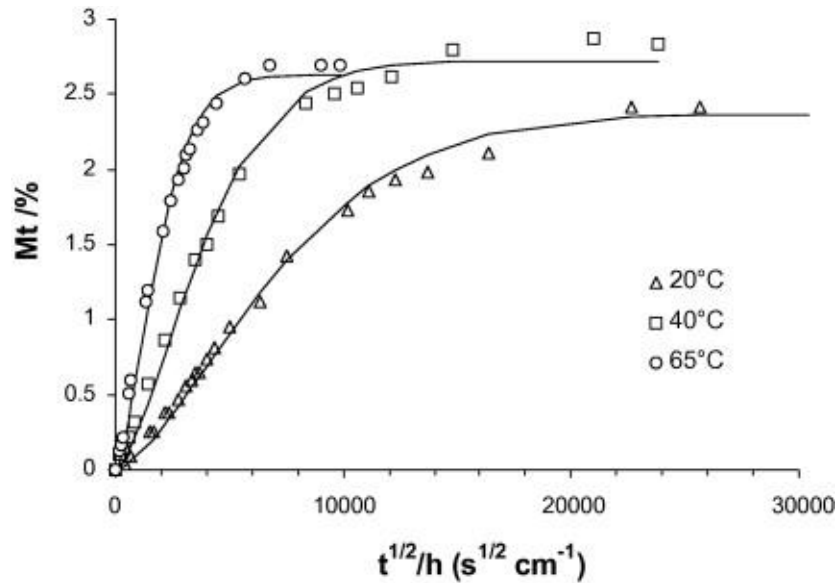


Figure 8. Moisture uptake curves demonstrating the change in diffusivity due to changes in ambient temperature. [10]

It becomes obvious that in polymers, mass diffusion is a thermally activated process, the changes are attributed to changes in the glass transition temperature of the polymer. Temperature dependent changes in diffusivity are represented using the Arrhenius reaction equation [21][17],

$$D = D_0 e^{\left(\frac{-C}{T}\right)} \quad (8)$$

where, the diffusion coefficient D directly depends on the initial diffusion coefficient D_0 , temperature T , as well as a constant C which is composed of the activation energy ΔE , and the Boltzmann constant k . Values for activation energy and Boltzmann's constant are readily available for various polymer systems.

1.3.2. Free Volume

The free volume is a fundamental quantity within the realm of polymeric systems. Free volume in polymer systems manifests itself as small, unfilled volumes that occur at the end of a polymer chain (see Figure 9). Combined, these small voids constitute the free volume fraction of a polymer. Mathematically, the free volume is defined as the difference between the measured volume and the occupied volume [9]. Free volume theories are commonly cited as a basis in describing several molecular transport phenomena (moisture diffusion e.g.) within polymeric systems. [9][17][12]

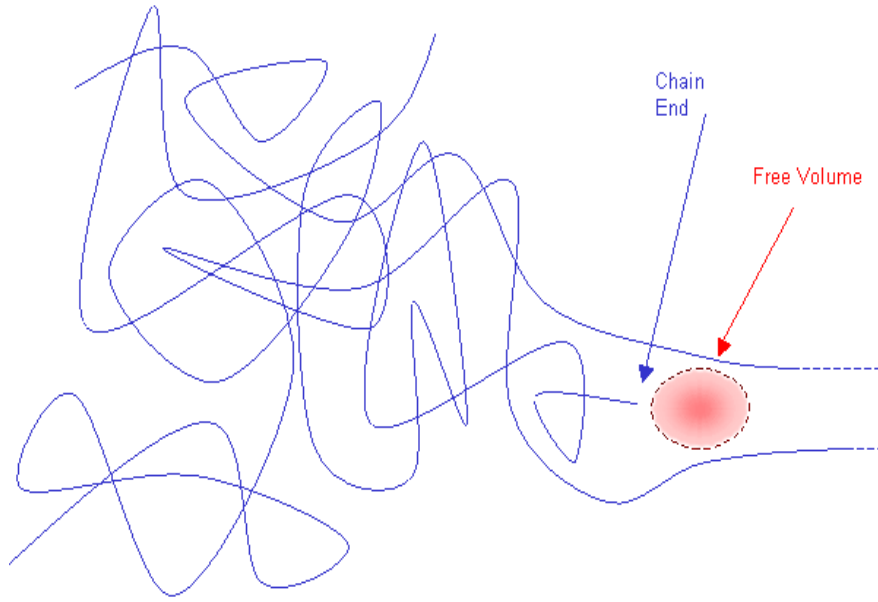


Figure 9. A Simple representation of how polymeric chains end, resulting in a void, which becomes free, unfilled, volume within the structure.

1.3.3. Maximum Absorption Capacity

Neumann and Marom have proposed a relationship between maximum absorption capacity and free volume fraction [9]. They proposed that free volume and maximum absorption capacity are directly related by a ratio of the density of the diffusing fluid (water for this case) to the density of the matrix material

$$M_{\infty} = v_{f0} \frac{\rho_w}{\rho_m} \quad (9)$$

where, v_{f0} is the unstressed free volume fraction of the matrix material, and ρ_w and ρ_m are the densities of water and the matrix respectively. This expression states that the weight gain M_{∞} is directly dependent upon available free volume and the relative density of the diffusing fluid in comparison to that of the matrix material. This relationship is for a pure resin system with no fibers or other constituents involved, a free volume value of nearly 3% is commonly reported for epoxy resin systems [20]. Consequently, for a stressed system the absorption capacity will change, due to the change in free volume.

$$M_{\infty\sigma} = v_{f\sigma} \frac{\rho_w}{\rho_m} \quad (10)$$

Fundamentally it is consistent that the transport mobility of molecules in any given system is directly dependent upon how tightly the system is packed. A higher free volume fraction would lend itself to higher equilibrium moisture content, as there is more free space for the moisture molecules to diffuse into. Conversely, with a lower free volume there is less free space, leading to lower equilibrium moisture content. Therefore, under the assumption that there is a direct correlation between Fickian moisture diffusion and the amount of free volume it can be postulated that as the free volume fraction of the epoxy changes as will its resulting diffusion characteristics.

1.3.4. Diffusivity

The diffusion coefficient in amorphous polymers may be described in terms of the free volume fraction, where D is directly proportional to an exponential of a ratio of critical void volume to free volumes [9], where v^* and v_f are the critical void volume and available free volume respectively.

$$D \propto e^{\left(\frac{-v^*}{v_f}\right)} \quad (11)$$

This corresponds nicely to concepts presented by Fahmy and Hurt in 1980 [12]; they proposed a model for calculating free volume changes due to externally applied stresses in an amorphous epoxy resin system. Their model is based on the assumption that the entirety of the free volume of the polymer structure is constituted of spherical shells within the matrix, referring again to Figure 9, and that all of these spherical shells have the same inner and outer radii. The free volume fraction of the epoxy matrix then becomes the summation of all the resulting spherical volumes. Once an external stress is introduced into the system it follows that the epoxy matrix will be volumetrically strained, leading to a change in the free volume fraction. Using this development Fahmy and Hurt proposed an expression for the ratio of the diffusion coefficients of an epoxy resin in stressed and unstressed states,

$$\ln \frac{D_\sigma}{D_0} = a \left(\frac{1}{v_{f0}} - \frac{1}{v_{f\sigma}} \right) \quad (12)$$

where a is a proportionality constant which is empirically determined. The two free volume terms v_{f0} and $v_{f\sigma}$ represent the unstressed and stressed states respectively.

The previously discussed free volume concepts have developed relationships for a pure epoxy system, with no other constituents involved. A number of issues are introduced when discussing epoxy glass composite structures, predominately the effects the glass fibers will have on the resulting free volume fraction. As previously discussed, the only portion of the composite system which will undergo substantial moisture diffusion is the epoxy resin, thus it follows that only changes in the free volume of the matrix will cause changes in diffusion characteristics. When a composite plate is subjected to a stress field the entire structure will experience volumetric strain. The volume change of the matrix is calculated by subtracting the volume change of the fibers from that of the composite, these volume changes can be calculated through the use of laminate plate theory equations and will be presented in great detail within the development of the proposed model.

1.4. Model Development

1.4.1. Free Volume

Under the assumption that externally applied stresses cause changes in the free volume fraction, which in turn leads to changes in moisture diffusion characteristics it becomes of utmost importance to develop methods for calculating these free volume changes. The derivation is presented in Stoffels thesis (see link in introduction) however, the reduced form is seen below,

$$\begin{aligned}
(\Delta V/V_0)_m \phi_m = \sigma_x \left\{ \cos^2 \theta \left[\left(\frac{1 - 2\nu_{12c}}{E_{1c}} \right) - \phi_f \left(\frac{1 - 2\nu_{12f}}{E_{1c}} \right) \right] \right. \\
\left. + \sin^2 \theta \left[\left(\frac{1}{E_{2c}} - \frac{\nu_{12c}}{E_{1c}} - \frac{\nu_{23c}}{E_{2c}} \right) - \phi_f \left(\frac{\nu_{12f}}{E_{1f}} \right) \right] \right\} \quad (13)
\end{aligned}$$

According to the proposed model the magnitude of the volume strain of the matrix is directly dependent upon applied tensile stress, fiber angle, and elastic properties of the constituents. Through algebraic examination of the various quantities held within the final form it can be deduced that the fiber angle is ultimately the controlling parameter in deciding the magnitude of the volume strain. In other words, at a fiber angle of $\theta = 0^\circ$ there will be a very minimal volume strain changes with increasing applied tensile stresses, conversely at a fiber angle of $\theta = 90^\circ$ the changes in volume strain are great. This is due to the fact that at $\theta = 0^\circ$ the fibers carry the majority of the loading, with little being transferred into the matrix, and at $\theta = 90^\circ$ the matrix undertakes the most all of the loading (leading to larger values for volumetric strains).

1.4.2. Changes in Diffusion Parameters

When a unidirectional epoxy glass fiber composite plate is placed under tensile stress moisture diffusion parameters are altered due to changes in available free volume. Thus far, laminate plate theory has primarily been considered in the development of the volume strains that are experienced by the matrix when subjected to tensile stress. The volumetric changes are clearly defined; but now these strains must also be directly related to changes in both maximum absorption capacity and rate of diffusion of the composite plate.

1.4.3. Maximum Absorption Capacity

Changes in the maximum absorption capacity of a stressed composite material come about due to a change in the available free volume within the matrix. Following the previous development, the volumetric strain experienced by the matrix due to an applied tensile stress in the x-direction is known, shown above in equation (13). Volumetric strain is directly analogous to directional strain, as it is a dimensionless quantity that describes the change of volume experienced by a material due to some stress field. It follows that an expression for the stressed free volume fraction of the matrix can be found by adding the volume strain term of the matrix to the already known quantity for unstressed free volume v_{f0} .

$$v_{f\sigma} = v_{f0} + (\Delta V/V_0)_m \quad (14)$$

This represents the stressed free volume fraction of the unidirectional composite plate. The above expression for $v_{f\sigma}$ can now be inserted to the correlation presented earlier relating changes in maximum absorption capacity to free volume fraction, which then yields an expression for $M_{\infty\sigma}$ of a unidirectional fiber composite plate. Through using a number of previously defined relationships this expression can be manipulated into an alternate form, which directly incorporates the unstressed maximum moisture content of the composite.

$$M_{\infty\sigma} = [v_{f0} + (\Delta V/V_0)_m] \frac{\rho_w}{\rho_m} \quad (15)$$

$$M_{\infty\sigma} = M_{\infty 0} + (\Delta V/V_0)_m \frac{\rho_w}{\rho_c} \phi_m$$

1.4.4. The Diffusion Coefficient

The rate at which the diffusion process occurs in unidirectional fiber composite plates is heavily dependent upon the magnitude of applied tensile stresses. There have been models proposed which outline a relationship between the diffusivity in stressed and unstressed states in amorphous polymer composite structures [9][12][16]. Most commonly this has taken the form,

$$\ln \frac{D_\sigma}{D_0} = \frac{a}{\phi_m} \left(\frac{1}{v_{f0}} - \frac{1}{v_{f\sigma}} \right) \quad (16)$$

where, D_σ , D_0 , v_{f0} and $v_{f\sigma}$ are the diffusion coefficients and free volume fractions of the stressed and free states respectively, and a is a proportionality constant which is empirically determined. This has nearly identical form to the relationship outlined for that of an amorphous polymer structure, see equation (12), the only difference being the inclusion of the matrix volume fraction term ϕ_m . The inclusion of this term accounts for the fact that a composite materials structure is now being considered, where only the matrix is undergoing the diffusion process. Through substituting expressions previously derived for D_0 , v_{f0} and $v_{f\sigma}$ into equation (16) and algebraically rearranging the following expression used for calculating the stressed diffusion coefficient of a composite material is found to be

$$\ln \frac{D_\sigma}{D_0} = \frac{a}{\phi_m v_{f0}} \frac{(\Delta V/V_0)_m}{[v_{f0} + (\Delta V/V_0)_m]} \quad (17)$$

From analyzing the above expressions for the stressed maximum moisture content and diffusion coefficients it can be seen that as the volume strain of the matrix, $(\Delta V/V_0)_m$, increases as do the moisture diffusion parameters. As previously discussed, the volume strain is directly dependent upon fiber angle and tensile loading; in addition, it has also been noted that the volume strain of the matrix changes to a larger degree with applied stresses as the fiber angle increases ($\theta = 0^\circ \rightarrow \theta = 90^\circ$). Similarly, the amount at which the stressed maximum moisture content will vary from the corresponding unstressed state also increases with fiber angle. As a result, the largest variation between the moisture diffusion parameters in the unstressed and stressed states will occur at a fiber angle equal to $\theta = 90^\circ$.

1.5. Finite Element Simulation of Diffusion

1.5.1. Overview

Finite Element Analysis (FEA) is a useful tool to find solutions for complex problems across a wide breadth of engineering applications. It is fairly simple to arrive at a result, though the accuracy and usability of the result must be thoroughly investigated using other solution methods to ensure an accurate solution was found. Without proper knowledge of the intricacies that come along with using FEA software packages it becomes very simple to arrive at an erroneous result, and not realize that it is incorrect. Double-checking all input parameters and understanding how the system is modeled becomes of utmost importance in achieving accurate and meaningful results.

1.6. Thermal-Moisture Diffusion Analogy

Commonly, many modern Finite Element Analysis packages do not provide the necessary tools required to directly model the moisture diffusion process. Modeling temperature distributions within a system is frequently completed using finite element methods and is well understood and accepted. The thermal diffusion process behaves according to Fourier's law for thermal diffusion, which is mathematically equivalent to Fick's law for mass diffusion, and as such a Thermal-Moisture diffusion analogy can be employed [22]. Due to this similarity, opportunities arise to use the thermal diffusion capabilities of commercial finite element packages to solve Fick's diffusion equation; the following are the expanded forms of Fick's and Fourier's laws for mass and thermal diffusion,

$$\frac{\partial C}{\partial t} = D \left(\frac{\partial^2 C}{\partial x^2} + \frac{\partial^2 C}{\partial y^2} + \frac{\partial^2 C}{\partial z^2} \right) \quad (18)$$

$$\frac{\partial T}{\partial t} = \frac{k}{\rho c} \left(\frac{\partial^2 T}{\partial x^2} + \frac{\partial^2 T}{\partial y^2} + \frac{\partial^2 T}{\partial z^2} \right) \quad (19)$$

where, C is the moisture concentration equivalent to the temperature T , whereas diffusivity D is equivalent to thermal diffusivity $a = k/\rho c$. While these equivalencies are fairly clear, the correspondence between the thermal and moisture boundary conditions is not as straightforward. The primary problems that arise are the discontinuities seen at interfaces between two materials. For thermal analyses, the contact temperature between two materials is assumed to be the same value; this is not the case for a moisture diffusion analysis. To navigate this issue Wong and Koh [22] have introduced a saturation ratio term w , which is defined as $M(t)/M_\infty$. This is the ratio of the moisture concentration M at time t to the maximum moisture content M_∞ . Obviously, this saturation ratio has a maximum possible value of one once the system has reach full saturation, as $M(t) = M_\infty$. This saturation ratio parameter is considered to be continuous across a material interface and can consequently be used to establish boundary conditions throughout a finite element model.

Table 1. Thermal-Moisture Diffusion analogy FEA input properties

Property	Thermal	Moisture
Field Variable	Temperature, T	Saturation ratio, w
Density	ρ (kg/m^3)	1
Conductivity	k ($W/m \text{ } ^\circ C$)	$D * M_\infty$ (mm^2/hr)

1.6.1. Model Geometry

Finite element models for both a two and three-dimensional sample geometry will be presented. The two-dimension geometry was modeled directly as the mid-plane cross section of the sample, giving a clear representation of the concentration profile through the sample cross section. The approach for the three-dimensional geometry is slightly different in that, due to sample symmetry, the sample was halved along the x, y, and z directions leaving only one eighth of the geometry modeled. This allows for the moisture concentration profile throughout the interior of the sample to be thoroughly investigated, while reducing run time and required processing power.

Fibers clearly have significant effects on the moisture diffusion parameters of a composite material, as previously discussed. Though, for the purpose of modeling this system in ANSYS the fibers will not be physically included in the geometry of the finite element model, but the various fiber properties will merely serve in calculating orientation dependent input parameters such as the diffusivity and maximum moisture content. Omitting the fibers in this way simplifies geometry creation and allows much quicker calculation times, as the mesh density will not need to be increased at interfaces between the fibers and the matrix, while still maintain an accurate result output.

One of the most important parts of creating a successful finite element model is correctly choosing an element type for use in meshing the model. There are expansive catalogues built into the ANSYS infrastructure of element types available for use; each element has its own unique set of behavioral properties which defines how it responds to different loading conditions and which solution outputs it is capable of providing. The ANSYS element types selected were the PLANE55 for the two-dimensional model and the SOLID70 for the three-dimensional model. The PLANE55 element type is a two-dimensional 4-node thermal solid; this element carries thermal conduction capabilities and has a single degree of freedom, temperature, at each node. Similarly, SOLID70 is a three-dimensional 8-node thermal solid with thermal conduction capabilities and has a single degree of freedom, temperature, at each node. Both of the elements selected are applicable to either steady state or transient thermal analysis types and have the ability to provide average face temperatures of a selected element face. Below, the meshed finite element models for both the two and three-dimensional sample geometries are presented in Figure 10 and Figure 11.

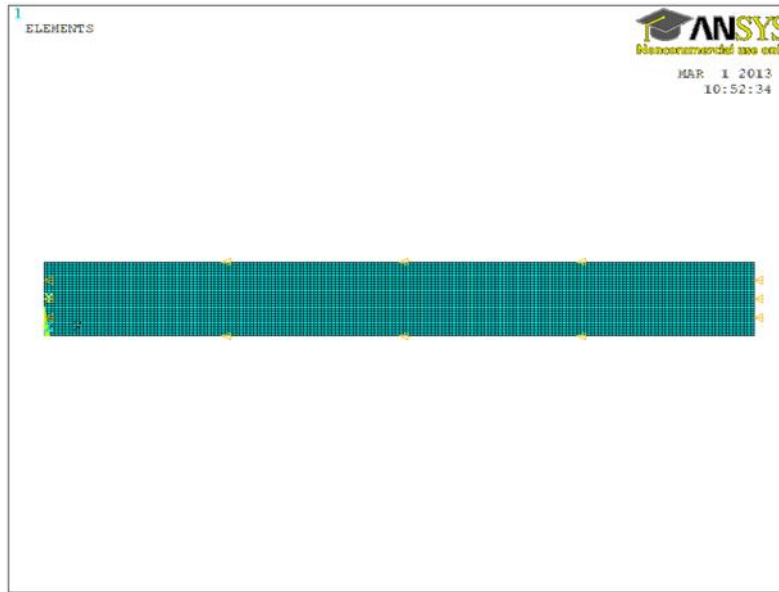


Figure 10. Meshed two-dimensional finite element geometry at the sample mid-plane, PLANE55 element type.

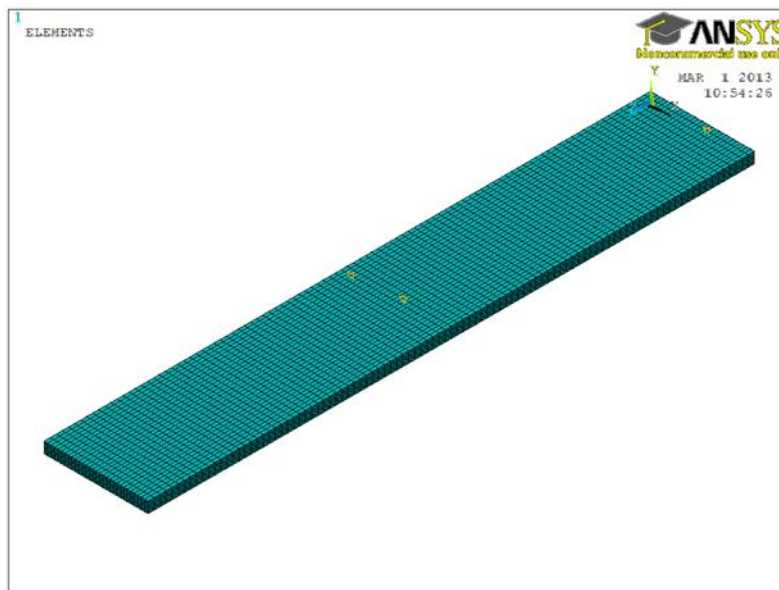


Figure 11. Meshed three-dimensional finite element geometry, one-eighth cross section of sample, SOLID70 element type.

1.6.2. Boundary Conditions

Properly establishing the boundary conditions on any given finite element model is paramount in attaining accurate results. Most commonly when undertaking thermal analyses using finite element methods the primary boundary conditions are temperatures, heat flows and fluxes and well as any amount of heat being generated. Returning to the thermal-moisture diffusion analogy previously discussed, it becomes obvious that the primary boundary condition that needs to be established is

the saturation ratio (temperature in a thermal analysis). Noting, that since the fibers are not physically included in the model heat and moisture flux boundary conditions are not needed. If the fibers were included in the model, and assuming that glass fibers do not absorb moisture, then a boundary condition of zero flux along all fiber-matrix boundaries would need to be established.

The saturation ratio has a maximum value of one, when $M(t) = M_{\infty}$, therefore a temperature boundary condition equal to one needs to be established along all surfaces of the model which are exposed to moisture. For the two-dimensional model this is simply equates to applying a temperature of one to all four of the outer edges. Again, the three-dimensional model is modeled such that it represents one eighth of the entire sample, where three of the six surfaces are exposed to a moist environment. A boundary condition of temperature equal to one was applied to the top, side, and back of the model.

Figure 12-Figure 25 present saturation ratio profiles of the two-dimensional geometry as the program moves through time steps from $time = 0$ hours to $time = 2000$ hours, at which point full saturation has been achieved. The nodal contours represent the extent at which the moisture has penetrated into the sample, with a maximum value of one (recall, for a given node the saturation ratio is defined as $M(t)/M_{\infty}$). Similar profiles for the three-dimensional geometry can be developed using nearly identical methods, though only one sample profile is provided in Figure 26.

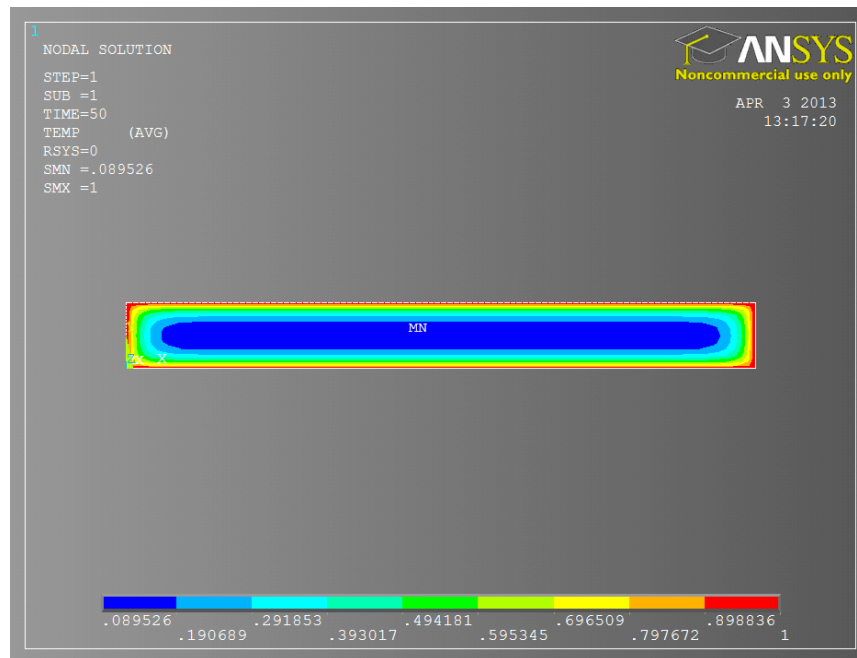


Figure 12. Saturation profile throughout the two-dimensional cross section at $time = 50$ hours. All edges are subjected to saturation conditions. Scale on bottom represents the wetness ratio, where a value of one denotes full saturation. Note: minimum saturation ratio value of only 0.089526 near center of the sample.

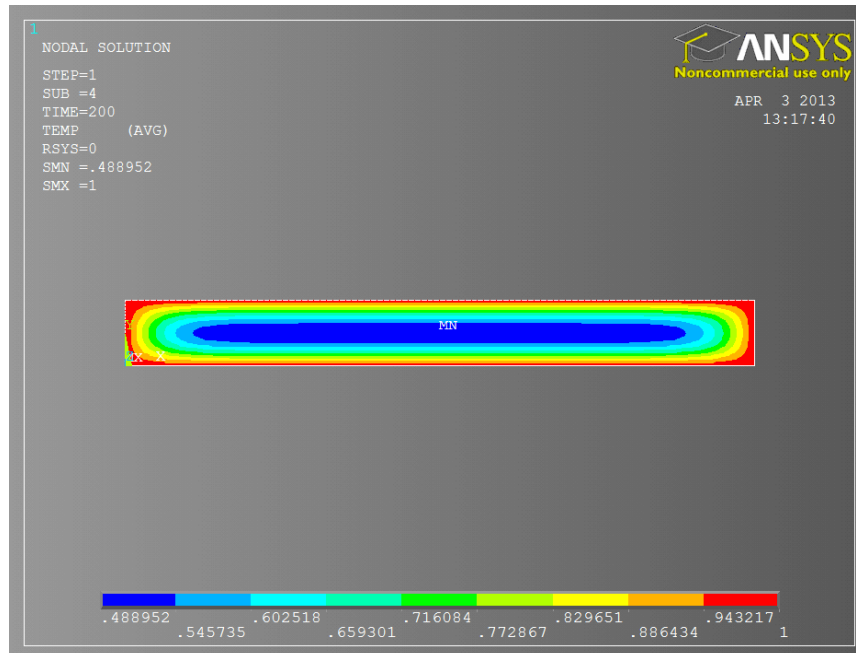


Figure 13. Saturation profile throughout the two-dimensional cross section at *time* = 200 hours.
 Note: minimum saturation ratio value of 0.488952.

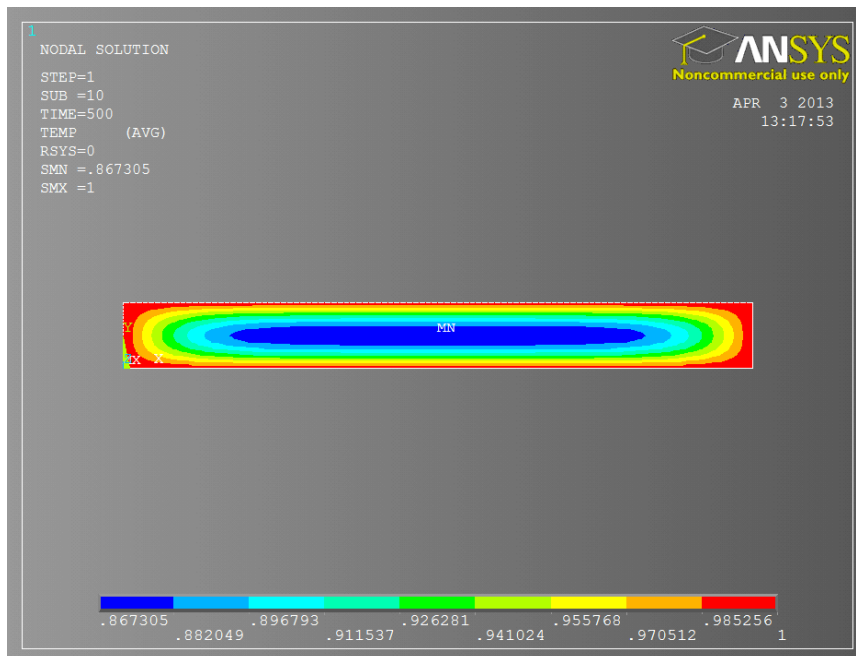


Figure 14. Saturation profile throughout the two-dimensional cross section at *time* = 500 hours.
 Note: minimum saturation ratio value of 0.867305.

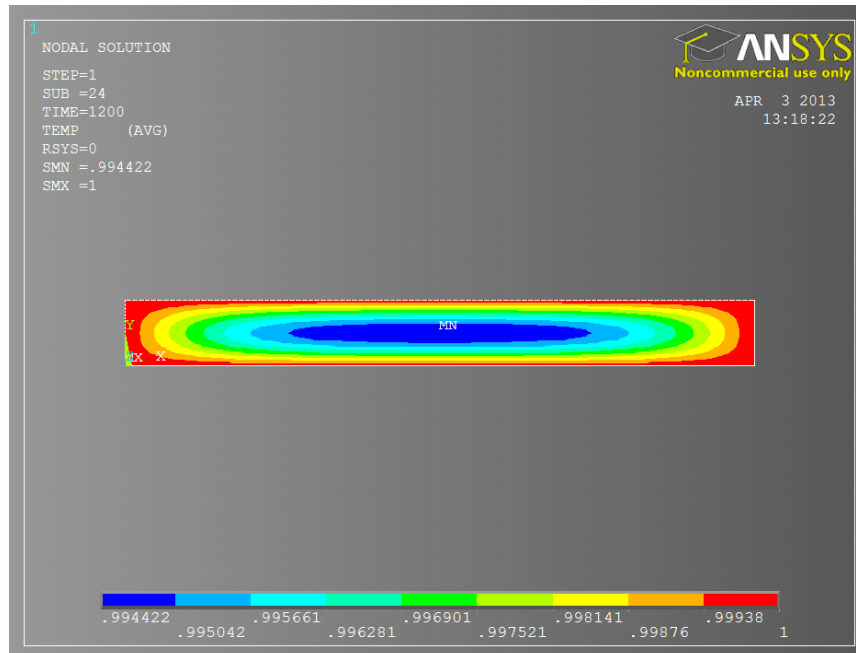


Figure 15. Saturation profile throughout the two-dimensional cross section at *time* = 1200 hours. Note: minimum saturation value of 0.994422. Consequently, at this time the sample is very nearly fully saturated.



Figure 16. Saturation profile throughout the two-dimensional cross section at *time* = 2000 hours. Note: minimum saturation value of 0.999855. The sample has reached full saturation.

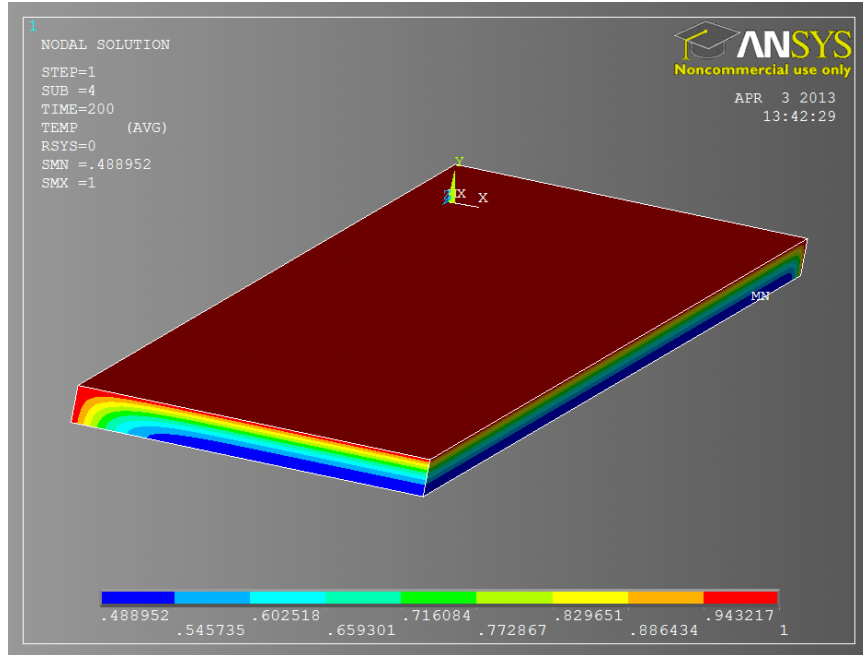


Figure 17. A typical saturation ratio concentration profile of the three-dimensional cross section geometry of the sample. Note only three sides of the samples are exposed.

These saturation profiles are merely plots of the nodal temperatures, which translates to a level of saturation, across the model at a specified time step. This gives a good visual representation of how the moisture diffuses into the structure but does not directly provide the user with important parameters, such as the maximum moisture content and diffusivity. In order to arrive at these values certain solution parameters saved within the ANSYS directory must be accessed and manipulated.

In order to use a finite element model to recreate a moisture uptake curve the percent moisture uptake at a specified time step must be calculated, through doing this at a number of time steps moisture uptake versus time curves can accurately be recreated. To find the moisture uptake for a specified time step the following relationship was employed,

$$M(t) = \left(\frac{\sum \text{Temperature at each node}}{\text{Total number of nodes}} \right) M_{\infty} \quad (20)$$

Once the moisture uptake curve was reconstructed from the finite element data the diffusivity of the system was easily calculated using previously established relationships.

1.7. Experimental Procedures

1.7.1. Experiment Overview

Knowing the mechanical strength of materials being used for structural applications is paramount for successful engineering designs. Under many circumstances the mechanical and physical properties of a given material system may degrade with time, especially those subjected to harsh operational conditions. The goal of this experiment is to simulate extended water immersion of unidirectional fiber epoxy glass composites, which are subjected to varying tensile stresses, and to characterize the changes seen in moisture diffusion parameters. A number of epoxy glass composite samples of varying fiber angles were manufactured and subjected to tensile stresses using stainless steel springs of various spring constants. The stressed samples were then submersed in water and weight gain measurements were taken throughout the saturation process until full saturation was achieved. The experimental setup allowed for investigation of the effects that both the fiber angle and magnitude of the tensile stresses have on the moisture diffusion process, and supports the inputs and results developed in the previous section.

1.7.2. Materials

The materials studied were continuous glass fiber reinforced epoxy polymer composites. The unidirectional glass fiber chosen was Saertex U14EU920-00940-T1300-100000 and the epoxy system chosen was Momentive's Epikote MGS RIMR 135 resin with Epikure curing agent RIMH 1366. The Saertex fibers, marketed as a unidirectional infusion fabric, were in the form of a stitched fabric where, by percent weight, 91% of the glass fibers were in the 0-degree direction and 8% were at 90-degrees, the remaining 1% is comprised of the stitching holding the fabric together. The crossply fibers are utilized to maintain alignment of the primary [0]'s during the infusion process. Momentive's Epikote is an epoxy resin system which when cured is known to have the material properties listed in Table 2 [23]

Table 2. Material properties of Momentive Epikure resin system. UTS and UCS represent ultimate tensile and compressive strengths respectively.

Property	Value
ρ (g/cm ³)	1.10 - 1.20
E (GPa)	2.9 - 3.2
UTS (MPa)	68 - 80
UCS (MPa)	80 - 100
Elongation at break (%)	7.0 – 10.0
Water absorption at 23°C	24h ~ 0.3% 7d ~ 0.5%

The SNL/MSU/DOE Composite Material Fatigue Database [19] is maintained by Montana State University with the purpose of providing the wind energy industry with an expansive composite material database for fatigue intensive applications. The database outlines numerous fiber and resin system which are commonly used in addition to the mechanical properties of possible composite layups. Both the Momentive resin system and Saertex fabric are detailed in the SNL/MSU/DOE

database, as well as properties for composite layups using the aforementioned constituents. A two-ply composite layup was chosen because the system would reach a fully saturated state in a much shorter time frame than thicker composite layups. Below, Table 3 presents material properties gathered from the SNL/MSU/DOE database are presented for a two-ply composite plate manufactured using Saertex glass fabric and Momentive Epikote epoxy systems.

Table 3. Material properties from SNL/MSU/DOE database for Saertex-Hexion [0]₂ composite plate. The designations 1 and 2 represent the material directions.

Property	Value
ϕ_f	0.52
ν_{12c}	0.27
E_{1c} (GPa)	38.4
E_{2c} (GPa)	12
UTS-1 (MPa)	863
UTS-2 (MPa)	66.7
UCS-1 (MPa)	-583
UCS-2 (MPa)	-197

1.7.3. Manufacturing Procedures

All samples were cut from a single unidirectional fiber composite plate, which was manufactured using Vacuum Assisted Resin Transfer Molding (VARTM). The VARTM process involves pulling a vacuum across the work piece in order to assist the infusion of the resin into the fabric system. Most commonly, there is a rigid mold to provide part geometry on one side and a thin flexible membrane, with outer atmospheric pressure compressing the fibers tightly against the mold, on the other. VARTM is a cost-effective method in the production of high-quality composite material parts, and consequently the process is very common across modern industry. One 30 x 20-inch unidirectional two-ply composite plate was manufactured using the VARTM method with all of the glass fibers at an angle of 0-degrees.

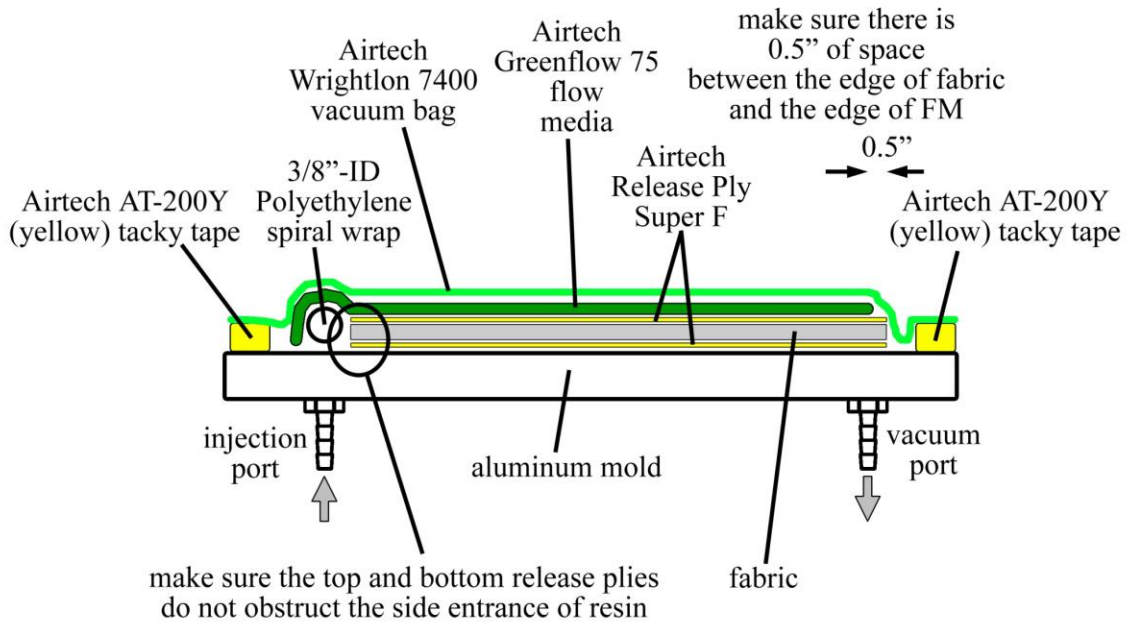


Figure 18. Configuration for vacuum assisted resin transfer molding process

The objective of the experiment is to test samples of both varying fiber angle and varying tensile stresses, therefore, to begin, samples of varying fiber angles were prepared. The geometric size that each sample was to be 4.5 x 0.6 inches; varying fiber angles were achieved by cutting the samples out of the unidirectional plate at the corresponding orientation. The size of the composite plate allowed for all samples to originate from one plate with proven consistency, and thus minimizing variations in material properties that could arise across multiple manufacturing processes. Fiber volume fraction was determined through a standard matrix burn-off procedure.

Following, presented in Table 4, is a summary of all samples manufactured by strictly adhering to the manufacturing procedures mentioned previously. It was of much importance to ensure the samples were as near to identically dimensioned as possible to ensure a small deviation in the magnitude of applied tensile stress.

Table 4. Summary detailing the total number of each sample variation manufactured. Recall θ is the fiber angle, ϕ_f is the fiber volume fraction, and σ_x is the magnitude of the tensile stress applied.

θ (deg)	ϕ_f	σ_x (MPa)	no. of samples
0	.52	0	2
		18	3
		30	3
20	.52	0	2
		18	3
		30	3

θ (deg)	ϕ_r	σ_x (MPa)	no. of samples
45	.52	0	3
		18	3
		30	3
90	.52	0	2
		18	3
		30	3
		Total:	33

With only a two-ply thick plate being used concerns arise when discussing the method of application for the tensile stresses due to the relatively small thickness. The approach chosen to achieve constant tensile stress in the samples was through using stainless steel compression springs. Various spring properties (spring constant and free length) were carefully measured and selected in order to provide the desired tensile stress in the composite samples. This procedure enabled a consistent and precise initial stress in the coupon. The springs were compressed using a hydraulic press and then restrained at both free ends using stainless steel pins, which were inserted through drilled holes near each end of the samples. In order to mitigate possibilities of the failure due to pin pullout one-inch tabs were also adhered onto both sides at either end of the samples. The holes for the pins were drilled directly in the middle of the tabs, a half-inch from end of each sample. After accounting for the locations of the holes the length of sample being stressed by the spring was calculated to be 3.5 inches. Through knowing the cross-sectional area of the composite sample, the distance between the drilled holes, and various spring parameters the resulting initial tensile stress a given spring will provide the sample can be estimated with reasonable accuracy. Any extension of the coupon due to creep, damage or swelling during the test is not accounted for in this test.

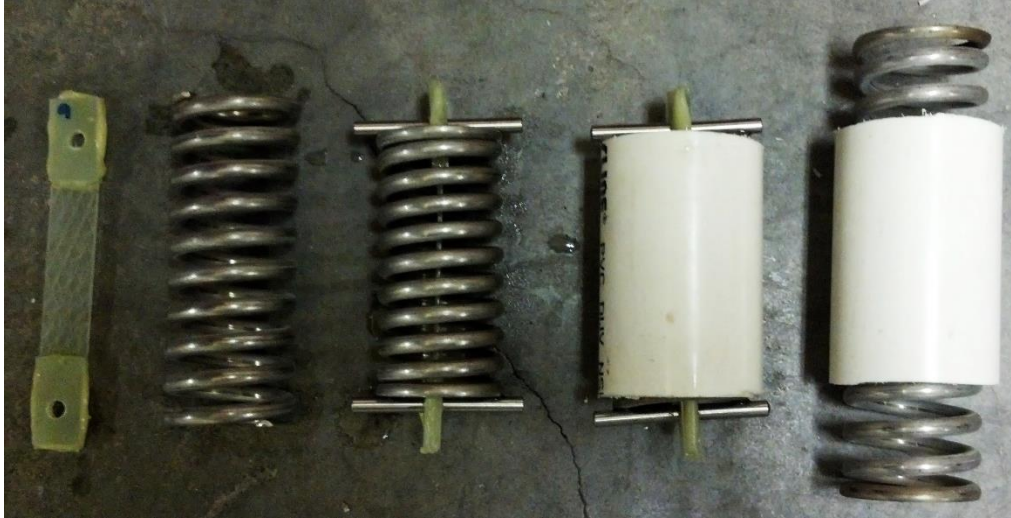


Figure 19. A completed composite sample as well as the springs used to provide the tensile stress to the sample. Note, at the right the PVC section is used to mitigate out of axis bending of sample as the spring has a large length.

1.7.4. Weight Gain Measurements

The stressed composite samples were submersed in water which was held in an oven at an elevated temperature of 50°C until a fully saturated state of the sample was achieved. Again, this elevated temperature expedites the diffusion process while leaving the maximum moisture concentration level of the system unaltered.

Establishing a consistent methodology of measuring the weight gain of the samples throughout the saturation process was of utmost importance. Initially, the dry weights of all the samples (without springs) were recorded; the springs were then pressed onto the samples and placed into the water bath. In order to take weight gain measurements, the stressed samples were removed from the water and using the hydraulic press the springs were removed. The composite samples were then dabbed dry using a microfiber cloth, being careful to not leave any residual contaminants that may skew the resulting weight gain measurements. The samples were then allowed to dry for an hour to allow the majority of the surface moisture to evaporate off; the purpose of this drying period is to minimize weight gains from sources not related to diffusion. The samples were then individually weighed on a scale, which was accurate to 0.0001 grams. Finally, the compression springs were once again pressed around the samples to re-initiate the tensile stress and placed back into the water bath to continue the saturation process. This process was rigorously followed for each weight gain measurement throughout the entire saturation process.

In order to accurately recreate the linear portion of the Fickian diffusion curve weight gain measurements were taken at frequent time intervals throughout the early stages of the soaking process. Once the moisture uptake curves began to visibly level off near the maximum moisture content level measurements at less frequent time intervals were taken. The samples were removed from the water bath and the springs removed from around the samples once a satisfactory level of saturation was reached.

1.8. Results and Discussion

1.8.1. Overview

The proposed theoretical model for the moisture diffusion parameters in stressed unidirectional composites was experimentally examined for a wide variety of composite samples encompassing differing fiber angle and tensile loadings. In addition, the results obtained from the finite element models were compared to both the results found through experimentation and those calculated using theoretical models. The two primary quantities, which were investigated, were the maximum moisture content and the diffusivity.

The prepared composite samples asymptotically approached their corresponding maximum moisture content level following Fickian diffusion principles. The moisture uptake curves exhibited initially linear portions of the curves before reaching a level of full saturation, which was dictated by both the fiber angle and magnitude of tensile loading applied to the sample. Overall, the collected weight gain data provided a solid representation of the expected Fickian diffusion curves, providing a good platform on which to undertake the calculations required to find the desired moisture uptake parameters. The experimental results found good agreement with the proposed theoretical model as well as the results obtained from the finite element model. Figure 20 presents the entirety of the collected weight gain data, where each data point represents the average weight gain for that particular fiber angle and stress level at the specified time.

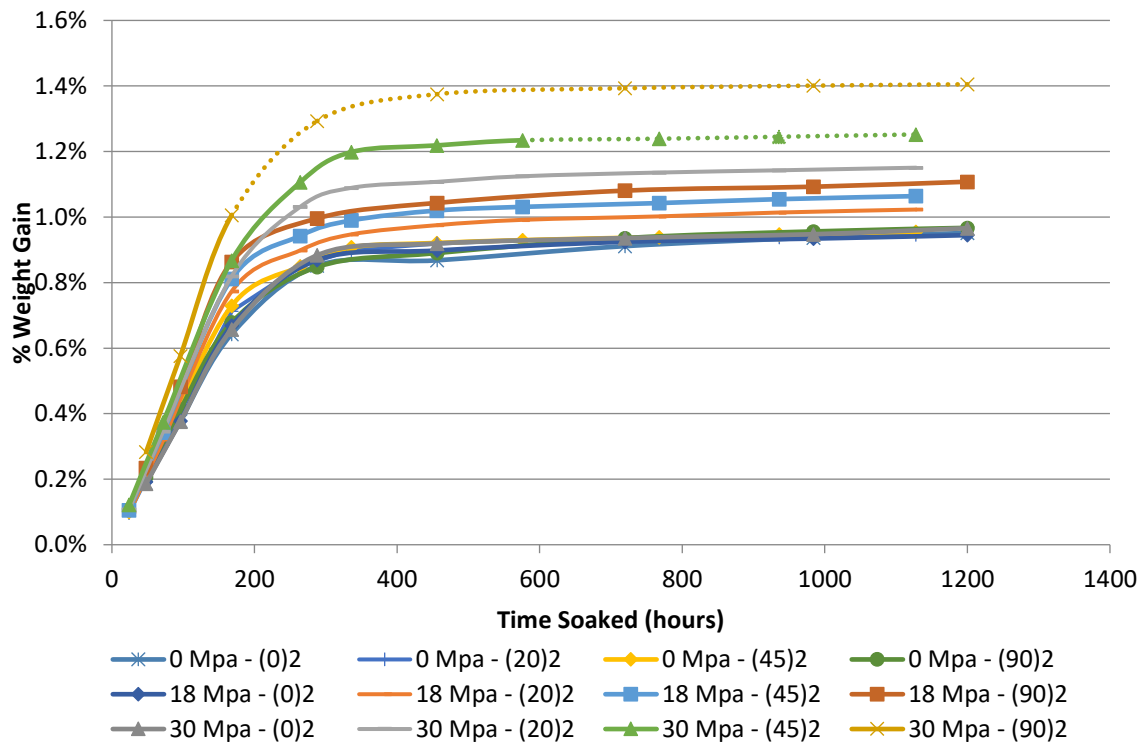


Figure 20. Experimental average moisture gain curves for all samples considered. Note the dashed lines represent extrapolated data due to sample fracture of the 45 and 90-degree 30 MPa samples.

1.9. Summary of Results

1.9.1. Maximum Moisture Content

The first diffusion parameter that will be investigated is the maximum moisture content. There are numerous combinations of fiber angle and tensile loading which have been presented in Figure 20. In order to gain a clear understanding and develop trends the data will be grouped first by loading level and then separated by fiber angle. Again, it should be noted that each data point represents an average of all samples of that particular loading level and fiber angle.

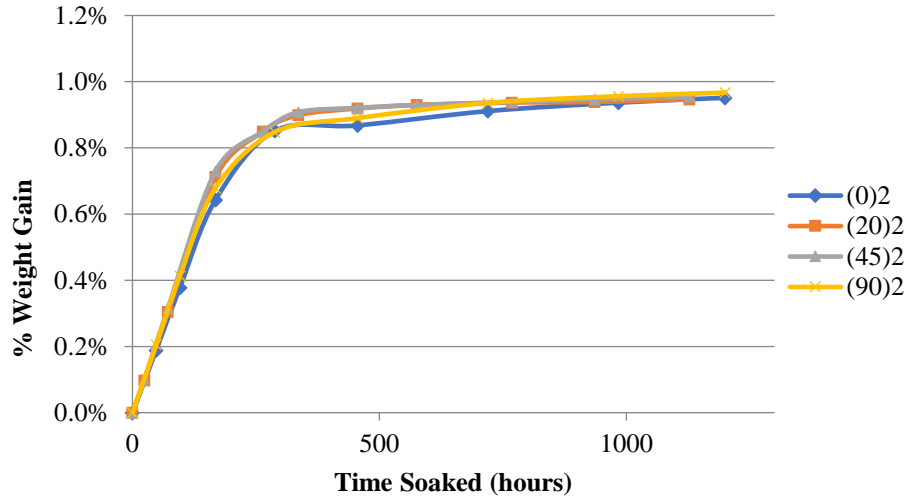


Figure 21. Experimental average weight gain curves for the 0 MPa samples.

The unstressed sample grouping is presented in Figure 21. The weight gain curve for all fiber angles followed nearly identical uptake profiles, as to be expected. All unstressed samples reached very similar maximum moisture contents, around 0.965%, regardless of fiber angle. As the primary focus of this study is to determine the effects of tensile stresses on the moisture diffusion parameters of the composite samples a control term should be established to serve as a baseline for comparative purposes to the stressed states. Now that it has been experimentally verified that all unstressed samples, regardless of fiber angle, exhibit nearly identical moisture uptake behaviors a control term can now be established as an average of all of the unstressed samples. The moisture diffusion parameters observed for the stressed states will be directly compared to this newly founded control curve.

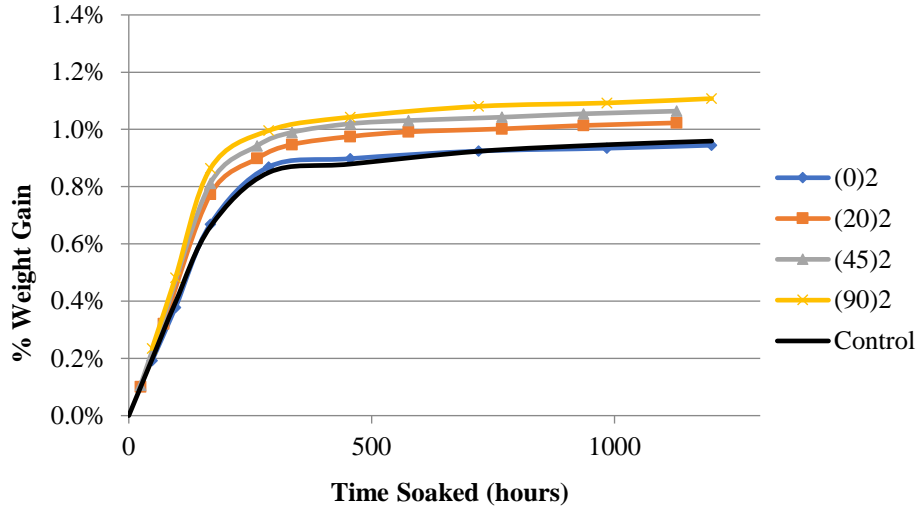


Figure 22. Experimental average weight gain curves for the 18 MPa samples. The control curve is an average of all fiber angles of the 0 MPa samples shown in Figure 21.

The 18 MPa sample grouping is presented in Figure 22. As expected, there is a certain degree of apparent separation between the weight gain curves throughout the fiber angle spectrum. The 18 MPa samples at a fiber angle of 0-degrees experience little to no variation from the control sample set, the degree of change seen increases with increasing fiber angle, where the largest change observed occurs at a fiber angle of 90-degrees. This reinforces the volume strain formulations presented earlier and makes arithmetical sense when examining the form given by equation (13). Additionally, it is observed that the initial slope of the uptake curves, which is directly proportional to the diffusivity of the sample, also vary to a significant degree. The issue of the variation in sample diffusivity will be discussed in further detail at a later point in the results sections.

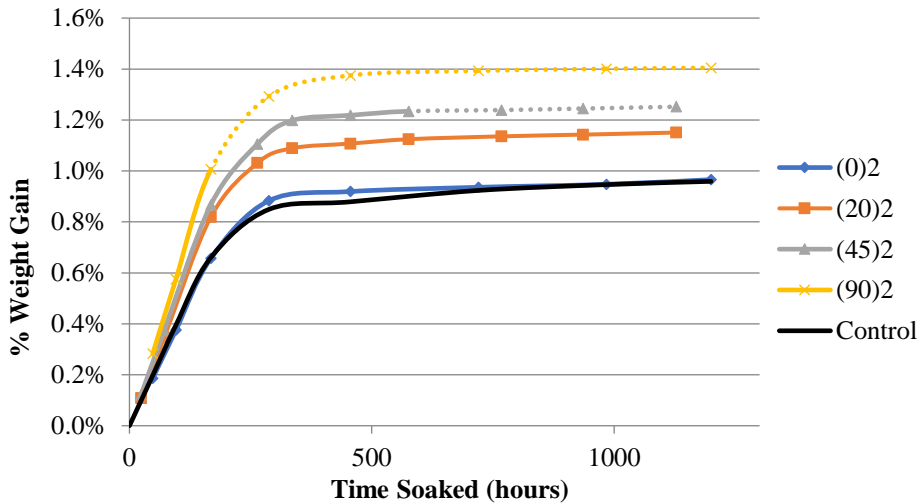


Figure 23. Experimental average weight gain curves for the 30 MPa samples. The control curve is an average of all fiber angles of the 0 MPa samples shown in Figure 21. Note the dashed lines represent extrapolated data due to sample fracture of the 45 and 90-degree samples.

The 30 MPa sample grouping is presented in Figure 23. The form that the weight gain curves exhibits similarities to the 18 MPa grouping, though the maximum moisture content has increased to

a greater degree with the 90-degree samples approaching 1.4% maximum moisture content versus about 1.15% for the 90-degree 18 MPa samples. The 0-degree samples experience negligible variations from that of the control sample set, which aligns with what was documented in the 18 MPa sample set.

All of the 45- and 90-degree samples loaded at 30 MPa did fracture prior to full saturation being achieved, the weight gain data was extrapolated from the last useable weight gain measurement recorded (denoted as dotted lines in the plot above). The fracture was unexpected, as the samples were loaded far below their ultimate tensile strengths, which according to the SNL/MSU/DOE Composite Material Fatigue Database is documented as being around 60 MPa. It appears as though the combination of elevated immersion temperature and prolonged tensile loading had detrimental effects upon the structural integrity of the samples, with the mechanical strength of the composite being significantly degraded. There was noticeable cracking that had propagated throughout the epoxy resin, shown below in Figure 24 - Figure 26. The 90-degree sample in particular underwent the greatest severity of degradation and is noticeably fragile, especially with regards to bending.



Figure 24. Fractured 45 and 90-degree 30 MPa samples alongside unstressed control samples demonstrating the severity of cracking seen within the structure of the samples.



Figure 25. 45-degree 0 MPa control sample alongside 30 MPa fractured sample detailing cracking in the epoxy.

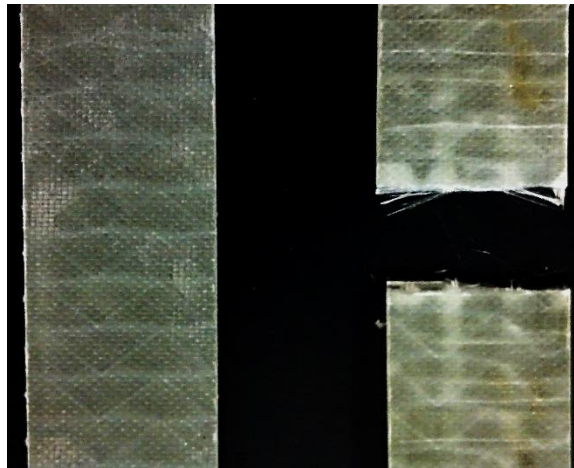


Figure 26. 90-degree 0 MPa sample alongside 30 MPa fractured sample detailing cracking in the epoxy.

Table 5 provides a comprehensive summary of all experimental maximum moisture content values as well as comparisons to values found through using ANSYS as well as those calculated purely using equation (15). Notice the ANSYS values and the calculated values are generally similar in magnitude, which is to be expected as the maximum moisture content is calculated using the same relationship for each case. Overall, the experimental values match both the ANSYS and calculated values relatively well. The percent error between the experimental maximum moisture content values and both the ANSYS and calculated terms are presented in Table 6. The largest departure from the experimental values is seen in the 90-degree samples loaded at 30 MPa with a percent error of nearly 16 percent. However, the experimental data for this particular sample set was extrapolated to the maximum moisture values, as the samples did fracture before full saturation was achieved. There does not appear to be a recognizable pattern in the relative magnitude of percent errors for the sample sets.

Table 5. Experimental, finite element model, and calculated values for the maximum moisture content level. Note the experimental values are presented as an average of all samples of that fiber angle, fiber volume fraction, and stress level.

θ (deg)	ϕ_f	σ_x (MPa)	M_{∞} (%)		
			Experimental	ANSYS	Calculated
0	.52	0	0.9692	1.0652	1.0652
		18	0.9453	1.0703	1.0676
		30	0.9758	1.0720	1.0718
20	.52	0	0.9466	1.0651	1.0652
		18	1.0235	1.0773	1.0776
		30	1.1510	1.0850	1.0852
45	.52	0	0.9559	1.0652	1.0652
		18	1.0644	1.1031	1.1027
		30	1.2523**	1.1354	1.1349
90	.52	0	1.0102	1.0652	1.0652
		18	1.1246	1.1363	1.1358
		30	1.4057**	1.1836	1.1829

** Note: The 30 MPa samples for both the 45 and 90-degree fiber angles fractured during the soaking process, maximum moisture content was extrapolated from existing weight values taken before sample fracture occurred.

Table 6. Percent error from experimental maximum moisture content data.

θ (deg)	σ_x (MPa)	Percent Error (%)	
		ANSYS	Calculated
0	0	9.91	9.91
	18	13.22	12.94
	30	9.86	9.84
20	0	12.52	12.53
	18	5.26	5.29
	30	-5.73	-5.72
45	0	11.43	11.43
	18	3.64	3.60
	30	-9.33	-9.37
90	0	5.44	5.44
	18	1.04	1.00

θ (deg)	σ_x (MPa)	Percent Error (%)	
		ANSYS	Calculated
	30	-15.80	-15.85

1.9.2. Diffusivity

As previously noted, the diffusivity of the samples also varies to a significant degree between the various combinations of tensile loading and fiber angle. Recall, the diffusivity of any given material system is directly proportional to the slope of the initially linear portion of the moisture uptake curve. In order to gain a clear understanding of this relationship Figure 27 - Figure 31 present the initial uptake portions (*time* = 0 hours to *time* = 200 hours) for each set of fiber angles, separated by magnitude of tensile loading.

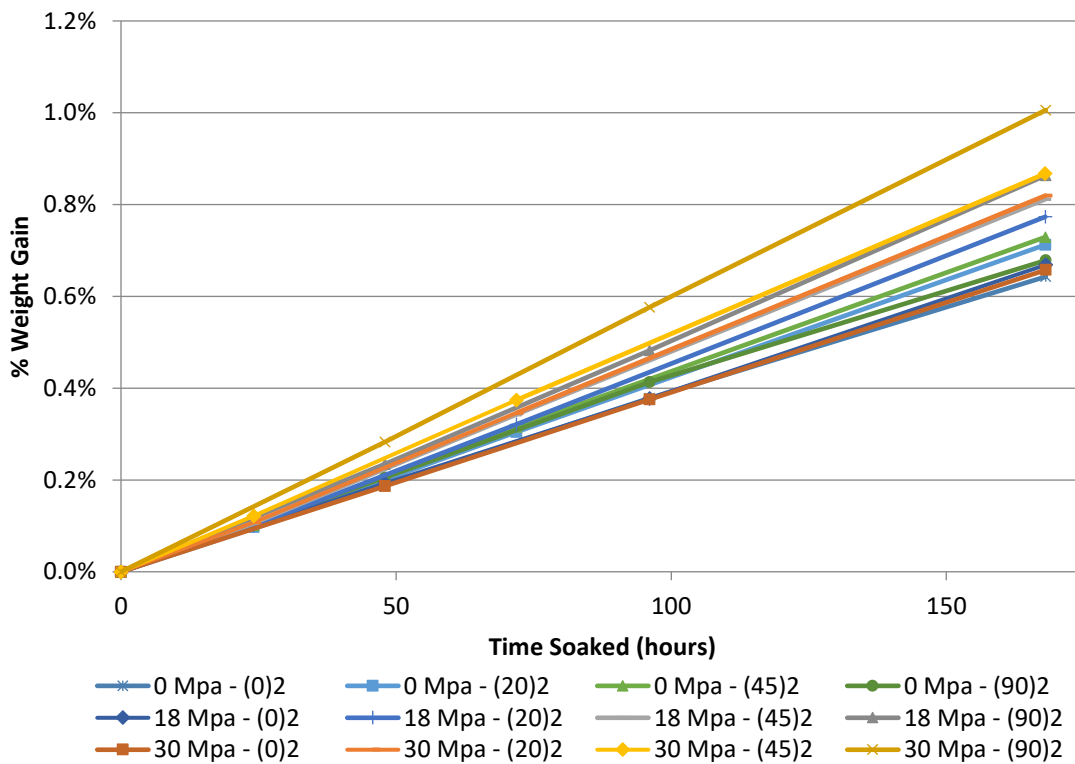


Figure 27. Initial linear portion of all moisture uptake curves, showing the relative changes in diffusivity between fiber angles and tensile loading. Where steeper slope represents a higher value of diffusivity.

Figure 27 presents the initial portions of the moisture uptake curves for the entire sample set, where the tensile loading is noted at the right. The 90-degree samples loaded to 30 MPa had the steepest uptake slope; this is to be expected, as it is both the largest tensile loading step as well as largest fiber angle. Conversely, there are a number of samples that occupy the bottom portion of the plot. These are constituted of all of the 0 MPa and 0-degree samples. It should be noted that 0-degree fiber angles and all three tensile loading levels are slightly lower than the 0 MPa counterparts at higher fiber angles.

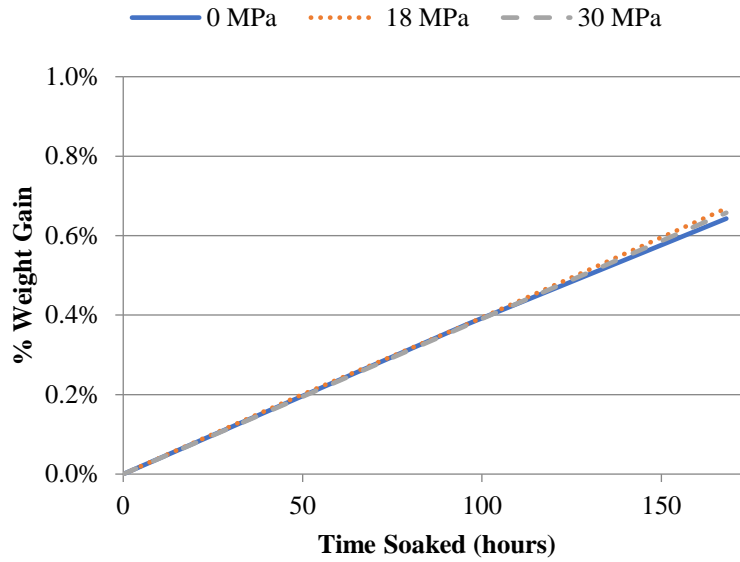


Figure 28. Initial linear portion of the moisture uptake curves for the 0-degree samples at all three magnitudes of applied tensile stress.

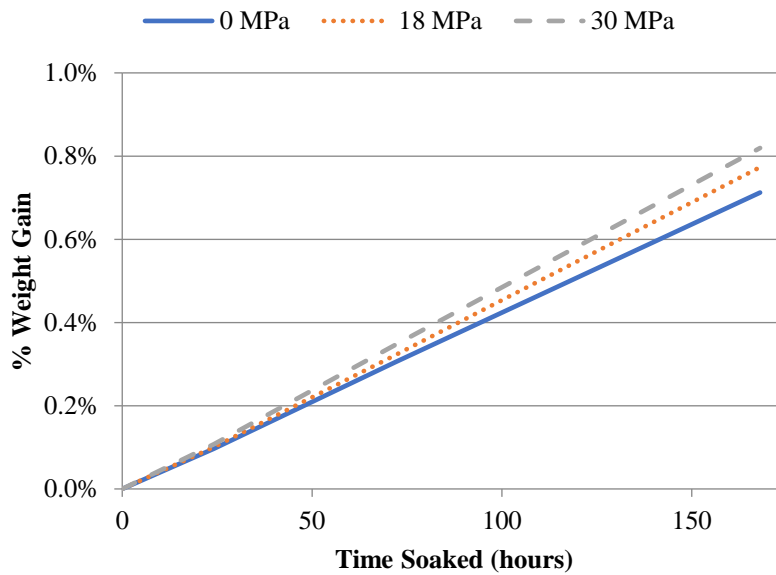


Figure 29. Initial linear portion of the moisture uptake curves for the 20-degree samples at all three magnitudes of applied tensile stress.

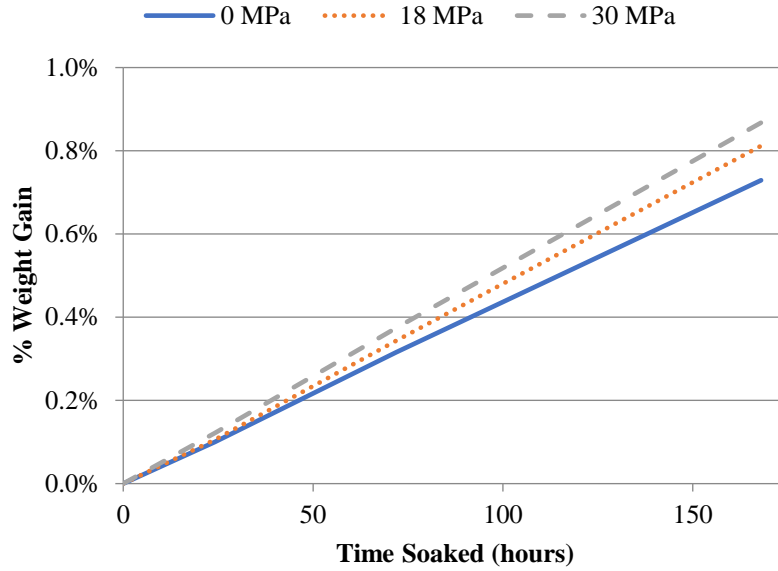


Figure 30. Initial linear portion of the moisture uptake curves for the 45-degree samples at all three magnitudes of applied tensile stress.

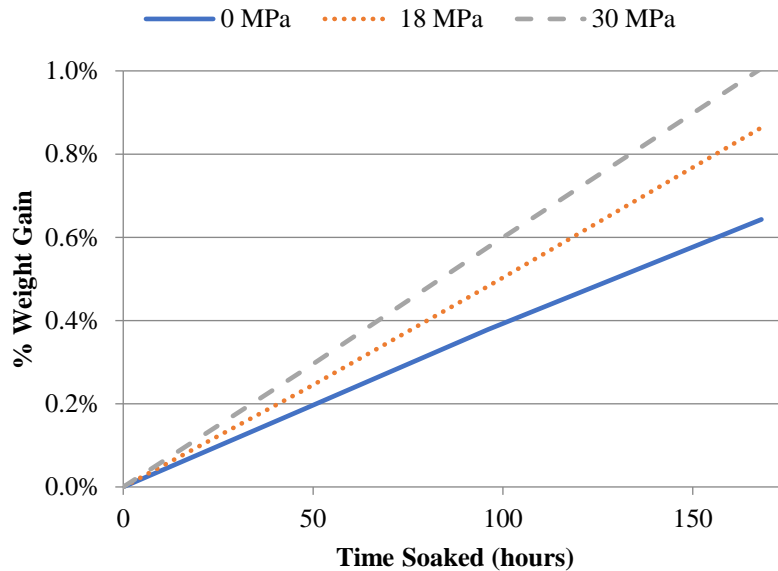


Figure 31. Initial linear portion of the moisture uptake curves for the 90-degree samples at all three magnitudes of applied tensile stress.

Figure 28- Figure 31 present the initial portions of the moisture uptake curves for fiber angles 0, 20, 45, and 90-degrees respectively. It is seen that the slopes, and therefore the diffusivities, of the 0-degree samples are very nearly identical, while the largest diffusivity value (steepest slope) is seen in the 30 MPa, 90-degree samples. Upon further investigation it can be noted that diffusivity increases to a larger degree as the fiber angle increases, which leads to the 90-degree samples having the largest degree of change seen in diffusivity values. Furthermore, it is again worth noting that slope of

the 0-degree samples are slightly lower than the 0 MPa counterparts at other fiber angles, which is not perfectly captured in the mathematical formulation presented previously.

Table 7 provides a similar summary for the diffusivity values. The ANSYS diffusivity values were calculated by first reproducing the moisture uptake curve using moisture content and time values obtained in ANSYS using equation (20), then through applying equation (4) the diffusivity was calculated. While the calculated values were found directly using the relationship for diffusivity of a unidirectional fiber composite plate presented in equation (5). This is due to the fact that the ANSYS program was set up to calculate the diffusivity separately for each direction, rather than combining the three into one representation. This accounts for the slight disparity seen between the two values. The percent error between the experimental values and both the ANSYS and calculated terms are presented in Table 8. The largest departure from the experimental values was seen in the 20-degree samples loaded to 30 MPa. Again, there does not seem to be a discernible pattern in magnitude of errors for the sample sets.

Table 7. Experimental, finite element model, and calculated values for the diffusion coefficient. Note the experimental values are presented as an average of all samples of that fiber angle, fiber volume fraction, and stress level.

$\theta(\text{deg})$	ϕ_r	σ_x (MPa)	D (mm ² /hour) * 10 ⁻²		
			Experimental	ANSYS	Calculated
0	.52	0	0.1073	0.1046	0.1076
		18	0.1156	0.1118	0.1075
		30	0.1120	0.1132	0.1074
20	.52	0	0.1250	0.1197	0.1134
		18	0.1374	0.1296	0.1366
		30	0.1813	0.1619	0.1559
45	.52	0	0.1237	0.1187	0.1211
		18	0.1444	0.1429	0.1482
		30	0.1911	0.1691	0.1743
90	.52	0	0.1195	0.1151	0.1177
		18	0.1705	0.1631	0.1699
		30	0.2132	0.1977	0.1987

Table 8. Percent error from experimental diffusivity data.

$\theta(\text{deg})$	σ_x (MPa)	Percent Error (%)	
		ANSYS	Calculated
0	0	-2.52	0.28
	18	-3.29	-7.01

θ (deg)	σ_x (MPa)	Percent Error (%)	
		ANSYS	Calculated
20	30	1.07	-4.11
	0	-4.24	-9.28
	18	-5.68	-0.58
	30	-10.70	-14.01
45	0	-4.04	-2.10
	18	-1.04	2.63
	30	-11.51	-8.79
90	0	-3.68	-1.51
	18	-4.34	-0.35
	30	-7.27	-6.80

1.10. Conclusions for Stress Assisted Diffusion

This investigation sought to gain further insight into the effects of tensile stresses on the moisture diffusion parameters of fiber reinforced polymer composite materials. A model was presented that attributed the changes in moisture diffusion parameters to changes in the free volume of the matrix material, which is equal to the volume strain. Through the use of laminate plate theory, a formulation for the volumetric strain of the matrix was found; this formulation was in terms of fiber volume fraction of the composite, magnitude of applied stress, fiber angle, as well as a number of elastic constants of the constituents.

Additionally, both two- and three-dimensional finite element models were developed using the ANSYS finite element analysis package. This FEA model utilized a mathematical analogy between thermal and mass diffusion in order to fully model the moisture diffusion process in the system. The model calculated diffusivities in the x, y, and z directions of the composite from the input parameters and ran through time steps until full saturation as obtained.

Results for maximum moisture content and diffusivity demonstrated good agreement between calculated values, values obtained from ANSYS, and experimental data. It was found that at a fiber angle of 0-degrees the diffusion parameters remain relatively unchanged with applied tensile stresses. Conversely, at a fiber angle of 90-degrees significant changes in the diffusion parameters were observed in the samples. These trends were adequately captured in the mathematical formulation presented.

In general, the model overestimates maximum moisture content and underestimates diffusivity values, through the largest departures at still within about 15% of the recorded values. The experimental values could be varying from the model values due to the averaging scheme used in distributing the loads to the matrix material. With a more precise method for determining what percentage of the tensile loading is transferred to the matrix the relative accuracy of the proposed model would increase. The averaging scheme chosen for use was the rule of mixtures, which holds merits for many applications and is the easiest to apply but is not necessarily the most accurate scheme available.

2. DAMAGE BEHAVIOR OF GFRP

Composite materials possess complex damage modes due to the different damage behavior of the constituents and the interaction between them. Anisotropy and the direction of applied load further complicate the damage mechanisms present in a composite laminate. The load-sharing relationship between the fiber and the matrix leads to interesting micro-mechanical damage mechanisms and that would not be present in a homogeneous isotropic material. Further, this load sharing capability of FRP's allows for the material withstand a sizable amount of damage prior to failure, making composites damage tolerant. The ultimate failure of the FRP depends on the coalescence and growth of these micromechanical damage into the global failure of the material. Understanding of this progressive damage behavior is essential to both development of better composite materials as well as better implementation composite design, particularly when fatigue is present. In terms of wind turbines and MHK devices, this includes incorporating environmental effects, damage mechanisms and progression.

2.1. Hygrothermally-Aged Composites

Enhanced mechanical properties compared to conventional engineering materials make FRP's a prominent choice for wind turbine and MHK devices, but environmental effects on these properties must be considered. The exposure of a material to a warm moist environment of materials is known as hygrothermal aging. Application of FRP materials exposed to hygrothermal environments is not a novel concept and has been a subject of study industries such as boating and marine, aerospace, and civil structures. However, many types of FRP's exist and hygrothermal effects can vary significantly between systems, making the characterization of the effects still a relevant materials and engineering problem

The study hygrothermal effects on a composite are three-fold: 1) understanding of how moisture diffuses into the composite, 2) the resultant change in the mechanical properties due to moisture, 3) determining the mechanisms responsible for the change in mechanical properties. Fortunately, diffusion of moisture into FRP's is well understood and predictable. Property degradation is correlated to moisture uptake, but the exact mechanisms for the degradation are not well understood. Degradation due to hygrothermal aging presents a complex multifaceted problem and can be attributed to a variety of chemical and physical factors singularly or in combination, including hygro-strains, hydrolysis, interface degradation, matrix plasticization, amongst others. The extent of hygrothermal degradation and the mechanisms of degradation will vary significantly with different material systems.

2.1.1. Damage/Defect Effects on Diffusion

Diffusion behavior can be affected by other attributes of the FRP. Intuitively, voids and cracks in the laminate offer pathways for water to penetrate the composite. Many works suggest that diffusion of water into FRP's can cause irreversible damage and is evidence by changing diffusion rates.

2.1.2. Hygrothermal Aging Effects on Mechanical Properties

A variety of test methods may be employed to examine the effects of moisture on the mechanical properties of the FRP. A multitude of mechanical tests have been used to characterize hygrothermal effects on mechanical properties, including uniaxial tension in both static and fatigue [32, 43, 44, 47-52], flexure [51, 53], shear [35, 39], and delamination [54-56]. The resultant changes mechanical

properties are scattered amongst researchers. In general, moisture absorption typically results in a moderate reduction in strength and minor changes in modulus.

Even results between similar types of material systems show different varying hygrothermal effects. Mourad *et al.* showed found there to be no changes in mechanical properties for a hygrothermally aged glass-epoxy system [47], while research on another glass-epoxy system conducted by Garg *et al.* observed strength reductions of nearly 65% [44]. The variation between these different studies of comparable material systems emphasizes the need to address the hygrothermal aging for each FRP system as the specific chemical composition of the matrix, reinforcement and architecture, conditioning parameters, and manufacturing techniques may all have influence hygrothermal response.

2.1.3. Hygrothermal Degradation Mechanisms

As mentioned previously, moisture uptake occurs predominantly in the matrix material or in the fiber matrix interface regions. Consequentially, degradation in bulk mechanical properties due to aging is largely attributed to degradation of these two phases.

As moisture is absorbed into a composite swelling can cause physical damage in the microstructure. Swelling behavior of aligned fiber composites has been explored previously and can be modeled similarly to thermal expansion with varying expansion coefficients in-line and transverse to the fibers [57].

Additionally, moisture ingress into the composite can alter the molecular structure of the matrix and interface. Water is a known plasticizer in polymeric materials. Plasticization occurs when water occupies free volume between polymer chains and interrupts the secondary bonds between polymer chains and increases chain mobility. The nature of water in the polymer with varies depending on the material system.

Determining mechanical properties of thermoset polymers like epoxy can be difficult due to a brittle mechanical behavior. Mechanical test coupons are sensitive to fracture from defects induced during manufacturing such as porosity or stress concentrations on the specimen edges from post-processing operations. Due to the difficulty of testing thermosets such as epoxy, previous research characterizing the of hygrothermal effects on mechanical properties is sparse.

Although difficult to measure mechanically, the presence of plasticization and chemical interactions of water with the polymer may be observed by monitoring changes in the glass transition temperature of a polymer with aging. The glass transition temperature (T_g) indicates a physical change of a polymer and is an important attribute when defining the service conditions of a material.

The integrity of the fiber-matrix interface presents another aspect of concern for durability of hygrothermally aged composites. Changes in interfacial properties between commonly attributed to change in mechanical behavior due to hygrothermal aging [39, 43-45, 47, 53, 55, 60, 61].

Mechanical tests may also be implemented to better understand the interface behavior. Transverse tension, interlaminar delamination, and interlaminar shear strength (ILSS by short beam shear) tests can provide insight into interface strength fiber-matrix interface [51, 55, 62].

2.1.4. Acoustic Emission

Since FRP's tend to be damage tolerant materials, monitoring the damage state of the material is important to the evaluation of the integrity and residual life of the material. Non-destructive testing (NDT) and non-destructive evaluation (NDE) methods provide means to monitor this damage

without alteration of the material itself. These techniques are a subject of great interest for both structural health monitoring (SHM) applications and material characterization. Acoustic Emission (AE) monitoring, an NDE technique was implemented during the mechanical tests conducted in this work both to aid in describing the damage progression of hygrothermally exposed composites, as well as to evaluate the effectiveness of AE as an SHM method in MHK devices.

2.1.5. AE Analysis Techniques

For material characterization, the goal of acoustic emission monitoring is to identify the damage state of the material. Ideally, this includes identifying what type of damage has occurred and determining its severity. Due to the complexity of the AE waveforms, damage trends and behaviors must be correlated to waveform features and parameters. These parameters are attributes of recorded waveforms and include amplitude, energy, peak frequency by fast Fourier transform (FFT), counts, rise time, and duration. Figure 32 depicts some of these waveform features. A detailed explanation of these features can be found in previous work at MSU conducted by Michael Schuster [66].

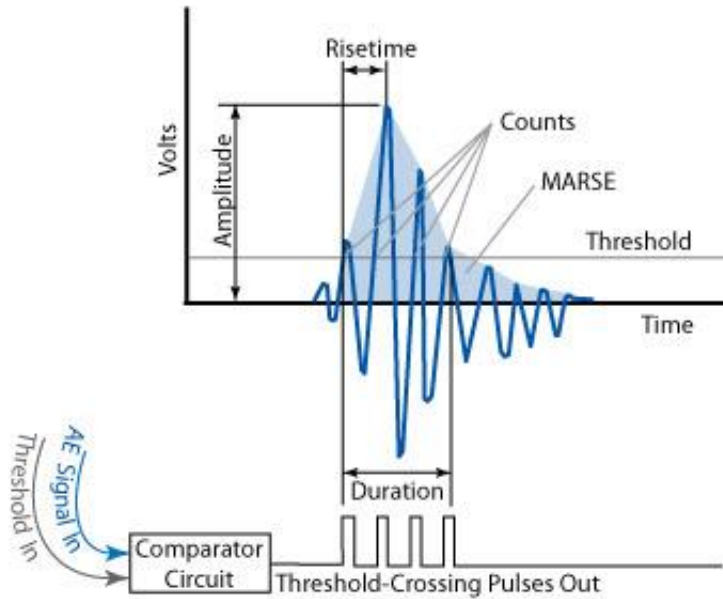


Figure 32. Typical AE waveform features.

A multitude of analysis techniques exist to interpret the AE results including single parameter methods, multiparameter methods, and waveform analysis. Figure 33 summarizes AE data collection and analysis techniques.

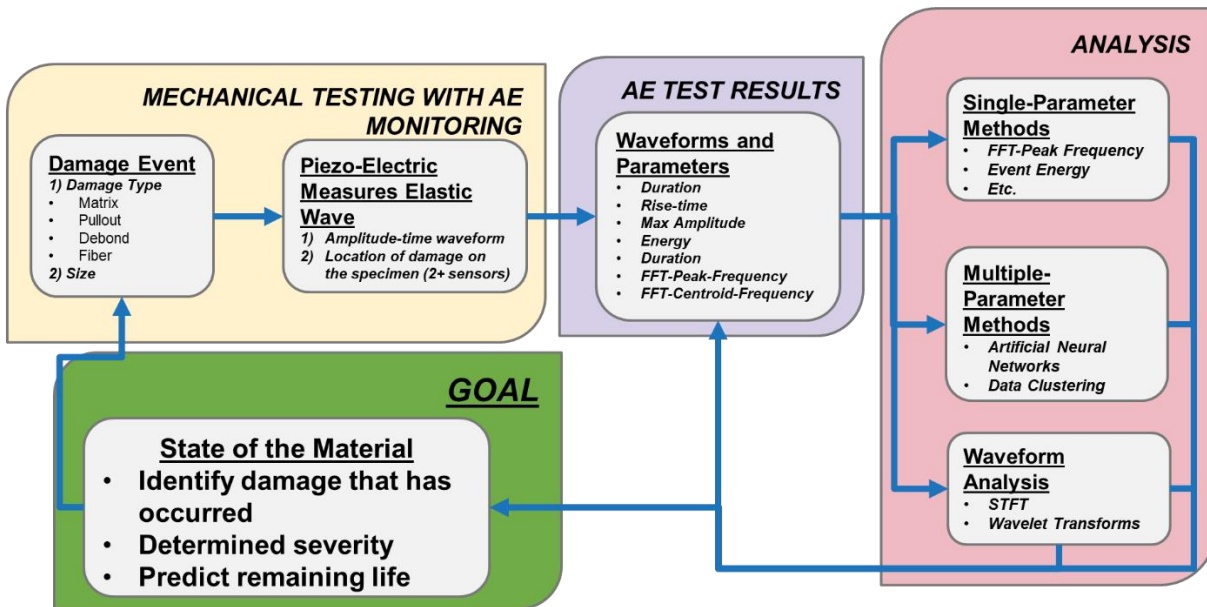


Figure 33. AE Data collection and processing flow chart.

Single parameter methods were implemented to categorize and quantify the damage in a composite. As the name suggests, this method categorizes damage events based off one sole parameter. FFT-peak-frequency and energy have been the dominant parameters for differentiating damage, either by size or mechanism. FFT-peak-frequency has made a consistent appearance in literature as a way to distinguish damage mechanisms [67-71]. Damage mechanisms of matrix cracking, fiber matrix debonding, fiber pullout, and fiber fracture were correlated to different ranges of frequencies. Often, debond and pullout events are combined to be described as interphase events. Schuster explored this technique for an assortment of fabric architectures, specifying the frequency bins for glass-epoxy material to be 50-120kHz for matrix cracking, 120-180 kHz for debonding, 180-300 kHz for fiber/matrix debonding, and fiber breakage for events greater than 300 kHz [66].

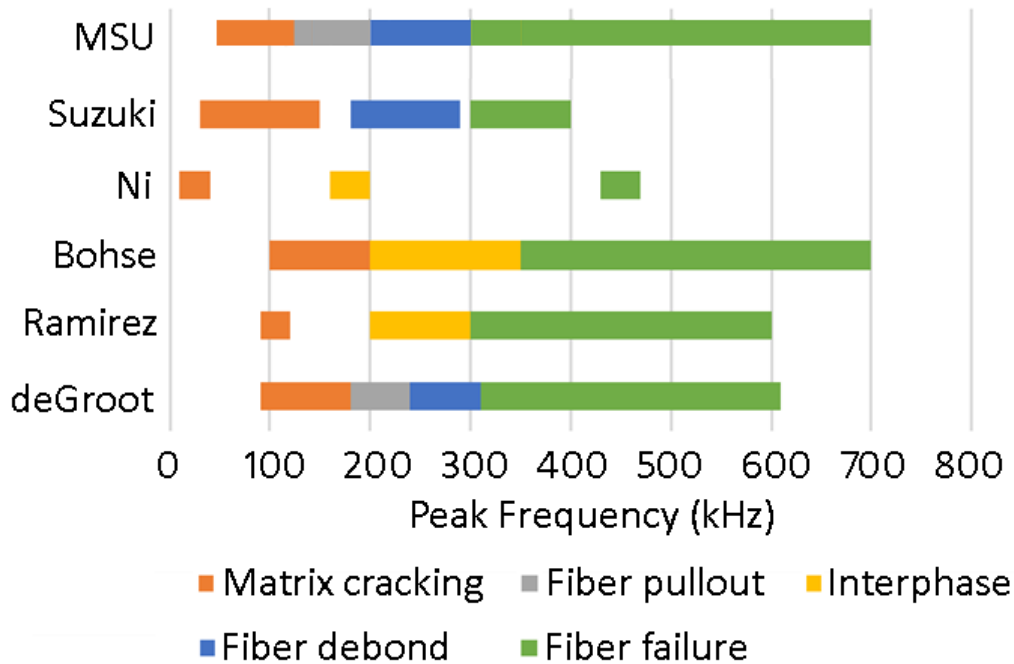


Figure 34. FFT-Peak-frequency bins from literature review and previous work at MSU.

Another single parameter often used to interpret AE data is energy. The energy of the elastic wave, derived from the integration of the time-amplitude plot of each waveform, can be correlated to the dissipated energy of the material. Schuster explored this parameter with load-unload-reload tests and found that AE energy does correlate to dissipated energy and can be useful in predicting the amount of damage, and thus the residual life of the material [66]. This trend between AE energy and damage accumulation has been observed in several other studies [72,73].

Single parameter techniques, although often showing decent correlation, do not utilize all the available parameters to classify waveforms. Consequently, multi-parameter analysis techniques such as data clustering and artificial neural networks (ANN) have been a subject of current work in acoustic emission. The techniques allow data to be correlated based in multiple dimensions, incorporating more AE waveform features. Interestingly, clustering studies revealed that peak frequency prevails as the only AE parameter with enough variance to isolate the data into clusters, which presumably represent damage mechanisms [74,75]. Detailed waveform analysis has also been a subject of AE analysis. Waveform analysis examines each waveform in detail in an attempt to isolate wave modes and ultimately lead to new waveform features that are more descriptive of the damage event [76, 77]. Surgeon *et al.* proposed that isolating the features of both the extensional and flexural wave simultaneously could provide more information indicative of source behavior and orientation, but robust techniques to determine these parameters were not well established [76]. Waveform analysis conducted by the author implemented a short-term four transform (STFI) to gather frequency components of just the extensional wave resulting in notable variation from classic FFT-peak-frequency results. However, concrete validation of damage mechanisms and their relation to received AE waveforms remains the ongoing challenge with AE monitoring. Though these advanced techniques possess merit, single parameter analysis of frequency and energy will be the primary techniques employed in this work.

2.1.6. AE and Hygrothermal Aging

AE provides a useful method for interpreting damage progression in composite materials, making AE a logical choice for studying effects of hygrothermal aging on damage behavior of FRPs. Since AE is an indirect method of measuring damage, the measured response is a convolution of the damage behavior itself and the elastic wave propagation/attenuation behavior. Hygrothermal aging may affect both the damage behavior of the material as well as its wave propagation behavior; thus, part of this research focuses on attempting to isolate these effects.

Previous work including AE monitoring with hygrothermal aging has shown significant changes in AE response due to hygrothermal aging. Hygrothermal aging in conjunction with AE was first demonstrated by Hamstad *et. al.* where the root-mean-square (RMS) energy emitted from a glass-epoxy system decreased after hygrothermal aging [78]. Later, Garg *et. al.* investigated damage initiation in hygrothermal aging of a graphite epoxy system [54, 55]. This work examined both interlaminar and intralaminar damage initiation by means of delamination and transverse-tension tests. Both tests experienced a reduction in cumulative AE event counts as well as RMS energy with hygrothermal aging; losses were attributed to moisture induced attenuation of the AE signal. Komai observed a similar trend in fatigue of aged and unaged CFRP, however, the reduced output was speculated to be a change in damage behavior due to a moisture induced increase in resin ductility [60]. Another investigation of a chopped strand composite speculated that the reduction in energy due to aging could be due to a combination of damage behavior and wave-behavior effects [79]. Collectively, the outcome of the works has shown changes in AE due to hygrothermal aging to be multifaceted, potentially affecting the damage behavior and wave propagation/attenuation behavior simultaneously.

2.2. Matrix Characterization

2.2.1. Thermal Analysis: DSC

Differential Scanning Calorimetry (DSC) is one of several methods available for conducting thermal analysis on polymers. Quantitatively, DSC results yield the glass transition temperature, T_g . Changes in T_g relate to changes in the microstructure of the polymer and subsequently indicate changes in mechanical behavior. Although this method does not provide measurable changes of the mechanical behavior, it can provide insight into the physical/chemical nature of water in the polymer and aid in interpretation of hygrothermal effects mechanical data of the composite material. The final test method for DSC tests is shown in Table 9.

Table 9. DSC Test method

Step number	Heating/Cooling ramp	End of ramp temperature (°C)
0	Start Test	Room-temperature (20-25 °C)
1	Heat: 10 °C/min	130°C
2	Cool: -10 °C/min	20°
3	Heat: 10 °C/min	130°C
4	Cool: -10 °C/min	20°
5	End Test	Room-temperature (20-25 °C)

To determine the nature of water in the neat epoxy system three series of tests were conducted. Each series consisted of five samples to determine an accurate T_g value. All samples were cured at 25 °C for 24 hours and 70 °C for 12 hours, meeting the manufacturing specifications. The first series of tests were conducted on control, as-manufactured, samples that experience no hygrothermal conditioning. The next series was of samples that had been aged in 50 °C distilled water for 300 hours. These tests were conducted to determine the effect of absorbed water on T_g . The final series of samples were subjected to the hygrothermal aging as the second set, but then dried/desorbed until no more moisture was released, determined by equilibrium in the sample mass. The reversibility of this process both in terms of the amount of desorbed moisture and change in T_g may explain the whether the absorbed moisture in this is interacting physically or chemically with the epoxy system. Figure 35 shows an example DSC curve for a hygrothermally aged sample and Table 10 shows the conditioning for DSC samples, moisture contents and measured T_g values. T_g is reported as the center of the transition region determined by the tangent line method.

2.2.2. DSC Results

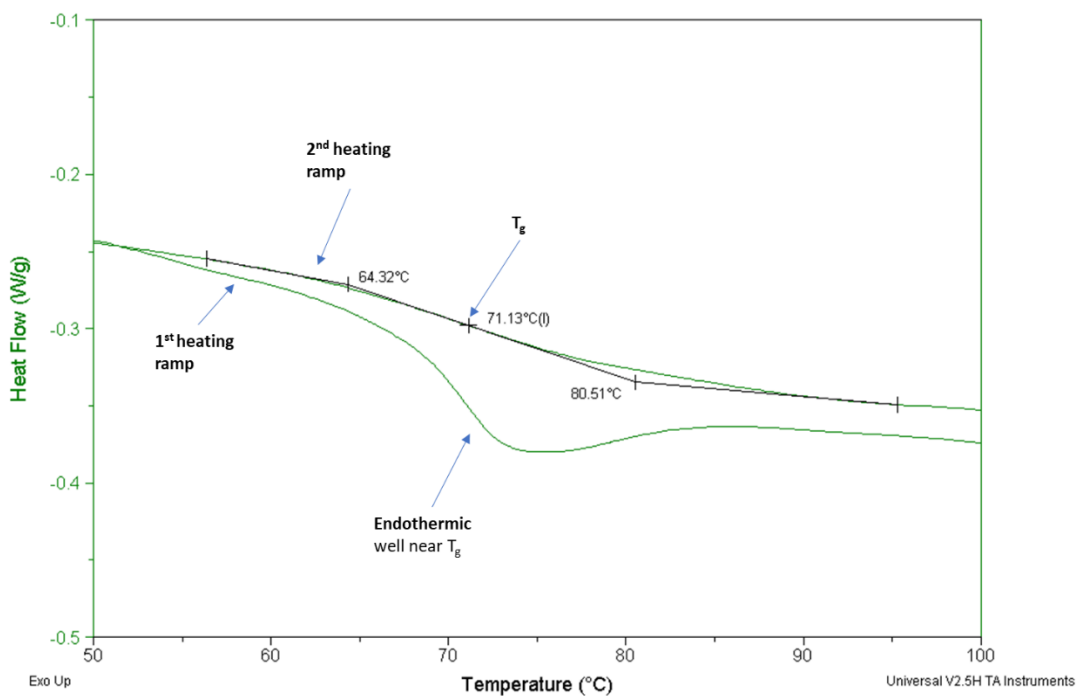


Figure 35. DSC heating curves showing T_g for Hexion 135/1366 with 4% moisture by mass.

As shown in Figure 35, the heating curves for the first and second temperature ramps showed different behavior. Most notably, the first ramp cycle experienced an endothermic-well near the glass transition. This correlates to a release of energy from the test sample itself. This could be attributed to primarily two mechanisms; the reaction of monomers that did not react during the curing cycle, or relief of residual stress from the curing cycle, known as enthalpic relaxation. Aside from the endothermic well, both the first and second heating cycles followed one another closely on both the heating and cooling cycles, which would suggest that the source of the endothermic-well did not change the reversibility or structure of the material. This observation supports the hypothesis that the endothermic-well was, in fact, enthalpic relaxation. Two-cycle DSC methods are recommended to deal with this anomaly [82].

Table 10 DSC sample conditioning and T_g results

Sample Type	Conditioning	Number of Samples	Tested bulk moisture content (%)	T _g measured from the second heating cycle.
Control	none	5	0.0%	86.9
Aged	312 hrs. 50°C distilled water	5	4.0%	69.9
Desorb	1) 312 hrs. 50°C distilled water 2) dried 620 hrs. 50°C	5	0.1%	90.9

The aging time of 312 hours resulted in a bulk uptake of 4%; however, samples had not reached Fickian equilibrium and therefore m_{∞} values of the system could be higher. Desorption returned the samples to a state of nearly 0% moisture content. Due to the small size of the samples, and the resolution 0.1 mg resolution of the mass balance used to weigh samples, the moisture content resolution was ~0.1%. The release of nearly all the moisture in the system at the same temperature as the aging process means most of the water molecules occupied the epoxy physically in free volume. However it is possible that the small amounts of water interacted chemically through hydrolysis or the secondary crosslinking network described by Zhou *et al.* [40]. Figure 36 shows the transition region on the second heating cycle for each test condition; both control and desorbed samples have a similar transition length, while the hygrothermally aged sample has a premature and prolonged transition region. T_g results at each condition level are depicted below in Figure 37. Error bars represent the standard deviation¹ of the five samples for each test and show consistency in the test method.

¹ Unless otherwise stated, error bars presented in throughout this work are standard deviations.

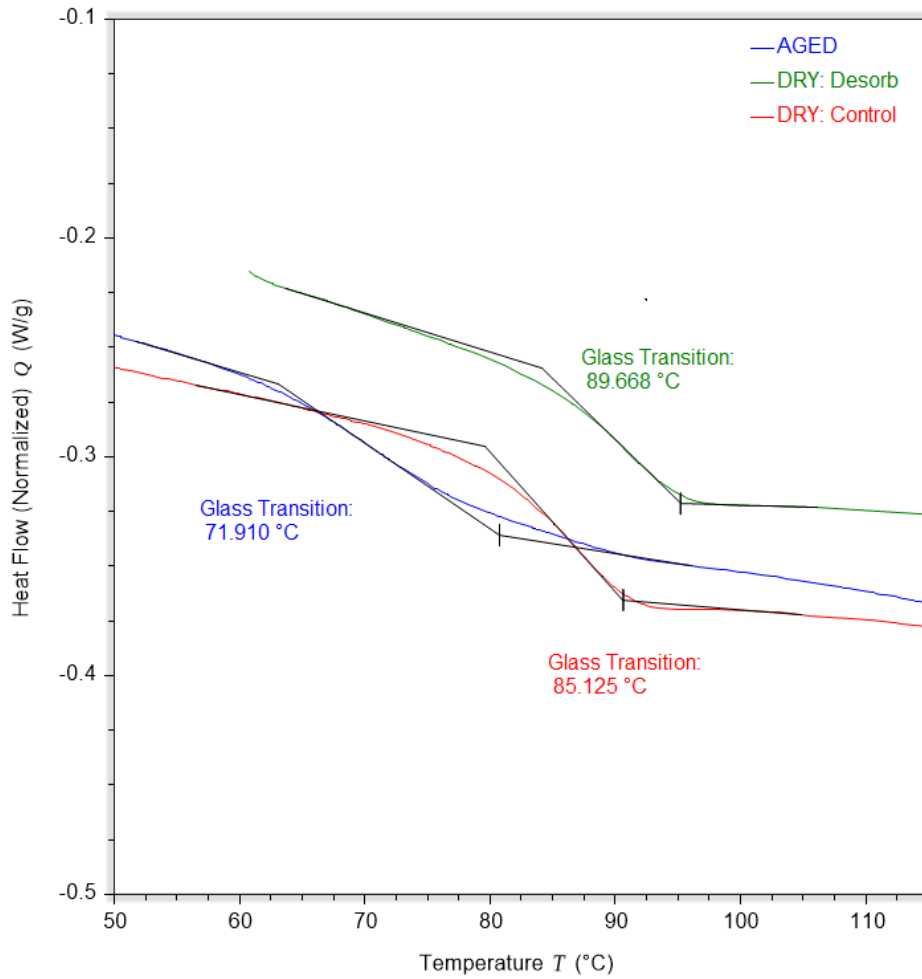


Figure 36. Example second-cycle heating curves for DSC samples of each condition.

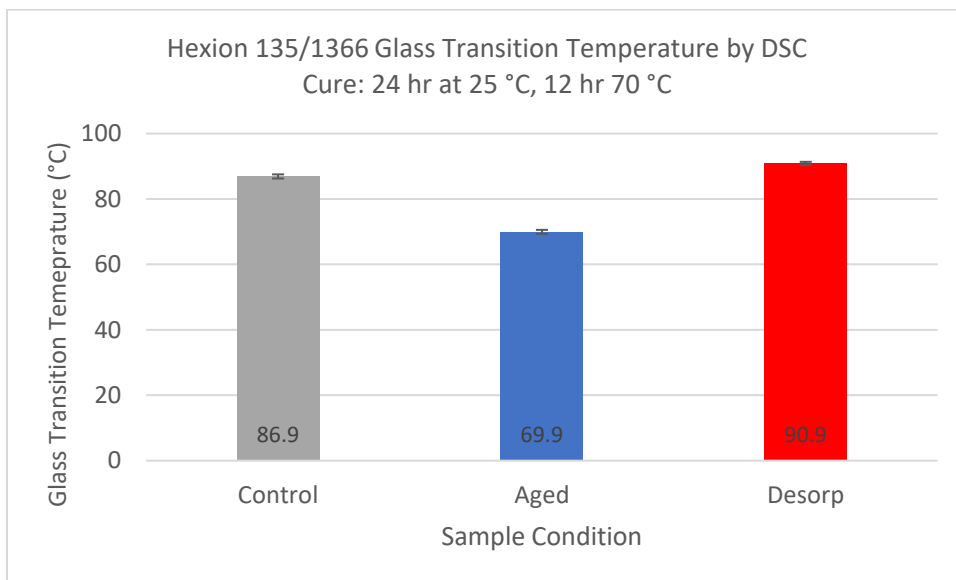


Figure 37. T_g results for hygrothermally aged Hexion 135/1366.

T_g depression from the control to aged state confirms that aging-induced matrix plasticization is present in this matrix system. Despite a 17 °C drop after hygrothermal conditioning, T_g was fully recovered and exceeded control T_g of the control samples by 4°C after the desorption process. Full recovery of T_g suggests that plasticization is reversible in conjunction with completing drying of the samples shows that water molecules do not chemically interact with the polymer. The increase of the desorbed samples compared to the controls could be in part to the temperature history due to prolonged exposure to elevated temperature or increased crosslinking from reactions occurring during the conditioning process.

Thermal analysis yielded several findings which will aid in understanding degradation in the composite. First, reversibility of the aging process through desorption shows presence of water in this material system mostly physical. However, small amounts of residual water could have interacted chemically through hydrolysis and crosslinking. T_g depression confirms that plasticization is present, and T_g recovery with desorption shows this process to be reversible. Literature has shown that plasticization correlates to changes in mechanical behavior including reduced strength and modulus of the matrix material [42, 58]

2.2.3. Neat Resin Diffusion and Swelling

Isolation of the diffusion characteristics of just the matrix material helps explain the diffusion and swelling characteristics of the composite. As moisture is diffused in a polymeric material, swelling occurs. Consequently, swelling can alter the internal stress state of the composite, potentially causing damage and alter the mechanical performance.

To determine hygro-strains, a set of large-geometry neat resin samples manufactured, so that average strains could be measured from larger geometric changes. Neat resin cubes (5 cm x 5 cm x ~4.5 cm”) of Hexion 135/1366 were cast in a brass 3-piece mold shown in Figure 38 by hand pouring.



Figure 38. A 3-piece mold for manufacturing neat resin cubes.

After curing the cubes, the samples weighed to get initial masses. A digital caliper was used to measure the size of the cubes to a resolution of 0.05 mm. each face of the cube was measured in width and length from the center of one edge to the center opposite edge. These 12 length measurements could then be used to calculate the volume of the samples. After the initial measurements, the cubes were aged in distilled water at 50°C. The cubes were periodically removed from the water and dried so that mass and volume could be measured and monitored throughout the diffusion process. The bulk moisture uptake was calculated by Equation 2 and the average swelling strain was calculated from the measured change in cube dimensions at each measurement interval. Since the diffusion is a transient process, it is important to note, strain levels will vary spatially with moisture content. Three cubes were aged, and 3 cubes were kept in their control-dry state for later comparison.

2.2.4. Neat Resin Diffusion and Swelling Results

Figure 39 shows the bulk mass diffusion for the three neat resin cubes plotted versus the square root of time. The diffusion behavior of the pure matrix material appears linear in the square root of time domain, as anticipated for Fickian behavior. However, due to the size of the samples, the diffusion process takes an exceedingly long time to reach equilibrium, and as seen in Figure 39, the neat resin cubes have not yet begun to approach the asymptotic equilibrium value. The final data point published in this work was for an aging time of 5000 hours. After 5000 hours of aging, samples absorbed 5.72% moisture by mass and could increase with continued aging. This value is more than observed in the DSC test (not soaked to equilibrium) and is on the upper end of the 2-7% expected for an epoxy system [40]. These values will be compared to the *in situ* matrix-uptake values of composite specimens in the subsequent section.

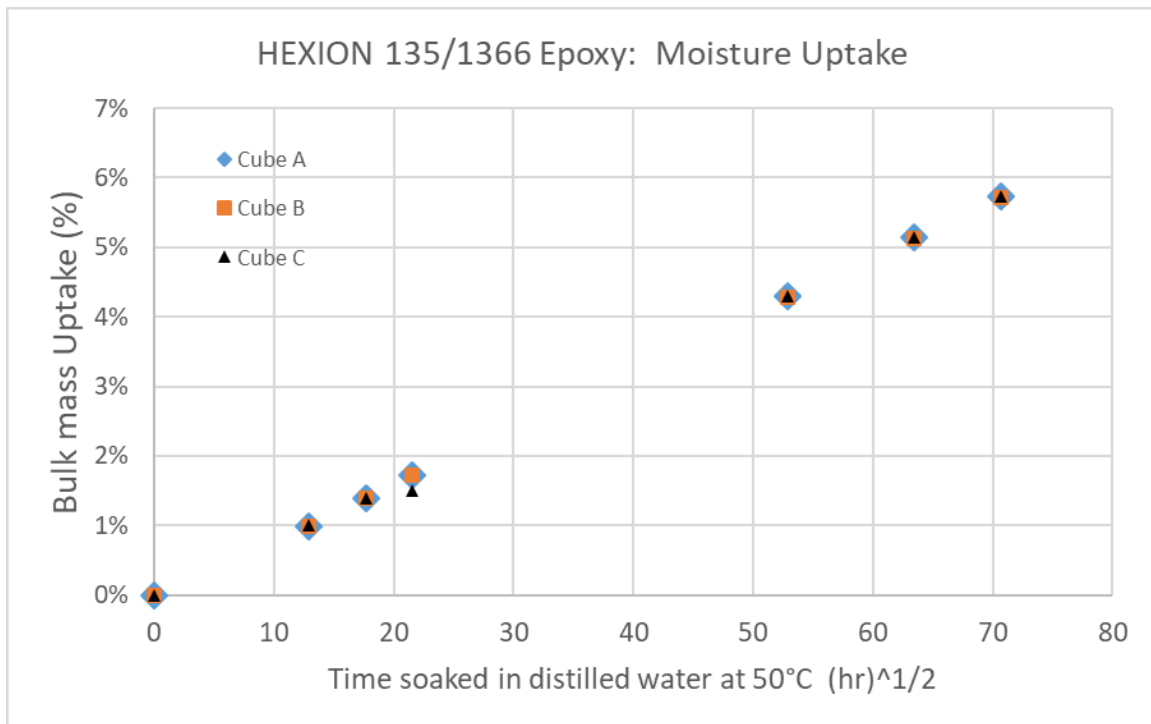


Figure 39. Neat resin cube bulk diffusion

A significant amount of moisture uptake resulted in a significant swelling strain, shown in Figure 40. After 5000 hours, strains reached an average of 1.94% strain. The increase in swelling strain correlates well with the increase in moisture content.

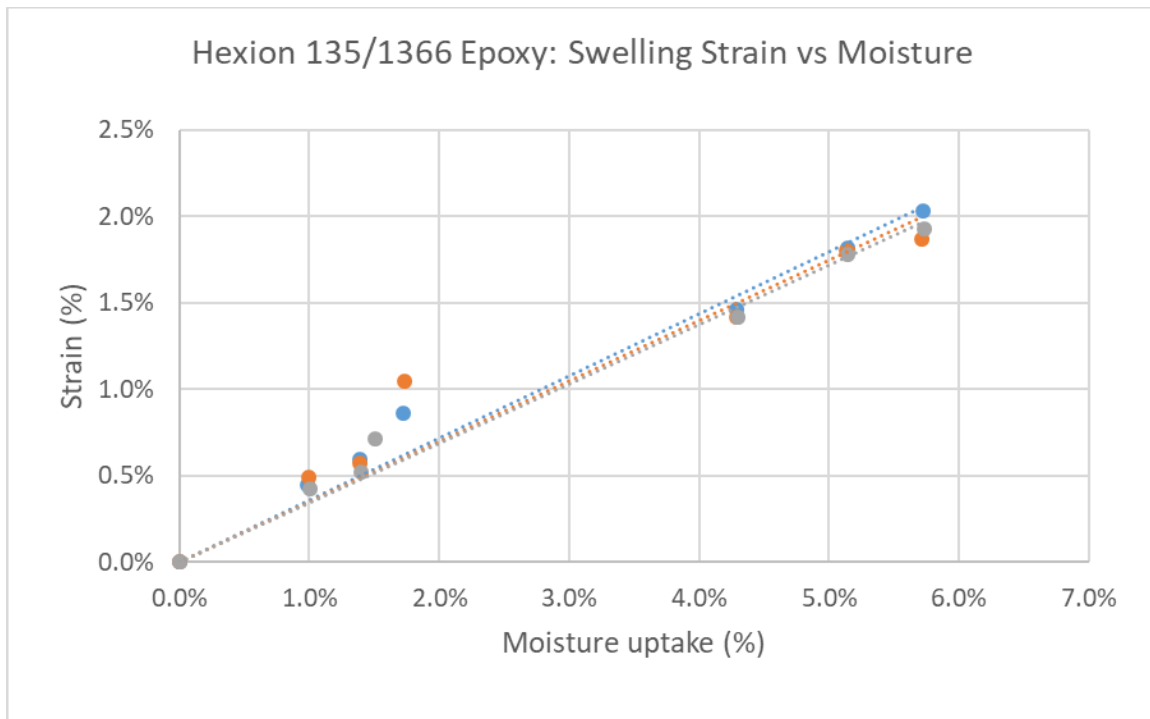


Figure 40. Swelling strains during transient diffusion of neat resin cubes.

Moisture uptake and swelling of this magnitude possess the ability to cause large internal stresses which could damage the composite or alter the damage progression upon loading. Using the bulk strain and moisture uptake, a hygrothermal swelling coefficient for the matrix material β_m can be determined for this epoxy system as shown in Equation 7.

$$\beta_m = \frac{C}{\epsilon} \quad (7)$$

C is the bulk moisture uptake of the isotropic material and ϵ is the strain. The slope of the strain plots shown in Figure 40 gives this value. For the Hexion 135/1366, β_m is 0.35 (% ϵ / %m). Theoretical hygro-stresses in composite laminates will be evaluated using laminate theory in the subsequent static test section.

Comparison of hygrothermally aged neat resin cubes control samples revealed significant changes in the appearance due to aging. Changes in appearance from a control to aged state include both changes in color and opacity as well as visible damage within aged samples. Figure 41 shows this obvious change in color from the aging process and notes areas where the damage occurred. Figure 42 shows the cross-section of the cubes, where the internal damage can be observed.

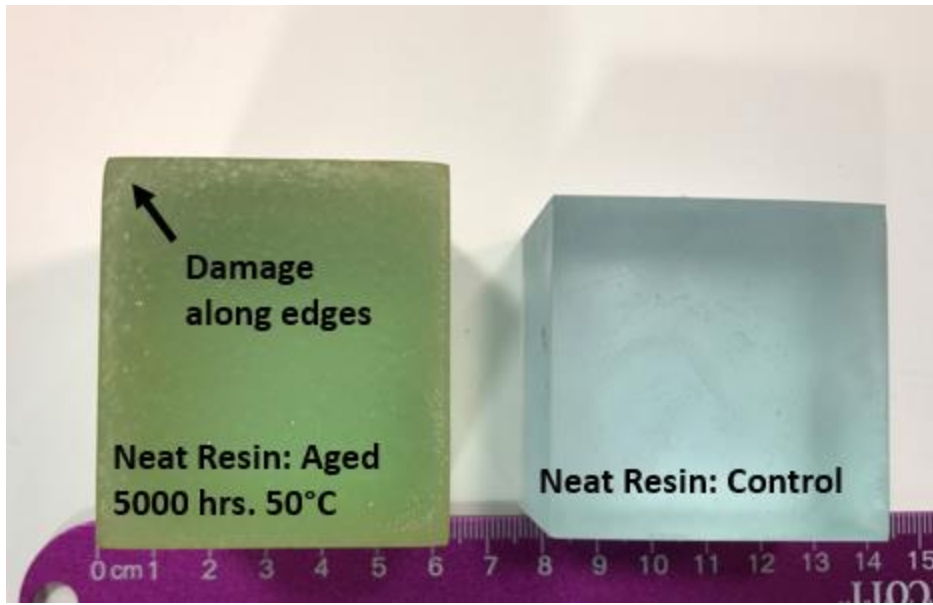


Figure 41. Neat resin cubes aged 5000 hours (left) and control (right)

As seen in by the cross-sections in Figure 42, many cracks formed along the edges of the cube and ranged in size from 0.4mm to 2mm. High moisture contents along the boundaries of the cube caused large amounts of localized swelling, which ultimately lead to damage.

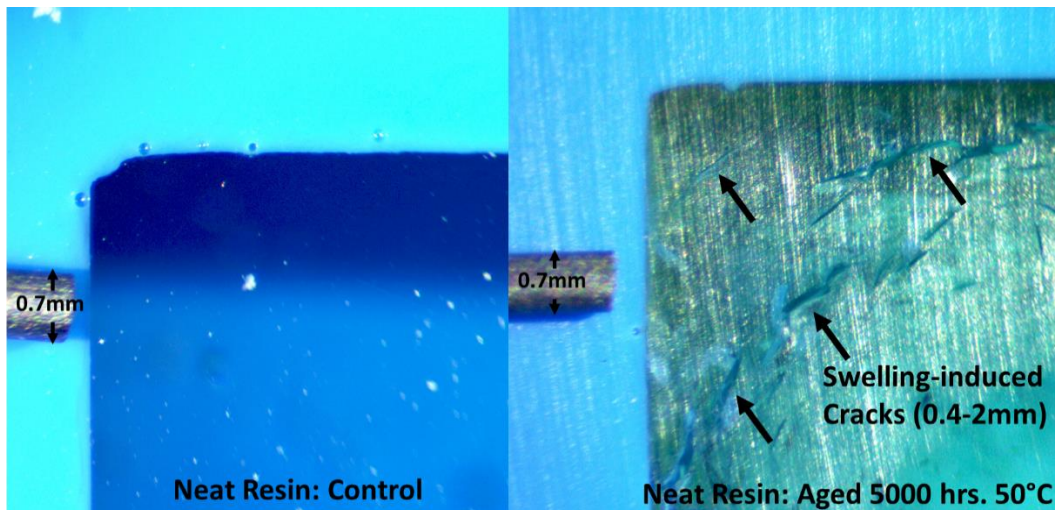


Figure 42. Cross section of swelling damage of neat resin (Hexion 135/1366) under an optical microscope (5X).

2.3. Static Tests

2.3.1. Test Design

The results of this study will aid engineers in the application of this material system in the design of MHK devices and offshore wind turbines, as well as provide further insight into mechanisms of hygrothermal degradation and methods to identify these mechanisms in future studies involving diverse material systems.

To aid in the evaluation of the changes in the static strength of cross-ply laminates, this work adds tensile tests of unidirectional laminates in both the longitudinal and transverse directions. Little work has been done to classify aging effects from constituent unidirectional laminates to multi-directional laminates. With damage mechanisms and damage progressions of unidirectional and cross-ply laminates being well understood, comparison of laminates in aged and unaged states should give insight into the hygrothermal degradation mechanisms at large in this material system. Additionally, this work includes test samples that have been soaked and dried or desorbed to determine the reversibility of the degradation mechanisms. To verify that changes in performance are not an artifact of elevated aging temperatures altering the temperature history of the FRP, samples with just temperature exposure were also tested. Five tensile were tested for each laminate in each condition. Table 11 shows the mechanical tests conducted in this study.

Table 11. E-LT3800 Mechanical Test Matrix.

Layup	Condition	Test Method	Number of Samples	Acoustic Emission
[0] ₂	Dry: control	Static-Tensile	5	Yes
[0] ₂	Saturated	Static-Tensile	5	Yes
[0] ₂	Dry: desorb	Static-Tensile	5	Yes
[90] ₂	Dry: control	Static-Tensile	5	Yes
[90] ₂	Saturated	Static-Tensile	5	Yes
[90] ₂	Dry: desorb	Static-Tensile	5	Yes
[0/90] _s	Dry: control	Static-Tensile	5	Yes
[0/90] _s	Saturated	Static-Tensile	5	Yes
[0/90] _s	Dry: desorb	Static-Tensile	5	Yes
[0/90] _s	Temperature only	Static-Tensile	5	No
[90/0] _s	Dry: control	Static-Tensile	5	Yes
[90/0] _s	Saturated	Static-Tensile	5	Yes
[90/0] _s	Dry: desorb	Static-Tensile	5	Yes
[90/0] _s	Temperature only	Static-Tensile	5	No

The conditions of the test coupons, Dry-control, Saturated, Dry-desorb, Saturated, and Temperature-only (no moisture) will be explained in detail in “Experimental Methods” section. In addition to the results of the mechanical testing, AE data was collected to aid in described the changes experienced by hygrothermal aging. Further, this work will include both macro and microscopic evaluation of damage occurring laminates due to hygrothermal aging as well as evaluation of failure types observed during static testing

2.4. Experimental Methods

2.4.1. Materials and Manufacturing

Infused, textile-type, E-glass FRP's have been the material of choice in the wind industry, with static and fatigue properties for these types of materials being well characterized and readily available. Consequently, with the emerging MHK designs sharing many of the same design parameters, these materials present a viable choice for selection in these new energy harvesting devices. The laminates of this work were manufactured with Vectorply E-LT3800 fabric and a Hexion 135/1366 two-part epoxy. The manufacturer's specification sheet for these materials can be found in Appendix A. The E-LT 3800 is a stitched, predominantly unidirectional consisting of 1138 g/m² (91%) of longitudinal tows and 114 g/m² of transverse backing strands, stitched together with polyester thread. Although this fabric is truly a biaxial fabric, it will be considered a unidirectional lamina due to a large number of fibers in the longitudinal direction. In the stacking sequence, backing strands are oriented towards the centerline of the laminate so a $[0/90]_s$ is equivalent to a $[0_b \setminus 90_b]_s$ laminate, where "b" indicates the location of the fabric backing². Presence of backing strands but be considered when interpreting static test results.

Laminates were manufactured using the VARTM process. An aluminum plate was used as a mold, featuring an inlet and an outlet port at either end of the infusion process. The mold was treated with a mold release agent to prevent the laminate from bonding to the mold surface. A layer of peel ply was placed above and below the fabric stacking sequence aid in the demolding process. Flow media, a plastic mesh was placed on top of the upper peel ply to allow the resin to flow across the top of the laminate and diffuse downward through the thickness. Synthetic rubber sealing tape was placed along the perimeter of the mold, and the layup was sandwiched beneath a plastic bagging film to seal the one-side mold. A vacuum pump attached to the outlet port via a plastic was used to infuse resin into the fabrics.

The resin was mixed per the manufacturer's specification (100g RIMR 135 to 30g RIMR 1366). Mixing was achieved using a motorized spindle at a speed that was fast enough to agitate the resin but slow enough to prevent porosity from turbulent flow. Mixing was conducted for 4 minutes to thoroughly mix the two-part resin. After mixing the resin, the tube connected to the inlet port was placed in the container of mixed resin, and the infusion process was started. Depending on the laminate, diffusion times could vary, ranging between 10 and 15 minutes.

The laminates were cured using the two-step cure cycle recommended by the manufacturer. The first step was a 24-hour room temperature cure (25°C) on the mold after which the laminate could be removed from the mold and placed in the post-cure oven. The post-cure was maintained at a temperature of 70°C with a temperature controller and lasted 12 hours. Matrix burn-off tests were completed for each laminate with the fiber volume fractions ranging between 55 and 58%.

After curing, laminates cut into tensile test coupons using a water-lubricated diamond abrasion saw. The coupon geometries were a nominal 30 mm by 300 mm, but actual sample dimensions, including thickness, were measured using digital calipers and recorded. These sample dimensions were chosen to provide enough area to capture an adequate amount AE data. After the conditioning process, but before the tensile testing, tabs made of G10 fiberglass plates were adhered to the test samples using

² "s" indicates a symmetric laminate; $[0/90]_s$ is equivalent to $[0/90/90/0]$.

adhesive. Tabs measured 64 x 32 millimeters and alleviate some of the damage from the grips of the testing machine during the static tests. This sample layout is depicted in Figure 44.

2.4.2. Sample Conditioning

To simulate a marine environment, samples were subjected to hygrothermal aging. Samples hygrothermally-aged samples were soaking in 50°C distilled water. Distilled water was chosen over synthetic seawater because previous work at MSU has found that salt build up on the coupon surfaces can alter moisture content measurements; further, distilled water usually results in more moisture uptake into the composite and would represent more conservative case. Further, EDX/EDS have shown that salt does not diffuse into the composite as a compound or an ion [47, 48]. Prior to hydrothermal aging, the initial mass of the sample was obtained using a digital scale to the resolution of 0.001 grams. After subsequent periods of hygrothermal exposure this mass could be remeasured to give the bulk moisture content of the sample by the Equation 3. Samples were aged until the bulk moisture content plateaued to equilibrium as shown in **Error! Reference source not found.** After reaching equilibrium, samples were removed from the water, and tabs were applied with an epoxy adhesive and allowed to cure at ambient conditions for 12-16 hours. Specimens were tested within 24 hours of removal from the water to prevent significant loss of moisture. These samples reached the maximum moisture content and will be referred to as “Saturated” and the moisture content reported is the moisture content before tabs were applied. An additional set of saturated samples were then placed in a 50 °C environment and dried to remove moisture. The process of drying is known as desorption; thus, aged-then-dried samples are referred to as ‘Dry-desorbed’. Like the saturated samples, the desorbed samples were tabbed and tested after an equilibrium was reached. Another set of control samples referred to as “Temperature-only” were aged in a dry 50 °C environment for the same duration as the saturated samples to isolated temperature history effects of the accelerated-aging process.

2.4.3. Mechanical Testing Procedures

Samples were tested monotonically in quasi-static tension until ultimate failure in accordance with ASTM D3039 [83]. Testing took place in an Instron 8562 servo-electric load frame in position control with a cross-head displacement rate of 15.2 *mm/minute* for all samples. The hydraulic grip pressure of 21 MPa was applied for laminates containing 0° plies and 7 MPa for transverse ([90]₂) samples. Strain was measured with an Instron 12.7 mm gage section extensometer; Figure 43 shows the experimental setup. Both load data and strain data were collected using the Mistras AE system. To prevent damage to the extensometer at final failure, the gage was removed between 1% and 1.5% strain. The strain rate of the last 0.2% of collected strain was linearly extrapolated to ultimate failure so that stress-strain curves could be generated for these tests. For unknown reasons, parametric outputs shorted-out during some tests and thus strain data is not available for all samples; however, ultimate loads were collected for all samples.

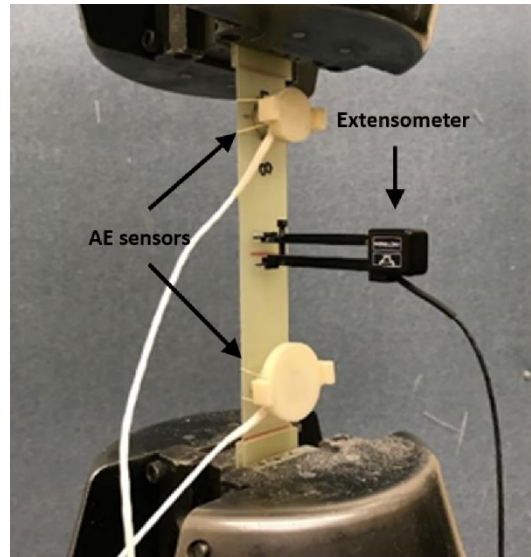


Figure 43. Tensile test experimental setup.

2.4.4. Acoustic Emission Setup and Data Collection

All tensile tests except the temperature-only tests were monitored with a Mistras PCI- Micro-II system. This AE setup parameters utilized in this work were developed by Michael Schuster; a more detailed explanation of the system operation and setup can be found in his thesis [66]. To use the linear-locating functionality of the system, two Physical Acoustics wideband sensors were attached to the test specimens in a linear array as shown in Figure 44. Sensors were spaced 128 mm apart and centered across the width of the sample. 40 dB external amplifiers magnified the AE signals. A thin layer of vacuum grease ensured good contact with the test specimen.

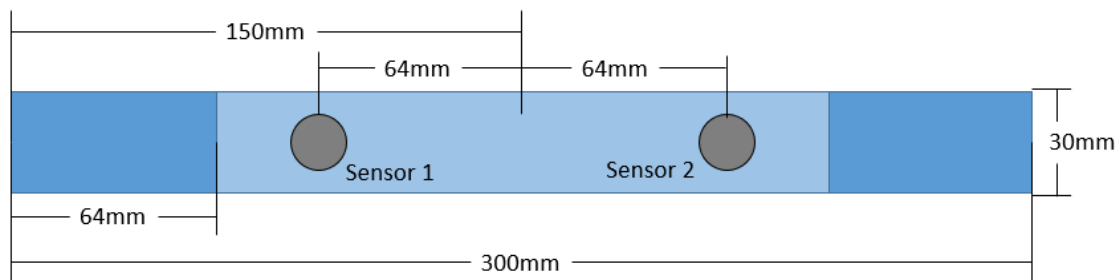


Figure 44. Tensile test sensor layout.³

The Mistras system featured an AE sampling rate of 3 MHz and a bandpass filter for the range of 50-400 kHz. A threshold of 40 dB was sensitive enough to pick up damage-induced AE activity without collecting ambient noise. Events were collected with 128k of pretrigger and a total waveform length of 1024k. The timing parameters peak definition time (PDT), hit definition time

³ Jake Nunemaker

(HDT), hit lockout time (HLT), and max duration was set to 50, 100, 300, and 99 microseconds. A time of flight-based filter used to limit recorded events to those occurring between the sensors.

In preparation for the mechanical test, two system tests were conducted. The first system test was the sensor test using the Acoustic Property Matrix Generator (APMG). The sensor test uses the AE sensors as actuators to pulse the system. Time of flight between sent and received pulses determine the wave speed and compare the response of the sensors. If energy and amplitude response between sensor varied by more than 10%, the sensors were reapplied and tested again. The second system test simulated an acoustic emission event by conducting a pencil lead break (PLB) test to generate an elastic wave. Breaking pencil lead on the sample in various locations verifies that linear locating is working correctly and that no extraneous noise events are picked up. Upon completion of these tests, a collection of AE is initiated followed by the start of the static test. AE data were collected through the ultimate failure of the test specimens and truncated at the ultimate load in the post-processing.

2.5. Results

2.5.1. Moisture Absorption and Desorption

The moisture absorption curves and desorption results are shown below in Figure 45 and Figure 47 for both unidirectional and cross-ply laminates. The absorption diffusion curve, plotted against the square root of time, matches Fickian behavior. The behavior is linear for the first portion and then asymptotically approaches equilibrium. Two-ply samples soaked for 1150 hours to reach equilibrium while 4-ply specimens required 5100 hours to achieve equilibrium. A thickness normalized diffusion curve (Figure 46) was used to compare the diffusion rates of both 2-ply and 4-ply laminates to incorporate the effect of thickness in Eqn. 4. Diffusivity values were calculated for the linear portion and ranged between $1.03\text{e-}3 \text{ mm}^2/\text{hour}$ and $1.09\text{e-}3 \text{ mm}^2/\text{hour}$ for both 2-ply and 4-ply laminates using Eqn. 4. These results combined with the consistent diffusion trends between $[0]_2$ and $[90]_2$ suggests that edge diffusion was minimal. Bulk moisture content at saturation ranged between 0.89% and 0.94%. Rule of mixtures was applied to determine the *in situ* M_∞ of the epoxy (Equation 21).

$$M_\infty = \frac{M_{bulk}}{\rho_{matrix}} * (v_f \rho_{fiber} + (1 - v_f) \rho_{matrix}) \quad (21)$$

For the range of bulk moisture contents, the measured volume fraction, and a measured matrix and glass density of 1.128 g/cm^3 and 2.55 g/cm^3 , respectively, the in-situ M_∞ for the epoxy was 2.64 - 2.84 % by mass. As shown in the matrix characterization section, neat resin samples for the Hexion 135/1366 absorbed 6 % moisture and had not yet reached equilibrium. The variance between the in-situ matrix absorption and neat resin absorption implies there is a stress equilibrium associated with aging, with reinforcement fibers acting as a limiter to swelling strains and preventing moisture uptake.

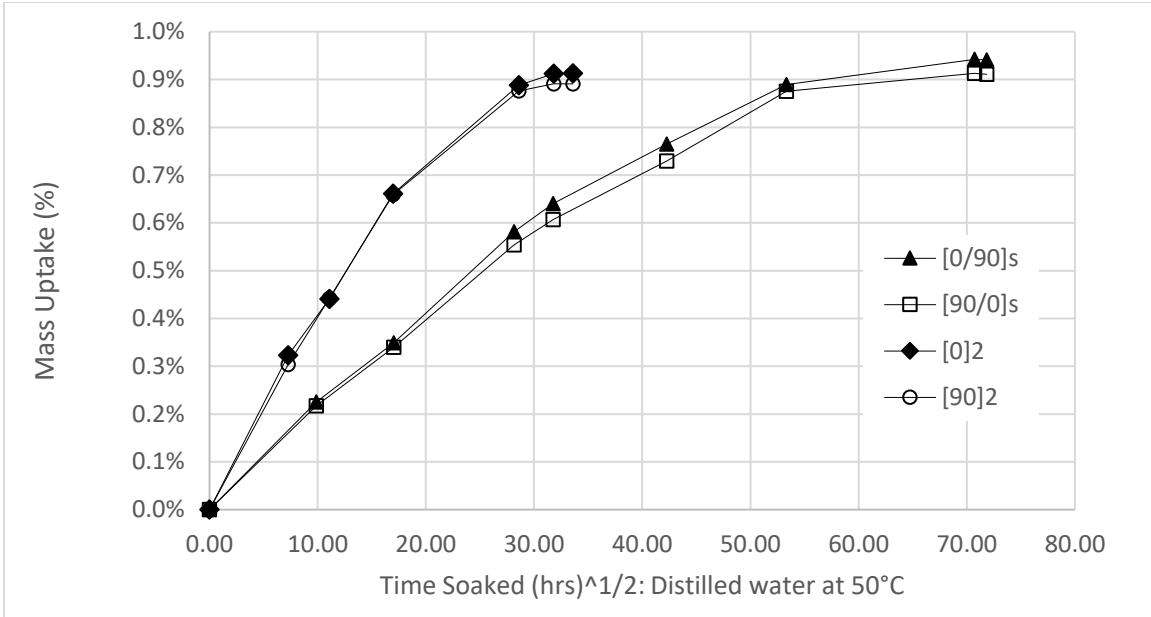


Figure 45. Bulk moisture absorption curves.

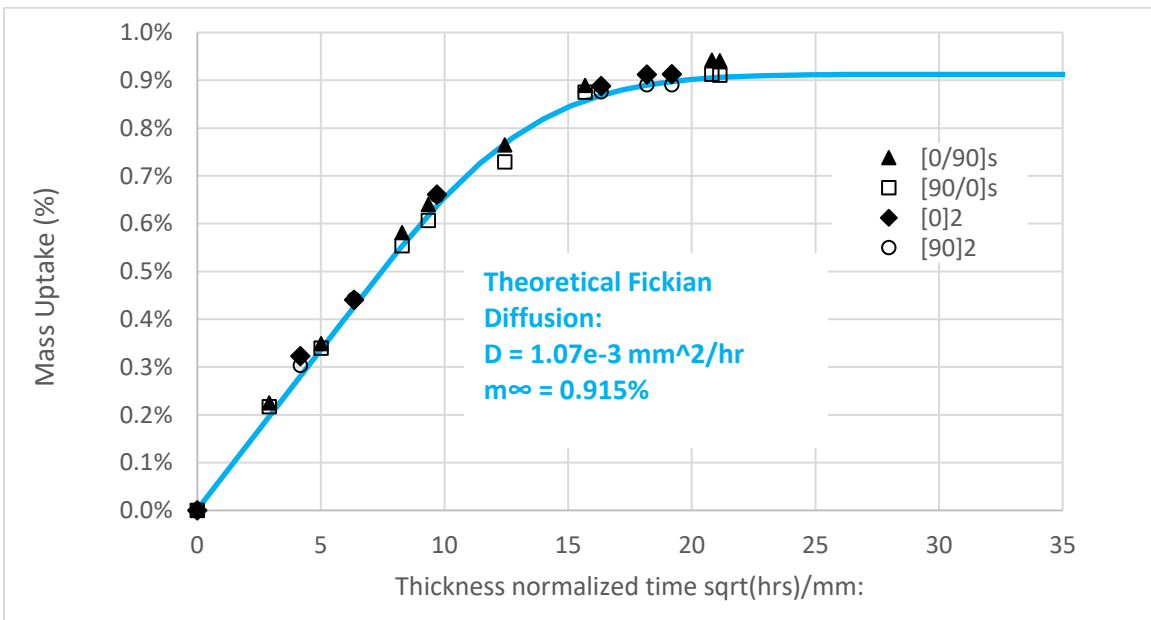


Figure 46. Thickness-normalized absorption curves with theoretical Fickian diffusion.

Desorption samples also showed a consistent Fickian trend. Four-ply laminates asymptotically approached a zero-moisture state, with less than 0.02% moisture by mass remaining. Two-ply laminates showed a similar trend but showed a net loss in mass ranging from -0.21% to -0.06%. A loss in mass could indicate leaching of the matrix material into the water; however, 2-ply desorption samples were conditioned several months after the months after manufacturing and could have absorbed ambient moisture prior to conditioning, skewing the initial mass reading. The total drop in the mass of about 0.9% correlates the M_{∞} value and would indicate that all mass losses were due to loss of water. However, chemical interaction of water molecules could have degraded the epoxy causing leaching of the polymer into the water resulting in mass loss.

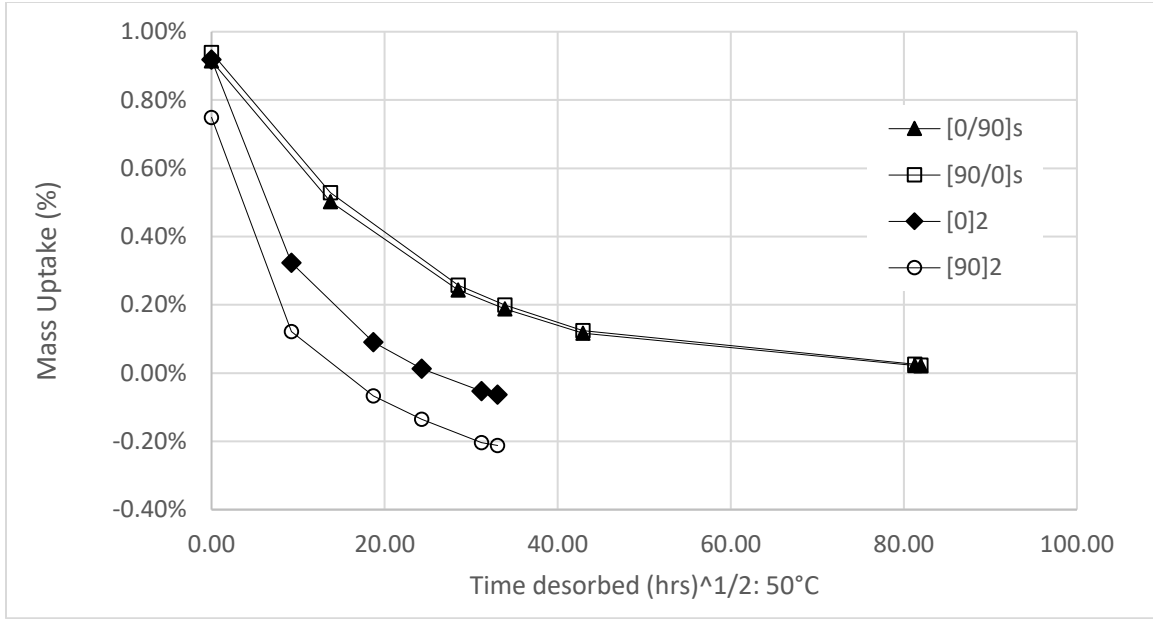


Figure 47. Bulk moisture desorption curves.

The Fickian absorption suggests that the occupation of moisture in the polymer is physical in nature, occupying free volume rather than chemical interaction through secondary bonding or hydrolysis. Further, nearly all the moisture was desorbed at the same temperature as the absorption temperature. This coincides with the findings from the matrix characterization section and provides evidence that most of the water occupied the composite physically. If chemical interactions such as a secondary bond network or hydrolysis occurred, interacting water molecules would not be able to be expelled at without elevating the drying temperature above the original conditioning temperature [40].

2.5.2. Theoretical Swelling Stresses in FRP laminates

A lamina-based model was implemented to determine the theoretical stresses induced by hygrothermal swelling. Since non-organic fibers are considered impermeable, expansion coefficients for a transversely isotropic lamina can be calculated from just the expansion value for the neat resin determined in the matrix characterization section. Equations 22a and 22b show the formulations for the hygro-expansion coefficient in the longitudinal β_L , and transverse direction, β_T . [57]

$$\beta_L = 0 \quad (22a)$$

$$\beta_T = \frac{\rho_c}{\rho_m} (1 + \nu_m) \beta_m \quad (22b)$$

Expansion in the fiber direction is considered negligible due to high fiber stiffness in comparison to the matrix. In the transverse direction, the expansion coefficient is related to the matrix mass fraction, Poisson ratio of the matrix, ν_m and the swelling coefficient of the matrix. Using previously mentioned densities for glass and the Hexion 135/1366 epoxy, an average fiber volume fraction of 56% and assuming an epoxy Poisson ratio of 0.33, the β_L can be calculated as 0.8 (% ϵ / %m). These

expansion coefficients, implemented with classical plate theory, can give the lamina stresses induced by swelling alone. To do this, the swelling coefficients must be transposed to the global coordinate system using the transformation matrix $[T]$, as shown in Equation 23 [33].

$$\begin{Bmatrix} \beta_x \\ \beta_y \\ \frac{1}{2}\beta_{xy} \end{Bmatrix} = [T]^{-1} \begin{Bmatrix} \beta_L \\ \beta_T \\ 0 \end{Bmatrix} \quad (23)$$

Stress can be solved by using the global stiffness matrix for the material. Strain can be induced by mechanical loads of extension and bending, thermal, and hygro-strains. For analysis of hygro-swelling, only the hygro-strains are considered (Equation 24)

$$\{\sigma\} = [\bar{Q}](\{\varepsilon_0\} + \{k\}z - \{\alpha\}\Delta T_0 - \{\beta\}\Delta C) \quad (24)$$

If hygrothermal loads are the only loads applied, they must equilibrate and therefore satisfy the force- stress balance in Equation 25.

$$\{N\} = \int_{-h/2}^{h/2} \{\sigma\}dz = 0 \quad (25)$$

These stresses were calculated for the laminates tested in this study. Although truly a biaxial fabric, the E-LT 3800 will be considered as a purely unidirectional lamina for this analysis. The analysis was conducted using classical plate theory. The input data for the E-LT 3800 Hexion/135/1366 lamina is shown below in Table 12.

Table 12. Lamina-swelling stress model inputs for Hexion/ Vectorply E-LT3800.⁴

Input	Symbol	Value	Units
Longitudinal Modulus	E_1	40.2	GPa
Transverse Modulus	E_2	15.9	GPa
In-plane Poisson Ratio	ν_{12}	0.27	n/a
Out-of-plane Poisson Ratio	ν_{23}	0.35	n/a
In-plane Shear Modulus	G_{12}	3.54	GPa
Out-of-plane Shear Modulus	G_{23}	5.889	GPa
Longitudinal coefficient of Moisture Expansion	β_1	0.0	% ε /%m
Transverse coefficient of Moisture Expansion	β_2	0.8	% ε /%m

⁴ Dan Samborsky: Summary of Vectorply E-LT 3800 Fabric Properties

Input	Symbol	Value	Units
Moisture content	C	0.92%	%m

2.5.3. Lamina-Swelling Results

Application of the swelling model induced strain in the unidirectional layups of $[90]_2$ and $[0]_2$, but with no transverse plies to limit swelling, no stress was induced. The model did not account for backing strands in the fabric architecture which could allow stresses to develop. Cross-ply laminates, however, saw a change in internal stress from hygro-swelling, causing the 90° plies to undergo a compressive stress, and 0° plies to undergo a tensile stress. This axial stress distribution is shown below in Figure 48.

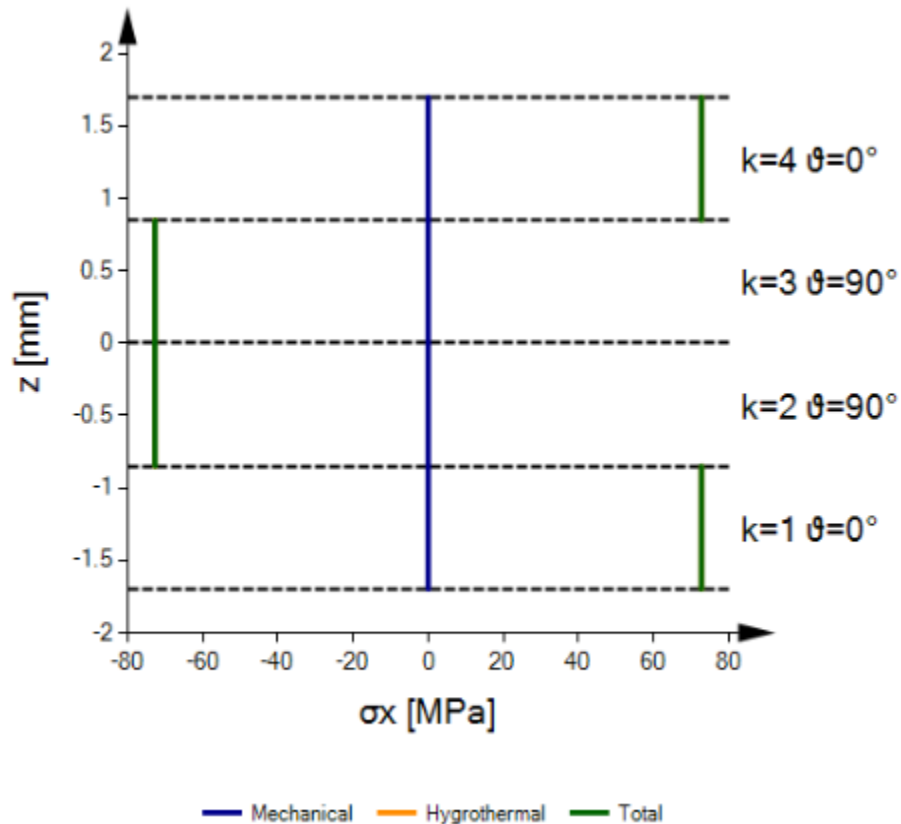


Figure 48. Cross-ply hygrothermal stress distribution (k = lamina number; ϑ = ply angle).

The stress levels in the cross-ply laminates reached a magnitude of 72 MPa. This swelling stress is significant and could certainly influence the mechanical loading of the composite, as well as induce damage. The lack of recoverability of laminate strengths with desorption (“Mechanical Properties” section) would indicate that the swelling stress state alone does not account for the degradation of the material system. However, the stresses are high enough that damage could occur on a micromechanical level. Figure 50 in the next section shows the spatial variability of the volume fraction in textile laminates which would be the means for variability in expansion coefficients and

ultimately large stress gradient which could cause damage. Interestingly, the stress gradient between 0° and 90° lamina in the cross-ply laminates could cause large shear stress between plies and thus be a source of interply damage and attribute to the larger strength drops in the cross-ply laminates in the “Mechanical Properties” section.

2.5.4. Hygrothermal-aging Damage

Physical damage to the aged composite laminates apparent upon inspection of conditioned laminates. Visual inspection of coupons after aging showed streaking in tows of all layups. An example of the damage is shown below in Figure 49.

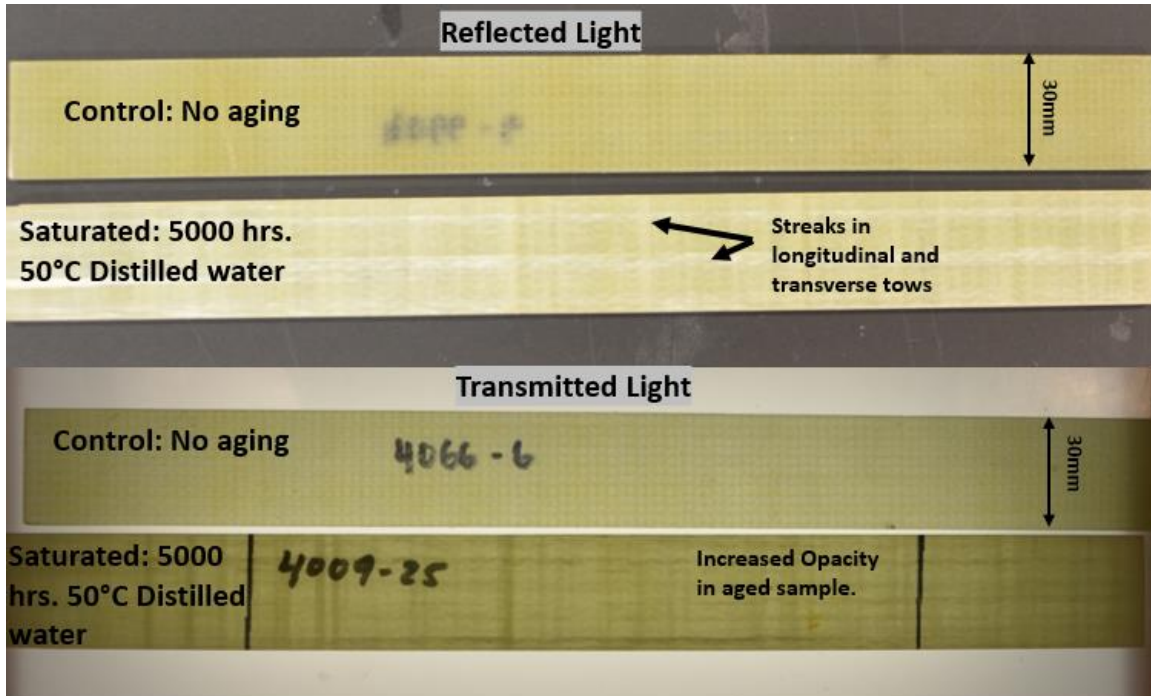


Figure 49. Visible damage from hygrothermal aging in the cross-ply laminate.

In reflected light, the damage streaks reflect light, lightening the color of the composite. In transmitted light, the damage streaks increase the opacity, darkening the composite. Damage in a transparent material creates surfaces which scatter and reflect light, ultimately altering the optical properties. Further, the damage remained after the desorption process which would indicate the change in opacity was physical and not a result of entrapped water altering the optical properties. Interestingly, streaks correlated with fiber tows which would suggest physical damage of fiber-matrix interface

To explore the nature of this aging damage, SEM microscopy was performed on both control samples and hygrothermally aged samples in their untested states. Both 2-ply and 4-ply coupons were examined. Samples were cut with a tile saw and then cast into a puck using quick-set acrylic. Preparation involved sanding with 1000, 2400, and 4000 grit sandpaper, polishing with 0.3 μm alumina compound, and ultrasonically cleaned in distilled water. Dry-control samples of all layups showed no visible damage under the SEM in all layups. Macro-damage in fiber tows was visible in hygrothermally laminates but was not widespread as the optically visible damage.

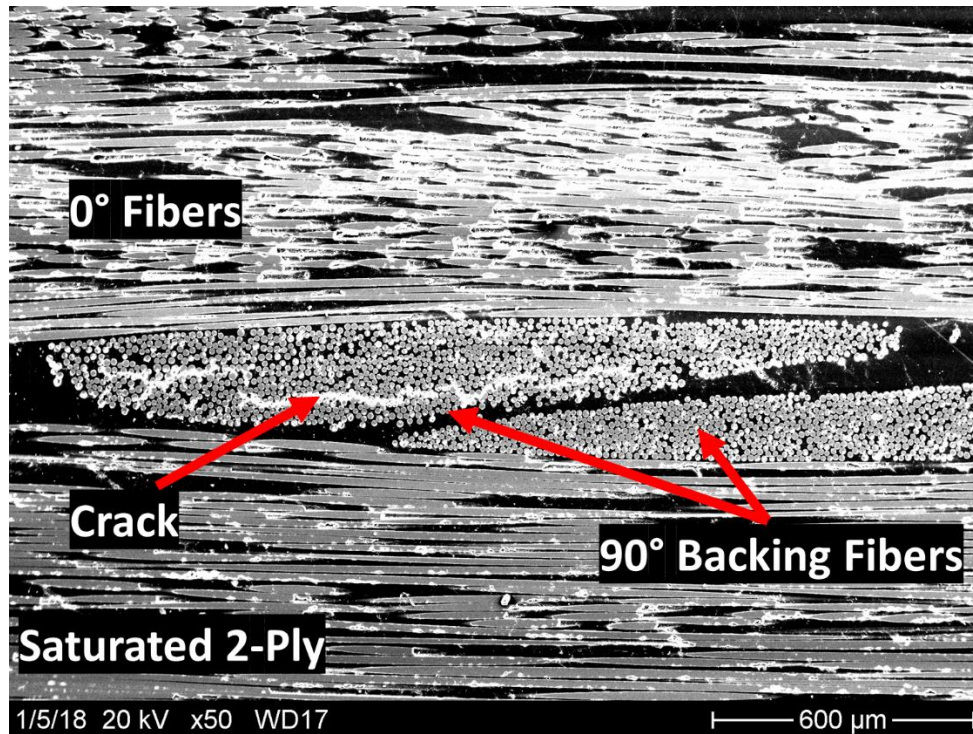


Figure 50. SEM: Crack in a backing strand in un-tested, saturated, 2-ply laminate.

2-ply laminates experienced cracking in the backing strands of plies which are shown above in Figure 50. This damage feature was present in some but not all of the backing strands. Inspection of micro-level damage was not possible at this level of polishing (Figure 51), thus higher magnification was inconclusive in determining whether these cracks propagated in the matrix or along fiber-matrix interfaces. Cracks in the backing strands propagated from areas resin-rich areas; spatially varying volume fractions of this architecture could cause large differentials and concentration from swelling stresses.

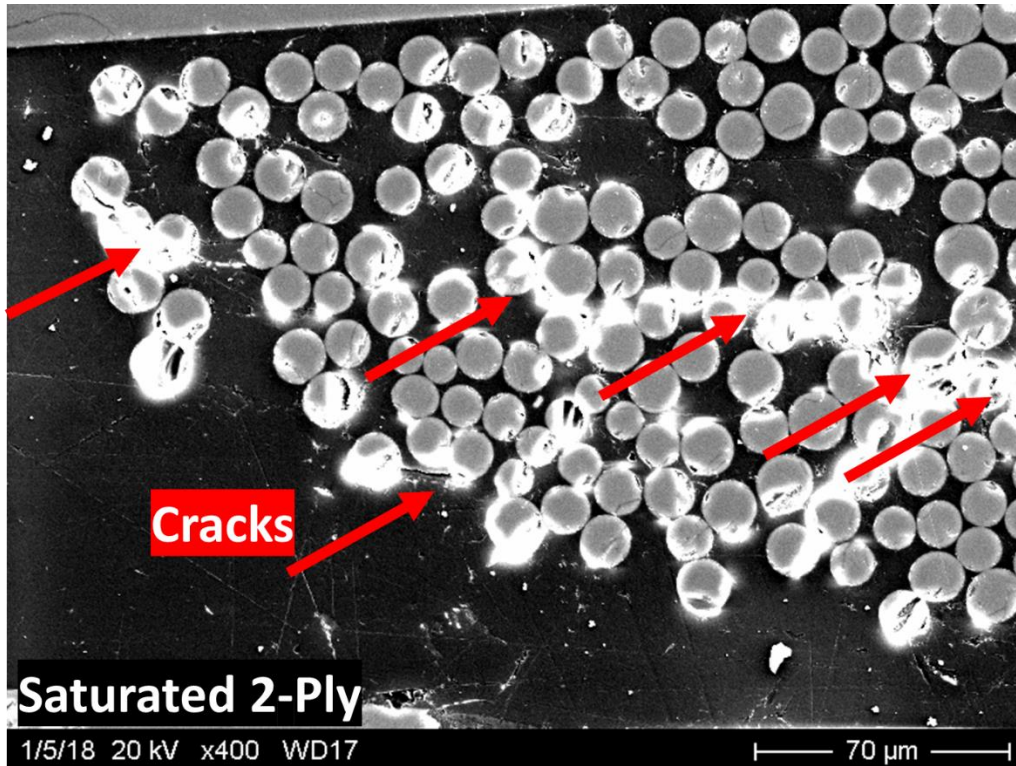


Figure 51. SEM: High magnification of crack in saturated 2-ply coupon.

Cracks were observed in the SEM inspection of saturated-untested 4-ply laminates but were less prevalent and less consistent than those found in the 2-ply laminates. Figure 52 shows one of the cracks in the outer 90° ply of a 4-ply (cross-ply).

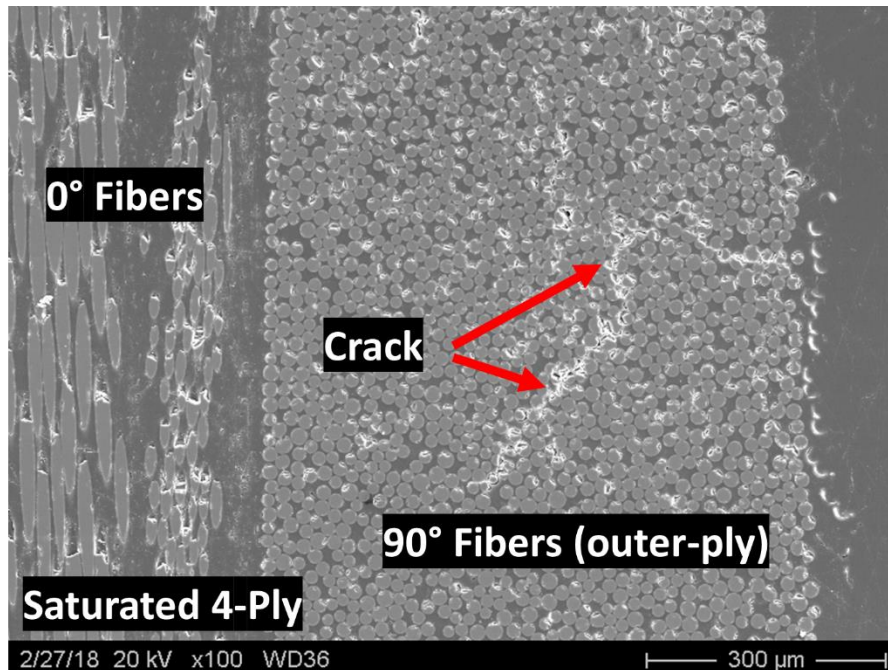


Figure 52. SEM: crack in outer 90° ply of saturated, untested, 4-ply laminate.

The damage from hygrothermal aging was quite apparent through visual inspection of samples but was less apparent in an inspection by SEM. However, the cracks observed under SEM were large, spanning whole tows; with damage of this magnitude, it is possible that swelling-induced micro-damage has also occurred. More extensive sample polishing would be necessary to observe micro-damage. Regardless, the presence of hygrothermal damage could alter the damage progression of the laminates, as the damage has already been initiated prior to any load being applied. The damage observed from swelling was confined to the fibrous-tow regions of the laminates which would suggest that damage occurring to both the interface and matrix material.

2.5.5. Mechanical Properties

The average mechanical properties of static tensile tests are below in Table 13.

Table 13. Static test results

Layup	Condition	Ultimate Stress (MPa)	Ultimate Load (N/mm)	Modulus (GPa)
[0] ₂	Dry: control	971	1754	40.1
[0] ₂	Saturated	591	1062	40.3
[0] ₂	Dry: desorb	653	1162	38.9
[90] ₂	Dry: control	90	165	13.6
[90] ₂	Saturated	53	98	12.8
[90] ₂	Dry: desorb	55	98	13.8
[0/90] _s	Dry: control	564	1955	27.9
[0/90] _s	Saturated	258	892	27.3
[0/90] _s	Dry: desorb	282	974	28.1
[0/90] _s	Dry: temp. only	586	2045	27.9
[90/0] _s	Dry: control	585	1986	28.1
[90/0] _s	Saturated	266	907	26.9
[90/0] _s	Dry: desorb	263	891	28.1
[90/0] _s	Dry: temp. only	621	2110	28.7

Hygrothermal aging-induced strength reductions were widespread across all layups tested. Figure 53 graphically shows these reductions in strength. From dry-control to the saturated condition [0]₂ and [90]₂ laminates experienced strength drops of 39% and 41%, respectively; [0/90]_s and [90/0]_s laminates each experienced a reduction of 54%. These strength reductions indicate a reduced damage tolerance due to aging, especially in cross-ply laminates.

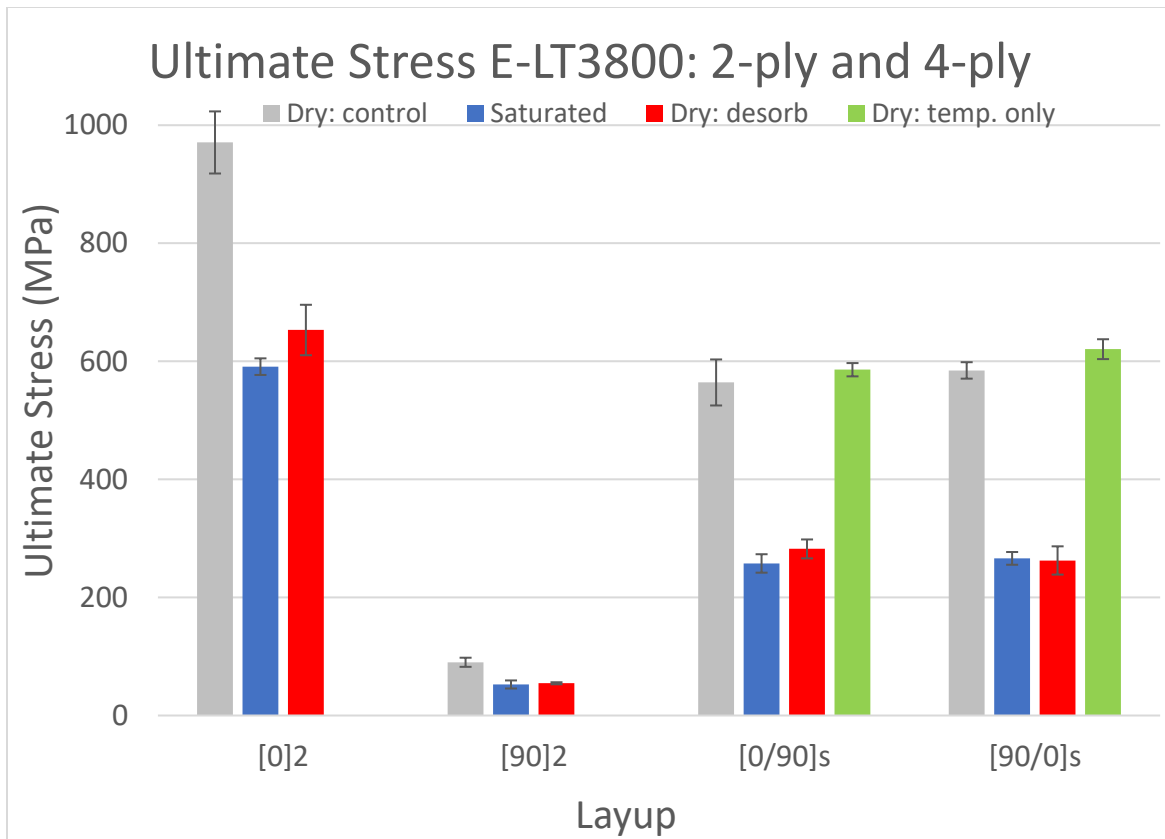


Figure 53. Ultimate strengths for E-LT 3800/Epoxy system.

Cross-ply laminates exposed to temperature-only conditioning retained the strength properties of the dry-control specimens. This finding validates the conditioning temperature history was not responsible for changes in performance, and that all changes in properties can be attributed solely to moisture-related mechanisms. This also validates that the aging temperature of 50°C was adequate for this material.

The dry-desorbed test samples, although containing no moisture, did not recover strengths to those of unconditioned samples. Slight recoveries of the strength of the [0]₂ and [0/90]_s were observed but were minimal. In general, the dry-desorbed strengths matched those of the saturated samples. Plasticization of the matrix material was shown to be reversible with moisture desorption; therefore, it is evident that constituent mechanical behavior due to plasticization of the matrix was not the hygrothermal mechanism responsible for changes in mechanical performance in this material. Further, this suggests that mechanical performance was reduced due to physical damage occurring due to swelling during the hygrothermal aging process, which was irreversible.

The difference in strength reductions between unidirectional laminates and cross-ply laminates indicates hygrothermal aging affects unidirectional and multiangle laminates differently. To convey this change, ultimate loads were compared in addition to ultimate strengths. Stress normalizes load across the thickness of the sample, describing a uniform average stress, but in the case of multiangle laminates, this stress state is not uniform. In cross-ply laminates, transverse plies offer negligible load carrying capacity in comparison to longitudinally-oriented plies. Thus, cross-ply laminates contained two 0° plies, making their ultimate loads relatable to those of the [0]₂ laminates.

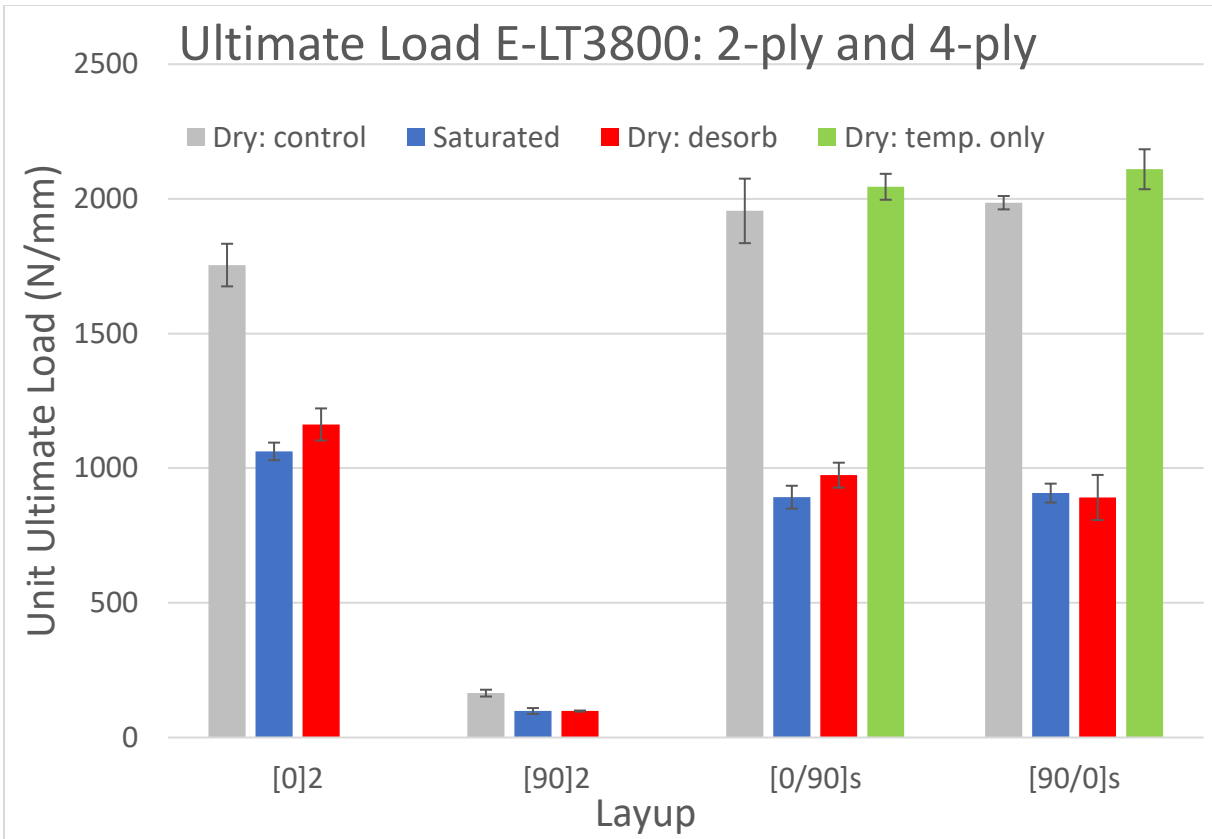


Figure 54. Ultimate loads for E-LT 3800/Epoxy System.

In the dry-control condition, cross-ply laminates withstand more load than $[0]_2$ samples. This suggests that in the control state, transverse plies add strength to cross-ply laminates. However, in the saturated and desorbed conditions, cross-ply laminates are significantly weaker than $[0]_2$ laminates. This result suggests that ply interactions are affected by aging, causing even greater reductions in damage tolerance in laminates containing multi-angle plies. Consequently, material properties from testing of hygrothermally-aged unidirectional laminates may not be adequate when designing structures with multiangle laminates using lamina-based models.

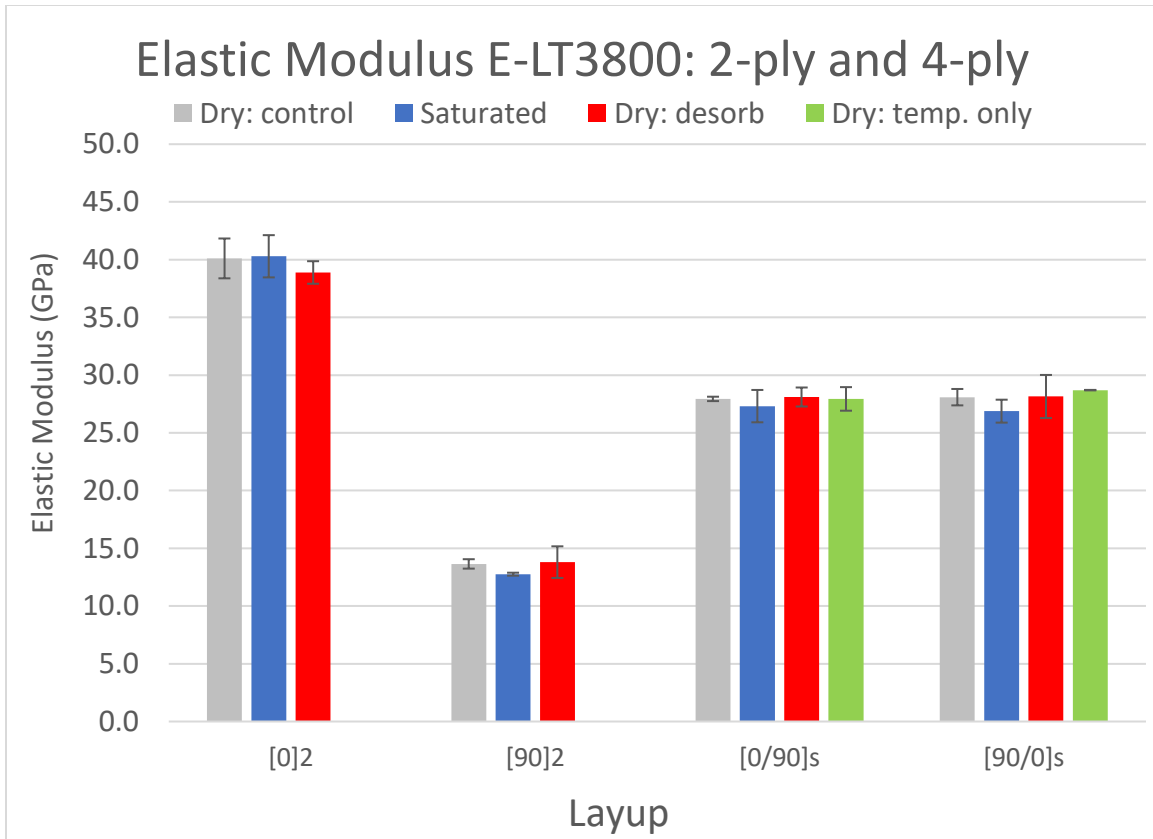


Figure 55. Elastic moduli for E-LT 3800/Epoxy system.

Figure 55 shows the elastic moduli all laminates to be unaffected by hygrothermal aging. Two observations can be made regarding the hygrothermal degradation mechanisms. First, it shows matrix plasticization and the anticipated reduction in modulus was not apparent in the composite. Unidirectional-dominated laminates should not see significant reductions in modulus, but the matrix dominated [90]₂ should be sensitive to these changes. Negligible reductions in the modulus of the matrix imply that the matrix can still efficiently transfer load between fibers. Second, damage in composite materials may affect the residual modulus. Hygrothermally-induced damage, although apparent, did not affect the modulus, indicating that the damage occurred on the micromechanical level or did not affect the global stiffness along the loading axis.

2.5.6. Stress-Strain Response

Inspection of stress-strain curves can often provide insight into the damage mechanics and damage progression of the material. Transverse plies, lacking reinforcement in the loading direction, making these plies susceptible to damage at low strain levels. Figure 56 shows the stress-strain response of transverse, [90]₂ samples.

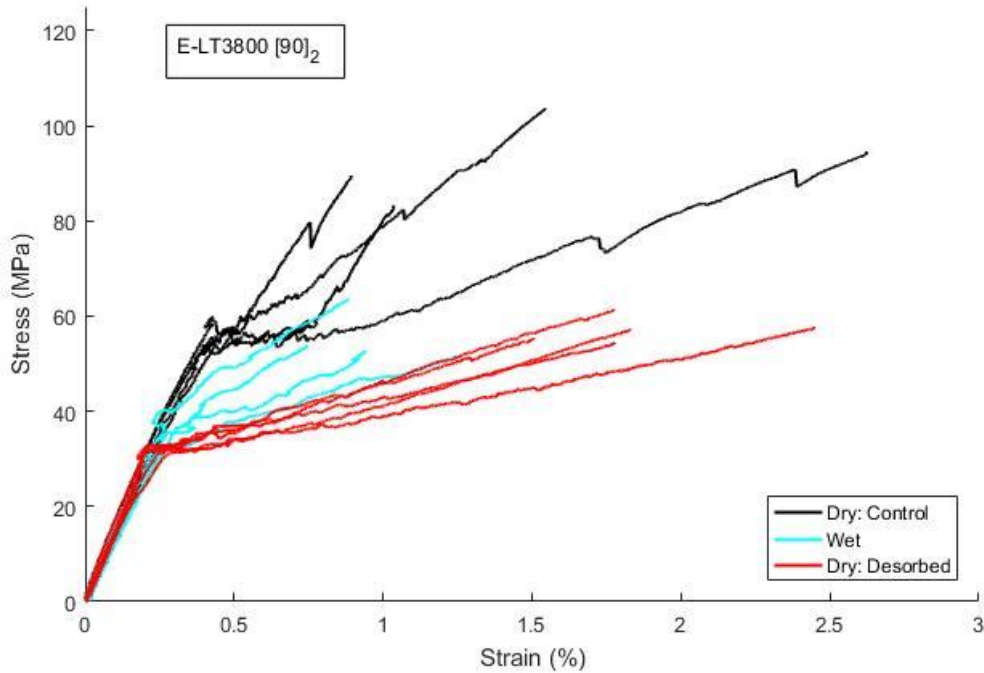


Figure 56. Stress-strain response of [90]₂ samples.

It must be noted that longitudinally-oriented backing strands are still present in these samples. Typically, in a purely transverse laminate, the first crack would propagate across the cross-section and cause ultimate failure. With the addition of a few longitudinally orient strands, global failure does not occur after the first crack, resulting in the bilinear behavior in Figure 56. The knee following the linear-elastic portion, therefore, correlates to the onset of transverse failures and reduces the material stiffness. Stress-strain beyond this point can be variable due to variation in the backing strands both in terms of number, spacing and alignment/waviness, as well as variation in strain collection due, do localized damage within the small-gage section of the extensometer. The nature of these failures are attributed to matrix cracking and debonding of the fiber-matrix interface. These are competing mechanisms; thus, the nature of transverse failures is difficult to discern. Interestingly, for this material system, the hygrothermal conditioning affects strain levels at which transverse failures occur. In the dry-control samples, damage begins at 0.43% strain, while in saturated samples, damage begins at 0.28% strain. Desorbed samples follow closely the behavior of the saturated samples with damage beginning at 0.3% strain. The lower initiation strains of saturated and dry-desorbed samples would reflect damage growth of existing damage induced by the aging process.

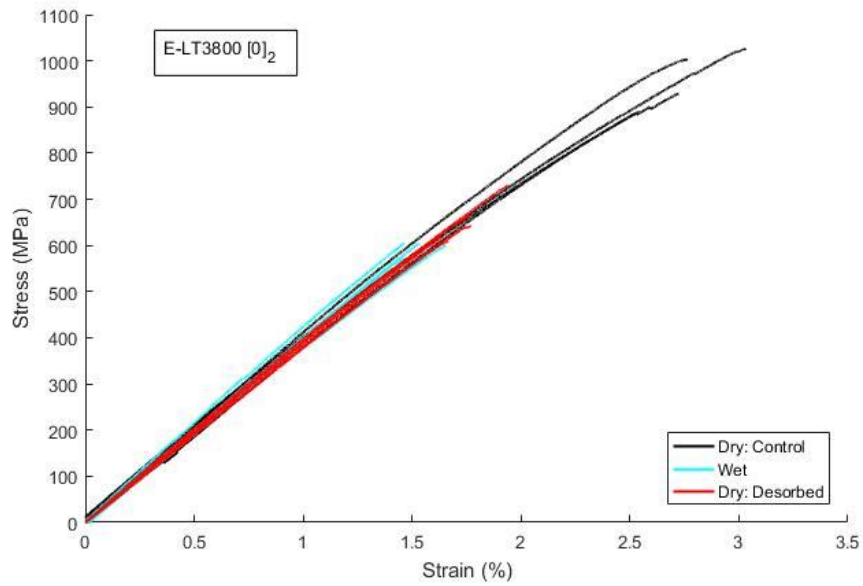


Figure 57. Stress-strain response of $[0]_2$ samples.

Figure 57 shows the stress-strain curves for $[0]_2$ samples. Since the predominant damage mechanism in longitudinal plies is fiber breakage, minimal strain energy is released until final failure. $[0]_2$ laminates of all conditions follow the stress-strain response, with condition samples being truncated due to premature failure; there is no energy release to foreshadow this behavior.

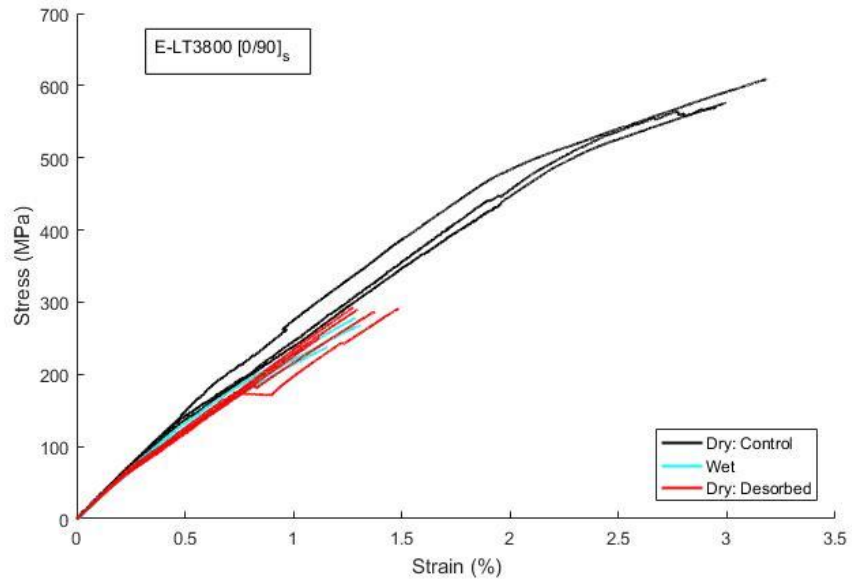


Figure 58: Stress-strain response of $[0/90]_s$ samples.

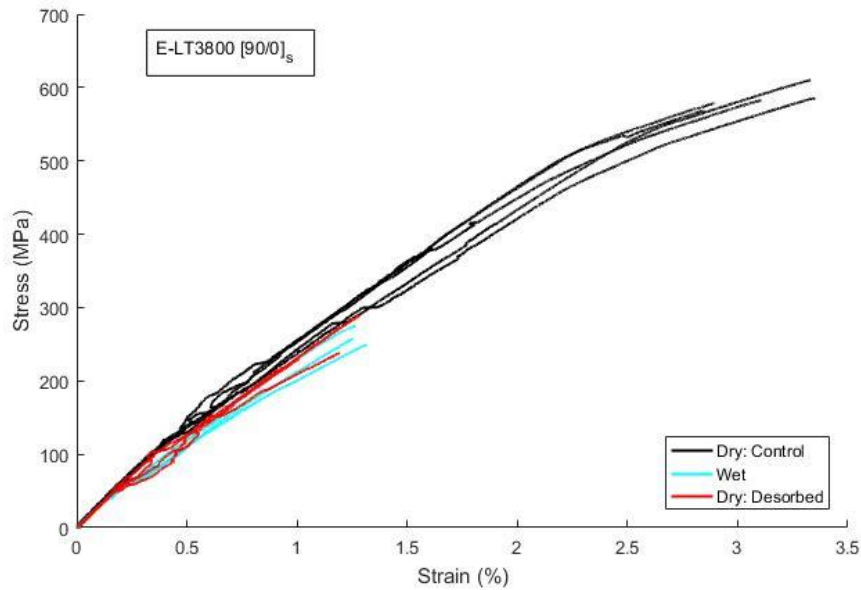


Figure 59. Stress-strain response of [90/0]_s samples.

The stress-strain curves for the cross-ply laminates are shown in Figure 58 and Figure 59. Both layups displayed similar behavior between at each level of conditioning; however, the results for to [90/0]_s tend to be noisier than the [0/90]_s. Damage to 90° plies of the [90/0]_s layup induced noise in the strain measurement, as the strain measured beneath the extensometer did not reflect the global strain level. Interestingly, the cross-ply laminates show a bilinear behavior as see in the [90]₂ samples, with modulus being reduced after failures in the traverse plies. Again, samples that subjected to hygrothermal aging experienced this knee at lower strains than the control samples, causing separation between the control and conditioned curves around 0.3% strain. The premature growth of damage could be in part due to the increased stress state from swelling, but the knee does not recover after desorption, which would suggest that damage onset was from the growth of damage accrued during the aging process.

2.5.7. Sample Failure Inspection

Inspection of failed test specimens provides qualitative information about the damage progression in composite laminates, specifically damage progression at final failure. Figure 60 shows failed [90]₂ samples for dry-control, saturated and desorbed samples. The longitudinally oriented backing strands of this laminate allowed the laminates to develop transverse cracks. Crack saturation resulted in the ultimate failure of the [90]₂ laminates. Red ink was used as a penetrant to make crack more visible during inspection; ink was only applied to one side of the coupon. The control sample experienced uniform crack distribution and a crack density of 4 cracks/cm. Saturated and desorbed samples featured a more random crack pattern with a lower crack spacing of 2.7 and 3.0 cracks/cm, respectively. Without exact failure strains, it is difficult to compare these numbers as crack density is related strain level. Regardless, the crack behavior still offers an interesting point of discussion. Matrix plasticization could cause stress redistribution and reduce stress concentrations resulting in lower crack densities of saturated samples. However, desorbed samples, with no moisture and theoretically no plasticization, failed in a similar form. Another possibility would be internal damage

in both the matrix and the interface [51] which could also reduce stress concentrations and lower crack density.

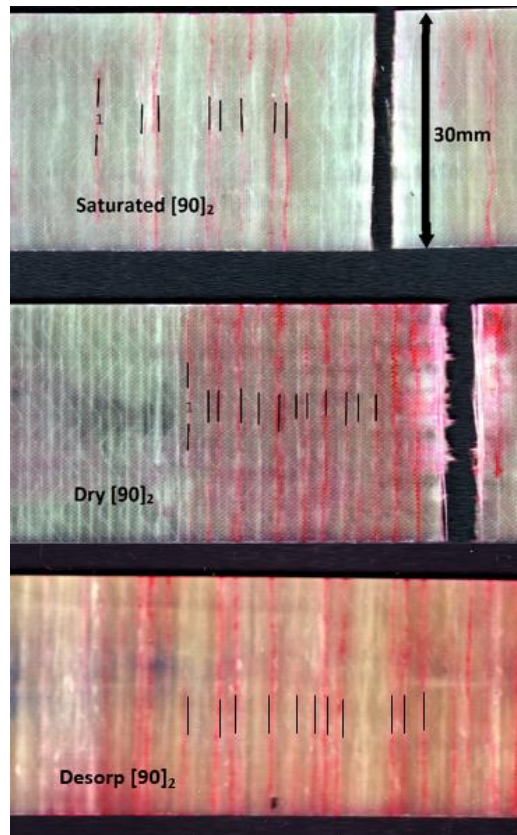


Figure 60. Failed $[90]_2$ coupons: Saturated (top), Dry (middle) desorbed (bottom).

$[0]_2$, $[0/90]_s$, and $[90/0]_s$ are shown in Figure 61, Figure 62, Figure 63, respectively. Due to the large strain energy release during the failure of 0° plies, these coupon failures are often explosive and result in widespread damage to the coupon. This behavior was present in dry control samples which experience significant splitting (Figure 61), brooming

Figure 62), and widespread delamination

Figure 63). In the saturated and the desorbed cases, the damage was less explosive with failures confined to localized areas. This observation would suggest that damage coalesces and grows at much lower global strain energies than in dry samples. However, high local strain energies are still necessary to propagate damage. Stress concentrations from aging-induced damage could serve as nucleation points for damage. This premature damage initiation would result in earlier onset of cascading damage in hygrothermally- exposed samples.

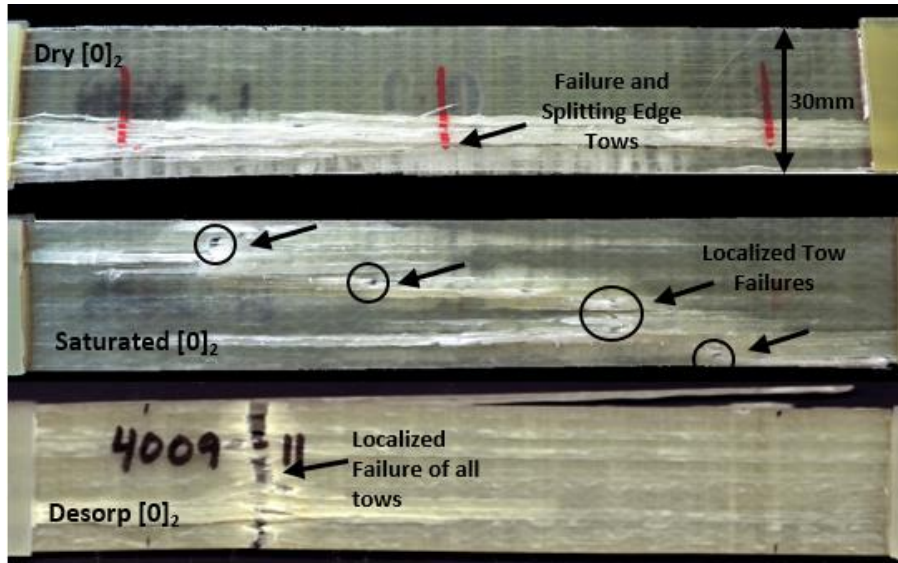


Figure 61. Failed $[0]_2$ coupons

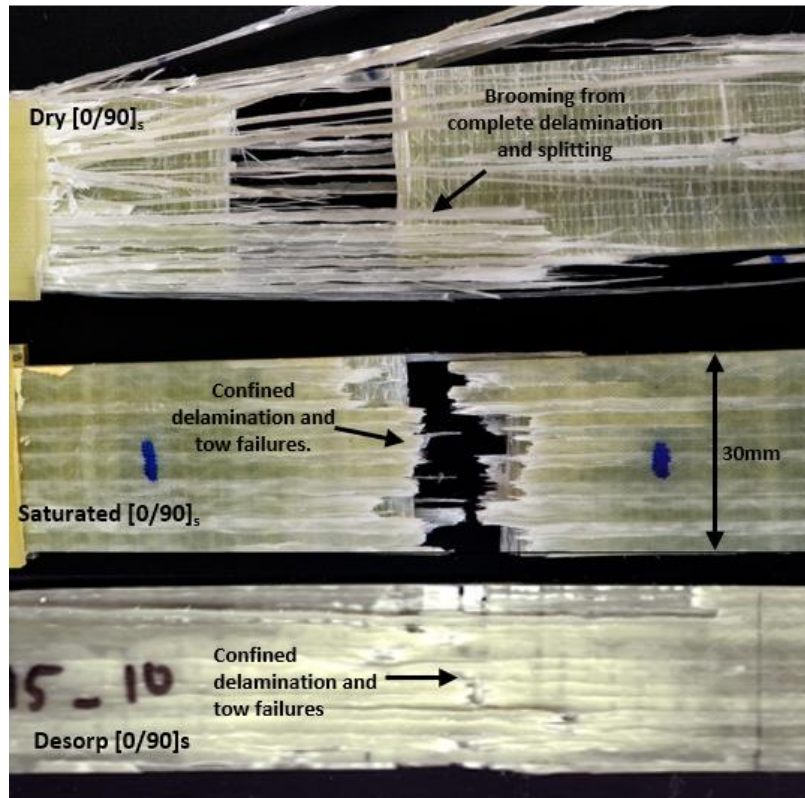


Figure 62. Failed $[0/90]_s$ coupons.

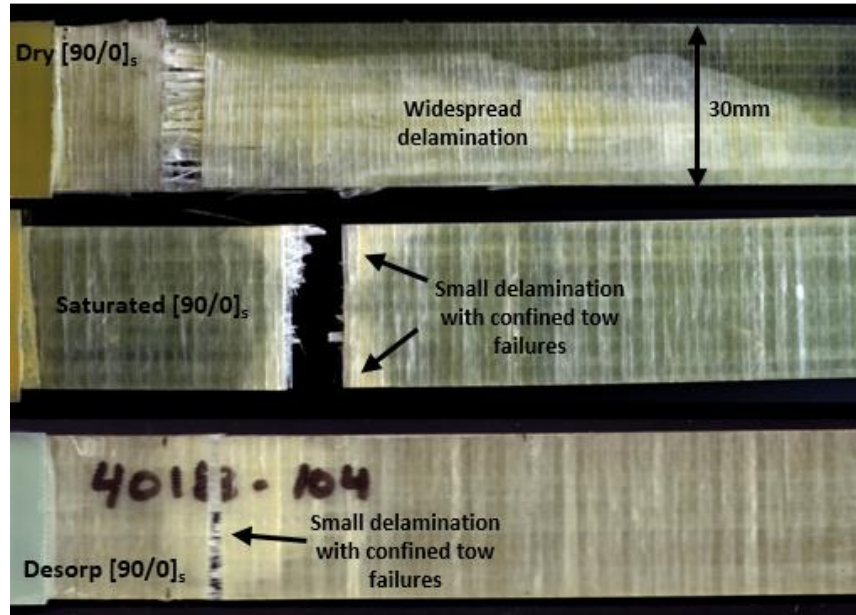


Figure 63. Failed [90/0]_s coupons.

2.5.8. Acoustic Emission

AE monitoring acquired during these tests aids in interpreting the hygrothermal mechanisms responsible for changes in the damage progressions. As discussed in the background section, many analysis techniques exist to correlate AE data to damage in FRP's, and validation of these techniques resides as an ongoing focus of study in composite material research. The analysis for this dataset will be two-fold. First, general trends in the level of activity will be analyzed; then frequency analysis technique will be applied to describe the nature of specific damage mechanisms in the material and their response to hygrothermal aging. All analyses were conducted on data collected up to ultimate failure; events occurring after ultimate failure were truncated. AE data is stored in a MATLAB structure and scripts were written for data processing.

Several AE parameters are of interest for describing the overall AE behavior, these include number of events, accumulated energy, and detected damage initiation. Table 14 outlines the general AE average results for each laminate and condition tested.

Table 14. AE general trends (averages).

Layup	Condition	Number of events	Total Accumulated Energy ⁵ (aJ)	Average Energy per Event (aJ)	Initiation Strain by AE (%)
[0]2	Dry: control	9463	9.8E+08	1.0E+05	0.31
[0]2	Saturated	611	9.3E+07	1.5E+05	0.34
[0]2	Dry: desorb	1546	2.3E+07	1.5E+04	0.19

⁵ aJ = 10⁻¹⁸ J

Layup	Condition	Number of events	Total Accumulated Energy ⁵ (aJ)	Average Energy per Event (aJ)	Initiation Strain by AE (%)
[90]2	Dry: control	984	4.1E+09	4.1E+06	0.55
[90]2	Saturated	586	3.4E+08	5.8E+05	0.25
[90]2	Dry: desorb	914	6.5E+08	7.1E+05	0.22
[0/90]s	Dry: control	13157	3.1E+09	2.3E+05	0.20
[0/90]s	Saturated	789	1.3E+07	1.7E+04	0.08
[0/90]s	Dry: desorb	2144	4.4E+08	2.0E+05	0.14
[90/0]s	Dry: control	7113	1.2E+10	1.7E+06	0.13
[90/0]s	Saturated	1769	1.3E+08	7.2E+04	0.08
[90/0]s	Dry: desorb	2584	1.8E+09	6.8E+05	0.08

The number of AE events corresponds to the number of damage events that occurred in the gage section of the sample during the loading cycle. Although events can vary in size, the number events can serve as a metric for measuring the amount of damage sustained by the material and thus correlated to damage tolerance. Figure 64 graphically shows the number of events collected for each laminate under each condition.

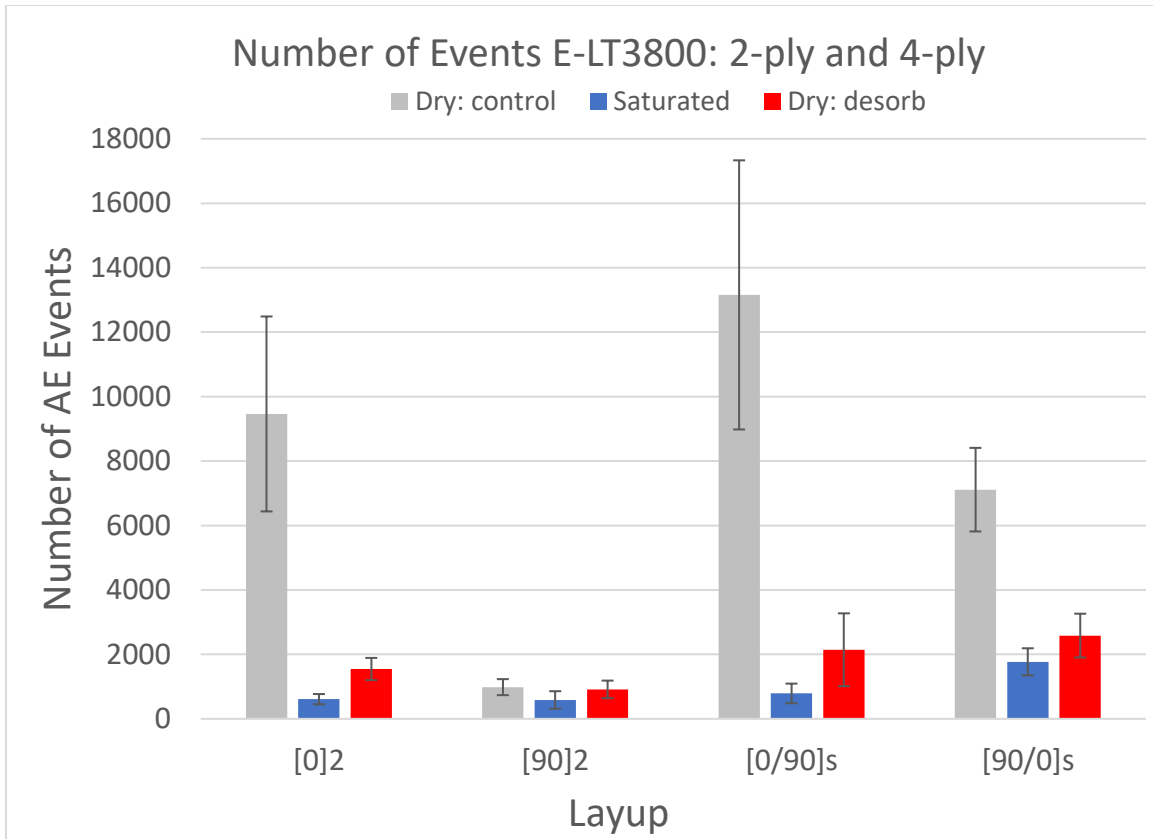


Figure 64. Average number of AE events.

From Figure 64, it is apparent that hygrothermal aging significantly reduced the number of detected damage events. [0]₂ samples in the saturated condition were reduced by over 90% from control samples. Similar reductions were present in the cross-ply laminates. Damage accrued during the aging process would be unaccounted for in the AE monitoring and would result in fewer recorded events. Correlation between the number of events and damage would indicate that hygrothermal aging reduces the damage tolerance of the material.

AE activity was not recovered by drying/desorbing the samples which would imply that the change in AE activity was not due to damping induced by plasticization which was shown to be recovered in the matrix characterization section. Attenuation of AE elastic waves due to damage or material damping is more thoroughly explored in the subsequent chapter and showed that aging did not affect the materials propagation or attenuation behavior.

Accumulated energy also serves as another metric for interpreting the amount of damage sustained in the material, accounting for the magnitude of damage event. AE energy can be considered representative of the energy dissipated of the composite. Dissipated energy is a measure of global-elastic strain energy that has been released due to damage to the material and can no longer be recovered during subsequent unloading cycles. AE energy is also a measure of strain energy released, but rather than measuring this release as a change in the global stress/strain energy state, it is a measure of the intensity of transient stress waves propagating through the material. In general, dissipated energy and AE energy have shown correlation [66], but since AE is an indirect measure of strain energy release, there are variations. For example, in a 0° plie, a matrix crack could occur, emitting a sizable stress wave. Locally, this would change the strain energy state, increasing the

stored energy in neighboring fibers, however, this would not result in a significant change in the global strain energy state, thus minimal dissipated energy. Despite this disconnect, accumulated energy can still provide insight into the amount of damage accumulated in the material.

The accumulated energy curves for all the layups are shown below in Figure 65 - Figure 68 (note: logarithmic scale). In all layups and conditions, the largest change in energy occurred between 0.1 and 0.6% strain, which correlates to the strain levels at which matrix cracking is expected. The $[90]_2$ laminates, shown in Figure 65 feature a large step in accumulate energy below 0.5% strain with little energy growth during the later portion of the loading cycle. This trend held true for all conditions, but the step does appear to occur at lower strain levels in laminates exposed to hygrothermal conditioning.

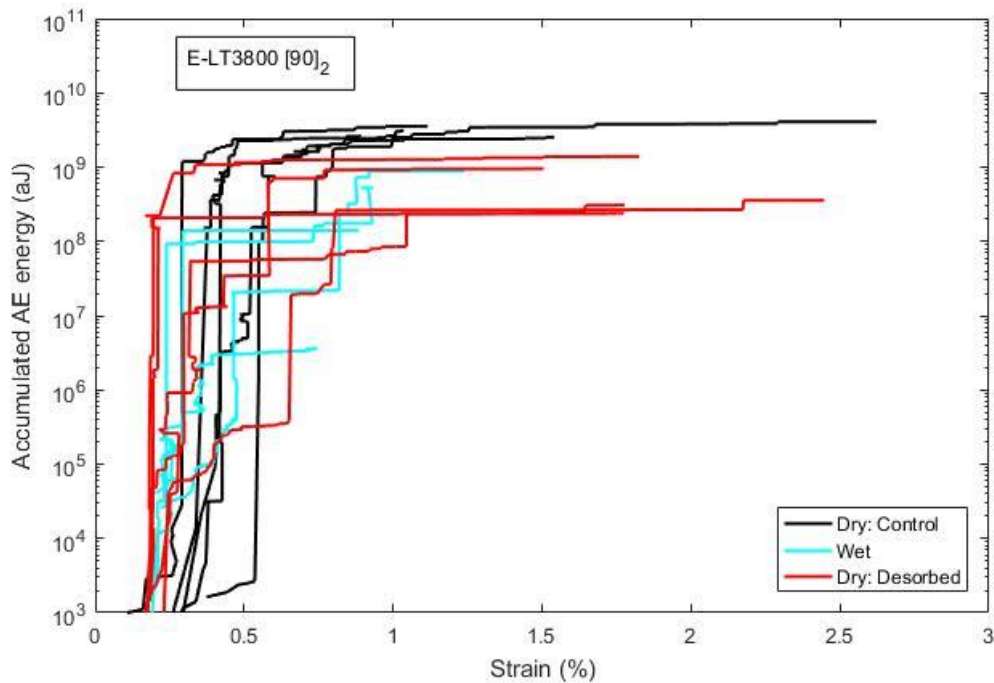


Figure 65. Accumulated AE energy for $[90]_2$ samples.

$[0]_2$ laminates, also show the initial step in energy, followed by a plateau in energy accumulation. $[0]_2$ laminates also experienced a sizeable increase in energy directly preceding failure. In terms of conditioning, laminates that have been hygrothermally aged begin to accumulate energy at lower strain levels, but plateau at lower total energy values. Cross-ply laminate energies, shown in Figure 67 and Figure 68, have a similar step in energy around 0.5% strain, but minimal growth in energy immediately preceding failure. In conditioned cross-plys, this step occurs at a lower strain level but plateaus at a lower total energy value. Total accumulated energies are compared directly in Figure 69 for all conditions and layups.

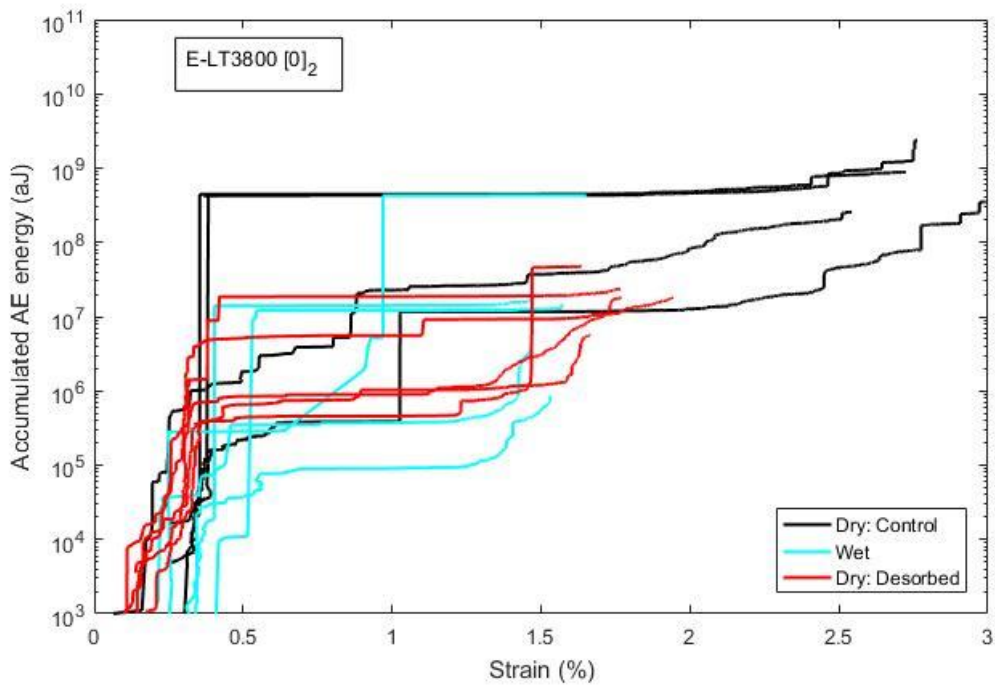


Figure 66. Accumulated AE energy for $[0]_2$ samples.

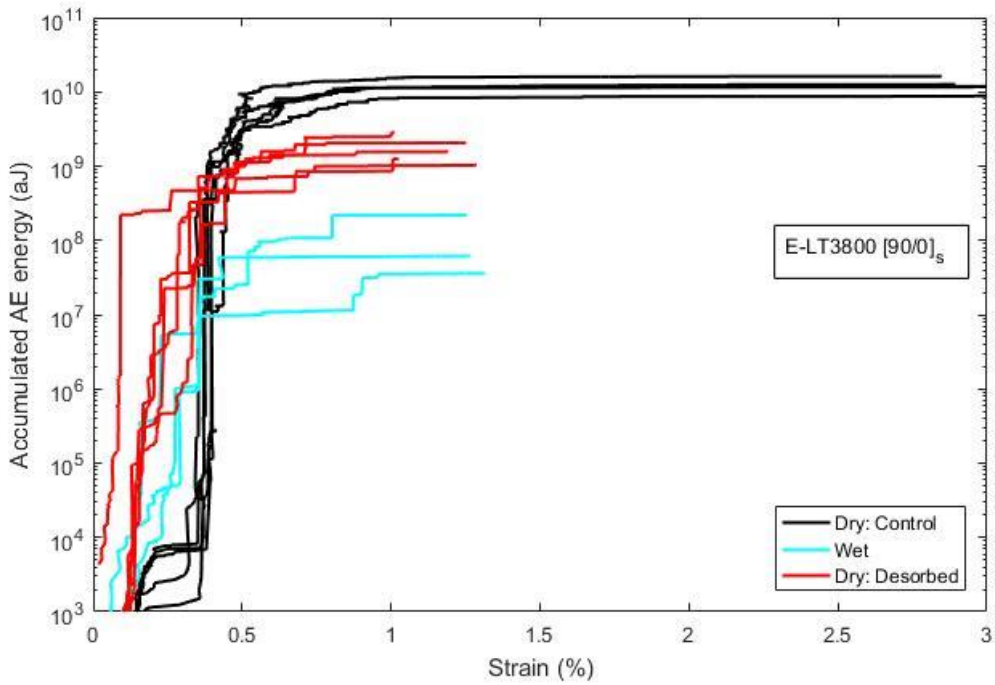


Figure 67. Accumulated AE energy for $[90/0]_s$ samples.

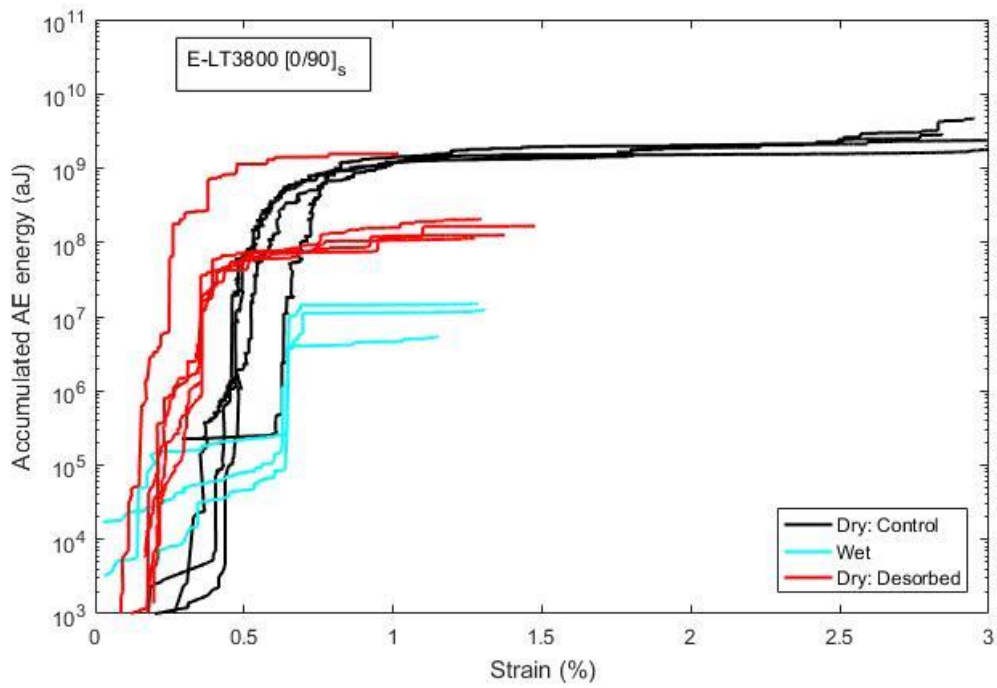


Figure 68. Accumulated AE energy for [0/90]_s samples.

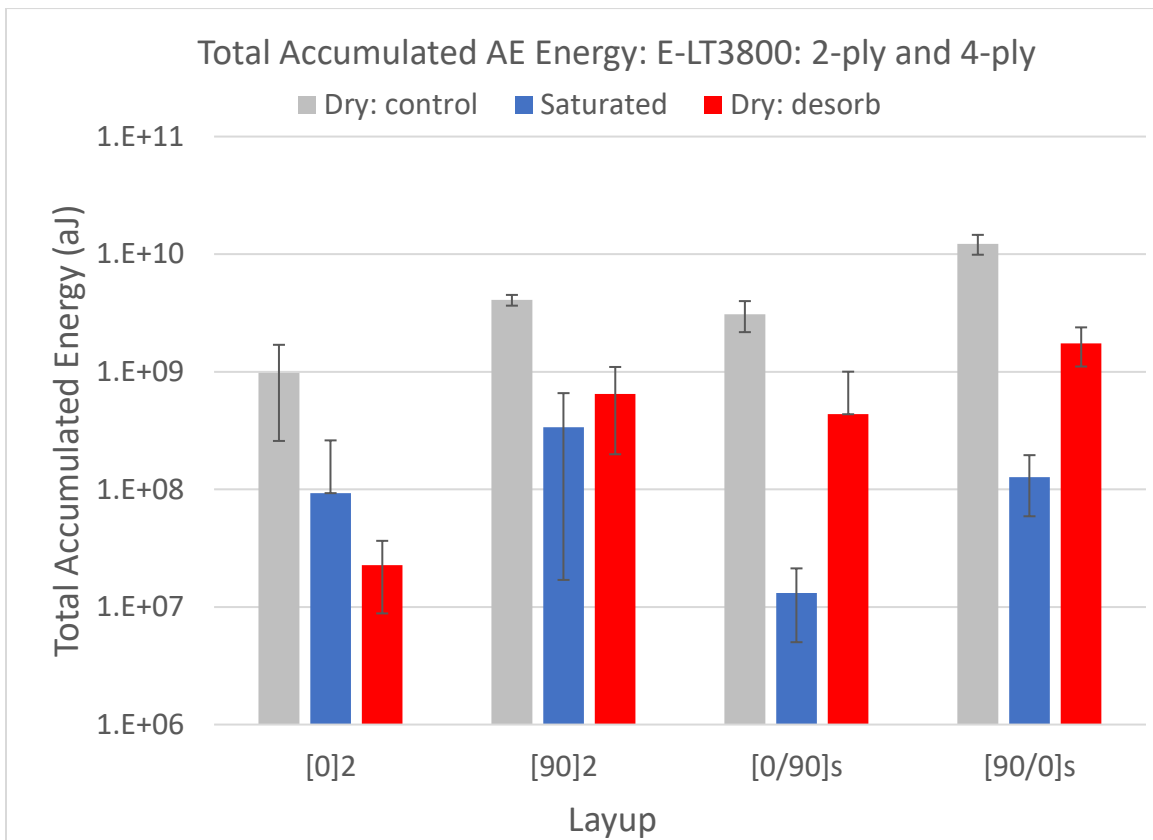


Figure 69. Total accumulated AE energies.

It should be noted that in Figure 69, the energy scale is logarithmic, thus reductions in AE accumulated energy from hygrothermal aging are quite significant. From control to saturated, energies were reduced one order of magnitude in, and two orders of magnitude in cross-ply laminates. Again, this larger change in the cross-ply laminates suggests that inter-ply effects influence damage tolerance of multi-angle laminates. Following desorption, energies were recovered partially in cross-ply laminates but were still far from those of the control specimens. From these results, it can be interpreted that the amount of damage sustained during the loading cycle was reduced by hygrothermal aging.

Aside from quantifying damage, AE is an excellent tool for detecting when a failure occurs in composites. In this study, the onset of damage was correlated to the onset of AE activity. Damage onset was prescribed as the strain level at the occurrence of the 10th event. If 10 events occurred, this would be deemed enough activity to be attributed to damage rather than anomaly or noise. Results of the damage initiation strains detected by AE are depicted in Figure 70.

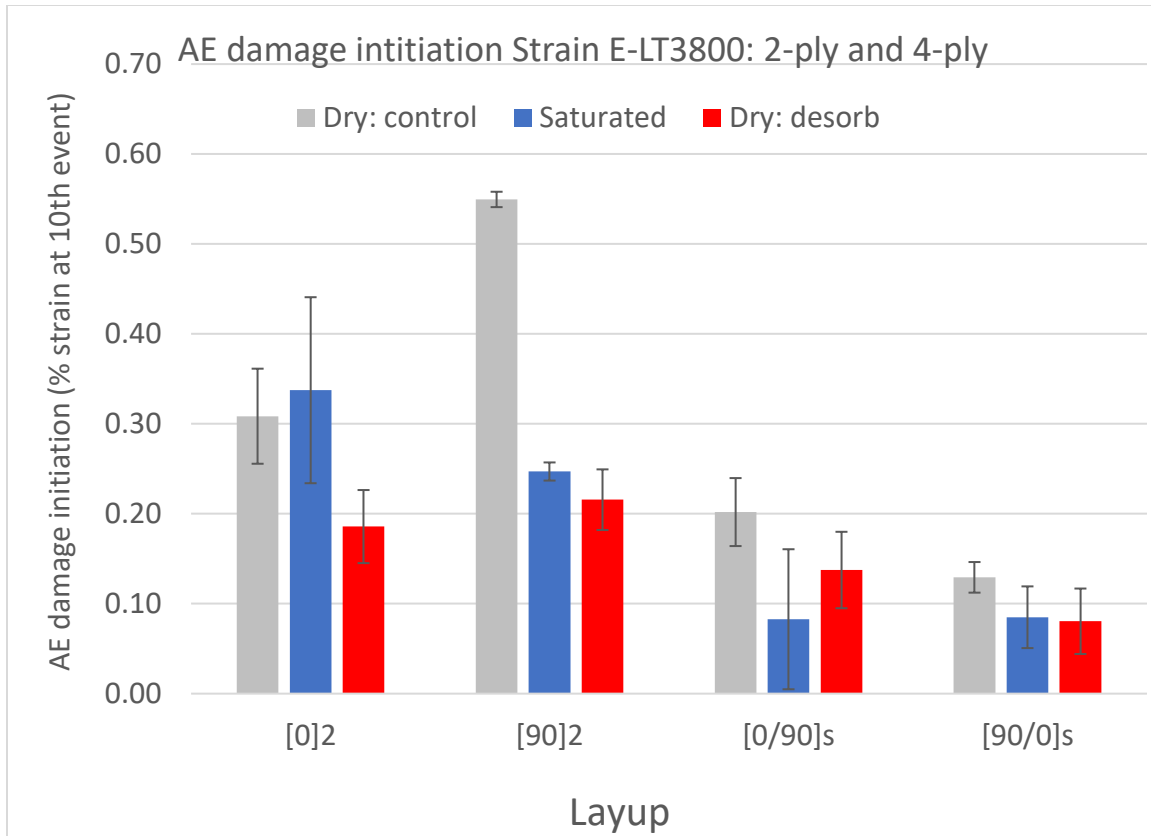


Figure 70. AE damage initiation strains.

In all laminates, except [0]₂, the damage was detected much earlier in the loading cycle for saturated samples than the control samples. This correlates to observed behavior in the stress-strain curves, where damage initiated at lower strains in saturated laminates. However, the actual strain values do not match perfectly. For example, [90]₂ control samples detect damage at 0.55% strain, whereas stress-strain data shows 0.43%. Perhaps changing the criteria for what is deemed relevant AE activity would yield more consistent results. Despite this slight inconsistency between methods, it is

confirmed that AE is effective for detecting damage onset in materials. Stress-strain data did not show clear damage onset for [0]₂ laminates, but AE data fills this void. Interestingly, control and saturated [0]₂ samples experience damage at similar strain levels, while desorbed samples initiated at much lower strain levels.

Together, these parameters support the mechanical data, indicating that hygrothermal aging reduces damage tolerance of the material and reduces the energy required to initiate/grow damage. However, it is important to verify these results are in fact due to changes in damage behavior and not a function of absorbed moisture affecting the nature of AE waves.

2.5.9. Frequency Analysis

Frequency analysis of AE waveforms provides a method to inspect the damage progression of a composite material in terms of types of damage mechanisms present. Changes in the damage mechanisms present during the loading of composite material with aging may provide insight on hygrothermal degradation mechanisms. For this work, the three damage mechanisms of interest were matrix failure, interphase failure, and fiber failure. The respective frequency bins for these damage mechanisms are shown below in Table 15. These bins are derived from literature review and previous work conducted at MSU [66]. Experimental validation and first-principal understanding of the relationship between the frequency and damage mechanisms is a subject of interest in on-going AE research.

Table 15. Frequency analysis bin ranges.

Bin	Damage Mechanism	FFT-Peak-Frequency Range (kHz)
Bin 1	Matrix	<120
Bin 2	Fiber/matrix interphase	120-300
Bin 3	Fiber	>300

Note: for this work, fiber-debond and pullout are combined into a singular fiber/matrix interphase bin. Normalizing the number of damage events in each frequency bin by the total number events gives the bin percentages, compared below in Figure 71-Figure 74. Examples of the progression of these events during the loading cycle are provided in Appendix B.

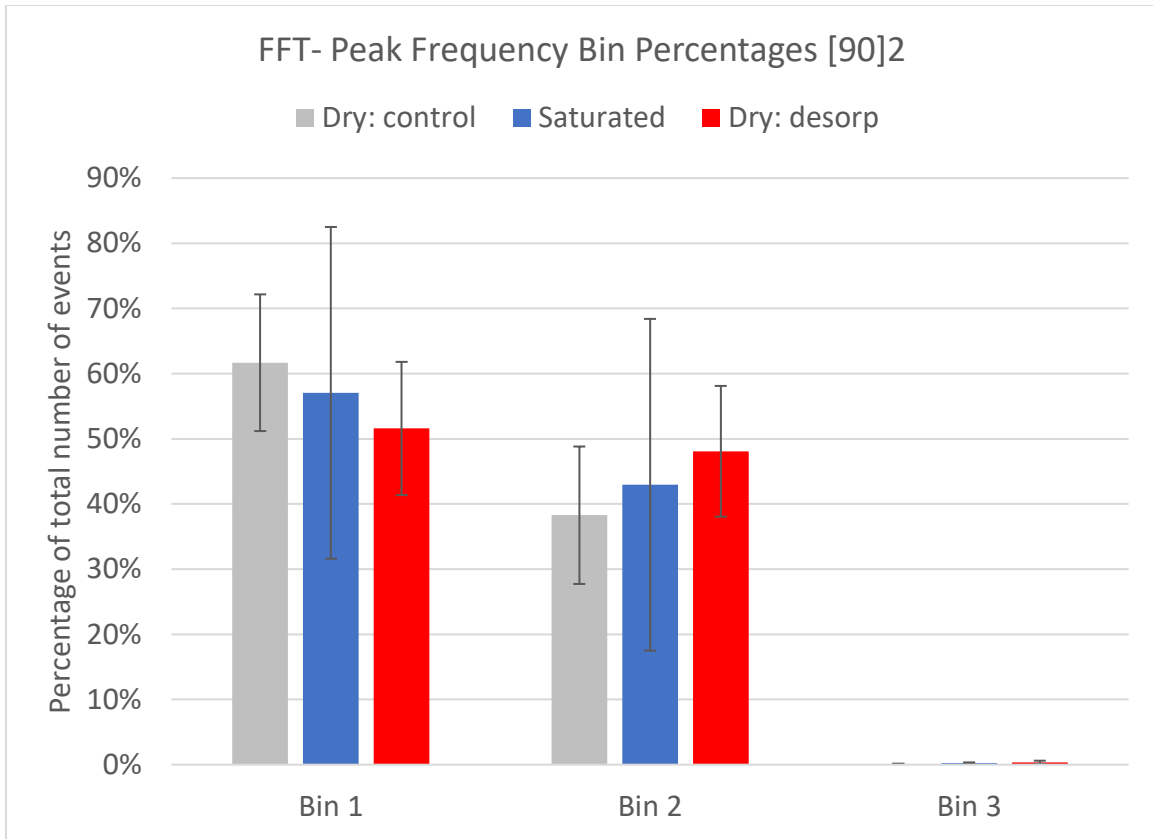


Figure 71. Frequency bin percentages [90]₂

As shown in Figure 71, damage in transverse tension consists of competing damage mechanisms of matrix crack and interphase failures. Slight increases in the contribution of interface failures were observed but were not statistically significant to be attributed to change in interface integrity. [0]₂ layups were dominated by interphase failures rather than matrix failures. Typically, 0° plies would also experience fiber failure as a damage mechanism, however, this mechanism occurs near ultimate failure of the composite and is therefore difficult to capture with AE monitoring.

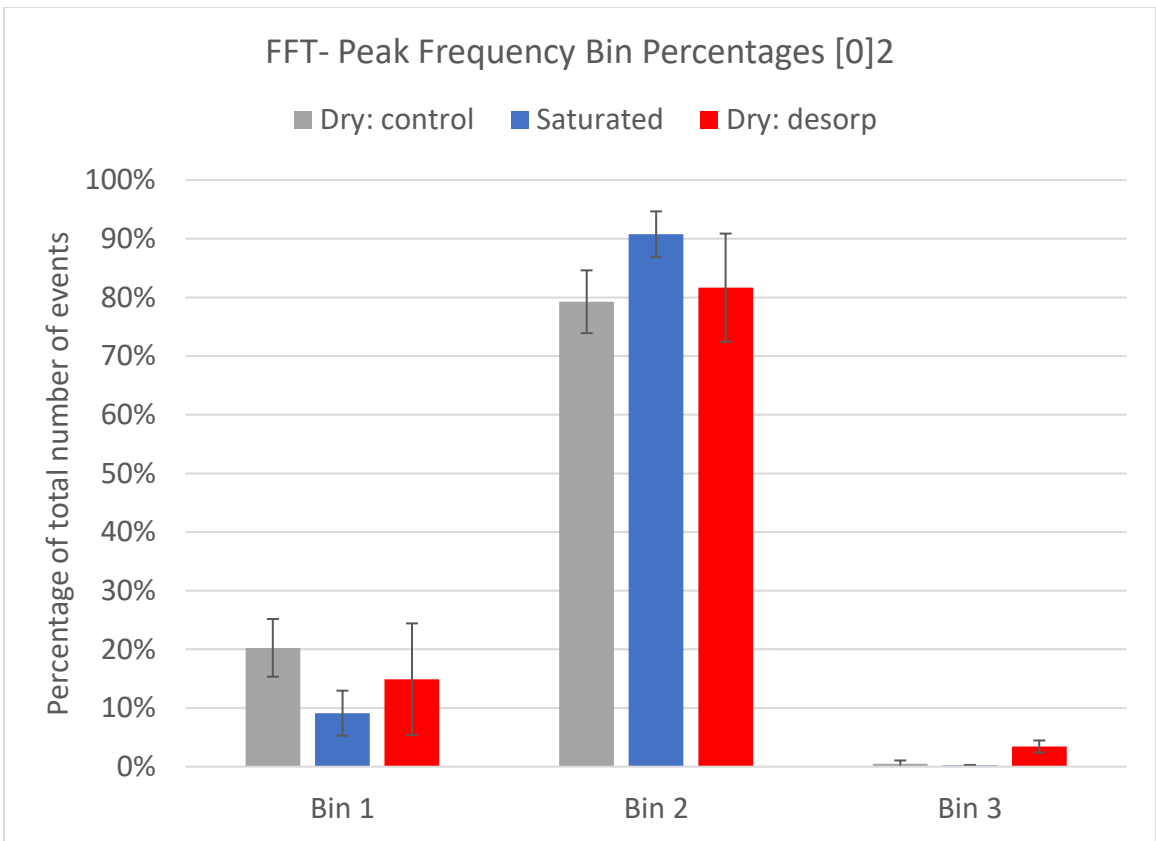


Figure 72. Frequency bin percentages [0]2

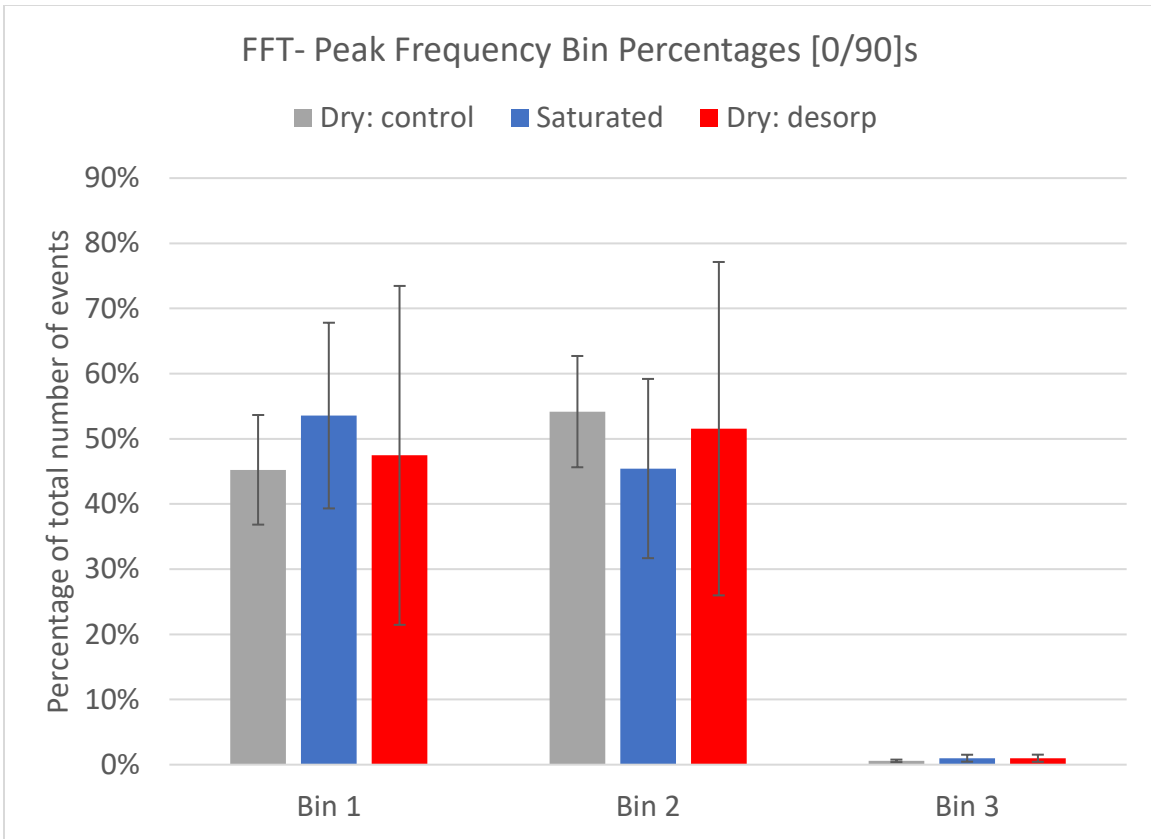


Figure 73. Frequency bin percentages [0/90]s

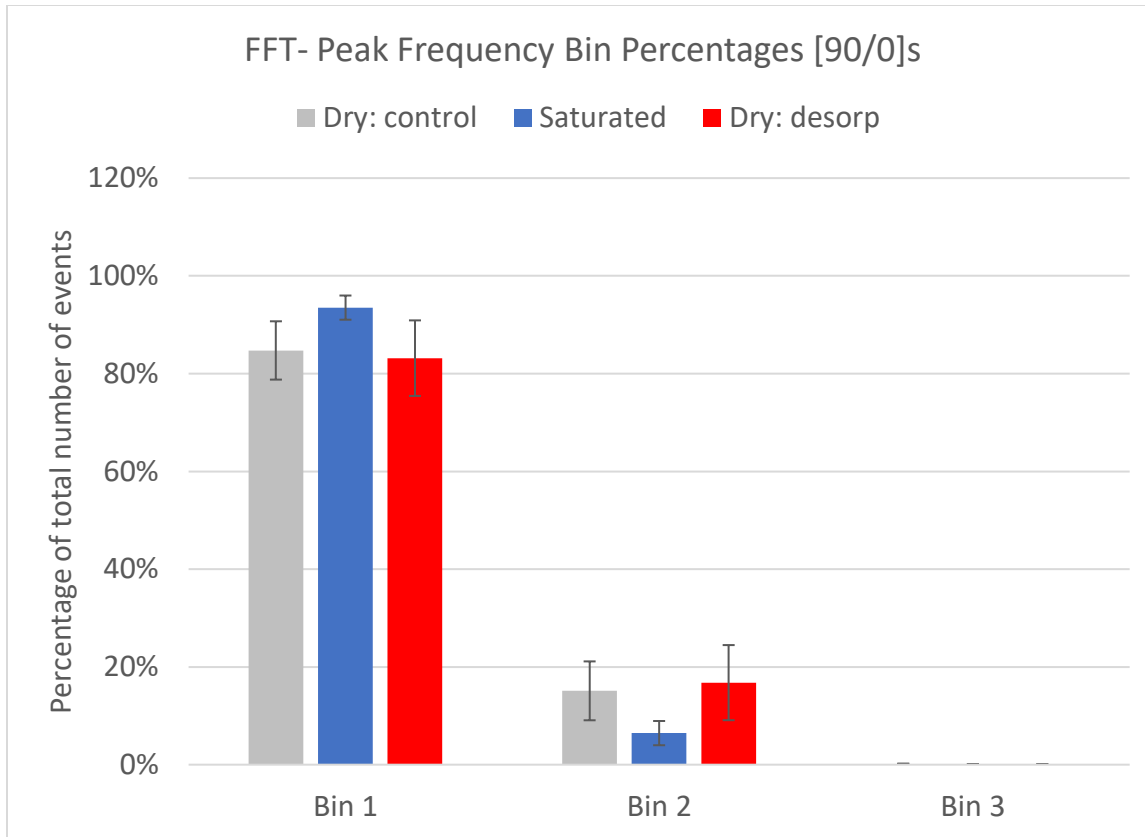


Figure 74. Frequency bin percentages [90/0]_s

[0/90]_s and [90/0]_s, shown above in Figure 73 and Figure 74, did not appear to be significantly affected by hygrothermal aging. Interestingly, the damage response of the two laminates is significantly different with [0/90]_s experiencing near-equal amounts of matrix failures and interface failures, while [90/0]_s are dominated by just matrix failure. It would be anticipated that both configurations of cross-ply would experience similar damage progressions. It could be hypothesized that the variation of the AE response is due to both attenuation and source behavior of damage mechanisms being dependent on ply location in the laminate. For example, cracking in the outer ply of the [90/0]_s laminate could attenuate waves propagating from the internal 0° plies of the and thus alter the received AE response between laminates. Also, the location of the transverse plies in the stacking sequence could alter the transmitted shear stress and result in varying transverse crack densities between the two cross-ply layups. Further investigation in AE analysis is necessary to understand this behavior. However, assuming the correlation between frequency of AE events and damage mechanisms exists, the consistency in frequency results between control, aged and desorbed samples suggest that the contribution of damage mechanisms themselves independent of hygrothermal-aging. The damage bins appear to accumulate in the same order throughout the loading cycle which implies that the sequence of damage evolution did not change with conditioning.

2.6. Wave Propagation and Attenuation

The changes in the AE response described above show significant changes in the damage behavior of hygrothermally-aged composite materials. However, further investigation into wave propagation and attenuation is necessary to verify the reason for these substantial changes in AE response. The

ingress of moisture into the composite may affect the AE activity in several ways. This effect can be divided into two main categories: effects on wave propagation and effects on source behavior.

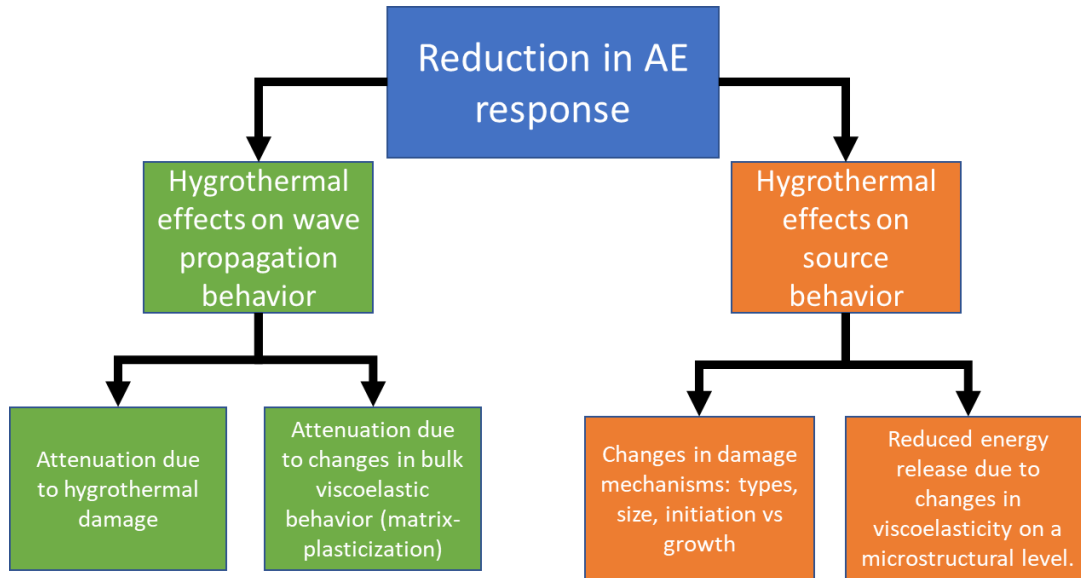


Figure 75. Root cause of the reduction in AE response.

Both the source behavior and wave propagation behavior can be affected by changes in the viscoelastic behavior of the matrix material. Plasticization typically increases the viscous response of the polymer resulting in energy absorption and dissipation of AE signals, both on a bulk composite level and a microstructural level. Additionally, damage accrued from loading or swelling may attenuate signals.

2.6.1. Sensor Test: Guided Ultrasonic

A sensor test was executed to simulate the propagation of an AE elastic wave. The sensor test, a built-in function of an AE acquisition system, may be implemented as a quasi-guided ultrasonic system [84]. Since both AE wave and ultrasonic waves are both lamb waves, attenuation of guided waves is representative of the attenuation of AE waves. The sensor test uses two AE senses to pitch and receive ultrasonic pulses as shown in **Error! Reference source not found.**

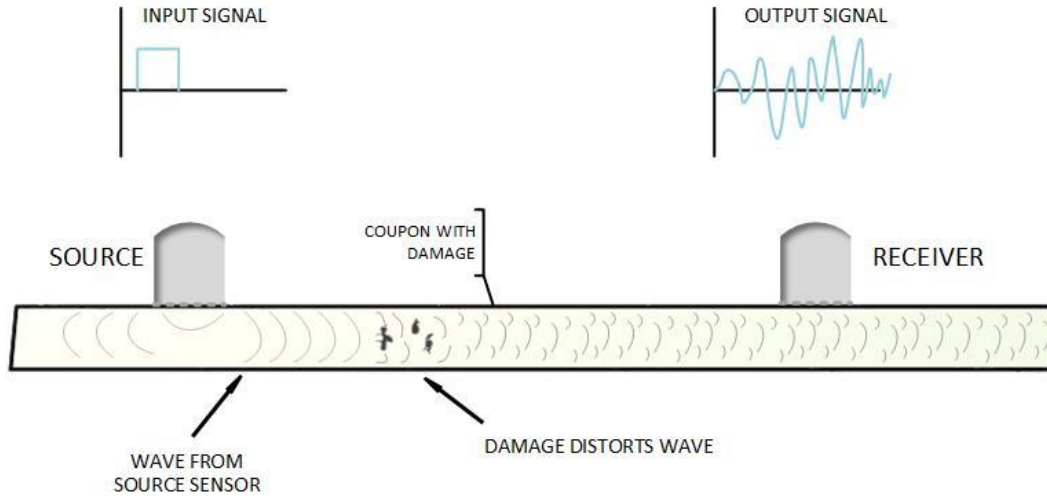


Figure 76. Sensor test schematic.

Sensor tests were conducted on untested 2-ply samples in both control and saturated conditions; **Error! Reference source not found.** outlines these tests. Two combinations of sensors were implemented per each specimen to eliminate the deviations to variation in sensor response. Each test yields a pulse for each sensor in the array; with six tests for five coupons, this results in 60 send-recv pulses for each laminate in each condition.

Table 16. Sensor-test test matrix

Layup	Condition	Number of coupons	Number of sensor combinations	Number of tests (per coupon)
[0] ₂	Control - untested	5	2	6
[0] ₂	Saturated - untested	5	2	6
[90] ₂	Control - untested	5	2	6
[90] ₂	Saturated - untested	5	2	6

The samples were tested without tabs in the unloaded configuration. Simply supported boundary conditions were implemented by placing the samples on pin supports spaced 220mm apart. The source generated a 5μs pulse. The recorded output metrics of the sensor tests were those corresponding to the receive-sensor including, time of flight, wave speed, amplitude, and energy (MARSE, not absolute). The averaged results from the sensor-tests are shown below in **Error! Reference source not found.**

Table 17. Sensor-test results (averaged)

Layup	Condition	Wave speed (m/s)	Received Amplitude (dB)	Received MARSE energy
[0] ₂	Control - untested	4.33E+03	78.1	78

Layup	Condition	Wave speed (m/s)	Received Amplitude (dB)	Received MARSE energy
[0] ₂	Saturated - untested	4.34E+03	77.3	68
[90] ₂	Control - untested	2.74E+03	64.7	17
[90] ₂	Saturated - untested	2.69E+03	65.2	15

The wave speed collected show minimal change with aging. Based on Equations 6a and 6b, this would be the anticipated as aging caused minimal changes in both the bulk elastic properties of the material (Figure 55). The amplitude and MARSE energy also showed minimal changes with aging, differing by less than 1 dB and 10 E, respectively. However, significant variability existed with these parameters from test to test, especially energy. Figure 77. graphically shows the received amplitudes as well as the standard deviations.

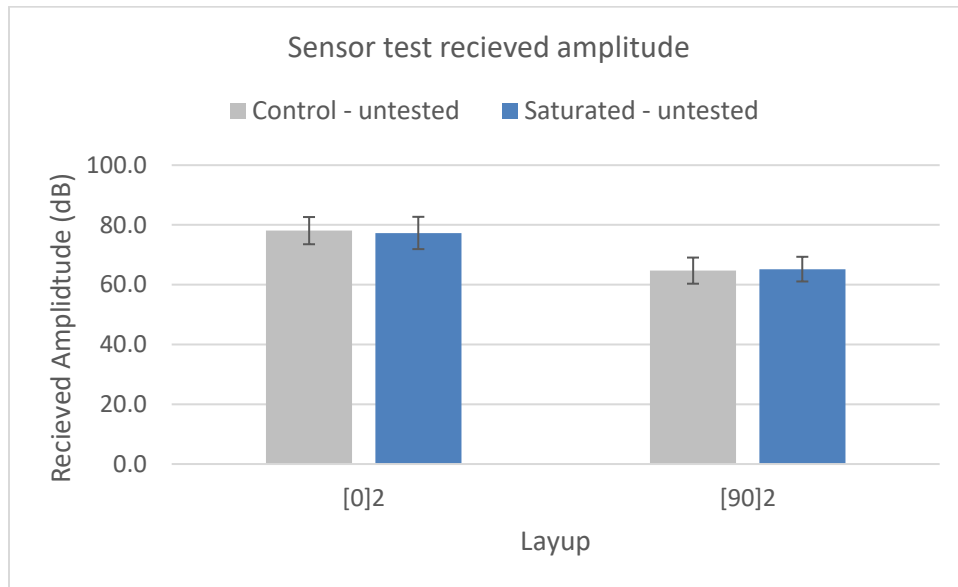


Figure 77. Sensor test received amplitude for untested two-ply laminates.

The standard deviation was significant, approximately 5 dB for both layups and conditions. Large deviations suggest variability in this test method; presence in all laminates shows the deviation to be symptomatic the test method rather than the material. In this case, however, a sufficient number of tests were conducted to show that the pulse from the sensor test did not change with aging. This would support that for this material system the propagation behavior of AE waves was not inhibited by moisture uptake, either from moisture-induced damping or damage-based attenuation. This result that a using this ultrasonic method to determine the presence of moisture or hygro-damage would not be effective of this scale; however, large propagation distances expected in the ultrasonic analysis of large structures may show more significant attenuation.

2.7. Conclusions from Damage Progression

Design and development of MHK devices and off-shore wind turbine requires classification of the effects of moisture on the durability and mechanical performance of the selected fiberglass-epoxy system. In this work mechanical performance was characterized by static strength, with the goal of comparing a cross-ply performance to constituent unidirectional lamina performance. The fiberglass-epoxy system studied in this work experienced significant static strength reductions due to hygrothermal aging across all laminates, with unidirectional laminate strengths reduced by 40% and cross-ply laminates experienced strength reductions of 54%. Variation between the strength reductions of unidirectional laminates and cross-ply laminates implies that performance of unidirectional laminates may not reflect the performance of cross-ply laminates and that interacting ply behavior increases the severity of hygrothermal effects.

This work also applied techniques to address the potential degradation mechanisms for the substantial reductions in static strength. It can be concluded that presence of water in the matrix was predominantly physical in nature since desorption revealed that little water was entrapped in the neat resin or the composite. T_g depression showed that plasticization was present, but not reflected in the elastic properties of the composite. Further, T_g -recovery did not correlate to the recovery of composite strength in desorbed. Additionally, control samples exposed to temperature condition without moisture verify that the degradation of the composite was not an artifact of the accelerated aging temperature.

Physical damage from the hygrothermal aging process was observed in both neat resin and composite samples. Large swelling strains caused cracking in neat resin samples, and through laminate theory, translated to large internal stresses within the composite, especially in the interply regions. Physical damage was prevalent in the composites after hygrothermal exposure and was visible both optically and through SEM. Mechanical properties were not recoverable with desorption which again supports the hypothesis of physical damage was induced during the aging process.

The physical damage induced by the aging process altered the damage progression of the composite and reduced the damage tolerance. Both stress-strain response and AE data showed damage occurred at lower strains in laminates that received hygrothermal exposure. Physical damage induced during swelling permitted damage to grow at lower strain energies rather than those needed to initiate damage in an unconditioned laminate. Premature damage growth accelerated that damage progression causing damage coalescence much lower in the loading cycle, which was evidenced by coupon failures as well as the reduced amount of AE response in terms of number of events and energy. This finding corresponds to a reduced damage tolerance from hygrothermal aging. AE frequency analysis revealed that the normalized contribution and sequence of damage mechanisms was unaffected by hygrothermal aging and supports the idea that aging-induced physical damage rather than altering the nature of damage mechanisms themselves. A guided ultrasonic test showed no change in lamb wave attenuation with hygrothermal aging, confirming that the changes in AE response did, in fact, correlate to changes in the damage behavior rather than changes in material damping.

3. MOISTURE EFFECT ON STACKING SEQUENCE AND OFF-AXIS STRENGTH

3.1. Test Design

The goal of this research was to investigate the effects of moisture absorption on the static strength and AE signatures of coupons at varying fiber angles and with different stacking sequences. First, six different 2-ply layups were chosen; three balanced and three unbalanced. The different stacking sequences tested were $[15]_2$, $[30]_2$, $[45]_2$, $[\pm 15]$, $[\pm 30]$, $[\pm 45]$. The selection of layups chosen above provides a wide variety of internal stress states. The balanced coupons were to produce a significant amount of shear between the two plies. As the fiber angles are increased, the inter-ply shear stress would increase as well. The unbalanced coupons were designed to produce the opposite effect. As both plies are in the same direction, there will be a negligible amount of inter-ply shearing stress. The internal stress state of these coupons instead focuses on the bonds between the fibers and matrix. As the fiber angle is increased the amount of normal force on the bonds increases and the shearing stress decreases. In the case of a $[0]_2$ sample, the only normal force pulling the fibers apart laterally within the sample is the contraction seen from Poisson's effect. However, in the case of $[15]_2$ samples, a portion of the tensile load is translated into a normal force on the bond.

The second portion of this research focused on how the effects of moisture absorption changed with the stacking sequence. As previous research has shown that the moisture diffusion follows Fickian diffusion principles, the amount of water at a specific point within the sample is dependent on both time and location. Given the assumption that the inclusion of moisture is affecting the material at the microstructural level, it follows that the stacking sequence should be very important during the diffusion process. For these coupons, it was chosen to produce samples that had the same tensile strength before diffusion but would have different strengths during the diffusion process. The two layups that were chosen were $[0/90]_s$ and $[90/0]_s$. Both layups have the same theoretical tensile strength as they both have the same amount of fibers in the tensile direction. In both coupon sets, the 0 degree plies provide the majority of the stiffness and strength in the tensile direction while the 90 degree plies provide lateral stability. However, as these coupons are subjected to a water environment and diffusion begins, the difference in stacking sequences will affect which plies are degraded first.

3.1.1. Materials

Two fiber systems were utilized for the research presented in this paper: Vectorply E-LT 3800 and Vectorply E-LT 3900. Both systems are unidirectional fiber systems utilizing E-Glass fibers woven into a mat. They both have 91% of their fibers in the 0° orientation, with 9% in the 90° orientation. Stitching accounts for less than 1% of aerial weight. Effects of fiber angle and moisture diffusion was completed using Vectorply E-LT 3900. Effects of stacking sequence and moisture absorption was completed using Vectorply E-LT 3800. More detailed information on the fiber systems can be seen in Appendix A.

The resin system chosen was a two-part epoxy from Momentive developed for the wind industry, Epikote™ RIMR 135 and hardener Epicure™ RIMH 1366. The post cure cycle specified by the manufacturer called for 24 hours at room temperature (23 C) and 12 hours at 70 C.

3.1.2. Water Submersion

For the first round of tests, the samples were soaked in synthetic sea water manufactured to conform with ASTM D1141. The manufactured saltwater and coupons were kept in sealed plastic containers and conditioned at 50 °C. The increased temperature significantly hastened the diffusion rate allowing for thicker samples to be tested in shorter time.

3.1.3. Test Matrices

For the first section of testing, fiber angle and moisture absorption were varied. In these tests, only two conditioning steps were studied: fully saturated and dry. The test matrix for this section can be seen below in Table 18. Table 18. Lists of tests completed to study the effects of moisture absorption on various off-axis laminates.

Table 18. Lists of tests completed to study the effects of moisture absorption on various off-axis laminates.

Layup	Fabric	# of Tests	Load Rate	Conditioning
[15] ₂	E-LT 3900	6	.05"/min	3 Dry, 3 Saturated
[30] ₂	E-LT 3900	6	.05"/min	3 Dry, 3 Saturated
[45] ₂	E-LT 3900	6	.05"/min	3 Dry, 3 Saturated
[±15]	E-LT 3900	6	.05"/min	3 Dry, 3 Saturated
[±30]	E-LT 3900	6	.05"/min	3 Dry, 3 Saturated
[±45]	E-LT 3900	6	.05"/min	3 Dry, 3 Saturated

For the second section, stacking sequence and moisture absorption were varied. It was chosen to study the effects of moisture absorption throughout the saturation process to explore partial degradation effects. Times were chosen that would represent various levels of moisture saturation evenly distributed between 0.0% moisture and M_∞. As the diffusion process is much faster at the beginning, the times selected ended up being weighted towards the beginning of the saturation process. The testing matrix can be seen below in Table 19.

Table 19. List of tests completed in order to study the effects moisture absorption on various stacking sequences.

Layup	Fabric	# of Tests	Load Rate	Conditioning
[0/90] _s	E-LT 3800	5	.06"/min	0.0% Moisture
[0/90] _s	E-LT 3800	5	.06"/min	0.2% Moisture
[0/90] _s	E-LT 3800	5	.06"/min	0.5% Moisture
[0/90] _s	E-LT 3800	5	.06"/min	0.7% Moisture
[0/90] _s	E-LT 3800	5	.06"/min	Fully Saturated

Layup	Fabric	# of Tests	Load Rate	Conditioning
[90/0] _s	E-LT 3800	5	.06"/min	0.0% Moisture
[90/0] _s	E-LT 3800	5	.06"/min	0.2% Moisture
[90/0] _s	E-LT 3800	5	.06"/min	0.5% Moisture
[90/0] _s	E-LT 3800	5	.06"/min	0.7% Moisture
[90/0] _s	E-LT 3800	5	.06"/min	Fully Saturated

3.2. Visual Inspection of Damage

When the saturated samples were removed from conditioning, damage was already visible. The damage appeared as regions of opaqueness parallel to the direction of the fibers. The damage was often visible at multiple places along the length of the coupon. Examples of the damage can be seen below in Figure 78. Coupon 2442-5 and the damage seen after the coupon was removed from the saltwater bath and Figure 79. Once these samples were subjected to tensile loading, the damage would propagate further along the fiber angle. A few samples were removed from testing and the damage was inspected using optical microscopy. Cross sections through the areas of opaqueness were cut and various levels magnification were used. Unfortunately, the damage was not obviously visible at a microscopic level. Future work will include SEM analysis as the capability is available.



Figure 78. Coupon 2442-5 and the damage seen after the coupon was removed from the saltwater bath.



Figure 79. Coupon 2444-11 and the damage after the coupon was removed from the saltwater bath.

3.3. Off-Axis Strength Reduction

3.3.1. Moisture Absorption

For the study of off-axis strength reduction, six different layups were tested: $[15]_2$, $[30]_2$, $[45]_2$, $[\pm 15]$, $[\pm 30]$, and $[\pm 45]$. Samples were manufactured from four different plates. Witness samples for each of these plates was placed in saltwater and measured periodically to document the absorption process. The resulting absorption curves can be seen below in Figure 80. The samples exhibited Fickian diffusion characteristics as expected. As the sample weights were measured it was noticed that there was significant salt buildup on the surface. The salt was not washed off prior to weight measurements until full saturation as it was difficult to verify that a consistent washing occurred. There was also a concern that the washing would induce additional diffusion further skewing the data. As the moisture curve leveled off to a consistent weight gain at 1000 hours, it was concluded that moisture absorption had ceased. The samples were conditioned for another 500 hours to ensure the samples were at full saturation. A thorough washing was then completed eliminating the salt buildup. This last weight measurement is representative of the amount of water absorbed into the material without the added weight of the salt build up.

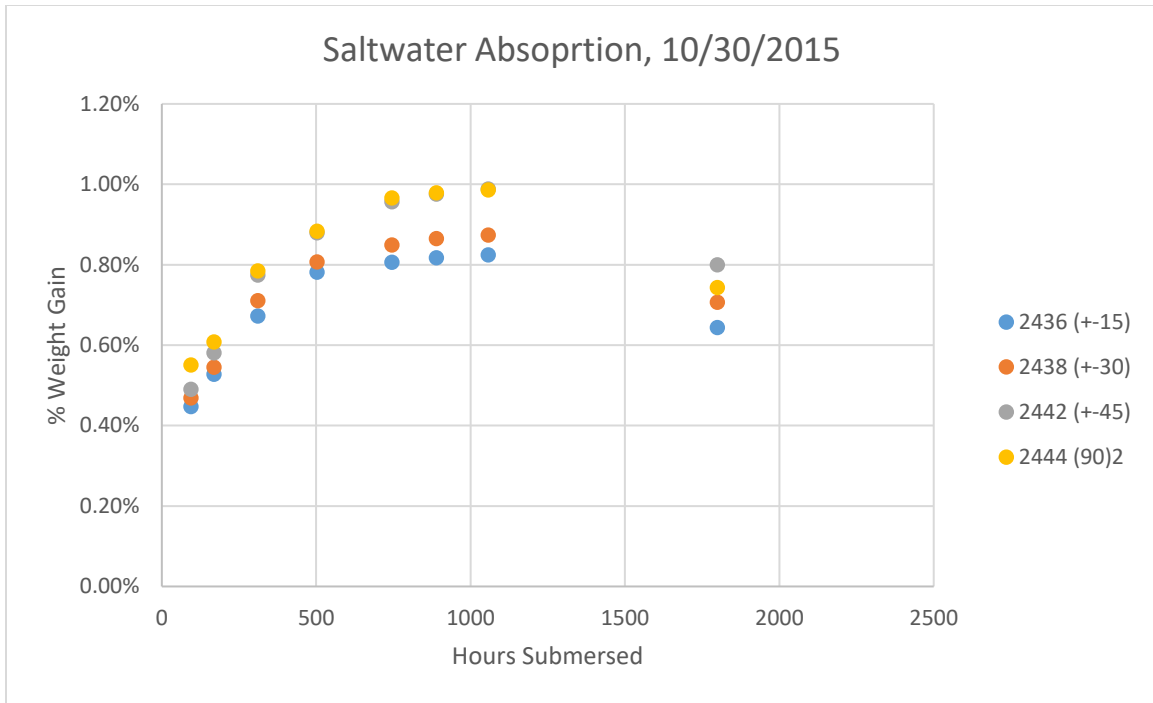


Figure 80. Moisture absorption for off-axis samples to study the effects of fiber angle and moisture diffusion on static strength and AE signatures.

3.3.2. Static Strength Reduction

Three samples of each layup were tested to static failure in both dry and saturated conditions. The average strength values for each layup in dry/saturated conditions can be seen below in Figure 81. **Error! Reference source not found.**

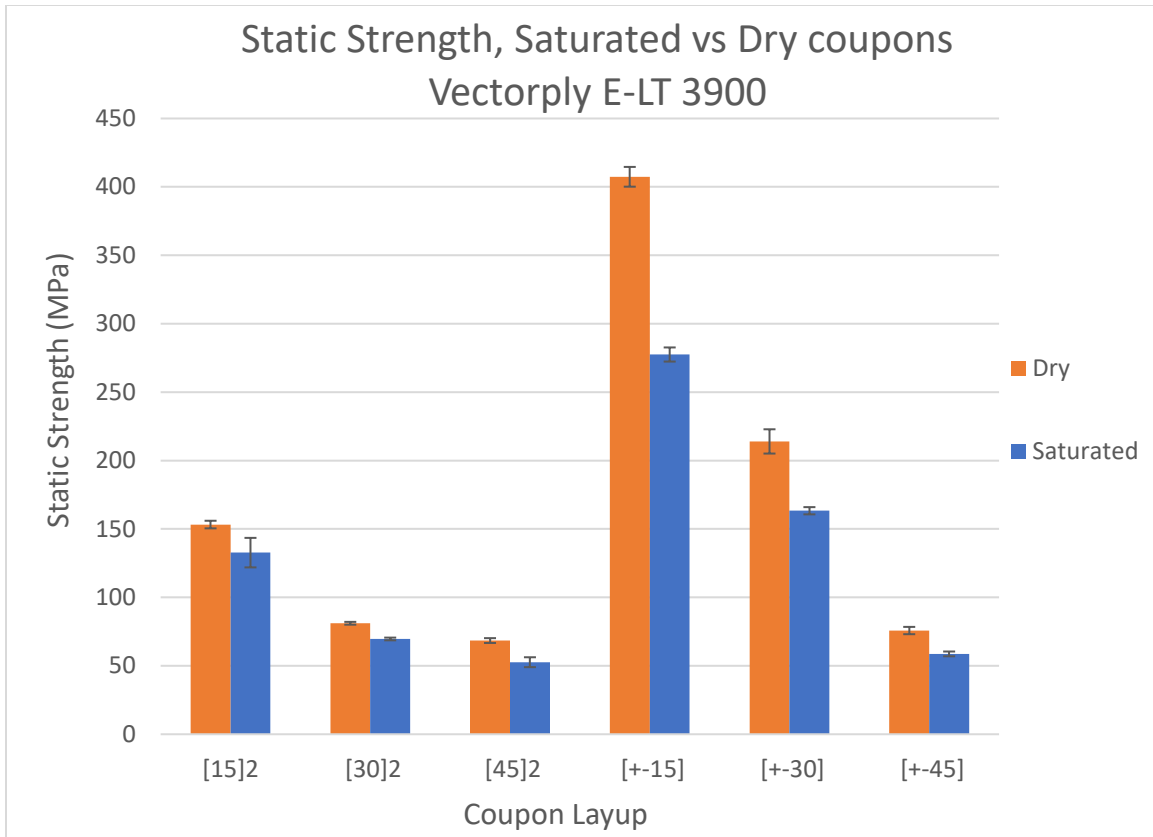


Figure 81. Static strength for both dry and saturated coupons at various fiber angles. Consistent failures occurred for all layouts and conditions.

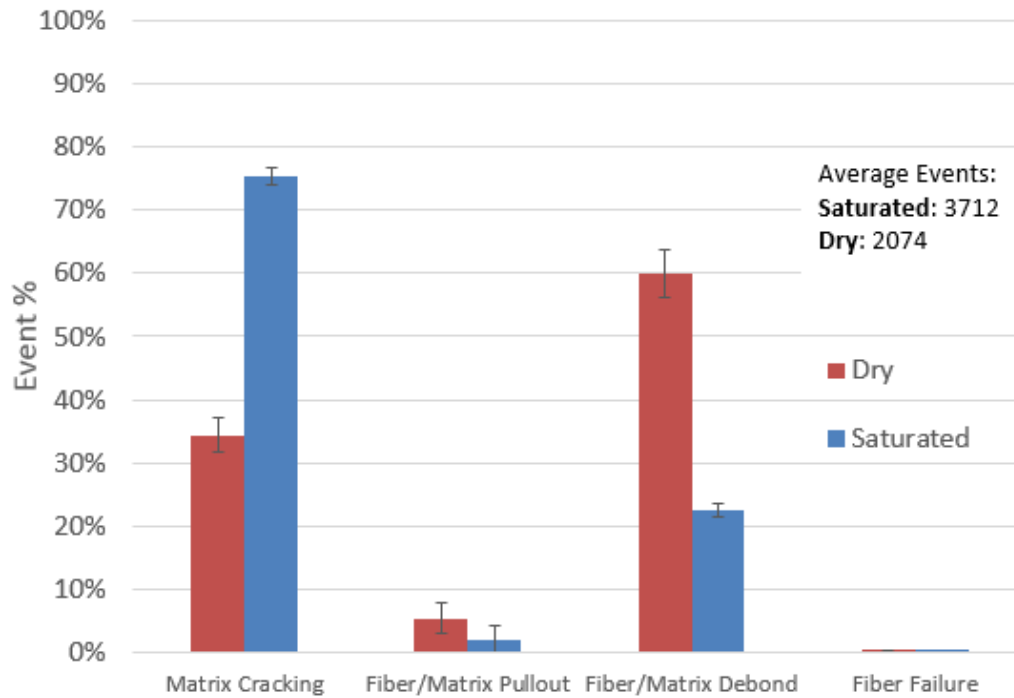
The static strengths of the dry laminates are in line with expected results from previous research at MSU. The strength reductions in the off-axis laminates are similar to those seen in unidirectional laminates. Interestingly, the inclusion of water affected the strength of the balanced coupons more than the unbalanced coupons. Strength in the [45]₂ samples was reduced by 23% while the [±15] samples were degraded by 32%. The standard deviation error bars show little variation in the strengths of the layouts at each condition.

3.3.3. AE Analysis

AE analysis was performed on the tests presented above to further study the effects of moisture inclusion. The waveforms were analyzed utilizing an FFT and the peak frequency of the events was recorded. The events were then collected into the discrete damage bins discussed earlier, each representing a different failure mechanism. As the purpose of the research was to investigate the difference in failure mechanisms between dry and saturated samples, the percentage of different damage bins will be presented for the two conditions. Using the percentage of events in each bin provides a better comparison between tests as the number of individual events can change drastically. Below in Figure 82 - Figure 87, the AE results of each laminate set are displayed. Each set keeps the same format which shows the bin percentages summarized on the left chart for each condition. Standard deviation error bars are added to show the variation of the data. On the right side of the page, frequency distribution plotted against stress is shown for one test of each condition. These charts are important as they show the progression of damage as opposed to a snapshot at the end of the test.

The bin percentage charts show very similar results across the different laminates. All laminates showed a decrease in events classified as fiber/matrix debond and an increase in matrix cracking. For saturated samples, the percentage of matrix cracking events exceeded 70% for all three sample sets while percentages for the dry samples varied from 34.4% to 42.0%. The percentage of fiber/matrix pullout (bin 2) events remained relatively consistent throughout all balanced layups with a slight decrease after moisture saturation. For saturated samples, the percentage of events classified as fiber/matrix pullout varied from 1.9% to 2.1% while the dry samples had a range from 3.8% to 9.4%. Fiber failure was negligible for all laminates tested as expected.

Percentage of Damage Mechanisms [± 15] E-LT 3900



Note: 3 samples tested for saturated and dry conditions, standard deviation error bars

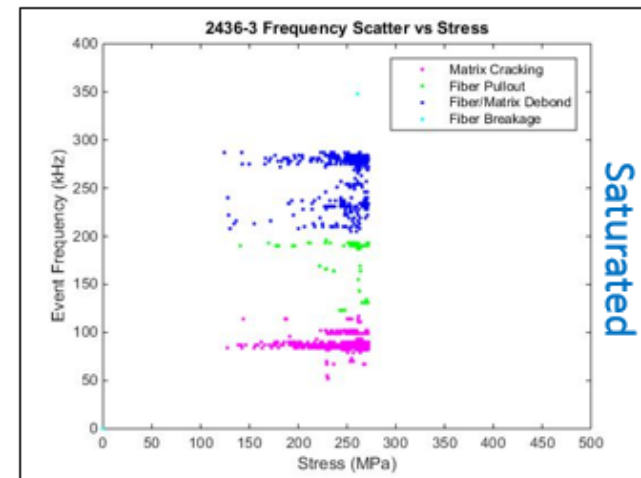
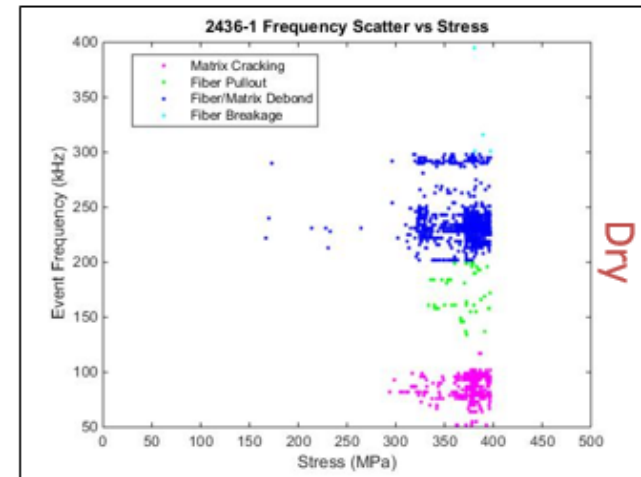
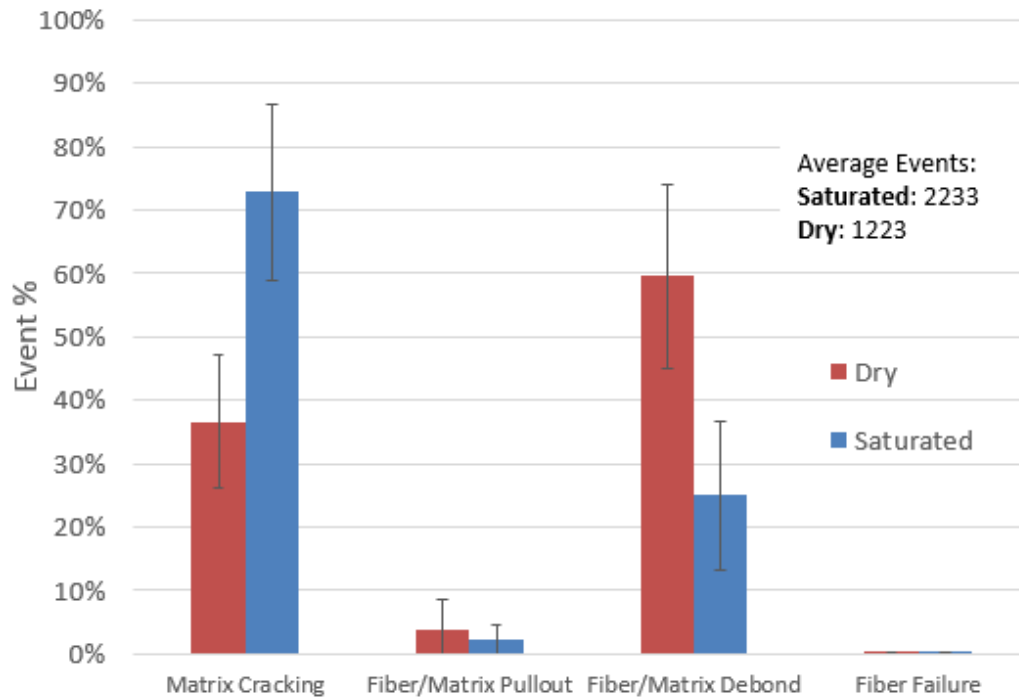


Figure 82. Percentage of damage mechanisms for [± 15] samples. Frequency scatter plots are shown to the right, showing the development of damage throughout the test.

Percentage of Damage Mechanisms [± 30] E-LT 3900



Note: 3 samples tested for saturated and dry conditions, standard deviation error bars

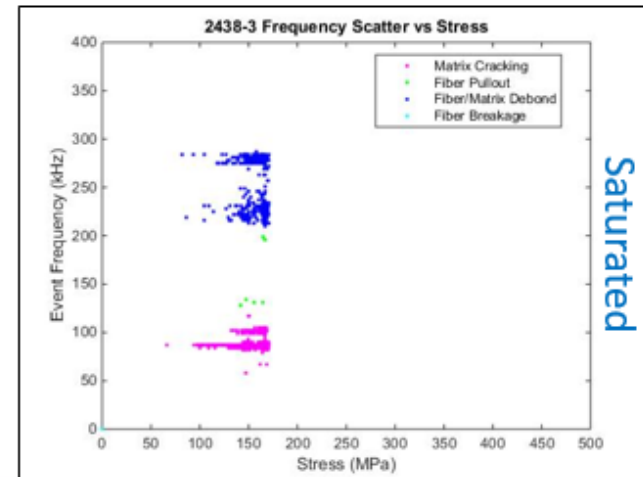
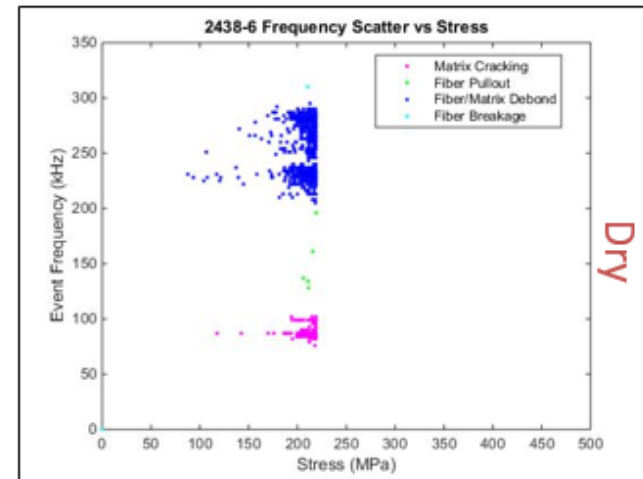
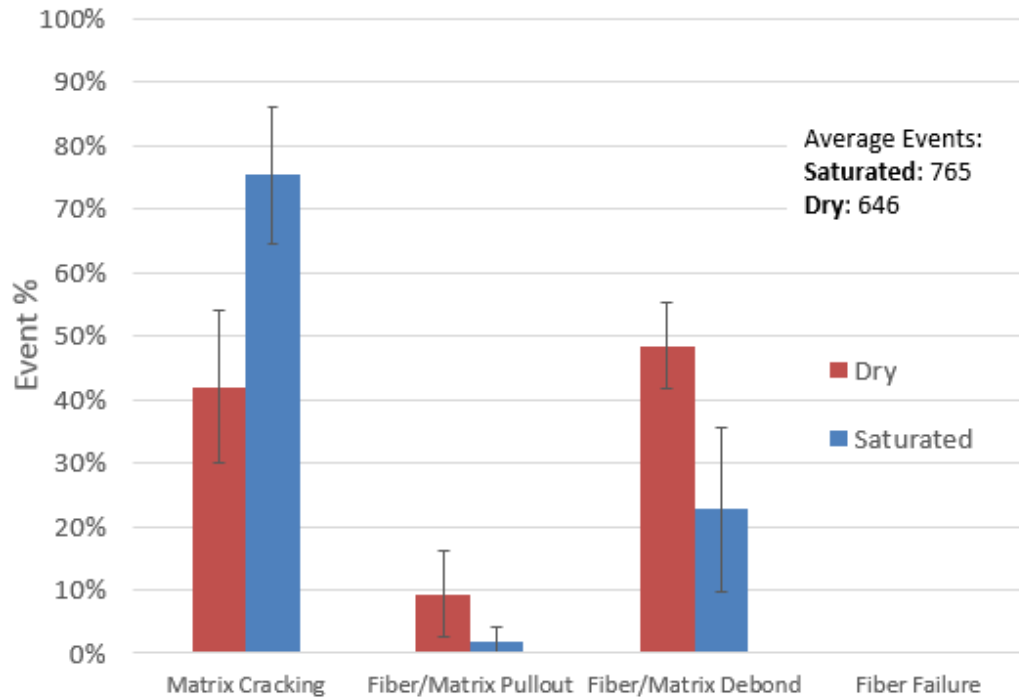


Figure 83. Percentage of damage mechanisms for [± 30] samples. Frequency scatter plots are shown to the right, showing the development of damage throughout the test.

Percentage of Damage Mechanisms [± 45] E-LT 3900



Note: 3 samples tested for saturated and dry conditions, standard deviation error bars

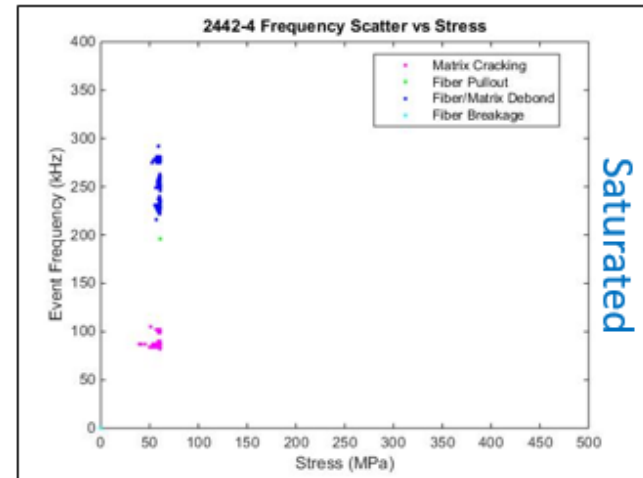
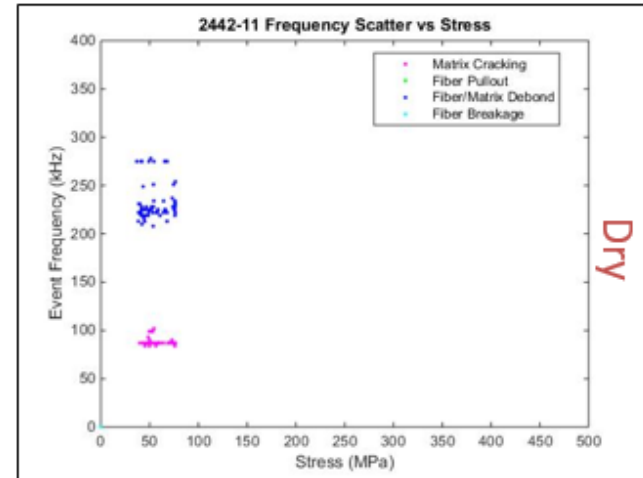
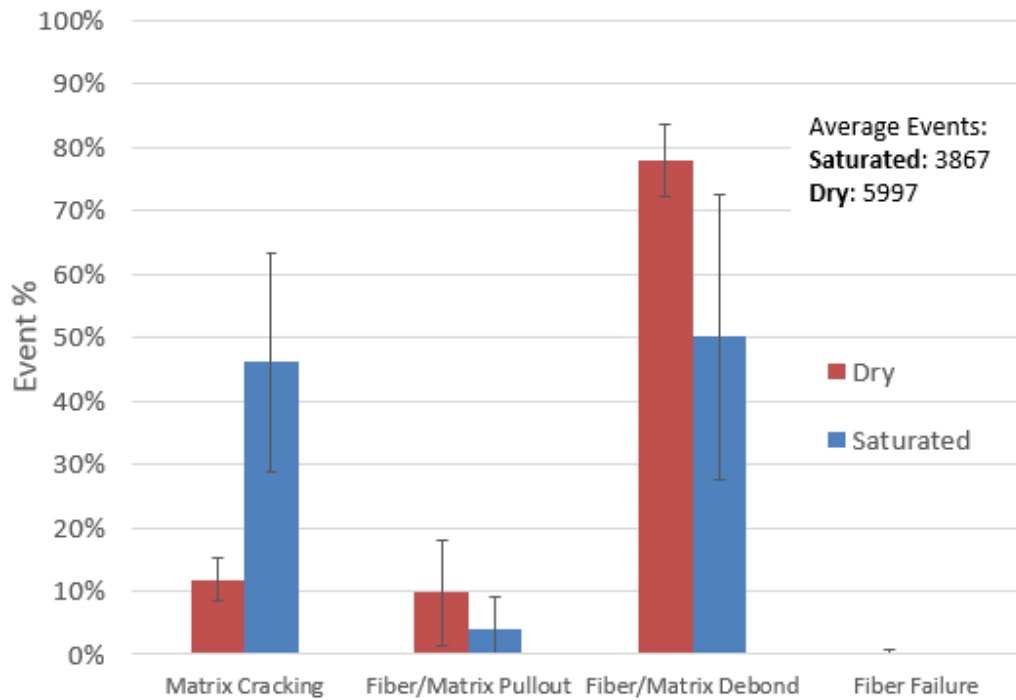
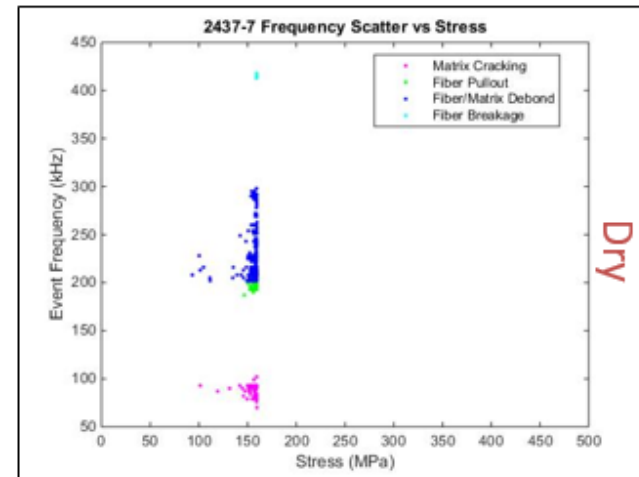


Figure 84. Percentage of damage mechanisms for [± 45] samples. Frequency scatter plots are shown to the right, showing the development of damage throughout the test.

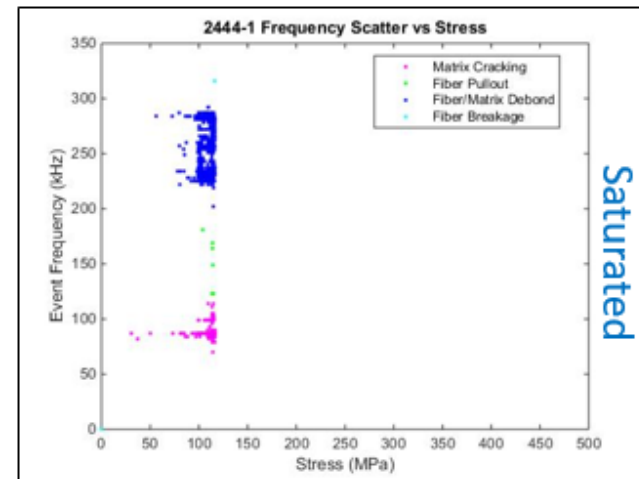
Percentage of Damage Mechanisms [15]₂ E-LT 3900



Note: 3 samples tested for saturated and dry conditions, standard deviation error bars



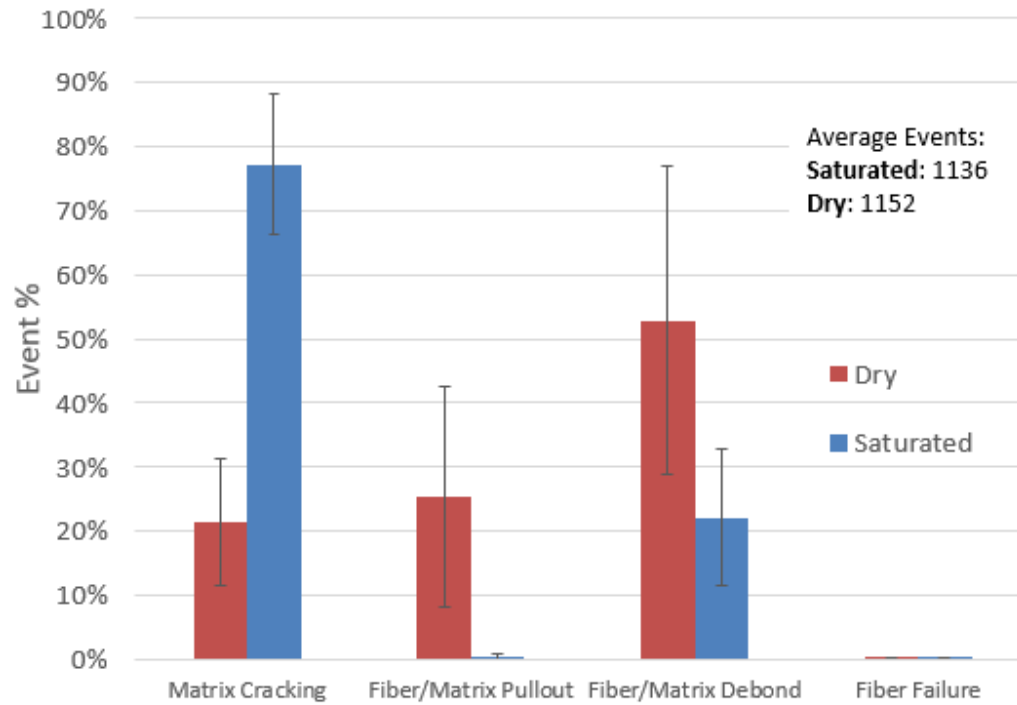
Dry



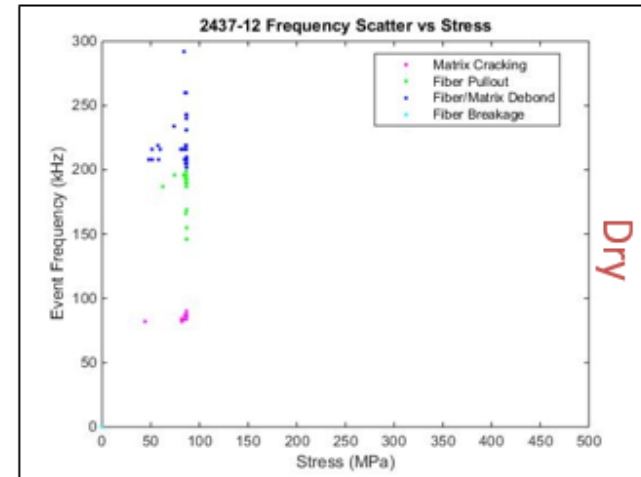
Saturated

Figure 85. Percentage of damage mechanisms for [15]₂ samples. Frequency scatter plots are shown to the right, showing the development of damage throughout the test.

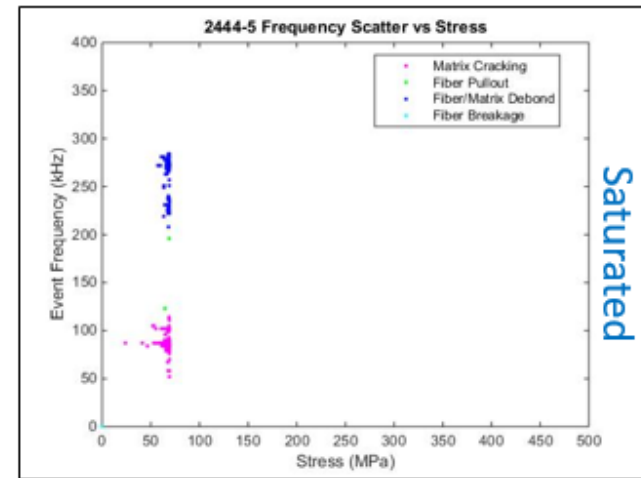
Percentage of Damage Mechanisms [30]₂ E-LT 3900



Note: 3 samples tested for saturated and dry conditions, standard deviation error bars



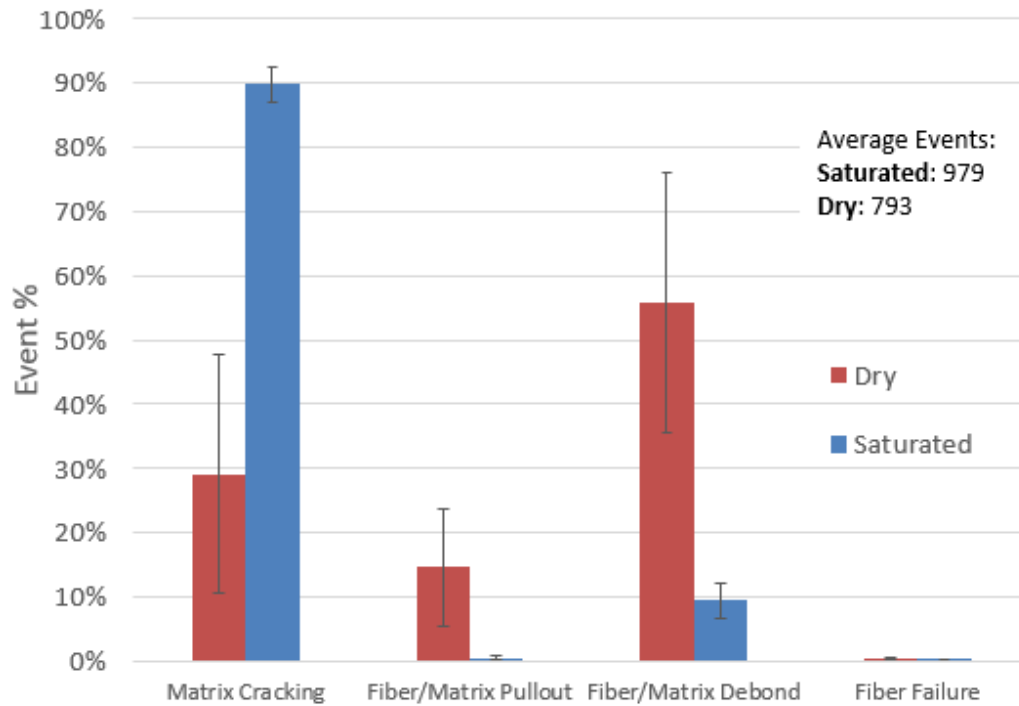
Dry



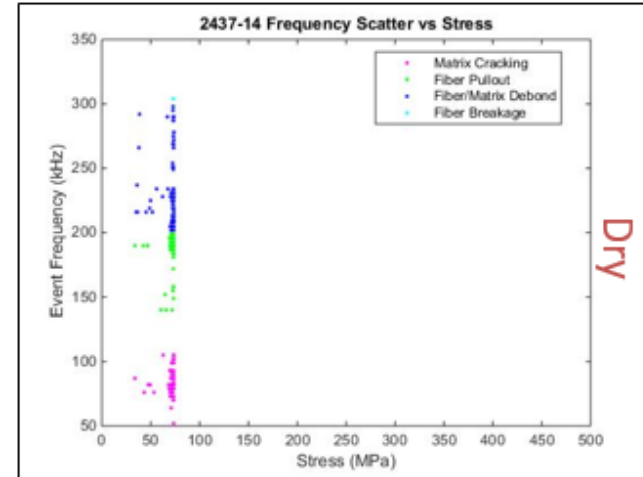
Saturated

Figure 86. Percentage of damage mechanisms for [30]₂ samples. Frequency scatter plots are shown to the right, showing the development of damage throughout the test.

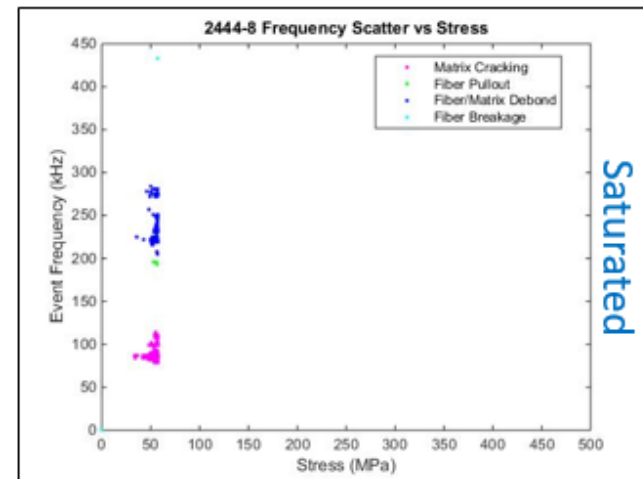
Percentage of Damage Mechanisms [45]₂ E-LT 3900



Note: 3 samples tested for saturated and dry conditions, standard deviation error bars



Dry



Saturated

Figure 87. Percentage of damage mechanisms for [45]₂ samples. Frequency scatter plots are shown to the right, showing the development of damage throughout the test.

The AE results provide further insight at a micromechanical level into the specific effects of the moisture absorption. All laminates tested had a decreased amount of fiber/matrix debond damage events and an increase in matrix events post saturation. The increase of matrix cracking events may indicate that the saturated matrix material is failing prior to the bonds of the unconditioned samples. This also appears evident when the AE events are plotted against stress. It can then be seen when damage mechanism bins become prevalent during the test.

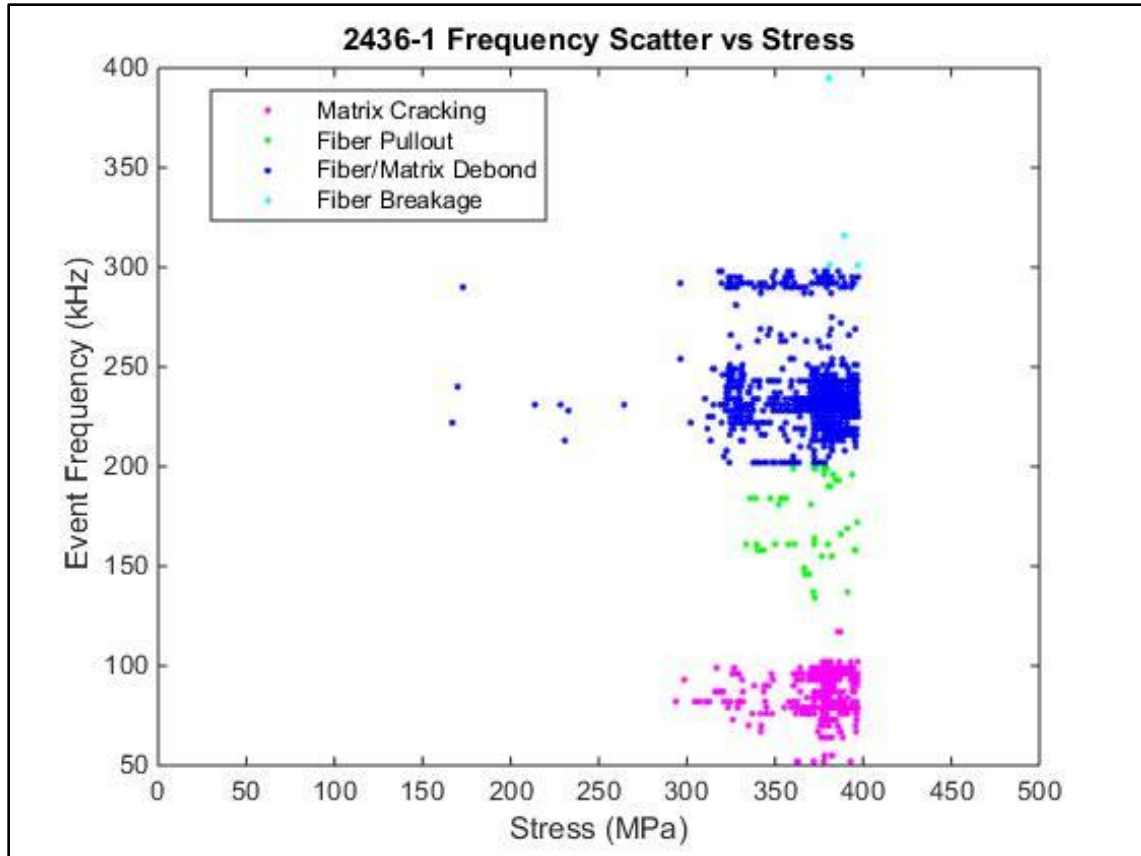


Figure 88. Frequency distribution plotted against stress for a dry [±15] sample.

Figure 88 shows the damage events plotted by frequency at the load they occurred at. There is a build-up of events occurring in bin 3 (fiber/matrix debond; blue) prior to failure but the events in bin 1 (matrix cracking; pink) occur much closer to failure. This contrasts with the events diagram for the saturated sample seen below in Figure 89.

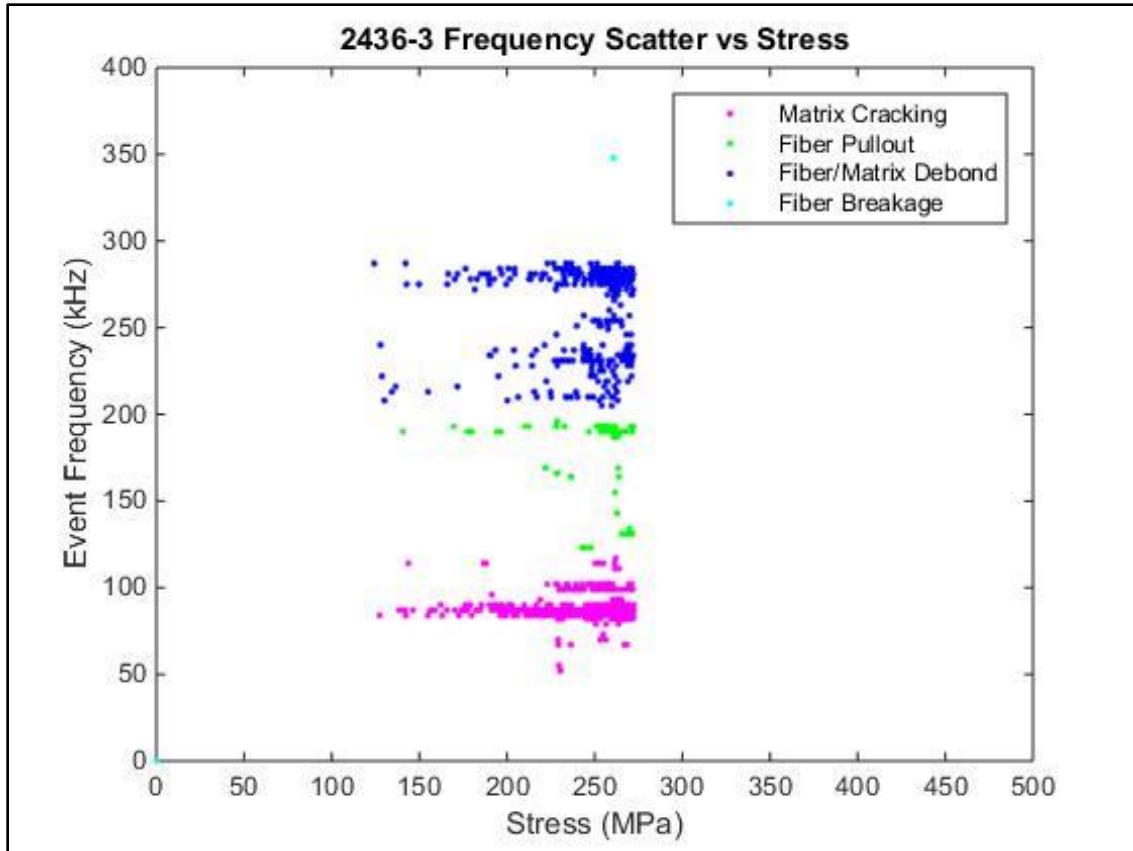


Figure 89. Frequency distribution plotted against stress for a saturated $[\pm 15]$ sample.

For the saturated sample, the matrix cracking events begin to occur much earlier prior to failure. In this case, the matrix cracking begins prior to the fiber/matrix interface failures. This indicates that the matrix failing prematurely, may be overloading areas of fiber/matrix interface causing further damage to the microstructure of the material. This effect would result in a premature failure as seen throughout mechanical testing. It is also evident from this chart that the matrix cracking bin is far more prevalent than fiber/matrix debond. These results are consistent throughout all laminates tested and can be seen throughout all scatter diagrams shown in Figure 82 - Figure 87.

3.4. Partial Saturation Strength Reduction

3.4.1. Static Strength

Five samples of each layup outlined above were tested for each time step. Both layups tested had very similar static strengths in the control set. As the samples were subjected to the marine environment, the strength of both layups decreased throughout time. The strength of the samples vs time and vs saturation percentage can be seen below in Figure 90. Ultimate strength vs time soaked for $[0/90]_s$ and $[90/0]_s$ coupons. Note: five tests performed for each layup at each time step. and Figure 91. Ultimate strength vs % weight gain for $[0/90]_s$ and $[90/0]_s$ coupons. Note: five tests performed for each layup at each time step.

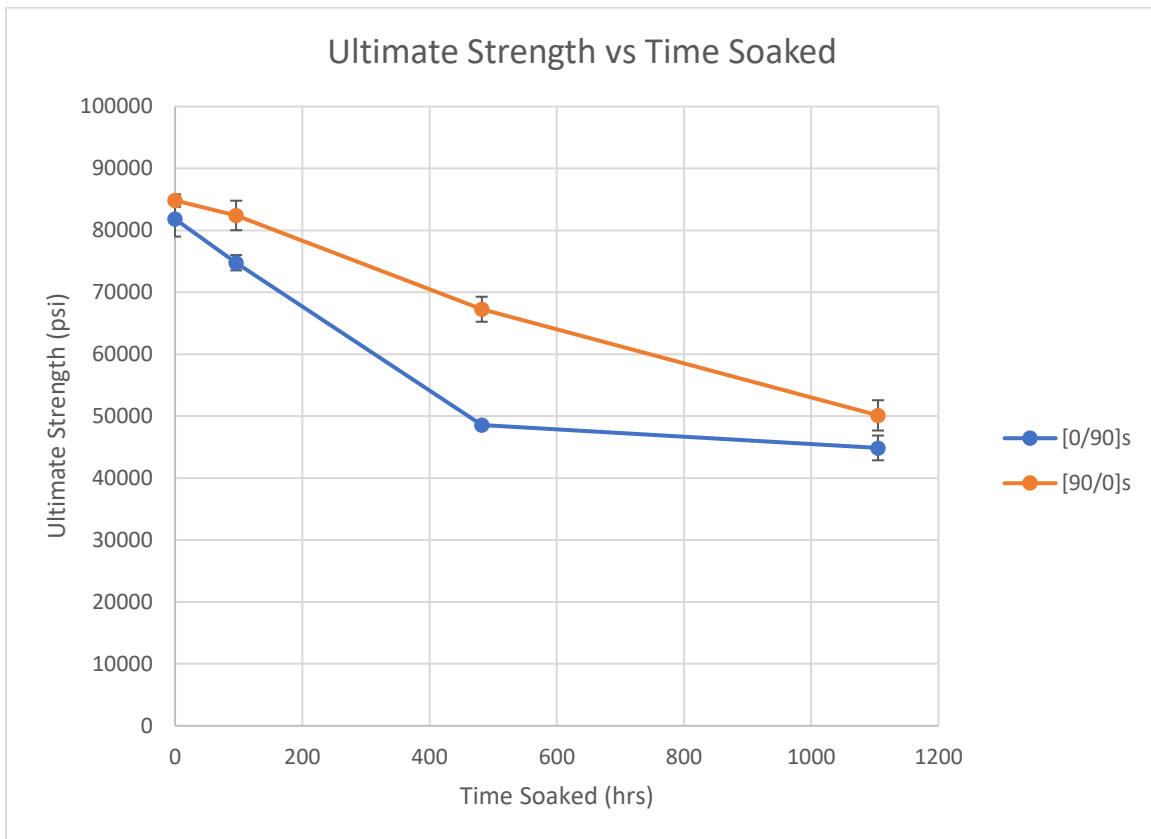


Figure 90. Ultimate strength vs time soaked for $[0/90]_s$ and $[90/0]_s$ coupons. Note: five tests performed for each layup at each time step.

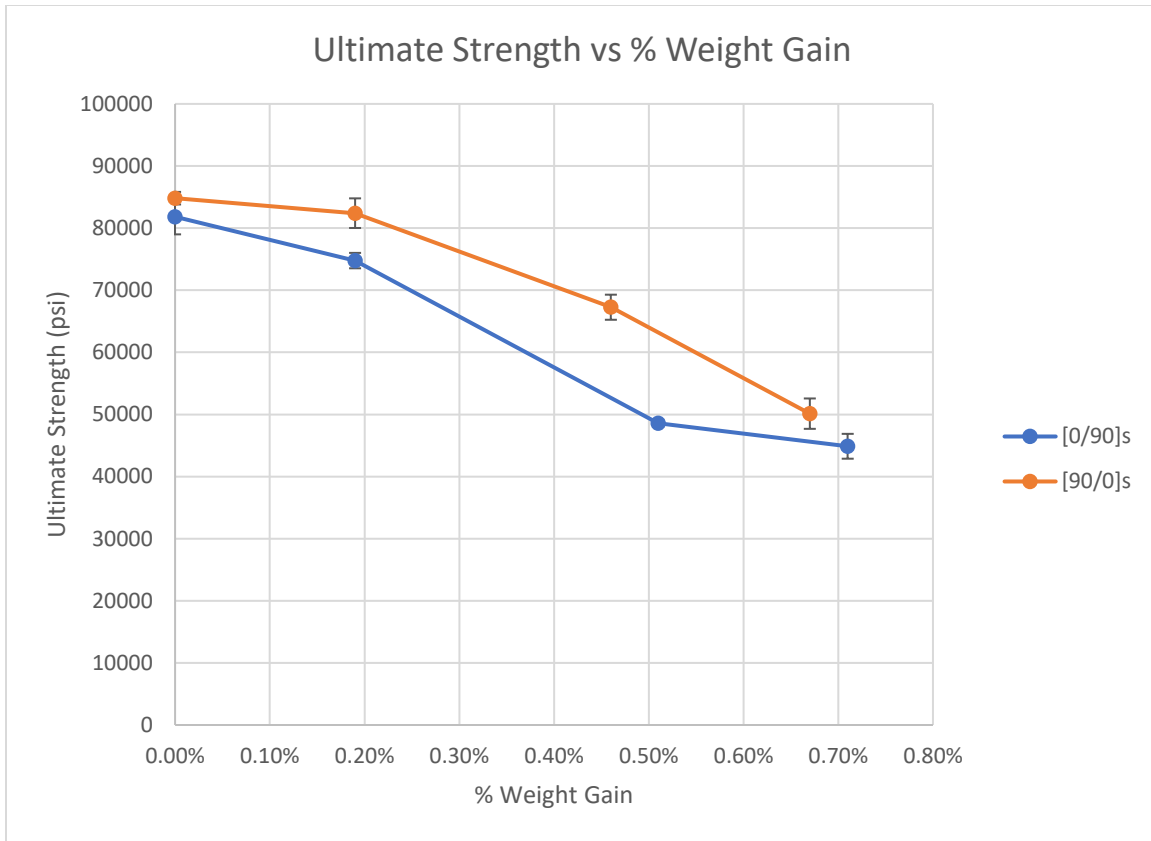


Figure 91. Ultimate strength vs % weight gain for [0/90]_s and [90/0]_s coupons. Note: five tests performed for each layup at each time step.

As expected, the [0/90]_s samples saw a larger decrease in the first part of the moisture saturation curve than the [90/0]_s samples as the primary load bearing plies were subjected to the moisture first. The full saturation data points are not in the charts as they have not been able to be completed yet. The samples are still undergoing conditioning and are expected to be complete in a couple months. The trend for the 0.6% and 0.8% moisture sample sets shows that the samples are approaching the same value again as expected.

As discussed above, this is a simple extension of the Fickian diffusion laws but it has the potential to be very important to MHK designers. In traditional composite design, the stiff plies are placed on the outside to maximize the bending strength they provide to the structure. The results above provide another consideration as it may be beneficial to design structure with sacrificial layers on the outside. These layers would protect the load bearing plies from significant degradation for a significant amount of time. Moisture detection methods could be installed as well allowing repairs to the surface to be completed prior to the primary plies being damaged.

3.4.2. AE Data

Acoustic emission testing was utilized in the analysis of the tests to explore the specific mechanisms affecting the strength degradation. Unfortunately, the data collected did not add any value to the discussion due to unforeseen circumstances. The stacking sequence of the layup influences the acoustic emission signature significantly. This was supported by the results in this study as the number of events in each bin was significantly different for the two layups in the control set. The

[90/0]_s samples exhibited primarily matrix cracking while the [0/90]_s samples had a more varied signature. The summary of the control samples can be seen below in Figure 92.

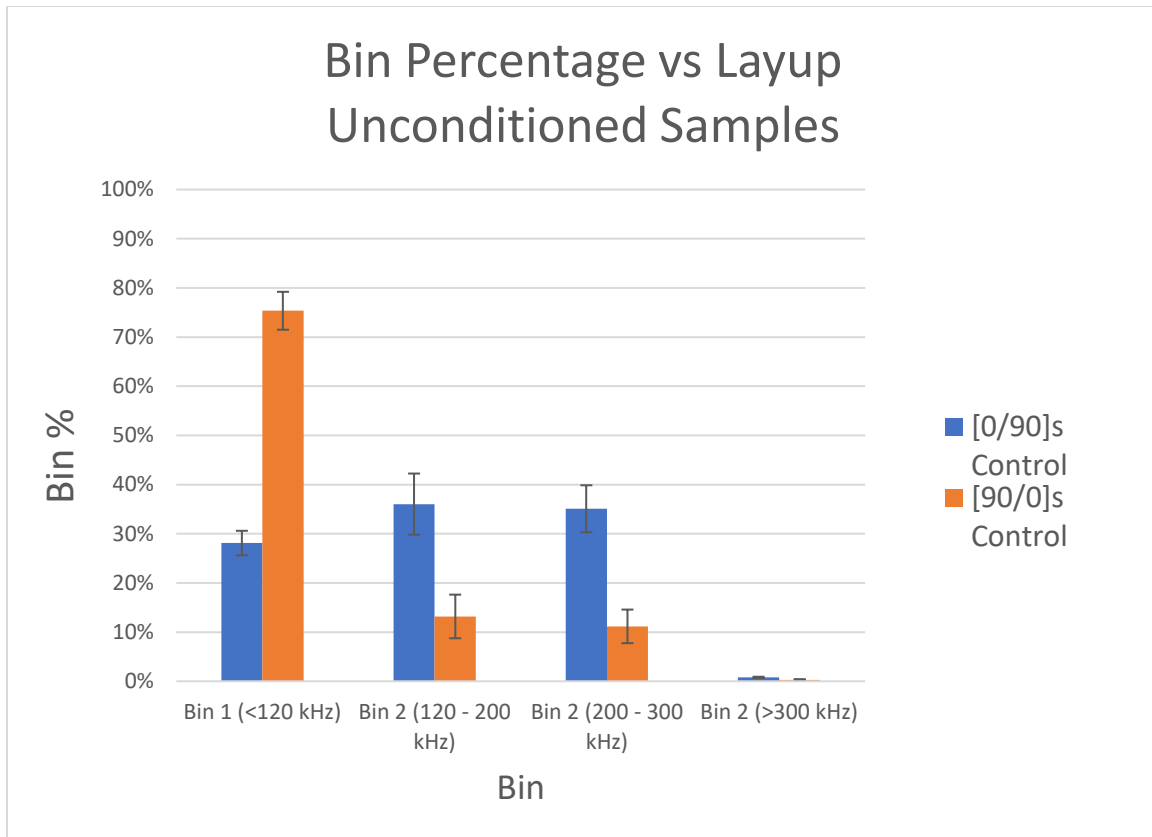


Figure 92. Bin percentages for both layups in the control set

As seen above, there is a significant difference between the two layups tested, even within the unconditioned control samples. The question arises as to whether this effect is caused by a difference in the failure of the material, or how the elastic waves are perceived by the sensors. As both layups have the same theoretical strength in the tensile direction, it is assumed that this effect is due to the AE signals. During testing of these samples, the 90-degree plies build up a lot of damage prior to final failure of the coupon. This damage begins occurring at approximately 0.4% strain. It is likely that the 90-degree plies being in direct contact with sensors is skewing the number of events towards matrix cracking. The sensors are picking up the damage in the transverse plies first due to the proximity and then shutting out the other damage occurring further within the material. Further examples of this effect can be seen below in Figure 93 and Figure 94.

Unfortunately, this effect causes the AE data for the two layups to not be able to be compared. The relative change in the percentage of the events in each bin was sought after in these tests. As the control samples do not show similarity, conclusions cannot be drawn from the changes in each layup at this time. Future work will explore this effect as the reasons for it are currently unknown.

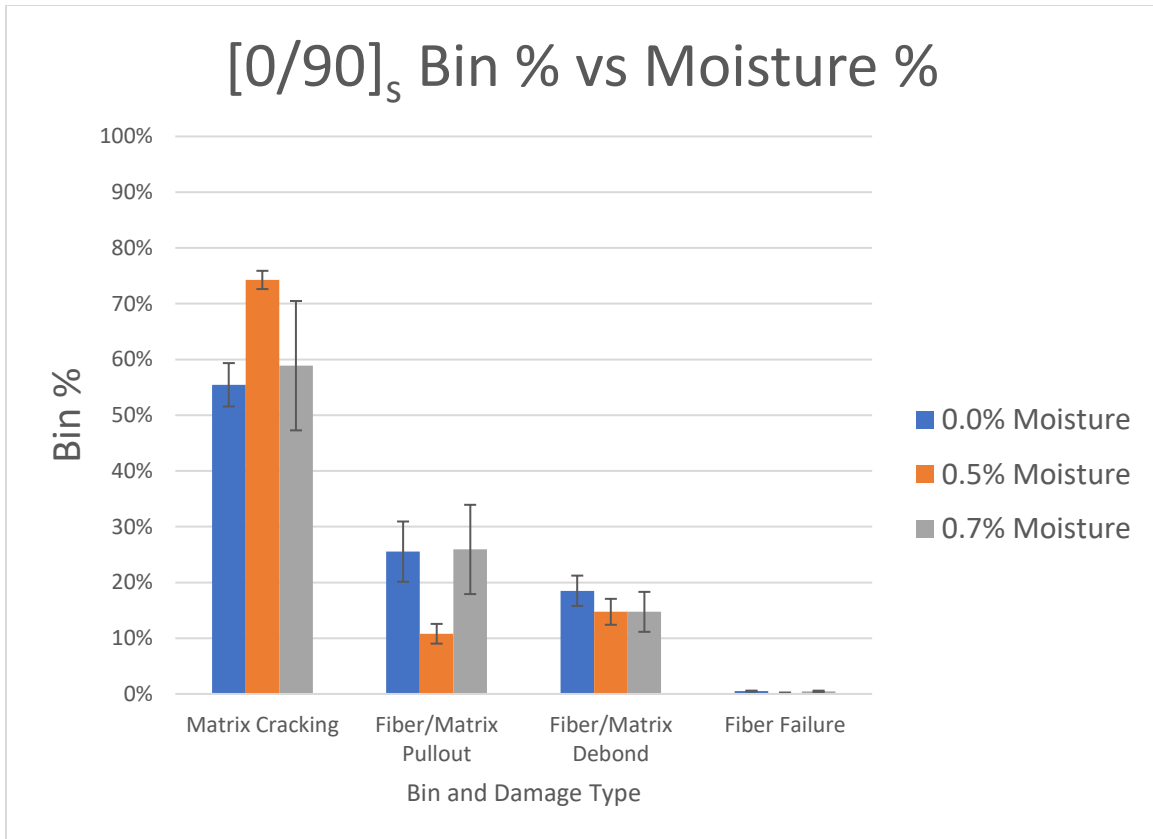


Figure 93. Percentage of AE events in each bin for [0/90]_s samples, varying moisture percentage.

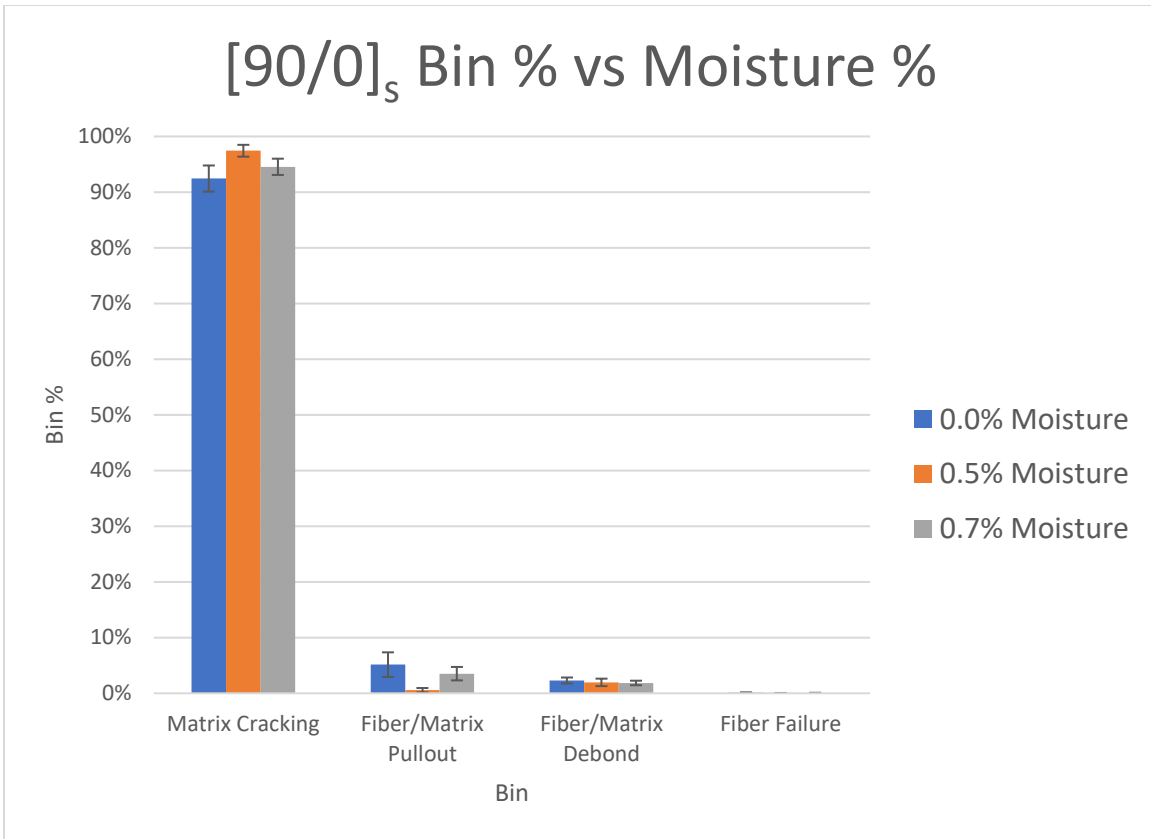


Figure 94. Percentage of AE events in each bin for [90/0]_s samples, varying moisture percentage.

3.5. Conclusions for Off-Axis Plies and Stacking Sequence

Strength reductions seen in off-axis epoxy/fiberglass laminates were consistent and in line with previous unidirectional results. The six laminates tested provided a breadth of strength values at fiber angles not normally tested. Both the unconditioned and saturated ultimate strengths are directly applicable to industry. Preliminary MHK designs will need accurate strength values for both conditions to ensure proper durability throughout device lifetime. This research also began to expand test data into mechanical analysis with a broad application to potentially minimize future mechanical testing required. However, interactive failure criterion did not adequately describe the failure stresses seen in the experimental results. The inconsistencies were present in the prediction of the unconditioned samples and are indicative of deficiencies in off-axis prediction methods. The amount that each lamina strength value is contributing to the laminate strength is unknown and makes further classification of strength reduction difficult.

Further analysis was completed to understand the strength reductions on a micromechanical level. Acoustic emission analysis was performed and provided a unique insight into a potential change in damage progression due from moisture inclusion. Matrix cracking damage events, picked up by the AE system, began to accumulate at earlier points prior to failure in saturated samples. In unconditioned samples, fiber/matrix debond damage events start happening before or at a similar time to matrix cracking. The change in damage progression within the laminate due to the inclusion of moisture complicates the mechanical analysis as well. The extent to which each lamina strength is contributing to the laminate strength likely changes in addition to the change in damage progression. This information combined with the mechanical analysis points towards interply matrix regions as a key area for future study. This region of matrix material is often subjected to large shear stresses in off-axis laminates.

Partial saturation testing was successful in extending the importance of stacking sequence on the evolution of strength reduction. This idea is novel in composites design as the primary load bearing plies are typically placed on the outside of a laminate. The research presented above challenges this principal. In situations where damage to the outside of the MHK device occurs, it may be beneficial to have sacrificial layers exposed to the marine environment to protect the primary plies.

Acoustic emission analysis of partial saturation testing was inconclusive. The difference in the two layups resulted in the frequency bin percentages varying significantly between the control sets. Analysis was not able to be completed into how damage mechanisms evolved throughout absorption as this effect outweighed any other trends. However, it did reveal the effects of stacking sequence on the peak frequency of events, which could be investigated further in future work.

4. HYGROTHERMAL AGING AND ACOUSTIC EMISSION STUDY OF DIVERSE MATERIALS FOR MHK APPLICATIONS

4.1. Material Summary

The MSU composites group and Sandia National Laboratories solicited various industry contacts to provide composite materials for mechanical characterization which are applicable for MHK devices. A summary list of the materials provided is shown in Table 20. Materials were received in plate and coupon form.

Table 20. Summary of materials included in MHK study.

LABEL	Resin	Fabric Info	Layup	Volume Fraction
J1	Eastman Copolyester 5011, PETG	Vectorply E-QX 4800	[0/45/90/-45]4	53.8
J2	Derakane 470 HT-400 VE	Vectorply E-QX 4800	[0/45/90/-45]4	54.6
J3	Applied Poleramic SC18	Vectorply E-QX 4800	[0/45/90/-45]4	53.6
J4	Derakane 470 HT-400 VE	OCV WR27TW	[(0/90/)(45/-45)]4	58.4
J5	Applied Poleramic SC18	OCV WR27TW	[(0/90/)(45/-45)]4	59.1
J6	Applied Poleramic SC18	TPI 4582 (2x2 twill), T700 12K 670 gsm	[(0/90/)(45/-45)]4	60
J7	Applied Poleramic SC18	Vectorply C-QX 2300, T700 12K Quad	[(0/45/90/-45]4	59.5
J8	Derakane 470 HT-400 VE	TPI 4582 (2x2 twill), T700 12K 670 gsm	[(0/45/90/-45]4	60
CE1	Pro-set INF 114/211	Zoltek UD600, E-BX 1700	[(+45/-45)g/0c]s	55
CE2	Pro-set INF 114/211	Vectorply CLA 1812, E-BX 1700	[(+45/-45)g/0c]s	55
CE3	Hexion RIMR 035c/RIMH 0366	Zoltek UD600, E-BX 1700	[(+45/-45)g/0c]s	55

Table 20 continued

LABEL	Resin	Fabric Info	Layup	Volume Fraction
CE4	Hexion RIMR 035c/RIMH 0366	Vectorply CLA 1812, E-BX 1700	[(+45/- 45)g/0c]s	55
CE5	Crestapol 1250PUL urethane Acrylate	CLA 1812, E-BX 1700	[(+45/- 45)g/0c]s	55
CE6	AME 6001 VE +1.5% MCP	ELT-2900, E-BX 1700, ELT-2900	[0/+45/-45/0]	55
N1	Elium	JM 086 - 4 layers	[0b]2s	56.7
P1	PP	E-glass w/AMB	[0/90]3	33.6
P4	PA6	E-glass	[0/90]3	34
P5	PA11	E-glass	[0/90]3	47.6
P6	PET	E-glass	[0/90]3	49.5
P9	PETG	E-glass	[0/90]3	37.3
P11	HDPE	E-glass	[0/90]3	38.8
P13	PP	E-glass	[0/90]3	38

4.2. Experimental Methods

4.2.1. Sample Preparation

No composites used in this study were manufactured at MSU, and manufacturing details are not explicitly known. Surface finish, materials used, and other characteristics such as volume fraction can be indicative of how a laminate was made. Using these indications, it is suspected that J1-8, CE1-6, and N1 were made by hand layup and vacuum assisted resin infusion, a method described in the background of this work. The remaining materials (P series) were made by heated press resin infusion. Wherein, thin sheets of the thermoplastic resin are alternated into fiber layup and a heated tool applies pressure, melting the resin, and forcing infusion.

Coupons of each system were cut with a water lubricated diamond abrasion saw to target geometries of 200 x 25mm. After cutting thickness and width measurements were made of each coupon with digital caliper and recorded. These dimensions were used in calculating modulus and stress after testing. Mass of each coupon was also measured with a digital scale with resolution of 1E-3 grams. Mass of each coupon was used in calculated moisture uptake. For J1-8, CE1-6, and N1, tabs were adhered with epoxy to the gripping are at each end, leaving a total gage section of 90 mm. The remaining systems (P1,4,5,6,9,11, &13) were left without tabs.

4.2.2. Conditioning and Moisture Uptake Measurements

A portion of the samples from each material system were conditioned in ASTM D1141 (without heavy metals) synthetic seawater (SSW) at 50°C to complete saturation. SSW was created by mixing the prescribed quantity and amounts of salts with distilled water. Previous research at MSU found that salt buildup in SSW can affect moisture uptake measurements. Despite this added complexity, SSW was selected to maintain consistency and comparability to a study conducted by Dan Samborsky on these same materials. Samples were stored in a sealed bath of SSW inside a temperature-controlled oven. Samples were removed from the oven at arbitrary sampling intervals to be dried of surface moisture and weighed for water uptake. These measurements were made with the same digital scale used to take initial measurements (1E-3 gram resolution). After weighing, samples were returned to the water bath in the oven.

Moisture uptake measurements for this study were taken from tabbed samples. This method is not recommended as tabbing material and epoxy adhesive absorb moisture at different rates than any of the materials here. It is best practice to take measurements from un-tabbed samples which have been conditioned in the same bath alongside tabbed samples. The technician conducting this study was not aware of these effects at the outset, and there were not enough materials or time to correct this mistake after it was realized.

4.3. Results

4.3.1. Moisture Absorption

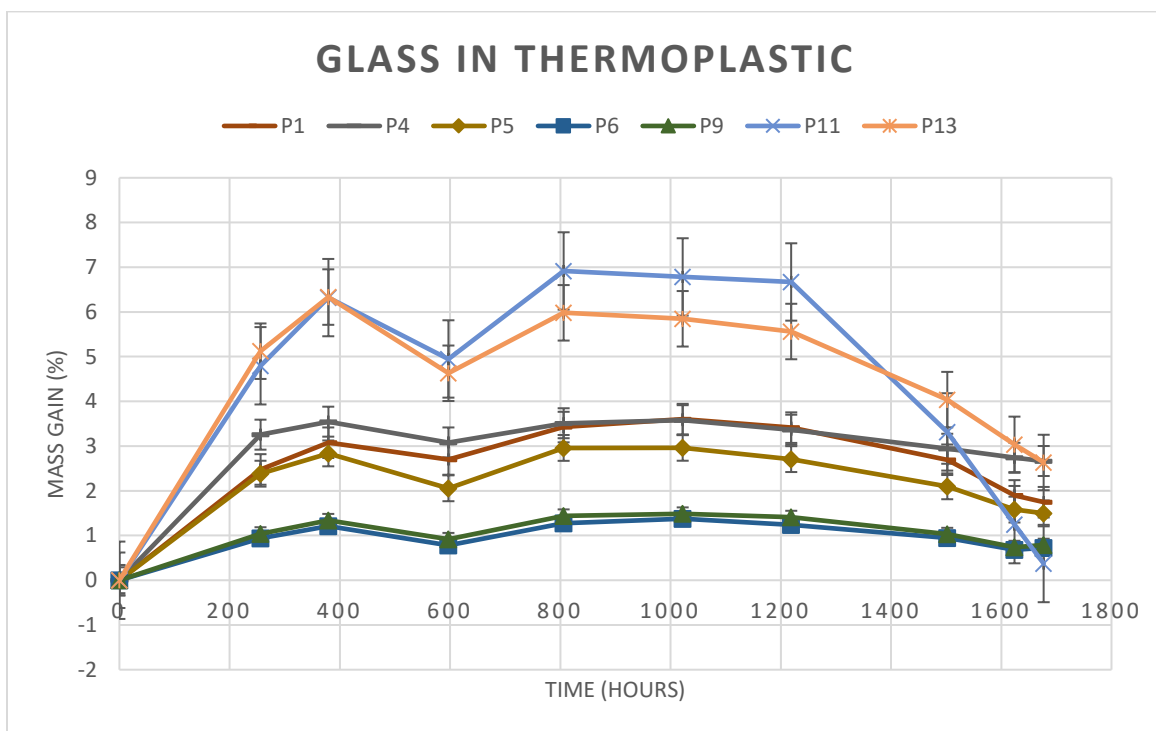


Figure 95. Mass uptake measurement curves for thermoplastic matrix systems.

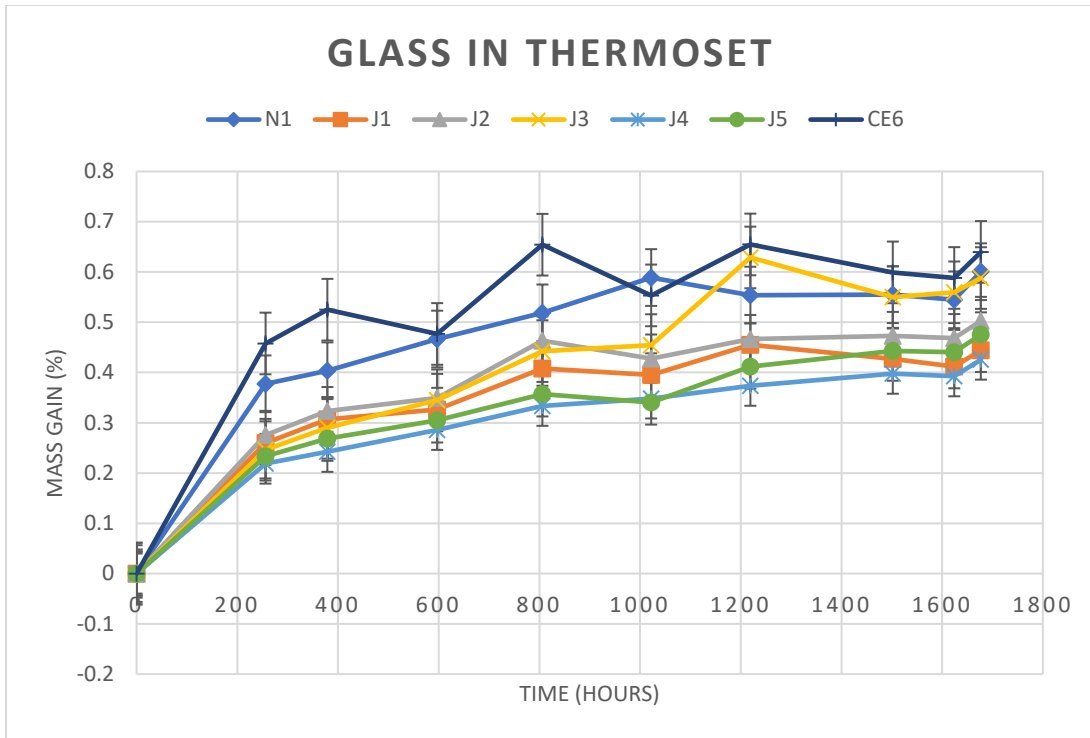


Figure 96. Mass uptake measurement curves for thermoset matrix systems.

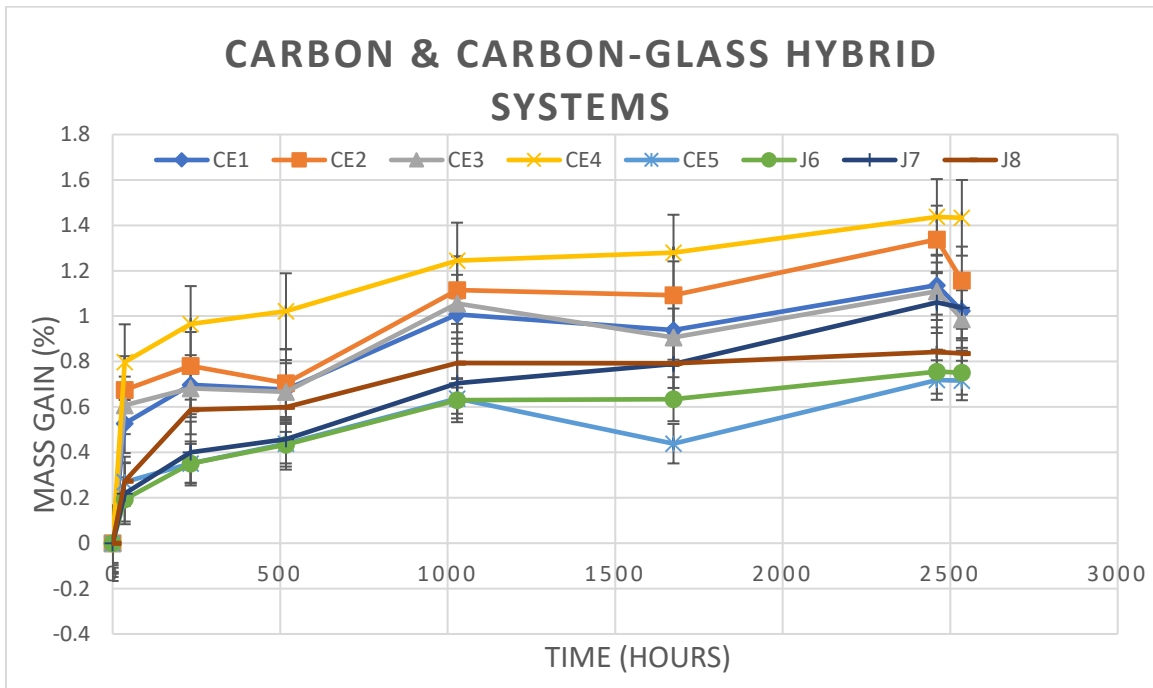


Figure 97. Mass uptake measurement curves for carbon and carbon-glass hybrid systems.

Considering these saturation curves (Figure 95, Figure 96, and Figure 97), significant inaccuracies occurred in moisture uptake measurements. The true cause of these imprecisions is not known but is likely due to inconsistent procedure. It is important to allow plenty of time for surface moisture to

evaporate from the samples before weighing, especially for the thermoplastic samples as they have significant surface porosity. Varying amounts of surface moisture between sampling times would cause the sharp increases and decreases in moisture.

Referring to Figure 95, it is interesting to note the consistent decrease in mass past approximately 1000 hours. Because the trend is smooth, it is unlikely this is a measurement artifact. There are multiple possible causes for this mass loss. Hydrolysis could have occurred in the matrix resulting in subsequent leaching of lysed monomers into the water bath. This process is commonly called 'leeching,' and it is the most likely culprit. Another possibility is loss of discrete particles or flakes into the water bath. Plastic and fiber near edges and corners would easily crack and slough off into the water bath as a result of swelling and/or handling during mass measurements. Still another, possibility is biological degradation. Bacterial contamination of the water bath is common. Biofilm growth in/on samples could be acting to degrade the polymer and expel byproduct into the water bath. However, this is especially unlikely as bacteria capable of breaking down these polymers are highly rare, and the process is very slow. Hydrolysis in combination with loss of discrete particles is the most likely possibility. It can be confidently stated that moisture was absorbed into these samples. Therefore, testing these samples does achieve the stated goal of investigating the effects of moisture absorption on mechanical properties and acoustic emission.

Moisture absorption between laminates with the same matrix should be similar, while considering volume fraction effects. This is not fully reflected in the saturation data. Starting with the thermoplastic matrices, there is a significant difference between P1 and P13, which are both polypropylene (PP) materials, but P1 has an unknown additive called AMB, which has shown here to reduce moisture absorption. Nylon 6 is shown to absorb similar amount to Nylon 11. The mass uptake for P4 (PA6) is slightly greater than P5 (PA11), but P4 has a lower volume fraction and should therefore absorb more moisture. So, the difference is insignificant. There is no discernable difference between polyethylene terephthalate (PET) and polyethylene terephthalate glycol (PETG), which is P6 versus P9. Finally, high density polyethylene (HDPE) in P11 absorbs the most water and is shown to lose the most mass near the end of conditioning. This is unexpected as HDPE is known for having good performance in water and a lower moisture permeability than many of the other plastics included here [139].

The thermoset matrix laminates absorbed less water than the thermoplastics, which follows expectations. Comparing between thermosets, all laminates with Applied Poleramic SC18 (J3, J5, J6, and J7) absorb similar amount of moisture. Laminates of Derakane vinyl ester have similar absorption between glasses (J2 & J4), but the carbon system, J8, absorbed more water and has a higher volume fraction. This increased absorption would suggest a fabric/fiber effect, but the trend does not appear in comparing to the Applied Poleramic resin. If there was an effect, J6 should have absorbed more than J3, J5, and J7 because it has the same fabric as J8, but this is not the case.

There does seem to be a fabric effect in the CE series. CE1 and CE3 both use the same Zoltek UD600 fabric and absorb more moisture than their counterparts, CE2 and CE4 respectively. This effect may arise from a preferred diffusion path at the interphase where the sizing, specific to that fabric, bonds to the matrix. The impact of sizing could be confirmed by contact angle measurement. Between plastics used in the CE systems, Pro-set INF and Hexion RIMR 035/0366, there is not definitive difference in moisture absorption. There can be no comparison made between these and the J series, as the fiber volume fractions are significantly different and uptake measurements are very inaccurate.

4.4. Mechanical Properties

Table 21. Mechanical data summary for materials included in MHK study*

Label	Conditioning (% Moisture)	Modulus (GPa)	Ultimate Stress (MPa)	Failure Strain (%)
J1	0.00	21.6	283	1.79
	0.44	19.4	324	2.10
J2	0.00	22.3	365	2.55
	0.50	22.4	339	2.28
J3	0.00	22.5	330	2.53
	0.59	21.5	196	1.13
J4	0.00	22.6	282	2.29
	0.43	25.4	301	1.95
J5	0.00	24.5	293	1.87
	0.48	24.4	291	1.75
J6	0.00	48.3	426	1.51
	0.85	43.6	465	1.72
J7	0.00	41.5	703	2.18
	1.14	41.5	550	1.57
J8	0.00	35.3	493	2.00
	0.84	35.4	510	1.77
CE1	0.00	53.6	781	1.50
	1.02	54.0	742	1.35
CE2	0.00	56.8	780	1.43
	1.44	48.1	695	1.56
CE3	0.00	48.4	739	1.58
	1.13	49.9	643	1.30
CE4	0.00	53.8	773	1.52
	1.07	51.4	748	1.54
CE5	0.00	53.1	744	1.41
	0.79	52.4	678	1.40
CE6	0.00	29.5	626	2.65
	0.64	30.7	621	2.54

Table 21 Continued

Label	Conditioning (% Moisture)	Modulus (GPa)	Ultimate Stress (MPa)	Failure Strain (%)
N1	0.00	36.6	852	2.82
	0.60	41.7	622	1.50
P1	0.00	15.1	321	2.29
	1.75	15.7	230	1.55
P4	0.00	22.2	457	2.33
	2.67	20.5	267	1.33
P5	0.00	17.9	366	2.21
	1.49	18.7	284	1.65
P6	0.00	17.5	395	2.74
	0.73	16.1	313	2.24
P9	0.00	17.1	395	2.70
	0.79	15.6	282	2.05
P11	0.00	14.9	248	1.90
	0.37	15.3	243	1.71
P13	0.00	12.3	277	2.58
	2.63	13.2	229	1.76

* averaged values presented from multiple coupons.

The thermoplastic materials had the lowest moduli and low strength. Moduli in these systems are matrix and volume fraction driven. The stiffest and softest were P4 (PA6) and P13 (PP) respectively. P4 was also the strongest P1 and P13 shared a matrix material (PP), but P1 incorporated an unknown additive called AMB, which increased the modulus and strength of the composite. Strength of the other materials did not follow any clear or discernable pattern without knowing the unreinforced strength of the matrix and the bonding quality to the fibers. Their failure strains were lower than their glass counterparts, which is likely a bond strength effect, as thermoplastics are difficult to bond to glass. Reduced bond strength will reduce damage tolerance. Examples of P series failed coupons are shown in Figure 98.

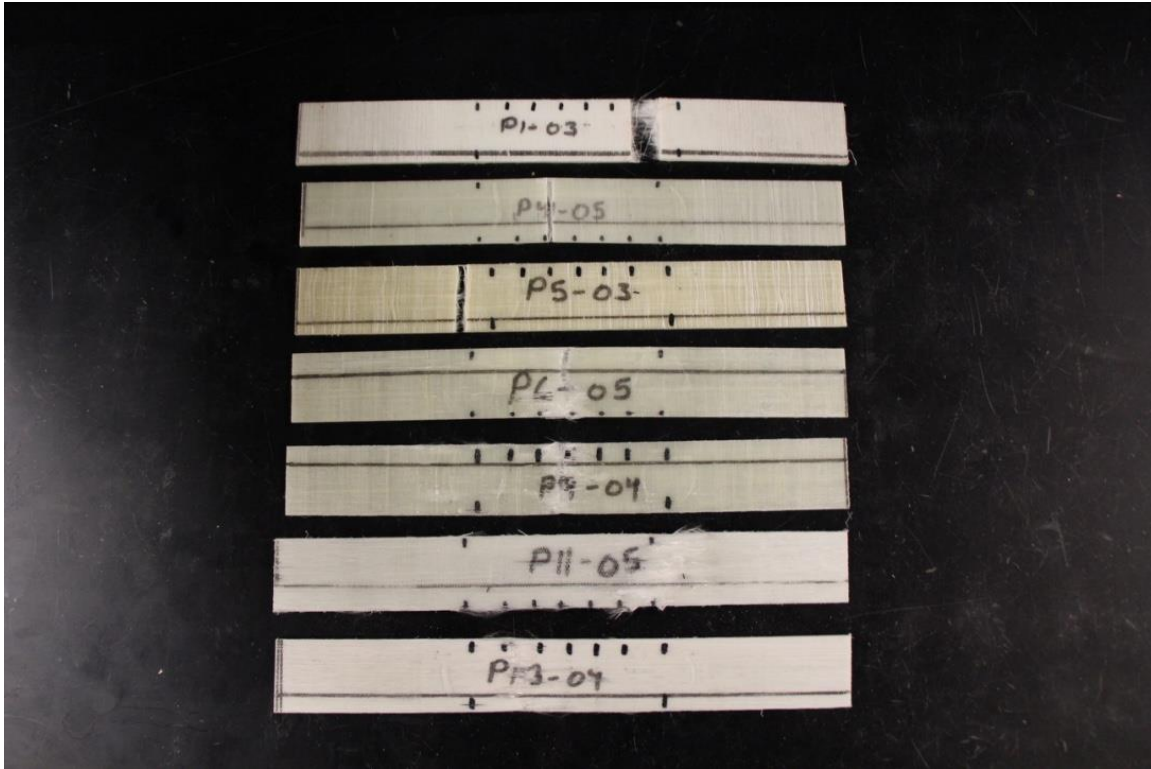


Figure 98. Examples of failed coupons of MHK study materials (P series) showing common failure modes for these materials.

J series materials had relatively low moduli and strength and erratic strain to failure. Quasi-isotropic laminates will have lower stiffness and strength, but results are more a consequence of the low quality. Porosity and dry spots were prevalent. These defects produced audible cracking and visible delamination during testing, well before final failure. This indicates a relatively high damage tolerance, but the appearance of such significant damage early in a static test does not bode well for fatigue testing or environmental durability. Early cracking and delamination will propagate and lead to early failure in a fatigue test and act as expedited diffusion paths for moisture in a humid environment. Examples of failed coupons are shown in Figure 99.

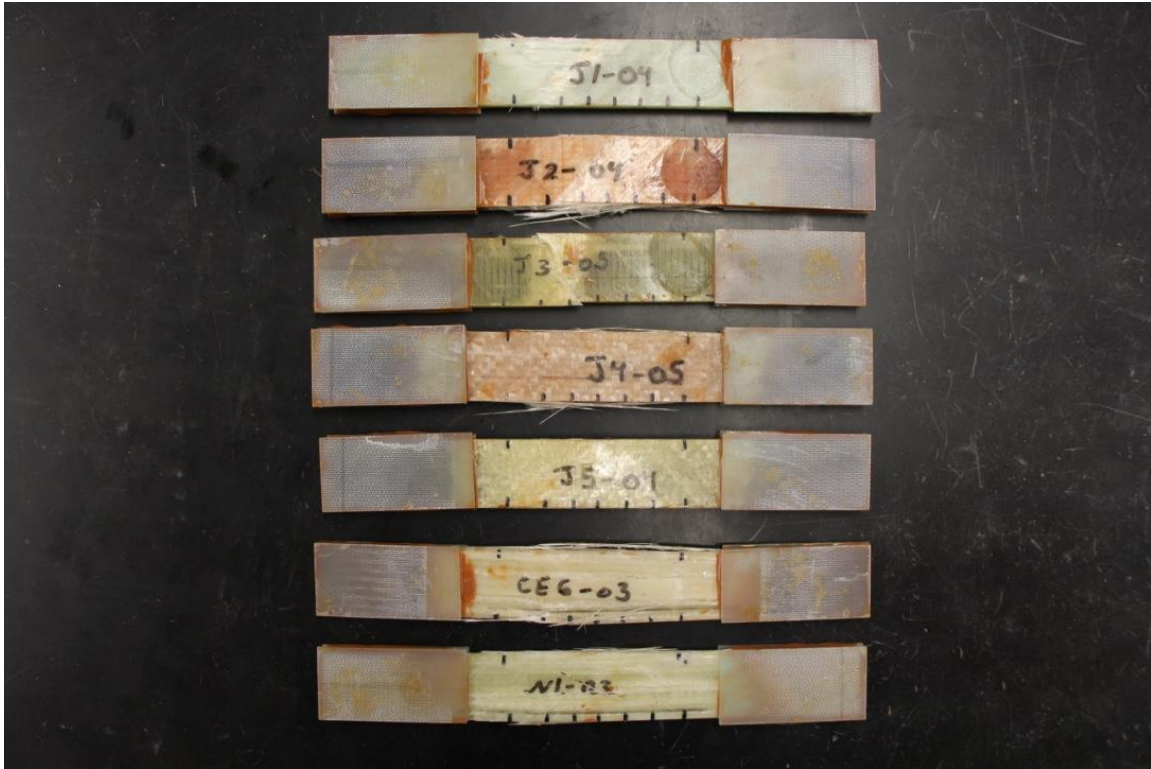


Figure 99. Examples of failed coupons of MHK study materials (J1-5, CE6, & N1) showing typical failure modes.

CE series were high performing laminates with high moduli, strength, and strain to failure for carbon reinforcement. These hybrid materials, composed of unidirectional carbon and +45 glass, performed higher than the other carbon laminates (J6-8) even with lower volume fractions. A contributor to these high values is a high proportion of 0-degree fibers. The best performing laminate was N1, with high modulus, strength, and strain to failure, though it was the most effected by moisture uptake in strength and strain to failure.



Figure 100. Examples of failed coupons of MHK study materials (J6-8 & CE1-5) showing typical failure modes.

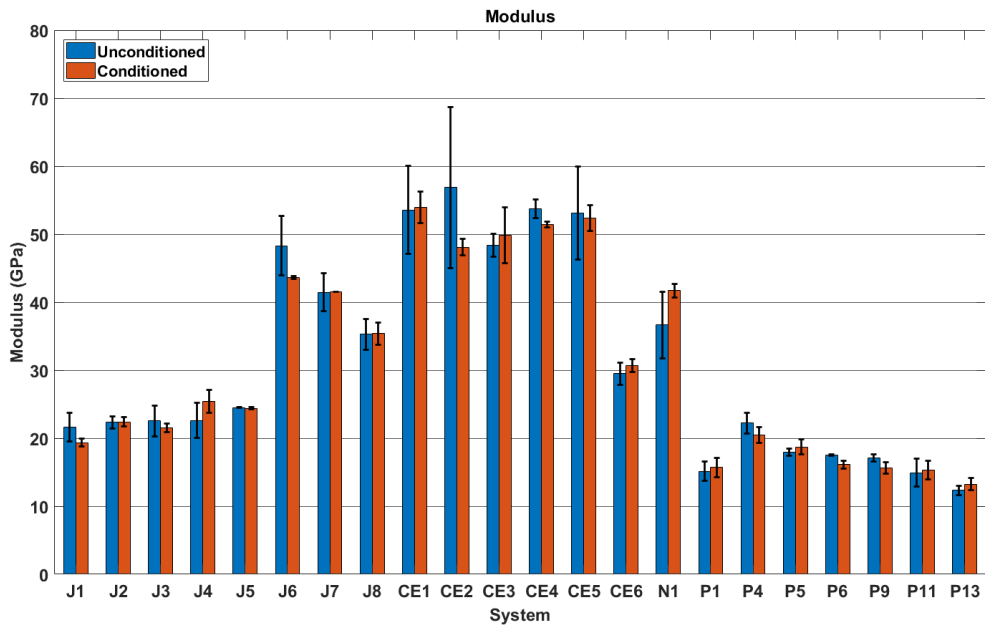


Figure 101. Summary of modulus degradation from conditioning. Error bars are range.

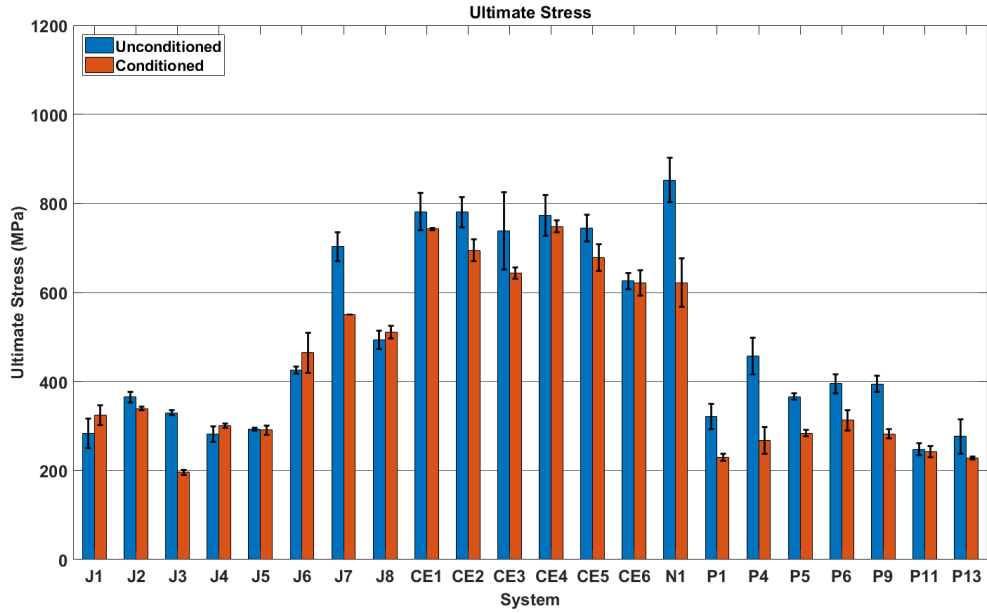


Figure 102. Ultimate strength degradation from conditioning. Error bars are range.

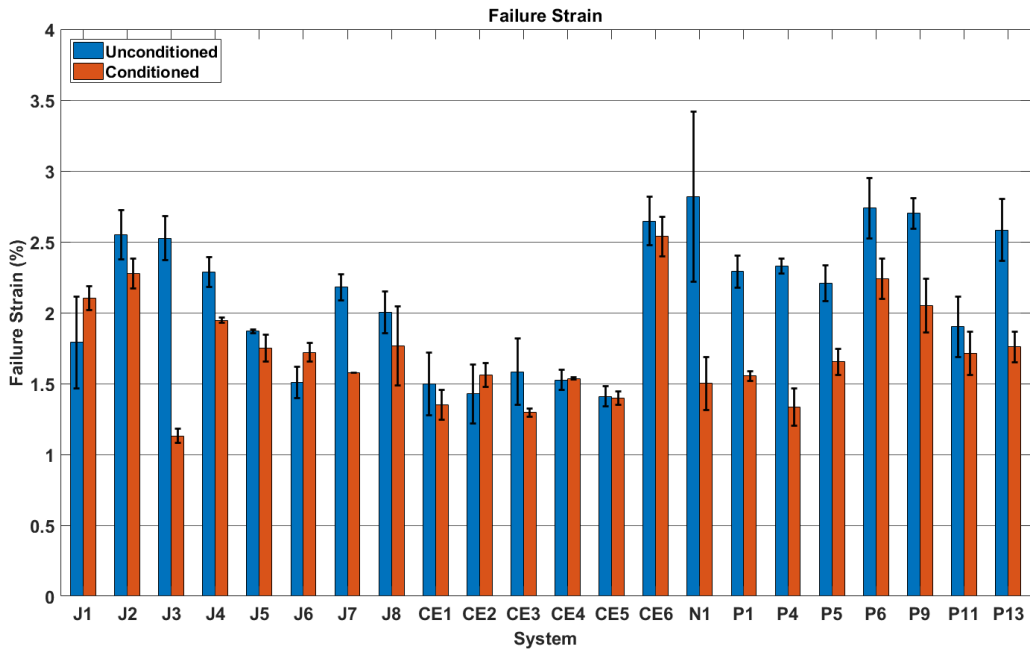


Figure 103. Failure strain degradation from conditioning. Error bars are range.

Considering scatter, there is little or no significant effect of conditioning on modulus of any laminate. This is surprising because water is a known plasticizer of polymers and should therefore soften the matrix. This effect may be minimal on the scale of a laminate (amount of plastic versus reinforcement), or the effect is not pronounced at only partial saturation. The proportion of saturation is not exactly known. From the shape of the saturation curve, it can be asserted that these coupons are more than 80% of complete saturation.

There is a general downward trend of strength and failure strain with conditioning. This concurs with previous research at MSU and outside research [131], [138], [140-145]. Thermoplastics show the greatest reduction in strength and failure strain. Scatter in these data make it impossible make further comparison of relative mechanical effects between fabrics and matrix materials.

4.4.1. Acoustic Emission

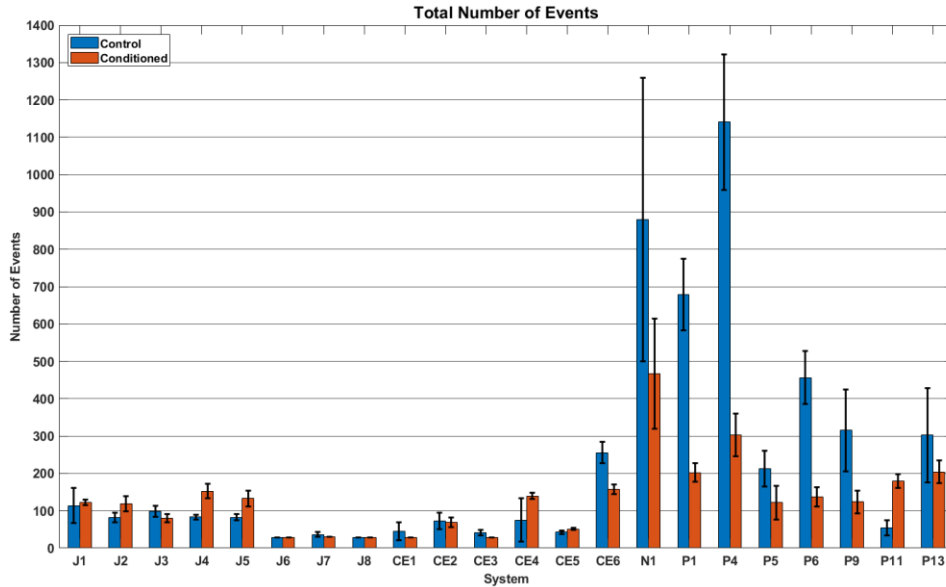


Figure 104. Mean number of AE events for MHK study materials showing variability/consistency and the greater number of events from thermoplastics.

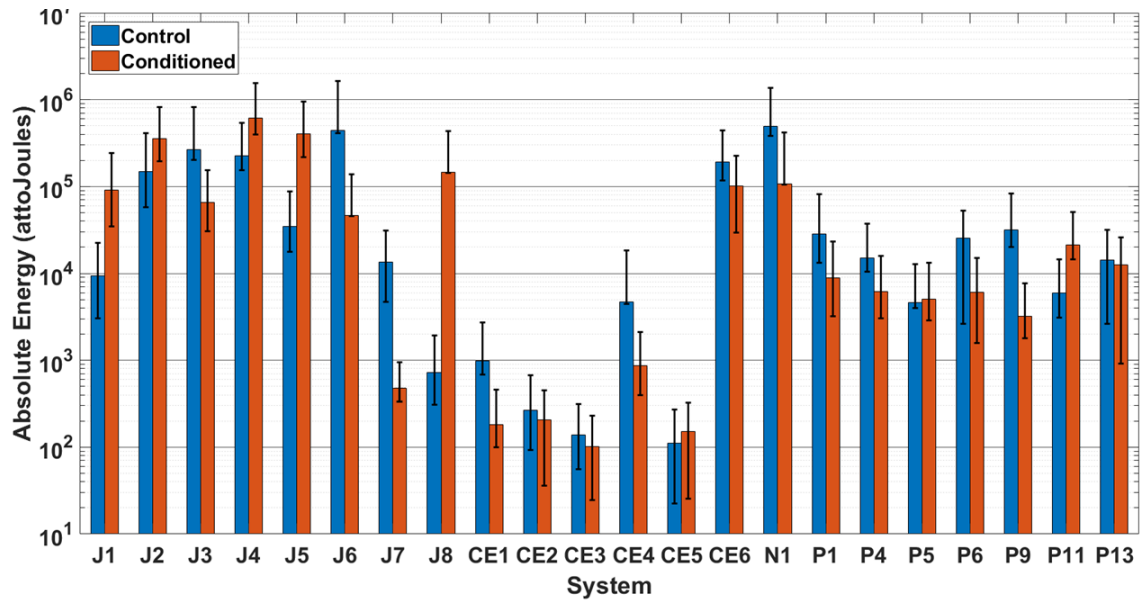


Figure 105. Mean absolute energy per AE event showing variability.

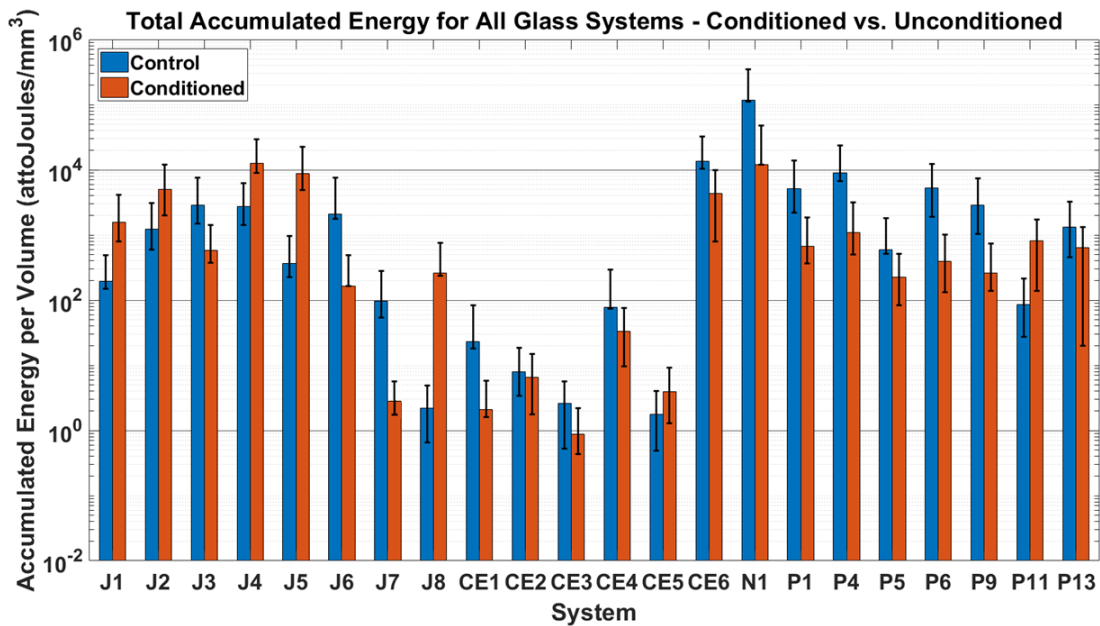


Figure 106. Mean accumulated absolute energy per coupon showing variability.

Thermoplastics are found to produce fewer events with conditioning. In all P-series systems excluding P11, accumulated energy release also decreased. Changes in mean absolute energy per event were varied and mostly indeterminate. These changes combined with the loss in ultimate strength indicate increased matrix ductility (plasticization) for most thermoplastics. P11 is anomalous and puzzling, with no real mechanical effects and significant increase in AE activity.

Energy activity effects present no overall, matrix-based, or fabric-based trends in the thermoset laminates. Most systems do not show changes in overall activity (number of events), and the changes in energy yield are erratic. Some materials release more energy with moisture uptake while some release less. Because there is no change in number of events, those changes that occur in accumulated energy are due to a change in mean absolute energy. Further study is required to determine the nature of changing energy release with conditioning.

4.4.2. Frequency Content

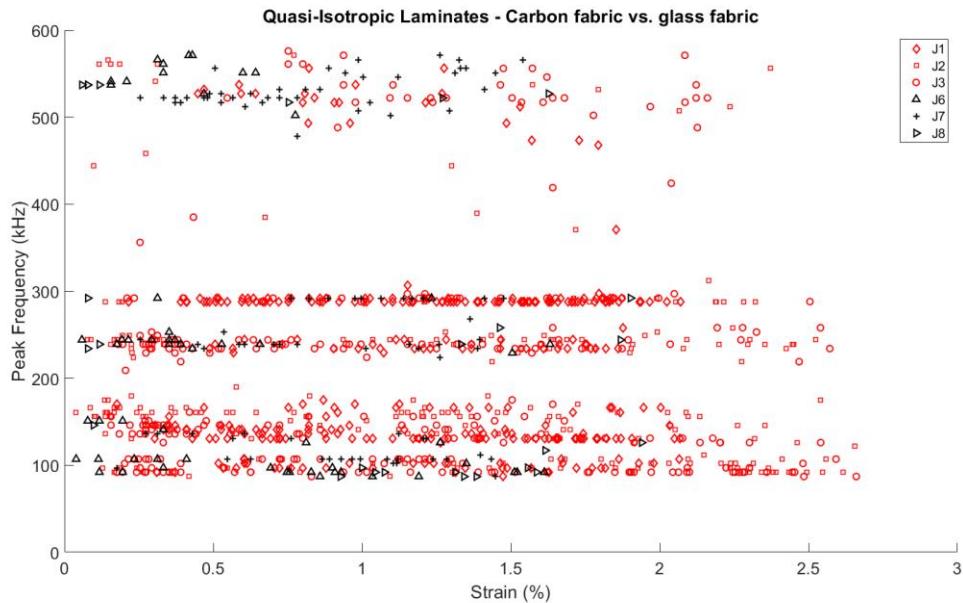


Figure 107. Peak spectral frequency versus strain for glass and carbon fabric quasi-isotropic laminates.

All materials are found to have similar but non-identical frequency content. The most general comparison to be made in this material set is carbon versus glass reinforcement. Shown in Figure 107 is a scatter plot of peak spectral frequency versus strain for quasi isotropic laminates of comparable materials. That is J3, 5, 6, & 7 use the same matrix, AP SC18, but different fabrics, Likewise for J2, 4, & 8, using Derakane Vinyl ester but different fabrics. Inspecting this plot, there is no clear difference in frequency content on a reinforcement, fabric, or matrix level. Glass materials show more events between 120 and 200 kHz, but there are simply more events in the glass systems. The probability of event occurrence in this range for carbon materials is the same. This absence of a difference in frequency content between carbon and glass is unexpected because carbon much stiffer than glass and would be expected to produce higher frequency events. However, this result appears in previous research [105].

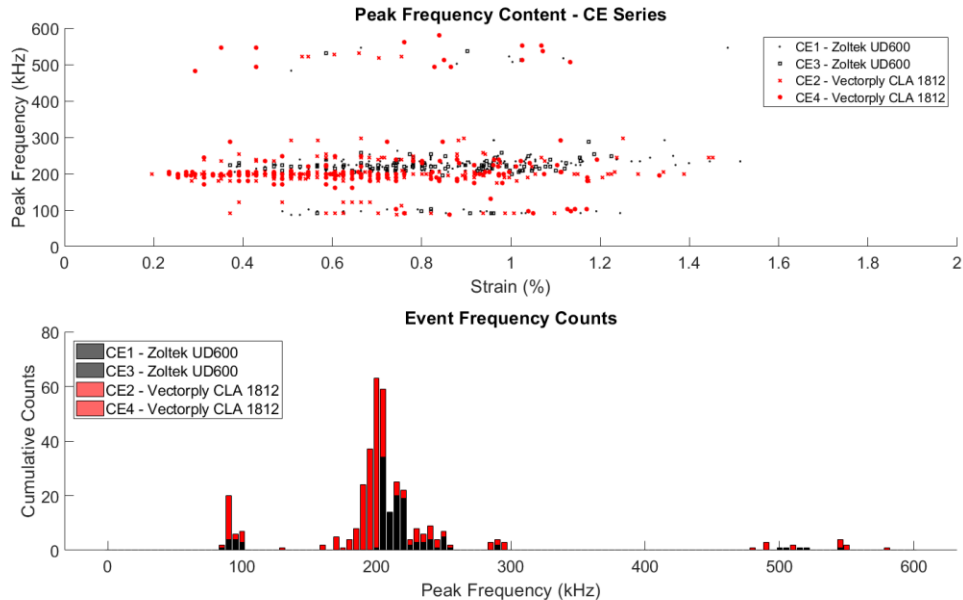


Figure 108. Peak spectral frequency versus Strain (Top) and cumulative peak spectral frequency histogram (Bottom) for CE1, 2, 3, & 4 showing frequency shift in interphase activity (~150-250 kHz).

Many more comparisons are made between similar layups. One result of these investigations was a shift in a sub-range of the mid-level frequency range associated with interphase failures. CE1 and CE3 use the same fabric (Zoltek UD600 with E-LT 1700) but use different resins. CE2 and CE4 also use the same fabric (Vectorply CLA 1812 with E-LT 1700) and difference resins. In comparing their frequency content based on fabric, there is a shift in the mid-range frequency band ~150-250 kHz associated with interphase failure. This shift appears to be fabric driven with the epoxy resins used for these materials. This assumes that the interphase activity seen here is from the longitudinal fibers, not the glass fibers. The glass fibers are the same biaxial fabric (E-BX 1700 [45/-45]). Because there is a frequency shift in two materials with the same angle-ply fabric and coupon geometry, it will be assumed that the activity originates from longitudinal carbon fibers. There is no appreciable difference in mechanical properties between the materials. So, it would be difficult to make an association with interphase strength and frequency.

4.5. Conclusions of Hygrothermal Aging and Acoustic Emission of Diverse Materials

Conducting frequency analysis of a diverse material set has provided valuable insight into the damage progression the differences in AE signals. Frequency shifts are observed to be a function of material, via interphase strength, layup, sensor sensitivity, AE timing parameters, and AE data acquisition system. It is also suspected that additional influences on frequency content originate in volume fraction, coupon geometry, and even coupon tabbing.

With these considerations, new frequency ranges were put forth to be associated with damage mechanisms. These frequency band centers and band widths have significant differences from commonly referenced publications in this field as well as previous researchers at MSU. The first is re-defining fiber pullout events to have higher frequency than fiber de-bond based on AE activity

between layups as well as the relationship between relaxation time material parameter and frequency. New frequency ranges were applied strictly to glass reinforcement material systems of this study. The ranges still generally apply to carbon reinforcement material systems, but new frequency content from carbon prepreg samples prohibit warrant further investigation. Ordering and ranges apply loosely to materials tested in other studies, but influences from AE data acquisition system, sensors, coupon geometry, and other factors make direct comparison impractical and inaccurate.

Mechanical properties of material types and layups yielded expected results. Reinforcement type, matrix material, and volume fraction are significant factors in stiffness and strength. Carbon fiber laminates are stiffer and stronger than glass laminates and exhibit lower strains to failure. Epoxy and other thermoset matrix materials will produce a stiffer and stronger laminates of comparable layups. Low fiber volume fraction will reduce mechanical performance, and layups with more fibers aligned along the coupons testing axis will result in higher stiffness and strength. Laminate quality is also found to be a major contributor to all mechanical performance. Fiber alignment, wetting out, and other good manufacturing practices are imperative to creating a high-quality laminate.

For those laminates included in the hygrothermal conditioning study, moduli across all systems was not significantly affected by conditioning. There is a significant downward trend of strength and strain to failure with conditioning, which is most accentuated in the thermoplastic systems. This concurs with previous research. Poor quality laminates were less effected by conditioning indicating that swelling stresses or micro damage induced by moisture uptake are less detrimental than issues created by poor manufacturing methodology.

REFERENCES

- [1] Springer. "Moisture Absorption and Desorption of Composite Materials." *Journal of composite materials* (1976)
- [2] Miller, David, John Mandell, Daniel Samborsky, Bernadette Hernandez-Sanchez, and Todd Griffith. "Performance of Composite Materials Subjected to Salt Water Environments." *2012 ALAA SDM Wind Energy Session*. (2012)
- [3] Su, Jun-Feng, Xin-Yu Wang, Zhen Huang, Yun-Hui Zhao, and Xiao-Yan Yuan. "Thermal conductivity of microPCMs-filled epoxy matrix composites." *Polymer Science*. 289. (2011): 1535-1542.
- [4] Chin, Joannie, Tinh Nguyen, et al. "*Sorption and Diffusion of Water, Salt Water, and Concrete Pore Solution in Composite Matrices*." (1998)
- [5] Gellert, E.P., and D.M. Turley. "Seawater immersion ageing of glass-fibre reinforced polymer laminates for marine applications." *Composites Part A: Applied Science and Manufacturing*. 30.11 (1999): 1259-1265. Web.
- [6] Barbero, Ever. *Introduction to Composite Materials Design*. 2nd ed. Boca Raton: CRC, 2011. Print.
- [7] Barjasteh, E., and S.R. Nutt. "Moisture absorption of unidirectional hybrid composites." *Composites Part A: Applied Science and Manufacturing*. 43.1 (2012): 158-164. Web.
- [8] Lundgren, Jan-Erik, and Peter Gudmundson. "A Model for Moisture Absorption in Cross-Ply Composite Laminates with Matrix Cracks." *Journal of Composite Materials*. 32.24 (1998)
- [9] Neumann, Shoshana, and Gad Marom. "Prediction of Moisture Diffusion Parameters in Composite Materials Under Stress." *Journal of Composite Materials*. 21.1 (1987): 68-80.
- [10] Perrin, F.X., Minh Hanh Nguyen, et al. "Water transport in epoxy-aliphatic amine networks - Influence of curing cycles." *European Polymer Journal*. 45.5 (2009): Web.
- [11] Wong, T.C., and L.J. Broutman. "Moisture Diffusion in Epoxy Resins Part 1. Non-Fickian Sorption Processes." *Polymer Engineering & Science*. 25.9 (2004): Web.
- [12] Fahmy, A.A., and J.C. Hurt. "Stress Dependence of Water Diffusion in Epoxy Resin." *Polymer Composites*. 1.2 (1980): 77-80. Web.
- [13] Haberman, Richard. *Applied Partial Differential Equations*. 4th ed. Upper Saddle River: Pearson Prentice Hall, 2004.
- [14] Pilli, Siva P., Kevin L. Simmons, et al. "A novel accelerated moisture absorption test and characterization." *Composites Part A: Applied Science and Manufacturing*. 40.9 (2009): Web.
- [15] Aronhime, Marc T., Shoshana Neumann, and Gad Marom. "The anisotropic diffusion of water in Kevlar-epoxy composites." *Journal of Materials Science*. 22. (1987): 2435-2446.
- [16] Verpoest, Ignaas, and George Springer. "Moisture Absorption Characteristics of Aramid-Epoxy Composites." *Journal of Reinforced Plastics and Composites*. 7.2 (1988): Web.
- [17] Broutman, L. J., and Gad Marom. "Moisture in Epoxy Resin Composites." *Journal of Adhesion*. 12.2 (1981): 153-164. Web.
- [18] Laurenzi, S., T. Albrizio, et al. "Modeling of Moisture Diffusion in Carbon Braided Composites." (2007)

- [19] Samborsky, Dan. (2012): *SNL/MSU/DOE Composite Material Fatigue Database*.
- [20] Leendert, Cornerlis, and Elisa Struik. *Physical Aging in Amorphous Polymers and Other Materials*. 1977.
- [21] Dewimille, B., and A.R. Bunsell. "Accelerated Ageing of a Glass Fiber-Reinforced Epoxy Resin in Water." *Composites*. (1983): 35-40.
- [22] Wong, E.H., S.W. Koh, et al. "Advanced Moisture Diffusion Modeling & Characterisation for Electronic Packaging." (2002): 1297-1303.
- [23] Momentive. "*Technical Data Sheet*." 2012.
- [24] Pollard, A., R. Baggot, et al. "Influence of hydrostatic pressure on the moisture absorption of glass fibre-reinforced polyester." *Journal of Material Science*. 24. (1989): 1665-1669.
- [25] "The Advantages of Epoxy Resin versus Polyester in Marine Composite Structures." SP. <<http://www.catamaransailingphuket.com/EPOXY-VINYL-ESTER.pdf>>.
- [26] Shirangi, M.H., and B. Michel. "*Mechanism of Moisture Diffusion, Hygroscopic Swelling, and Adhesion Degradation in Epoxy Molding Compounds*." (2010): Web.
- [27] Gopalan, R, and B.R. Somashekar. "Environmental Effects on Fibre-Polymer Composites." *Polymer Degradation and Stability*. 24. (1989): 361-371. Web.
- [28] *U.S. Energy Information Administration*. Electric Power Monthly 2016; Available from: <https://www.eia.gov>.
- [29] *Marine and Hydrokinetic Resource Assesment and Characterization*. 2017.
- [30] Mishnaevsky, L., et al., *Materials for Wind Turbine Blades: An Overview*. Materials, 2017. **10**(11): p. 1285.
- [31] Samborsky, D., J. Mandell, and D. Miller, *The SNL/MSU/DOE Fatigue of Composite Materials Database: Recent Trends*, in *53rd ALAA/ASME/ASCE/AHS/ASC Structures, Structural Dynamics and Materials Conference*. 2012, American Institute of Aeronautics and Astronautics.
- [32] Barbero, E.J., *Introduction to Composite Materials Design, Second Edition*. 2010: Taylor & Francis.
- [33] Bergan, A., et al., *A Mode I cohesive law characterization procedure for through-the-thickness crack propagation in composite laminates*. Composites Part B: Engineering, 2016. **94**(Supplement C): p. 338-349.
- [34] Cantwell, W.J. and J. Morton, *The significance of damage and defects and their detection in composite materials: A review*. The Journal of Strain Analysis for Engineering Design, 1992. **27**(1): p. 29-42.
- [35] Reifsnider, K., *FATIGUE BEHAVIOR OF COMPOSITE-MATERIALS*. International Journal of Fracture, 1980. **16**(6): p. 563-583.
- [36] Stoffels, M., *Effects of externally applied tensile stresses on the moisture diffusion characteristics of epoxy glass composites*, in *Mechanical Engineering*. 2013, Montana State UNiversity.

- [37] Shen, C.H. and G.S. Springer, *Moisture Absorption and Desorption of Composite-Materials*. Journal of Composite Materials, 1976. **10**(Jan): p. 2-20.
- [38] Tsai, Y., et al., *Influence of hygrothermal environment on thermal and mechanical properties of carbon fiber/fiberglass hybrid composites*. Composites Science and Technology, 2009. **69**(3): p. 432-437.
- [39] Zhou, J.M. and J.P. Lucas, *Hygrothermal effects of epoxy resin. Part I: the nature of water in epoxy*. Polymer, 1999. **40**(20): p. 5505-5512.
- [40] Zhou, J.M. and J.P. Lucas, *Hygrothermal effects of epoxy resin. Part II: variations of glass transition temperature*. Polymer, 1999. **40**(20): p. 5513-5522.
- [41] Nogueira, P., et al., *Effect of water sorption on the structure and mechanical properties of an epoxy resin system*. Journal of Applied Polymer Science, 2001. **80**(1): p. 71-80.
- [42] Grammatikos, S.A., et al., *On the response to hygrothermal aging of pultruded FRPs used in the civil engineering sector*. Materials & Design, 2016. **96**(Supplement C): p. 283-295.
- [43] Garg, M., et al., *Effect of hygrothermal aging on GFRP composites in marine environment*. Steel and Composite Structures, 2017. **25**(1): p. 93-104.
- [44] Tsenoglou, C.J., S. Pavlidou, and C.D. Papaspyrides, *Evaluation of interfacial relaxation due to water absorption in fiber-polymer composites*. Composites Science and Technology, 2006. **66**(15): p. 2855-2864.
- [45] Perreux, D. and C. Suri, *A study of the coupling between the phenomena of water absorption and damage in glass/epoxy composite pipes*. Composites Science and Technology, 1997. **57**(9): p. 1403-1413.
- [46] Mourad, A.-H.I., et al., *Effect of Seawater and Warm Environment on Glass/Epoxy and Glass/Polyurethane Composites*. Applied Composite Materials, 2010. **17**(5): p. 557-573.
- [47] Miller, D., et al., *Performance of composite materials subjected to salt water environments*. 2012 AIAA SDM Wind Energy Session, 2012.
- [48] Nunemaker, J.D., *Effects of saltwater saturation on the static strength and acoustic emission signatures of epoxy glass composites* in *SAMPE Conference Proceedings*. 2016, Society for the Advancement of Material and Process Engineering. : Long Beach, CA.
- [49] Nunemaker, J.D., *Static strength reduction and acoustic emission analysis of fiberglass-epoxy samples subjected to various levels of moisture absorption* in *SAMPE Conference Proceedings*. 2017, Society for the Advancement of Material and Process Engineering – North America: Seattle, WA.
- [50] Liao, K., C.R. Schultheisz, and D.L. Hunston, *Effects of environmental aging on the properties of pultruded GFRP*. Composites Part B-Engineering, 1999. **30**(5): p. 485-493.
- [51] Siriruk, A. and D. Penumadu, *Degradation in fatigue behavior of carbon fiber-vinyl ester based composites due to sea environment*. Composites Part B-Engineering, 2014. **61**: p. 94-98.

- [52] Xin, H., et al., *Hygrothermal aging effects on flexural behavior of pultruded glass fiber reinforced polymer laminates in bridge applications*. Vol. 127. 2016. 237-247.
- [53] Garg, A. and O. Ishai, *Characterization of Damage Initiation and Propagation in Graphite/Epoxy Laminates by Acoustic-Emission*. Engineering Fracture Mechanics, 1985. **22**(4): p. 595-608.
- [54] Garg, A. and O. Ishai, *Hygrothermal influence on delamination behavior of graphite/epoxy laminates*. Engineering Fracture Mechanics, 1985. **22**(3): p. 413-427.
- [55] Liu, P.F., J. Yang, and X.Q. Peng, *Delamination analysis of carbon fiber composites under hygrothermal environment using acoustic emission*. Journal of Composite Materials, 2017. **51**(11): p. 1557-1571.
- [56] Hahn, H. and R. Kim, *Swelling of Composite Laminates*, in *Swelling of Composite Laminates*. 1978.
- [57] Papanicolaou, G.C., et al., *Water absorption mechanism and some anomalous effects on the mechanical and viscoelastic behavior of an epoxy system*. Journal of Applied Polymer Science, 2006. **99**(4): p. 1328-1339.
- [58] Netravali, A.N., et al., *Effects of water sorption at different temperatures on permanent changes in an epoxy*. Journal of Applied Polymer Science, 1985. **30**(4): p. 1573-1578.
- [59] Komai, K., K. Minoshima, and S. Shiroshita, *Hygrothermal degradation and fracture process of advanced fibre-reinforced plastics*. Materials Science and Engineering: A, 1991. **143**(1): p. 155-166.
- [60] Assarar, M., et al., *Influence of water ageing on mechanical properties and damage events of two reinforced composite materials: Flax-fibres and glass-fibres*. Materials & Design, 2011. **32**(2): p. 788-795.
- [61] Ray, B.C., *Temperature effect during humid ageing on interfaces of glass and carbon fibers reinforced epoxy composites*. Journal of Colloid and Interface Science, 2006. **298**(1): p. 111-117.
- [62] Gaur, U., C.T. Chou, and B. Miller, *Effect of hydrothermal ageing on bond strength*. Composites, 1994. **25**(7): p. 609-612.
- [63] Bradley, W.L. and T.S. Grant, *The effect of the moisture absorption on the interfacial strength of polymeric matrix composites*. Journal of Materials Science, 1995. **30**(21): p. 5537-5542.
- [64] Gorman, M.R., *Plate wave acoustic emission*. The Journal of the Acoustical Society of America, 1991. **90**(1): p. 358-364.
- [65] Schuster, M., *Characterization and Energy Analysis of Fiber Reinforced Polymer Composites by Acoustic Emission Analysis*, in *Mechanical Engineering*. 2014, Montana State University.
- [66] deGroot, P.J., P.A.M. Wijnen, and R.B.F. Janssen, *Real-time frequency determination of acoustic emission for different fracture mechanisms in carbon epoxy composites*. Composites Science and Technology, 1995. **55**(4): p. 405-412.
- [67] Ramirez-Jimenez, C.R., et al., *Identification of failure modes in glass/polypropylene composites by means of the primary frequency content of the acoustic emission event*. Composites Science and Technology, 2004. **64**(12): p. 1819-1827.

- [68] Suzuki, M., et al., *Fatigue Fracture Mechanism of Class A-SMC by Acoustic Emission Method*. Journal of the Society of Materials Science, Japan, 1987. **36**(411): p. 1402-1408.
- [69] Bohse, J., *Acoustic emission characteristics of micro-failure processes in polymer blends and composites*. Composites Science and Technology, 2000. **60**(8): p. 1213-1226.
- [70] Ni, Q.-Q. and M. Iwamoto, *Wavelet transform of acoustic emission signals in failure of model composites*. Engineering Fracture Mechanics, 2002. **69**(6): p. 717-728.
- [71] Bourchak, M., et al., *Acoustic emission energy as a fatigue damage parameter for CFRP composites*. International Journal of Fatigue, 2007. **29**(3): p. 457-470.
- [72] Kumar, C.S., V. Arumugam, and C. Santulli, *Characterization of indentation damage resistance of hybrid composite laminates using acoustic emission monitoring*. Composites Part B-Engineering, 2017. **111**: p. 165-178.
- [73] Gutkin, R., et al., *On acoustic emission for failure investigation in CFRP: Pattern recognition and peak frequency analyses*. Mechanical Systems and Signal Processing, 2011. **25**(4): p. 1393-1407.
- [74] Pashmforoush, F., M. Fotouhi, and M. Ahmadi, *Acoustic emission-based damage classification of glass/polyester composites using harmony search k-means algorithm*. Journal of Reinforced Plastics and Composites, 2012. **31**(10): p. 671-680.
- [75] Surgeon, M. and M. Wevers, *Modal analysis of acoustic emission signals from CFRP laminates*. Ndt & E International, 1999. **32**(6): p. 311-322.
- [76] Voth, M.M., *Exploring frequency based analysis methods for damage identification in fiberglass-epoxy composite systems*, in *SAMPE Conference Proceedings*. 2017, Society for the Advancement of Material and Process Engineering – North America: Seattle, WA.
- [77] Hamstad, M., *Local characterization of fiber composites by acoustic emission*. The Journal of the Acoustical Society of America, 1983. **73**(6): p. 2230-2230.
- [78] Czigány, T., Z.A. Mohd Ishak, and J. Karger-Kocsis, *On the failure mode in dry and hygrothermally aged short fiber-reinforced injection-molded polyarylamide composites by acoustic emission*. Applied Composite Materials, 1995. **2**(5): p. 313-326.
- [79] Su, Z., L. Ye, and Y. Lu, *Guided Lamb waves for identification of damage in composite structures: A review*. Journal of Sound and Vibration, 2006. **295**(3): p. 753-780.
- [80] Castaings, M. and B. Hosten, *Ultrasonic guided waves for health monitoring of high-pressure composite tanks*. NDT & E International, 2008. **41**(8): p. 648-655.
- [81] Instruments, T., *Interpreting Unexpected Events and Transitions in DSC Results*.
- [82] *Standard Test Method for Tensile Properties of Polymer Matrix Composite Materials*. 2014, ASTM International.
- [83] Murdy, P., *Detecting damage progression in gfrps through use of ultrasonic impulses and acoustic emission for structural health monitoring*, in *SAMPE 2016*. 2016: Long Beach, CA. p. 1916-1928.

- [84] D. o. E. DOE. (2015). *Quadrennial Technology Review*. Available: http://energy.gov/sites/prod/files/2015/09/f26/Quadrennial-Technology-Review-2015_0.pdf
- [85] W. J. Cantwell and J. Morton, "THE SIGNIFICANCE OF DAMAGE AND DEFECTS AND THEIR DETECTION IN COMPOSITE-MATERIALS - A REVIEW," (in English), *Journal of Strain Analysis for Engineering Design*, Review vol. 27, no. 1, pp. 29-42, Jan 1992.
- [86] B. W. Kim and J. A. Nairn, "Observations of fiber fracture and interfacial debonding phenomena using the fragmentation test in single fiber composites," *Journal of Composite Materials*, vol. 36, no. 15, pp. 1825-1858, 2002 2002.
- [87] C. H. Shen and G. S. Springer, "MOISTURE ABSORPTION AND DESORPTION OF COMPOSITE-MATERIALS," *Journal of Composite Materials*, vol. 10, no. JAN, pp. 2-20, 1976 1976.
- [88] W. L. Bradley and T. S. Grant, "THE EFFECT OF THE MOISTURE ABSORPTION ON THE INTERFACIAL STRENGTH OF POLYMERIC MATRIX COMPOSITES," (in English), *Journal of Materials Science*, Article vol. 30, no. 21, pp. 5537-5542, Nov 1995.
- [89] G. Marom and L. J. Broutman, "MOISTURE IN EPOXY-RESIN COMPOSITES," *Journal of Adhesion*, vol. 12, no. 2, pp. 153-164, 1981 1981.
- [90] M. Stoffels, "EFFECTS OF EXTERNALLY APPLIED TENSILE STRESSES ON THE MOISTURE DIFFUSION CHARACTERISTICS OF EPOXY GLASS COMPOSITES."
- [91] D. Miller, "Evaluating performance of composite materials for MHK applications," *ASME 2011 International Mechanical Engineering Congress and Exposition, IMECE 2011*, vol. 8, pp. 47 - 51, 2011.
- [92] U. S. E. I. Administration, "Annual Energy Outlook 2018 with projections to 2050," *J. Phys. A Math. Theor.*, vol. 44, no. 8, pp. 1–64, 2018.
- [93] B. Bose, "Global Warming: Energy, Environmental Pollution, and the Impact of Power Electronics," *IEEE Ind. Electron. Mag.*, vol. 4, no. 1, pp. 6–17, 2010.
- [94] H. Reichle et al., "References 5.," vol. 302, no. December, pp. 1719–1723, 2003.
- [95] "U.S. Energy Facts - Energy Explained, Your Guide To Understanding Energy - Energy Information Administration." [Online]. Available: https://www.eia.gov/energyexplained/?page=us_energy_home. [Accessed: 10-Sep- 2018].
- [96] "Marine and Hydrokinetic Resource Assessment and Characterization | Department of Energy." [Online]. Available: <https://www.energy.gov/eere/water/marine-and-hydrokinetic-resource-assessment-and-characterization>. [Accessed: 07-Sep-2018].
- [97] P. Beiter et al., "A Spatial-Economic Cost- Reduction Pathway Analysis for U.S. Offshore Wind Energy Development from 2015–2030," no. September, 2016.

- [98] [DOE] U.S. Department of Energy, “Offshore Wind Initiatives at the U.S . Department of Energy,” Doe/Ee-1486, p. 4, 2017.
- [99] D. S. Jenne, Y. Yu, and V. Neary, “Levelized Cost of Energy Analysis of Marine and Hydrokinetic Reference Models Preprint,” no. April, 2015.
- [100] EIA, “Levelized Cost and Levelized Avoided Cost of New Generation Resources in the Annual Energy Outlook 2018,” no. March, pp. 1–20, 2018.
- [101] E. J. Barbero, *Introduction to Composite Materials Design*. 2015.
- [102] Z. Chen, X. Zhou, X. Wang, L. Dong, and Y. Qian, “Deployment of a smart structural health monitoring system for long-span arch bridges: A review and a case study,” *Sensors (Switzerland)*, vol. 17, no. 9, 2017.
- [103] W. A. Altabay and M. Noori, “An Extensive Overview of Lamb Wave Technique for Detecting Fatigue An Extensive Overview of Lamb Wave Technique for Detecting Fatigue Damage in Composite Structures,” *Ind. Syst. Eng.*, vol. 2, no. 6, pp. 1–20, 2017.
- [104] M. F. Schuster, “CHARACTERIZATION AND ENERGY ANALYSIS OF FIBER REINFORCED POLYMER COMPOSITES BY ACOUSTIC EMISIION ANALYSIS,” 2014.
- [105] K. L. Reifsnider, *Fatigue of Composite Materials*. 1991.
- [106] G. Camino, A. Y. Polishchuk, M. P. Luda, M. Revellino, R. Blancon, and J. J. Martinez-Vega, “Water ageing of SMC composite materials: A tool for material characterisation,” *Polym. Degrad. Stab.*, vol. 61, no. 1, pp. 53–63, 1998.
- [107] “66 Weatheirng study of glass-fiber reinforced polyester sheets by scanning electron microscopy - 10.1002@pen.760120109.pdf,” pp. 53–58.
- [108] L. Prian and A. Barkatt, “Degradation mechanism of fiber-reinforced plastics and its implications to prediction of long-term behavior,” *J. Mater. Sci.*, vol. 34, no. 16, pp. 3977–3989, 1999.
- [109] C.-H. Shen and G. S. Springer, “Moisture absorption and desorption of composite materials,” *Compos. Mater.*, vol. 10, pp. 2–20, 1976.
- [110] G. C. Papanicolaou, T. V. Kosmidou, A. S. Vatalis, and C. G. Delides, “Water absorption mechanism and some anomalous effects on the mechanical and viscoelastic behavior of an epoxy system,” *J. Appl. Polym. Sci.*, vol. 99, no. 4, pp. 1328–1339, 2006.
- [111] P. Nogueira et al., “Effect of water sorption on the structure and mechanical properties of an epoxy resin system,” *J. Appl. Polym. Sci.*, vol. 80, no. 1, pp. 71–80, 2001.

- [112] H. N. Narasimha Murthy, M. Sreejith, M. Krishna, S. C. Sharma, and T. S. Sheshadri, "Seawater durability of epoxy/vinyl ester reinforced with glass/carbon composites," *J. Reinf. Plast. Compos.*, vol. 29, no. 10, pp. 1491–1499, 2010.
- [113] M. R. Gorman, "Plate wave acoustic emission," *J. Acoust. Soc. Am.*, vol. 90, no. 1, pp. 358–364, 1991.
- [114] G. N. Morscher, "Modal acoustic emission of damage accumulation in a woven SiC / SiC composite," *Compos. Sci. Technol.*, vol. 59, no. 5, pp. 687–697, 1999.
- [115] N. R. Center, "AE Signal Features." [Online]. Available: [https://www.nde-ed.org/EducationResources/CommunityCollege/Other Methods/AE/AE_Signal Features.php](https://www.nde-ed.org/EducationResources/CommunityCollege/Other%20Methods/AE/AE_Signal%20Features.php).
- [116] P. J. de Groot, P. A. M. Wijnen, and R. B. F. Janssen, "Real-time frequency determination of acoustic emission for different fracture mechanisms in carbon/epoxy composites," *Compos. Sci. Technol.*, vol. 55, no. 4, pp. 405–412, 1995.
- [117] A. R. Oskouei, M. Ahmadi, and M. Hajikhani, "Wavelet-based acoustic emission characterization of damage mechanism in composite materials under mode I delamination at different interfaces," *Express Polym. Lett.*, vol. 3, no. 12, pp. 804–813, 2009.
- [118] M. G. R. Sause, A. Gribov, A. R. Unwin, and S. Horn, "Pattern recognition approach to identify natural clusters of acoustic emission signals," *Pattern Recognit. Lett.*, vol. 33, no. 1, pp. 17–23, 2012.
- [119] J. Martínez-Jequier, A. Gallego, E. Suárez, F. J. Juanes, and Á. Valea, "Real-time damage mechanisms assessment in CFRP samples via acoustic emission Lamb wave modal analysis," *Compos. Part B Eng.*, vol. 68, pp. 317–326, 2015.
- [120] J. Bohse, "Acoustic emission characteristics of micro-failure processes in polymer blends and composites," *Compos. Sci. Technol.*, vol. 60, pp. 1213–1226, 2000.
- [121] W. Haselbach and B. Lauke, "Acoustic emission of debonding between fibre and matrix to evaluate local adhesion," *Compos. Sci. Technol.*, vol. 63, no. 15, pp. 2155–2162, 2003.
- [122] C. R. Ramirez-Jimenez, N. Papadakis, N. Reynolds, T. H. Gan, P. Purnell, and M. Pharaoh, "Identification of failure modes in glass/polypropylene composites by means of the primary frequency content of the acoustic emission event," *Compos. Sci. Technol.*, vol. 64, no. 12, pp. 1819–1827, 2004.
- [123] A. Marec, J. H. Thomas, and R. El Guerjouma, "Damage characterization of polymer-based composite materials: Multivariable analysis and wavelet transform for clustering acoustic emission data," *Mech. Syst. Signal Process.*, vol. 22, no. 6, pp. 1441–1464, 2008.

- [124] S. Barrand M. L. Benzeggagh, "ON THE USE OF ACOUSTIC EMISSION TO INVESTIGATE DAMAGE MECHANISMS IN GLASS - FIBRE - REINFORCED POLYPROPYLENE," vol. 3538, no. 94, pp. 369–376, 1994.
- [125] M. G. R. Sause, T. Müller, A. Horoschenkoff, and S. Horn, "Quantification of failure mechanisms in mode-I loading of fiber reinforced plastics utilizing acoustic emission analysis," *Compos. Sci. Technol.*, vol. 72, no. 2, pp. 167–174, 2012.
- [126] N. Godin, S. Hugué, and R. Gaertner, "Integration of the Kohonen's self-organising map and k-means algorithm for the segmentation of the AE data collected during tensile tests on cross-ply composites," *NDT E Int.*, vol. 38, no. 4, pp. 299–309, 2005.
- [127] C. Suresh Kumar, V. Arumugam, R. Sengottuvelusamy, S. Srinivasan, and H. N. Dhakal, "Failure strength prediction of glass/epoxy composite laminates from acoustic emission parameters using artificial neural network," *Appl. Acoust.*, vol. 115, pp. 32–41, 2017.
- [128] P. Murdy, "Combining Acoustic Emission and Guided Ultrasonic Waves for Global Property Prediction and Structural Health Monitoring of Glass Fiber Composites," 2018.
- [129] Q. Q. Ni and M. Iwamoto, "Wavelet transform of acoustic emission signals in failure of model composites," *Eng. Fract. Mech.*, vol. 69, no. 6, pp. 717–728, 2002.
- [130] M. M. Voth, D. A. Miller, J. D. Nunemaker, P. Murdy, D. D. Samborsky, and D. S. Cairns, "Exploring Frequency Based Analysis Methods for Damage Identification in Fiberglass-Epoxy Composite Systems .," 2017.
- [131] M. A. Hamstad, "Local Characterization of Fiber Composites by Acoustic Emission," *J. Acoust. Soc. Am.*, vol. 73, no. 6, pp. 2230–2230, 1983.
- [132] A. Garg and O. Ishai, "Hygrothermal influence on delamination behavior of graphite/epoxy laminates," *Eng. Fract. Mech.*, vol. 22, no. 3, pp. 413–427, 1985.
- [133] A. C. Garg, "Intralaminar and Interlaminar Fracture in Graphite-Epoxy Laminates," vol. 23, no. 4, pp. 719–733, 1986.
- [134] K. Komai, K. Minoshima, and T. Shibutani, "Investigations of the Fracture Mechanism of Carbon/Epoxy Composites by AE Signal Analysis," *JSME Int. J.*, vol. 34, 1991.
- [135] T. Czigány, Z. A. Mohd Ishak, and J. Karger-Kocsis, "On the failure mode in dry and hygrothermally aged short fiber-reinforced injection-molded polyarylamide composites by acoustic emission," *Appl. Compos. Mater. An Int. J. Sci. Appl. Compos. Mater.*, vol. 2, no. 5, pp. 313–326, 1995.
- [136] N. Ning et al., "Realizing the enhancement of interfacial interaction in semicrystalline polymer/filler composites via interfacial crystallization," *Prog. Polym. Sci.*, vol. 37, no. 10, pp. 1425–1455, 2012.

- [137] M. M. Voth, "CHARACTERIZATION OF THE EFFECTS OF HYGROTHERMAL-AGING ON MECHANICAL PERFORMANCE AND DAMAGE PROGRESSION OF FIBERGLASS EPOXY COMPOSITE," no. April, 2018.
- [138] EVAL; KURARAY, "Technical Bulletin No . 110 G
- [139] AS BARRIER PROPERTIES OF The most outstanding property of EVAL ® resins is their ability to provide a barrier to gases such as oxygen , nitrogen , carbon dioxide and helium . This property is especially important when consider," no. 110, pp. 1–12.
- [140] J. D. Nunemaker, M. M. Voth, D. A. Miller, D. D. Samborsky, P. Murdy, and D. S. Cairns, "Effects of moisture absorption on damage progression and strength of unidirectional and cross-ply fiberglass – epoxy composites," pp. 427–438, 2018.
- [141] David Miller; John F. Mandell; Daniel D. Samborsky; Bernadette A. Hernandez- Sanchez; D. Todd Griffith, "Performance of Composite Materials Subjected to Salt Water Environments," 2012 AIAA SDM Wind Energy Sess., 2012.
- [142] J. F. Mandell, D. D. Samborsky, and D. S. Cairns, "SANDIA CONTRACTORS REPORT FATIGUE OF COMPOSITE MATERIALS AND by," Mont. Mag. West. Hist.
- [143] V. M. Karbhari and G. Xian, "Hygrothermal effects on high VFpultruded unidirectional carbon/epoxy composites: Moisture uptake," *Compos. Part B Eng.*, vol. 40, no. 1, pp. 41–49, 2009.
- [144] K. Liao, C. R. Schultheisz, and D. L. Hunston, "Effects of environmental aging on the properties of pultruded GFRP," *Compos. Part B Eng.*, vol. 30, no. 5, pp. 485– 493, 1999.
- [145] M. W. Keller, B. D. Jellison, and T. Ellison, "Composites : Part B Moisture effects on the thermal and creep performance of carbon fiber / epoxy composites for structural pipeline repair," *Compos. Part B*, vol. 45, no. 1, pp. 1173–1180, 2013.
- [146] J. D. Nunemaker, "EXPLORING THE EFFECTS OF FIBER ANGLE AND STACKING SEQUENCE," no. January, 2017.
- [147] A. J. Lolatte, "Influence of Fabric Architecture on Damage Progression as Evidenced by Acoustic Emission," no. July, 2016.
- [148] S. C. Woo and N. S. Goo, "Analysis of the bending fracture process for piezoelectric composite actuators using dominant frequency bands by acoustic emission," *Compos. Sci. Technol.*, vol. 67, no. 7–8, pp. 1499–1508, 2007.
- [149] T. Fu, Y. Liu, Q. Li, and J. Leng, "Fiber optic acoustic emission sensor and its applications in the structural health monitoring of CFRP materials," *Optics and Lasers in Engineering*, vol. 47, no. 10. pp. 1056–1062, 2009.

This page left blank

DISTRIBUTION

Email—Internal

Name	Org.	Sandia Email Address
Budi Gunawan	08822	bgunawa@sandia.gov
Peter Kobos	08822	phkobos@sandia.gov
Bernadette A. Hernandez-Sanchez	01815	baherna@sandia.gov
Technical Library	01977	sanddocs@sandia.gov

Email—External

Name	Company Email Address	Company Name
Lauren Ruedy	lauren.ruedy@ee.doe.gov	Department of Energy Water Power Technologies Office
David Miller	davidmiller@montana.edu	Montana State University

Hardcopy—External

Number of Copies	Name	Company Name and Company Mailing Address
3	David Miller	Mechanical and Industrial Engineering Dept. Montana State University 220 Roberts Hall Bozeman, MT 59717-3800

This page left blank



Sandia
National
Laboratories

Sandia National Laboratories is a multimission laboratory managed and operated by National Technology & Engineering Solutions of Sandia LLC, a wholly owned subsidiary of Honeywell International Inc. for the U.S. Department of Energy's National Nuclear Security Administration under contract DE-NA0003525.